CRANFIELD INSTITUTE OF TECHNOLOGY

SCHOOL OF INDUSTRIAL AND MANUFACTURING SCIENCE

PhD THESIS

ACADEMIC YEAR 1990-1991

T. KONEFAL

The use of Hall effect probes in the detection and sizing of cracks in steel structures

Supervisor : R. Allwood

February 1991

ABSTRACT

The most commonly used method for non-destructive testing (NDT) of welded tubulars in underwater locations is magnetic particle inspection (MPI). This method is effective in terms of crack or defect detection, but requires much diver effort. This work examines the use of Hall effect probes for crack detection and measurement in steel specimens and underwater pipelines and structures. A simple theory of magnetic leakage fields is developed, and how such fields relate to crack characteristics. The finite sizes of the Hall probes employed are taken into account, and an analytic expression for the field from a tapered crack is developed. Practical magnetic signals from a cracked Y-jointed tubular are taken, and shown to be consistent with MPI indications.

A double probe system is proposed which enables crack depth measurement to be made irrespective of a knowledge of the crack width or level of magnetisation in the specimen. Experiments using a prototype double probe system show encouraging results on artificial cracks in small specimens, though there is a troubling unknown background bias effect in the measured signals.

An instrument using a time differentiated probe signal has been developed which is capable of detecting a crack in a Y-joint at a scan height of up to 5mm with a level of magnetisation rather less than that used by MPI. A method of continuously monitoring a crack in a Y-joint is also described, using multiple differential pairs of probes. The method is found to give indications consistent and comparable with MPI.

CONTENTS

PAGE NO.

PAGE NO.

CHAPTER 4 THE LOHET II, CRACK DEPTH MEASUREMENT AND THE DOUBLE PROBE SYSTEM

CHAPTER 5 CRACK DETECTION AND MONITORING

CHAPTER 6 CONCLUSIONS AND RECOMMENDATIONS FOR FUTURE WORK

<u>**FIGURES**</u>

PAGE NO.

PAGE NO.

PAGE NO.

PAGE NO.

PAGE NO.

NOTATION AND UNITS

B	Magnetic induction field (1 Tesla = 10^4 Gauss)
H	Magnetic field intensity (Am^{-1})
M	Magnetisation (Am^{-1})
χ	Magnetic susceptibility
μ_o	Permeability of free space ($4\pi \times 10^{-7}$ Tesla $A^{-1}m$)
μ	Permeability (Tesla A^{-1} m)
μ_r	Relative permeability = μ/μ_o
$-\lvert e \rvert$	Electron charge (1.6×10^{-19} Coulomb)
J	Current density (Am^{-2})
σ	Conductivity (Ω^{-1} m^{-1})
E	Electric field (Vm^{-1})
NDT	Non-destructive testing
MPI	Magnetic particle inspection
MFL	Magnetic flux leakage

CHAPTER 1

INTRODUCTION AND LITERATURE SURVEY

1.1 Introduction

1.2 Literature Survey

1.1 Introduction

Events such as the Piper Alpha disaster which have taken place in recent years serve as continual reminders of the importance of monitoring and maintaining the integrity of offshore structures. As such structures and systems approach the end of their design life, the probability of structural and weld failure due to adverse conditions increases. In order to maintain safety standards in the light of increasingly squeezed profit margins, there is a need to improve underwater inspection techniques in terms of both efficiency and speed. The purpose of this project has been to help fulfil this requirement.

The work presented in this thesis was undertaken within the Structural Integrity Monitoring (SIM) Programme, a managed research programme sponsored jointly by industry and the SERC.

The technique under investigation was that of magnetic leakage field detection by use of Hall effect probes. It was desired to develop the technique to an extent which would allow the detection and monitoring of cracks in steel structures located underwater. In addition, a method was sought for which would allow measurement of cracks from their magnetic leakage fields.

The main agents responsible for the initiation and progression of cracks in offshore structures are those of fatigue and corrosion. These are discussed briefly in the following sections.

1.1.1 **Fatigue**

The effect of cyclic loading on a polished specimen is to initiate a crack. Experimental evidence indicates that frequently fatigue cracks originate in regions of slip which are associated with intrusions and extrusions on the surface. Thus theories of crack nucleation (1) concentrate on various possible slip processes.

Once a crack has initiated in a specimen, it will increase in length under continued cyclic loading. The growth of a crack involves the simultaneous lowering of strain energy and increase in surface energy. The increase in surface energy is a linear function of crack length while the decrease in strain energy depends on the square of the crack length. Hence, for a suitable crack of critical length, it is energetically favourable for the crack to propagate. Such is the process of brittle fracture. The inclusion of a term in the energy balance equation for the energy required to plastically deform a region at the crack tip (where the stress is above the yield stress) is a refinement of the model. However, such an energy balance approach is still inadequate in explaining the slow stable crack growth present in fatigue cracking.

Fatigue crack propagation will occur below the critical stress intensity factor K_c required for fracture. ($K_c \propto \sigma a^{1/2}$ where σ is the applied stress and 2a is the crack length). There have been many attempts to describe crack growth rates as a function of the number of fatigue cycles n, which are usually semi or wholly empirical in nature. The most widely used is the Paris equation:

$$\frac{da}{dn} = C(\Delta K)^m \qquad \text{(C, m are constants)}$$

ΔK represents the change in stress intensity factor occurring during the cycle.

Offshore structures are subjected to a considerably hostile environment. In particular they must withstand the periodic buffeting of waves and wind against the body of the structure, and also they must withstand the corrosive environment of sea water and air. It should be noted that, given the magnitude of stresses in offshore structures, critical crack lengths are of the order of microns, so that in offshore structures it is a question of propagation of cracks already present rather than initiation of cracks.

Wave motion is restricted to a region near the surface of the sea, and the motion of the water decays exponentially as we move to greater depth (2). As a wave form passes a point on the surface, an individual particle undergoes a circular orbital motion. The particle orbits become gradually smaller and more elliptical on moving to deeper regions until finally at the sea bed there is virtually a to and fro motion. The cyclonic belt near the surface causes a major hazard as far as fatigue cracking is concerned. Also for deep structures, motion at the surface results in amplified stresses near the base by a simple lever action, so that the cyclonic belt makes its presence felt at deeper regions than might at first be expected. about 5×10^6 waves will pass a North Sea installation during a year (3), which is an average of one wave every 6 or 7 seconds. This is of course a gross oversimplification and there is in practice a continuous spectrum of frequencies and amplitudes. The energy density of the waves at various frequencies is roughly a gaussian function of the wave period as in Figure 1, and the wave height probability distribution function follows the Rayleigh distribution, as in Figure 2. As wind speed picks up, and the sea becomes more turbulent, the peak in the energy spectrum moves towards lower frequencies (i.e. longer periods) and the most probable height of the waves increases.

Apart from the cyclic nature of the waves which tends to fatigue metal structures, other physical effects occur such as scouring, erosion, slamming and slapping which often defy analytical treatment.

1.1.2 Corrosion

Additional problems arise with corrosion of an offshore oil platform, which tends to weaken the structure by a chemical rather than a physical process. Corrosion in sea water is an electrochemical process involving the migration of electrons from regions of low electric potential to regions of high electric potential.

Differences in potential arise in various ways, see for example (5), (6). Pitting corrosion can result from a difference in potential between different areas of the same metal. Take for example the situation of an oxide film with a small break in it, exposing the bare metal underneath to sea water. Such a small area of oxide could easily be removed by the physical movement of water. The different positions of the oxide and metal in the electrochemical series results in a small e.m.f. which causes the metal to act as an anode. This results in Fe^{2+} ions going into solution, corroding the steel further.

Selective corrosion occurs when we have an alloy consisting of two or more metals which occupy different positions in the electrochemical series and so give rise to e.m.f.s within the metal.

Galvanic corrosion occurs when using two dissimilar metals in close proximity.

Crevice corrosion occurs in isolated areas such as crack tips where less oxygen is available for the repair of the oxide film than on a nearby exposed surface, setting up a potential difference.

The migration of electrons from regions of low electric potential to high electric potential results in oxidation of the former region and reduction of the latter. For example, the oxidation of iron can result in Fe^{2+} ions which are free to react with ions in the sea water such as OH^-, Cl^- or SO_4^{2-} to form the corrosion products iron hydroxide, iron chloride or iron sulphate. $FeCl_2$ and $FeSO_4$ will readily dissolve into the sea and thus a steel structure will be weakened as the steel is eaten away. $Fe(OH)_2$ may be precipitated but there will usually be sufficient oxygen present for it to be oxidised to common yellow rust, $Fe_2O_3.H_2O$ via

$$4Fe(OH)_2 + O_2 \rightarrow 2Fe_2O_3.H_2O + 2H_2O$$

A typical profile of corrosion rates for steel in the open sea is given by Tuthill and Schillmoller (7) in Figure 3. The vertical scale here depends on the particular structure in question. The worst area for corrosion is the splash zone, where corrosion products are regularly washed away by the eroding force of water slapping away at the structure, exposing fresh metal surface to the elements.

When fatiguing and corroding elements combine, we get the process of corrosion fatigue. A characteristic of corrosion fatigue is that the combined effect of the individual agents is greater than the sum of the individual agents, thus accelerating crack growth rates considerably.

One other process of crack formation of particular importance to welds is that of hydrogen induced cold cracking. This occurs when structures are welded in the presence of water, and hydrogen is inadvertently introduced into the weld material. Diffusion of hydrogen gas through the weld due to reduced solubility on cooling results in local gas pockets which can induce cracks.

1.1.3 Crack detection

The method most widely used for detecting cracks in offshore structures is magnetic particle inspection. In this technique the section of steel to be inspected is magnetised, usually by a nearby coil carrying a large current. If a surface or near surface crack is present, there will generally be a magnetic leakage field produced at the crack which serves as the means of detecting the crack. A 'magnetic ink' containing small ferromagnetic particles coated in bright paint is applied to the surface. The particles tend to conglomerate in the presence of the leakage field, and so the crack shows up as a coloured line on the surface of the metal. For underwater applications however, visibility is too poor to allow a coloured streak to be seen easily. A more usual method is to use an ink which contains particles coated with a fluorescent paint. The ink is applied to the specimen in the usual manner, but is viewed under ultraviolet light. This exposes any cracks as a bright green streak, greatly improving contrast.

The method is effective, but requires considerable diver effort. Typically, the diver must manipulate magnetising equipment, an ultraviolet lamp and photographic or video equipment, as well as actually applying the ink and responding to communications from the surface. In addition the suspect area must be cleaned of all marine growth before inspection can begin, using valuable diver time. MPI gives only visual information as to the location of a crack, and no effective measure of its width or depth. It is generally required that a fairly high field of 0.72

Tesla be present in the steel specimen (8).

The method of crack detection investigated in this thesis is that of leakage field detection by use of Hall effect probes. The Hall effect is described in various texts (9), but a comprehensive explanation is presented in Section 2.5.

1.2 Literature Survey

Hall effect probes have been used to some extent in non-destructive testing e.g. Ko and Francis (10), Sharif (11) and Marchant (12). In the latter case Hall effect probes have been employed in the non-destructive testing of lift machinery cables in the coal industry. The apparatus operates by magnetising the multi wire cable locally with permanent magnets and examining the leakage field from any cracks or wire breaks with the Hall effect probes, as in Figure 4. By virtue of the movement of the cable in service it is possible to bring each point of the cable under the scrutiny of the probes, having the apparatus in a fixed position at the earth's surface. A time varying signal is thus obtained from the probes.

By using suitably orientated probes, both the radial and axial components of field could be monitored. The question arises as to the form that these signals should take.

Zatsepin and Shcherbinin (13) considered a similar problem whereby the leakage field from a surface crack was calculated by considering the crack faces to be equally and oppositely magnetically charged (see Section 2.1). The problem is mathematically equivalent to solving for the electric field in the vicinity of a parallel rectangular plate charged capacitor. The vertical and horizontal fields at a height z and distance x out from the centre of an infinitely long crack of width 2b and depth h were found to be (see Figure 5)

$$H_{vert} = \frac{M}{4\pi} \ln\left\{\frac{[(h+z)^2 + (x+b)^2][z^2 + (x-b)^2]}{[(h+z)^2 + (x-b)^2][z^2 + (x+b)^2]}\right\} \text{Eqn.(1)}$$

$$H_{Tang} = \frac{M}{2\pi}\left\{\arctan\left(\frac{h+z}{x+b}\right) - \arctan\left(\frac{z}{x+b}\right) - \arctan\left(\frac{h+z}{x-b}\right) + \arctan\left(\frac{z}{x-b}\right)\right\}$$

Eqn. (2)

Here M is the magnetisation in the specimen. Eqns. (1) and (2) are plotted in Figures 6 and 7 respectively. The problem of a magnetised and broken strand of wire is not exactly the same but still involves a magnetic dipole, with a smaller area of magnetic charge. The general shape of signals obtained by Marchant from a known short break in a wire using the apparatus of Figure 4 are indicated in Figures 8 and 9 and it can be seen that the qualitative agreement is excellent. Marchant was able to use the apparatus to count the number of broken wires within a given length of cable, and from this basis the decision whether or not to reject the cable could be made. It was found that when the broken wire ends were only 1mm apart, the general background noise from the rope would overshadow the signal from the break. In general however, the wire ends would be pulled further apart than this because of the tension in the steel rope, and so detection was still possible.

Lord and Oswald (14) give a review of NDT methods in 1972 in which it is reported that Hall devices had seen limited use as leakage field detectors, mainly due to their fragility and temperature dependence at the time . They report work by Stumm (15) which backs up their own work (16) in finding that the leakage field amplitude is directly proportional to crack depth. Also reported (17) is the method of replacing an eddy current coil by a Hall probe in measuring the magnetic reaction field of an eddy current inducing coil. Lankford and Francis (18) report typical Hall probe sensitivities of the day as being between ¼ and 1μV per gauss.

Novikova and Miroshin (19) produced a model in which magnetic charges, not only at the crack surfaces, but also in the regions slightly behind the faces, could be taken into account. The object of such a model was to take into account the non-linearity of the magnetic characteristics of the materials used, and to produce a model which avoided the prediction of infinite fields. Eqn.(1) of Zatsepin and Shcherbinin and those of other authors cited by Novikova and Miroshin (20) (21) (22) predict an infinite field at the point of emergence of the crack at the surface. To avoid this problem the infinite strip dipole model of Zatsepin and Shcherbinin was replaced by an infinite and parallel linear dipole. The locations of the line dipole elements were at certain equal distances from the charged strips, within the bulk of the metal, and at a certain distance below the surface. They proposed that the tangential field maximum at x=0 in Figure 7 could be calculated from an equation of the form $H_{Tang} = f(M)g(x_p, y_p)$ where f and g are functions of magnetisation and the linear dipole coordinates respectively. They noted, in agreement with work which they cite by Sapozhnikov and Bol'shakov (23) that the field H_{Tang} increased in sympathy with the magnetisation of the material and so expressed the function f in the form f(M) = fM. The factor f was found empirically to obey an approximate law, i.e.

$$f = 0.9 \exp\left[- (1 + 2 \frac{\mu - 1}{\mu_{max} - 1})\right]$$

where μ and μ_{max} are the actual and maximum permeabilities respectively. The function g was represented by, when referred back to the crack width 2b and depth h,

$$g(2b,h) = \frac{bh}{(0.1b+0.05)\ (0.15h+b+0.05)} \quad \text{(b and h in mm)}$$

Experiments were undertaken by Novikova and Miroshin in which artificial flaws of width 36-230μm and depth 3-10mm were examined at a scan height of 0.9mm. Typical results for flaw depth dependence and the theoretical treatment are shown in Figure 10. Experimental data showing how H_{Tang} varies with applied field, and how this relates to the magnetisation of the specimen in both cast iron and steel are presented in Figures 11 and 12. It can be seen that the leakage field follows the magnetisation closely.

Burtsev and Fedorishcheva (24) take the linear dipole model a stage further and express the depression δ of the dipole beneath the surface as a function of crack depth h, crack width 2b and scan height z. This was in an attempt to model defects of larger size than had been studied by Novikova and Miroshin. The salient expression for the strip dipole model is

$$\bar{\delta} = \frac{1}{\sqrt{2}} \left(- \bar{q}_1 + (\bar{q}_1 + 12\bar{q}_2)^{1/2} \right)^{1/2} - \bar{z}$$

where
$$\bar{q}_1 = \bar{z}^2 + (\bar{z}+\bar{h})^2 - 2$$
$$\bar{q}_2 = \bar{z}^2 + (\bar{z}^2+1)(\bar{z}+\bar{h})^2 + 1$$

and the bar represents division by b. The vertical component of field is then

$$H_{Vert} = - \frac{2m}{b^2} \frac{2\bar{x}\ (\bar{z}+\bar{\delta})}{[\bar{x}^2+(\bar{z}+\bar{\delta})^2\ ]^2}$$

where m represents the dipole moment per unit length of the filaments and x is the distance along the line of scan. They then proceed from this simplified formula to produce an expression for the average field picked up by a Hall probe of finite width. They point out that the expression is complicated, but would be far more complicated if the original strip dipole model of Zatsepin and Shcherbinin had been used.

Ko and Francis (10) have taken into account the finite area of a Hall probe when sensing the vertical signal given by Zatsepin and Shcherbinin (13) from a surface crack. The calculation involved an integration of the field presented to the probe over the surface of the probe, and then division by its area. This assumes uniform sensitivity and that the probe output will therefore be an average of the field presented over its area. The calculation yielded an expression for the signal in terms of the scan distance x, scan height z, crack width 2b, crack depth h, probe dimensions 2l and 2K, and the acute angle θ which the long side of the probe (2l) makes with the line of the crack. One suggestion made was that during a scanning operation the probe should be rotated to find the angle at which the largest signal is obtained. They showed that the maximum signal should be obtained when θ=0° so that the direction of the crack could be determined. In their experiments a Hall probe of size 25μm x 100μm was scanned at a height of 13μm over a crack, and it was found that the ratio of signal peaks for θ=0° and θ=45° was 1.85. Their calculation showed the theoretical value to be 1.67, a 10% difference.

Ko and Francis were also able to show both by theory and experiment that when crack lengths were much larger than the probe size (in this case greater than 400μm), the peak vertical magnetic leakage field is directly proportional to the applied stress in the specimen. This is essentially because fracture mechanics shows the C.O.D. (i.e. the crack width) of a semi-elliptical surface crack (see Figure 13) to be approximately proportional to the remote applied stress (25). When the crack is long Eqn.(1) of Zatsepin and Shcherbinin is valid; this equation has the property that its maximum value of H_{vert} is directly proportional to the crack width, at least for sufficiently small crack widths. Thus the peak vertical magnetic leakage field is directly proportional to the applied stress.

The small value of lift off (13μm) used by Ko and Francis is rather restrictive in view of the surface finish that would be present in a general inspection offshore. Lord, Bridges et al. (26) have used a Hall probe to detect the vertical component leakage field profiles over slots as small as 300μm in width and 5mm in depth and 3mm in width and 2.5mm in depth. In the latter case it was found that the active leakage field H_{vert} of a 3mm wide slot increased in a linear fashion with depth h, and could be fitted to an equation of the form $H_{vert} = ah+b$, with a and b fitted constants. The constant a was independent of the magnetising current I, whereas b was found to increase with I, though not linearly. Typical active leakage fields are as indicated in Figure 14. The horizontal scale in Figure 14 is not indicated in the original paper. It can be seen that there is a bias in the signal at regions far away from the crack that is not predicted by the equation of Zatsepin and Shcherbinin. Such biased signals were also found by Oehl and Swartzendruber (27) who suggested that the reason for the bias was imperfect alignment of the magnetisation vector within the body of the metal. There is in effect a component of magnetisation normal to the surface of the specimen, which results in an additional field normal to the surface which produces the bias. Oehl and Swartzendruber were able to fit their experimental curves to a modified version of Eqn. (1) by adding a spatially linear term to the field, though the origin of this field was not well understood.

Lord, Bridges et al. (26) measured residual leakage fields from their rectangular slots and found that while the signal amplitude was less than ten times the active leakage field (i.e. with a magnetising current present), the bias in the signal was much less apparent; the classical signal shapes of Figures 6 and 7 were much better represented. They pointed out that it was necessary to assume a particular value for the magnetisation M in order to obtain agreement between the theoretical and experimental signal profiles. This is a recurring problem when it comes to trying to predict defect parameters from leakage field profiles. Novikova and Miroshin (19) cite as examples (20), (21), (22). As the width of the crack increases, Lord et al. (26) found that plots of Eqn. (1) showed both the width and amplitude of the signals to increase, in contrast to Ko and Francis (10) who found the amplitude to vary linearly with crack width but that the signal width was independent of crack width. Lord does not mention what scan height he used, but it is clear from the plots that he gives (Figure 15) that he was using a scan height comparable with the crack width. This is evident because of the decrease in local slope at the origin compared to the immediate vicinity. Such behaviour is indeed predicted by Eqn.(1) for scan heights comparable to the crack width and under such circumstances a linear increase of signal width with crack width is also predicted. When the scan height is much greater than the crack width, the signal width becomes independent of crack width, according to Eqn. (1). Such a situation was modelled by Ko and Francis. Ko and Francis also used scan heights comparable to the crack width, but here the situation is complicated by the fact that the probe size is rather larger than the crack widths used. Ko and Francis showed that a finite probe width will tend to increase the signal width, though produced no explicit formula for this effect.

Lord and Hwang (28) have noted that the simple dipole model of Shcherbinin and Zatsepin could not be easily adapted to predict the signals from complex surface and subsurface flaws. To aid such predictions leakage fields have been modelled using a finite element method by Lord and Hwang (28) who have adapted the theory to the surface crack problem. Using a scan height comparable with the crack width, they found the signal width to be largely independent of crack depth, while the signal amplitude increased with depth as in Figure 16. These results are in agreement with experimental results by Zatsepin and Shcherbinin (29) and Lord and Oswald (16). Lord and Hwang found also that the signal width increases more or less linearly with crack width in contrast to Ko and Francis (Figure 17). However, in this case it is known that Lord and Hwang were modelling a scan height that was the same order or less than the crack width (scan height $z=0.5$ units in Figure 17) and under these circumstances even Eqn. (1) predicts a linear increase in agreement with their finite element techniques.

Lord and Hwang showed that as the angle that the crack made with the surface increased, so it introduced asymmetries into the leakage field profiles, as in Figure 18. Such behaviour was also demonstrated by Zatsepin and Shcherbinin (29) using their strip dipole model. Further modelling by Lord and Hwang produced a relationship between the shift ϕ of the total flux density profile $(B_{\mathrm{Vert}}^{2} + B_{\mathrm{Tang}}^{2})^{1/2}$ and the oblique angle θ. This is shown in Figure 19. Finally the normalised peak to peak field as a function of oblique angle θ was determined as in Figure 20.

These graphs formed the basis of a procedure for defect characterisation, namely:

1. Measure the peak to peak field and peak to peak distance.
2. Measure the shift angle ϕ from the total profile.
3. Estimate the width of the defect from Figure 17.
4. Estimate the oblique angle θ from Figure 19. With this value of θ estimate the normalised peak to peak magnitude from Figure 20.
5. Divide the peak to peak field from step 1 by the normalised value from step 4.
6. Find the effective depth of the defect from Figure 16.

This procedure should, in theory, be sufficient to characterise the width and depth of a crack. However, the modelling assumes that scan heights are used which are less than or of the same order as the crack width. Whilst this is fine for large width cracks or surfaces which have been finely polished so that probes can be held close to the surface, it would be of little value in sizing a fatigue crack in a steel specimen that had a rough surface finish, as will generally be the case in underwater inspection. In the latter regime we really ought to look at the case where the scan height is much greater than the crack width. Indeed it is realised by Lord and Hwang that it would be impossible to characterise a defect exactly from a given leakage profile, for the very important reason that there is not a one to one relationship between defect and defect signal. One criticism of the above characterisation procedure is that Figure 20 has been modelled using a particular value of depth and width of crack. The shape of this curve may well be different for other combinations. Hwang (30) points this out with respect to the width of the crack, so that having measured the width from Figure 17, we ought really to have several curves in Figures 16, 19 and 20 corresponding to different crack widths from which the characterisation procedure can be done. He illustrates this by modelling the effect of width in Figure 16. However, Hwang does not model the effect of depth in Figures 19 and 20 or point out the possibility that these curves could vary with depth of defect. If this were the case there would be several curves in Figures 19 and 20 for each crack depth, resulting in a range of solutions to the problem. The solution given by the particular curves shown would then be only an approximation. As a corollary, Hwang also concludes that it is impossible to characterise subsurface flaws from their leakage field characteristics. In all of Hwang's work it is necessary to be able to measure the level of excitation since the strength of the leakage field depends on this. The leakage field/applied current relationship follows that of the B/H curve for the material.

Hwang (30) has in addition used the finite element technique to model leakage fields from various defects such as triangular, semi-circular and sub surface defects. For a complete list see Ref. (30).

Francis and Moseley (31) have adapted Eqn. (1) to apply to finite cracks of a half penny shape as in Figure 21, which is a convenient model for a real fatigue crack. The model is at odds with their experimental data in two respects. These are that at the crack tips the signal amplitude becomes non-vanishing and the peak separation increases slightly, whereas the model predicts a zero amplitude and constant peak separation. They consider the finite amplitude to be due to a plastic zone beyond the crack tip in which the magnetic permeability may be expected to vary considerably, and so effectively increase the apparent length of the crack. This plastic zone is estimated from fracture mechanics and is incorporated in a model which successfully supports the evidence of a finite field beyond the crack tip. However, it fails to predict the observed widening of the peak separation, a discrepancy which is presented without being resolved. The lengths of crack studied were 0.762mm, 1.016mm and 1.270mm, with the scan height being 50.8µm. Once again, such a small stand off would be totally impractical for all but highly polished specimens. The crack widths involved are not specified.

Francis and Moseley seem to underestimate the importance of the fact that Eqn. (1) applies to an infinitely long slot. While their model works well over the centre portion of their cracks, where indeed the crack is apparently infinite (assuming the crack width is much less than 0.762mm), the crack at its tip is anything but infinite. Indeed it is semi-infinite. Symmetry argues that the field at the edge of a semi-infinite slot falls to exactly one half of the field over an infinite slot, following the method of Zatsepin and Shcherbinin. Thus there should not really be any surprise as to the non-zero field beyond the crack tip. Moreover the tip of the half penny shape of Figure 21 approximates to the corner of a crack which is an infinitely large square in shape. By moving beyond the crack tip we are effectively simultaneously increasing the stand off in a perpendicular direction. Under these circumstances Eqns. (1) and (2) predict an increasing separation of peaks and troughs in the two field directions perpendicular to that being measured in Francis and Moseley's experiment. Thus it is not unreasonable to assume that the method of Zatsepin and Shcherbinin will show that there should indeed be a separation in the third measured field direction also. A detailed calculation shows that this is indeed the case.

Lord and Palanisamy (32) have used Hall probes to detect changes in the crevice gap clearance of steam generator tubing. The crevice gap is the distance between the tubing and the surrounding support plates. This is important in ensuring an early warning system that indicates the possibility of tube denting. Using probe currents up to 1A, the probe output appeared as in Figure 22. The experiment was modelled by a finite element method and the predicted curve for a 0.6A current as indicated in Figure 22. They suggest that the discrepancy with experiment was due to incorrect B/H characterisatics used to model the magnetic behaviour of the steel. Nevertheless the technique is quite feasible.

Reviews by Bainton (33) and Beissner et al. (34) near the end of the 1970s showed the increasingly widespread use of magnetic leakage field techniques, but point out that while sensors such as moving coils and Hall probes provide more quantitative information than magnetic particle inspection, correlation of the measured field with the shape and size of defect still presented considerable difficulties.

In their review in 1980, Dobmann and Höller (35) outline the derivation of Eqns. (1) and (2) and discuss the work of Zatsepin and Shcherbinin (13) (29). Whilst there is a high level of coincidence between theory and experiment, it is necessary to assume a particular value of M in Eqn. (1) to produce this coincidence. In addition, the dependence of leakage signal on slot depth is found by experiment to be linear, whereas the model of Zatsepin and Shcherbinin predicts a saturation effect. Dobmann and Höller suggest that the discrepancy is due to an inexact selection of the distribution of M, which had inspired the work of Novikova and Miroshin (19), who tried to account for a magnetic charge density which varied volumetrically. The work of Shcherbinin and Pashagin (36) is described, who found, perhaps not surprisingly, that when the leakage signals from short length slots are measured, the field is considerably less than from long slots, other factors being held constant. With low levels of magnetic excitation, the 'infinite length' slot value of leakage field is reached for sufficiently large slot length l. However, even larger values of l are required to reach the infinite length value of leakage field for higher levels of magnetisation. This is something not predicted by the simple dipole model, and which Shcherbinin and Pashagin try to account for using a volume distribution of magnetic charge. The attempt is, however, unsuccessful.

Dobmann and Höller mention the work of Ko and Francis (10) and describe in some detail the finite element method of Lord and Hwang (28). Once again, the modelling predicts a saturation effect in the leakage signal amplitude dependence on slot depth. Dobmann and Höller conclude that there is a range of parameters which affect leakage fields, and are optimistic about the ability to characterise cracks from them. They do however emphasise the need for practical tests in the proof of this ability.

Förster (37) reexamines the problem of leakage field signals by modelling the case of a long and infinitely deep crack in ferromagnetic material by conformal mapping of an infinitely long strip, 2π wide, in the initial plane by means of the Schwarz-Kristoffel transformation function. The lines of force and constant magnetic field intensity cannot be found explicitly, and must be obtained by numerical methods. It is found that the vertical and tangential components so calculated are in agreement with Eqns. (1) and (2).

Förster points out that most people considered it necessary to measure fields at stand offs which were smaller than or comparable with the width of the crack. In addition to the authors mentioned so far Förster cites Dobmann (38) and Münnich (39). Using numerical methods Förster plotted the lines of constant intensity and realised that for stand offs greater than twice the crack width, the intensity lines transformed quite accurately into semicircles as in Figure 23. Using the notation of Zatsepin and Shcherbinin, he found on neglecting small terms in the transformation,

$$H_{Vert} = H_s \frac{2b}{\pi} \frac{x}{x^2 + z^2} \qquad \text{Eqn. (3)}$$

$$H_{Tang} = H_s \frac{2b}{\pi} \frac{z}{x^2 + z^2} \qquad \text{Eqn. (4)}$$

Where H_s is the field deep in the slit. An important point made is that various authors (38) (28) (26) had claimed that the peak separation should contain information about the crack width, indeed in some cases that it was linearly proportional to it. What Förster had shown was that for larger stand offs the width of the crack has no effect on the topographical factor on the right of Eqns. (3) and (4) i.e. the width only affects the amplitude, and in a linear fashion. By putting x=0 into Eqn. (4) Förster found that the peak tangential field from an infinitely deep crack should fall off inversely with stand off. He took a closer look at the resulting equation

$$H_{Tang}^{max} = H_s \, 2b \, \frac{1}{\pi z} \qquad \text{Eqn. (5)}$$

and for the first time took into account the magnetic and geometric properties of the magnetic circuit of which the slot formed a part. He considered the case of a toroidal specimen in which a crack of width 2b is introduced. If the thickness of the toroid is T then we assume T>>2b to simulate an infinitely deep crack. The mean diameter of the toroid is designated D. Förster reasons in a similar fashion to the following. We perform a loop integral $\int \underline{H} . d\underline{l}$ around the toroid for the two cases of no slit and slit S. For no slit,

$$\oint \underline{H}.d\underline{l} = nI = H_A \pi D \qquad \text{Eqn. (6)}$$

where nI is the total current through the loop and H_A is the applied field. For a slit of width 2b,

$$\oint \underline{H}.d\underline{l} = nI = H_m (\pi D - 2b) + H_s 2b \qquad \text{Eqn. (7)}$$

where H_m is the field in the magnetic material. The total flux ϕ in the slit is very much greater than the leakage field, so that to a good approximation $\phi = B_m A = B_s A$ or $\mu_o \mu_r H_m = \mu_o H_s$. Here μ_r is the relative permeability of the magnetic material. Using $H_m = H_s/\mu_r$ to eliminate H_m between Eqns. (6) and (7) we find

$$H_s = H_A \left[\frac{\pi D}{2b + \dfrac{\pi D - 2b}{\mu_r}} \right] \qquad \text{Eqn. (8)}$$

Assuming $\pi D >> 2b$ which will normally be the case, we can look at two extreme cases. When $\mu_r << \frac{\pi D}{2b}$ we find from Eqns. (8) and (5)

$$H_{Tang}^{max} = \mu_r H_A \frac{2b}{\pi z} \qquad \text{Eqn. (9)}$$

i.e the leakage field amplitude is directly proportional to the applied field and the crack width. If however, $\mu_r >> \frac{\pi D}{2b}$ we find

$$H_{Tang}^{max} = \frac{D H_A}{z} \qquad \text{Eqn. (10)}$$

so that the leakage field amplitude becomes independent of crack width. Any particular experiment will, depending on the circumstances, yield on amplitude dependence which contains each of these extremes in varying proportions. For very small width cracks and normal permeabilities we will find Eqn. (9) to hold whereas for large width cracks in small magnetic circuits and very high permeabilities, Eqn. (10) may make its presence felt. Intermediate cases will follow the relationship obtained by combining Eqn. (8) with Eqn. (5).

Förster went on to calculate the leakage field from a crack of finite depth h. He imagined a finite depth crack to be a superposition of two infinite depth cracks, whose surfacing points were displaced by the depth h. Thus the contribution of the lower infinite depth crack should be subtracted from the upper infinite depth crack to yield the field from a crack of finite depth h. Eqns. (3) and (4) allow the individual contributions to be calculated, so that a finite depth crack has a leakage field given by their difference,

$$H_{Vert} = H_s \frac{2b}{\pi} \left[\frac{x}{x^2 + z^2} - \frac{x}{x^2 + (z+h)^2} \right] \quad \text{Eqn. (11)}$$

$$H_{Tang} = H_s \frac{2b}{\pi} \left[\frac{z}{x^2 + z^2} - \frac{(z+h)}{x^2 + (z+h)^2} \right] \quad \text{Eqn. (12)}$$

He compares these results with those of Zatsepin and Shcherbinin (13) to find that the topographical factors coincide perfectly.

This latter result is disputed by McIntire (40) who claims that H_{Tang} is always positive, whereas experimental data and Eqn. (2) of Zatsepin and Shcherbinin show negative regions at large enough $|x|$. However, it is not difficult to verify that for large $|x|$ Forster's Eqn. (12) does indeed give a negative value for H_{Tang}. McIntire differentiates Eqn. (4) with respect to x to find the signal that would be produced from an infinitely deep slot by a device which effectively measures the first derivative of the leakage field, such as a moving coil. He concludes that such a signal would decay with scan height by a $1/z^2$ law.

In a review of experimental data in 1986, McIntire explains that the leakage field of a slot rises linearly with width in an active field up to a certain width of slot, above which the field saturates. This ties in well with the transition from linear dependence predicted by Eqn. (9) when 2b is small, to the null dependence on 2b predicted by Eqn. (10) when 2b is large. McIntire points out that the width at which saturation occurs is much greater than the width associated with common tight discontinuties.

Also described is the phenomenon of field reversal, whereby for very small activating fields, the residual leakage field has the reverse polarity to that which might be expected. At a certain activating field there is no residual leakage field and then as the activating field is increased still further, the expected polarity of residual leakage field is obtained. Increasing the slot width requires a greater activating field to break through the null point. McIntire indicates that such behaviour has been modelled by finite element analysis, and is related to the fact that at low activating field, only the steep portion of the magnetisation curve is reached.

McIntire concludes 'crack depth is difficult to measure with accuracy by magnetic flux leakage techniques, because the signals are caused by a variety of factors. In view of this, MFL signals should be considered a cause of flux leakage which requires further investigation'.

Edwards and Palmer (41) have modelled the leakage field produced by a surface breaking semi-elliptic cylindrical cavity as in Figure 24. The field is first calculated inside an infinitely long ellptic cylindrical cavity of major and minor axes h and b. Providing the aspect ratio n (=h/b) is greater than about 5, the field inside the cavity is given by

$$H = H_A \left(1 + \frac{n(\mu_r - 1)}{(n+\mu_r)} \right) \qquad \text{Eqn.(13)}$$

where the permeability μ_r is treated as a constant and the steel is magnetised below the knee of its initial magnetisation curve. H_A is the applied field. Using the method of images they argue Eqn.(13) to be approximately valid for the field inside a long surface breaking semi-elliptic slot (now of width 2b and depth h).

Edwards and Palmer calculate the surface magnetic charge over the faces of the cavity and show that it is virtually constant except near the base of the slot where it rapidly decreases to zero. They argue that a sufficiently deep slot can be replaced by an equivalent rectangular slot, with equal and opposite magnetic pole densities on each of the slot faces, effectively modelled by Zatsepin and Shcherbinin. They point out however that Zatsepin and Shcherbinin had not justified constant surface pole density or related its magnitude to the magnetising conditions.

Evaluating Eqn.(2) at the point x=0, z=0 and equating with Eqn.(13), Edwards and Palmer find

$$M = H_A \left(\frac{\pi\, n\, (\mu_r - 1)}{(n+\mu_r) \arctan(n)} \right) \qquad \text{Eqn.(14)}$$

The unity term in Eqn.(13) is omitted since Eqns.(2) and (1) refer to the field from the slot alone. (i.e. We must omit the background magnetising field H_A). When μ_r>>n the resulting expressions combining Eqn.(14) with Eqns.(2) and (1) give an almost linear dependence of signal on slot depth. This is observed experimentally by Zatsepin and Shcherbinin, but not predicted from their model with constant M. However, when n>>μ_r i.e. for very large depth cracks, Edwards and Palmer find that Eqn.(14) reduces to

$$M = 2H_A(\mu_r-1)$$

As Edwards and Palmer point out, in the bulk of the material remote from the crack we have $B=\mu_0(H_A+M)=\mu_0\ \mu_r H_A$. We would thus have to conclude that $M = 2H_A(\mu_r-1) = 2M$! The current author shows in Section 2.1 that the H field from a surface at which a magnetisation M terminates normally is given by M/2. The B, H and M fields near the slot surfaces and inside the surrounding metal are then as shown in Figure 25. Clearly the B field is preserved over the boundaries, as must be the case.

The author suggests that the source of the error is that Edwards and Palmer have incorrectly applied Eqn.(13) to the infinitely long slot of Figure 24. Since one half of the full elliptic cylindrical cavity to which the equation applies has been removed, symmetry considerations indicate that the field $H-H_A$ due to the cavity alone will reduce by a factor of one half at the point x=0, z=0, at least for n>5. Thus Eqn.(14) should properly be

$$M = \frac{H_A\ \pi\ n\ (\mu_r-1)}{2(n+\mu_r)\ \arctan(n)}$$

and the difficulty with Edwards and Palmer's paper is removed. Combining Eqn.(14) with Eqn.(1), they show that when n and μ_r are comparable,

$$H_{vert} = H_A \frac{n(\mu_r-1)}{4(n+\mu_r)\arctan(n)} \ln\left\{\frac{[(h+z)^2+(x+b)^2][z^2+(x-b)^2]}{[(h+z)^2+(x-b)^2][z^2+(x+b)^2]}\right\}$$

Eqn.(15)

Edwards and Palmer claim that this should hold even above the saturation limit of the magnetisation curve, and that the leakage field is thus proportional to the applied field in this region. They do not take into account the fact that μ_r varies with H. Above the saturation limit B is approximately constant so that defining $B=\mu_0 \mu_r H_A$ implies that in this region $\mu_r \propto 1/H_A$. Clearly when $n>>\mu_r>>1$ (e.g. a deep and narrow width slot) Eqn.(15) implies a saturation of the leakage field with strong applied fields.

Edwards and Palmer go on to model the field of a slot of finite length, and show that the field reduces to that of Eqn.(1) as the slot length becomes large. They carry out experiments using a solid cylindrical specimen which has milled slots of width 0.25mm and depths 0.5, 1.0, 1.5 and 2mm cut into the cylinder surface along its length. The slots are evenly spaced around the circumference of the cylinder, which is magnetised by a current carrying conductor through its centre. The reason for a cylindrical specimen is to avoid demagnetising effects which inevitably occur with rectangular specimens. They convert the modified leakage field equations into cylindrical coordinates and so are able to plot the theoretical radial component of field as a function of circumferential scan distance, even taking into account the finite size of their probes. They make a favourable comparison with experiment, but curiously do not extend their experimental measurements sufficiently far out from the centre of the slot to indicate whether or not the field dies to zero as it does in theory. Edwards and Palmer also develop a theory, based on their modification of Zatsepin and Shcherbinin's leakage field equations, which indicates the force on magnetic particles in the vicinity of a crack during MPI.

Förster (42) indicates the poor state of understanding of magnetic flux leakage techniques in 1986, remarking that several partly contradictory effects govern measured MFL signals. He cites his own experimental work (43) (44) which demonstrates a clear linearity between the field inside a defect and the leakage field. Using a micromanipulator and a Hall probe of active area 2×10^{-3} mm^2 and thickness 0.3×10^{-3} mm, Förster was able to measure the tangential field inside a real crack in a steel cylinder. The crack was 2mm deep and had a width of 0.3mm. It was found that the field deep inside the crack was roughly constant, and that it gradually fell near the mouth of the crack as in Figure 26. It is significant that Eqn.(2) predicts a near constant field inside the crack when z is sufficiently negative and h>20b, which is observed in Förster's experiment. However, at the point of emergence of the crack at the surface, the field is predicted by Eqn.(2) to drop to roughly one half its value deep in the crack, and this is not observed in practice.

Förster establishes by experiment that the topographical signal width of the vertical component signal remains constant, even after the large applied field has been removed to reveal the signal due to remanent magnetism. At small values of lift off (e.g. 0.25mm) the ratio of remanent field $H_{in}^{rem.}$ inside the crack to the field $H_{in}^{appl.}$ inside the crack, present with an external field applied, corresponds closely with the ratio of the tangential maxima of the leakage fields $H_{Tang}^{rem.}/H_{Tang}^{appl.}$. However, at larger lift offs (3 or 4mm) this ratio is different.

This appears to contradict the statement that the leakage field is proportional to the field inside the crack. At least, it indicates that this is only true for small values of lift off.

Förster presents a modified version of Eqn.(8), taking into account the depth h of a slit in a large specimen which has a permeability that is independent of field strength. The field in the slit is calculated as

$$H_s = \frac{\frac{h}{b} + 1}{\frac{1}{\mu_r}\frac{h}{b} + 1} H_A \qquad \text{Eqn.(16)}$$

Eqn.(16) was found to be in error with experiment, which indicated a greater field strength by a factor of 2.65. In Förster's experiments h was varied by a factor of 4 and the width 2b by a factor of 7. The discrepancy was attributed to the non-linear permeabilities of the materials used. Förster comments that in the theoretical plots of Lord et al. (26) in Figure 15 the assumption of constant magnetic charge per unit area (i.e. M) over the faces of the slit as the width and depth vary should not really be used. Instead, the magnetisation at the crack surface depends on the very geometry of the crack as suggested by Eqn.(16). In S.I. units, Förster suggests that the correct value of M to use is

$$M = \frac{\frac{h}{b} + 1}{\frac{1}{\mu_r}\frac{h}{b} + 1} \times 2.65 \times H_A \qquad \text{Eqn.(17)}$$

Förster's experiments with cracks showed that the internal field decreased with increasing width 2b, as predicted by Eqn.(16). Also, as 2b is increased, the leakage field declines more slowly into the surroundings, which results in a relative independence of leakage signal amplitude on crack width at sufficiently large stand off ($z>1mm$). Experimental data is presented which shows a linear increase of both tangential and vertical components with crack depth, which varied in Forster's experiment from 1.02mm to 2.54mm, with 2b=0.381mm. As with Lord (26) it is unclear what scan height Förster (42) used, although it appears to be 64µm. If a scan height of 3-4mm were used, even assuming constant magnetisation, Eqn.(1) would predict a near linear increase of signal amplitude on crack depth. Smaller scan heights would show a saturation of amplitude with depth, but this is not observed experimentally. Förster's signals show classical behaviour far from the crack i.e. the signal dies to zero, with no bias effect.

Uetake and Ito (45) also find a linear increase of signal amplitude on artificial defect depth, even to depths of as much as 8mm, long after saturation is predicted by Eqn.(1) with constant M. They make no attempt to interpret their results, but it is clear that this linear dependence can be explained by Förster's modification of M given by Eqn.(17). Effectively, in the topographical saturation region as $h\to\infty$ in Eqn.(1), M is still increasing linearly. In Uetake and Ito's experiment $h/b\approx40$ when $h=8mm$ (c.f. Eqn.(17)).

Uetake and Ito measure the dependence of leakage field on lift off z, citing authors (46) (47) who have found a z^{-2} and z^{-4} dependence. They themselves measure a z^{-1} dependence, and for a slot of width 0.4mm the leakage field can be fitted empirically to an equation of the form

$$B = c\frac{h}{z} + k$$

where c and k are fitted constants. These will evidently vary with the level of magnetisation and crack width. Nevertheless, they propose a method of depth sizing, valid if c and k can be measured, involving two probes scanned simultaneously at heights of z_1 and z_2 ($z_2>z_1$). Using the previous equation, the depth appears as

$$h = \frac{(z_2-z_1)}{c} \quad \frac{(B_{z1}-k)\,(B_{z2}-k)}{B_{z1}-B_{z2}}$$

This method is developed further in this thesis, where it is demonstrated that the level of magnetisation and crack width are variables which do not have to be known. Uetake and Ito do not provide any examples of their signals, which indicate a finite field $B=k$ even when $h=0$. This may have been due to background bias effects.

Kalwa and Piekarski (48) have used Hall probes in the non-destructive testing of steel ropes, using apparatus similar to that used by Marchent (12). They have used Hall probes in a differential mode and investigated the types of signal produced. In particular they have shown (49) that in addition to the radial defect signal, there is a non zero background signal $B_r(x)$ which has the property $B_r(x)=-B_r(-x)$. Therefore probes used in differential mode at a distance 2c apart produce a background signal $2B_r(c)$, which they reduce to zero via a potentiometer in their equipment. This is the field observed by Oehl and Swartzendruber (27) and which they approximated by a linear term Dx in the expression for the field. Evidently this has the necessary antisymmetric property required. The sensitivity of their measurements was increased by the use of magnetic concentrators. These took the form of two ferromagnetic rods with the Hall probe sandwiched between them. The actual rods were about 3mm in diameter and 20mm in length, and allowed an increase of sensitivity by a factor of 2.5. Both radial and tangential components of field could be detected. This was necessary since Kalwa (50) had shown that when multiple breaks were present their radial leakage fields would cancel out partially and so reduce the average field detected. The tangential field however would increase with multiple defects so that a tangential sensor could be used to good effect under this circumstance. It is pointed out that a differential tangential field detector would not be as good as a single detector when trying to detect multiple breaks.

Atherton and Czura (51) have measured the effects of stress on leakage fields from simulated corrosion pits in pipelines of diameter 91cm. It is found that the signals initially decrease with increasing pressure, until a pressure of about 2.8MPa is reached inside the pipe. Thereafter, there is an increase in signal with pressure. The effects are reversible with pressure and independent of defect penetration. They try to ascribe the effect to local stress induced permeability changes, and to this end model their experiment using a finite element technique in which the permeability of their steels as a function of pressure is provided as data for the programs. They conclude, however, that the changes in permeability (only 10 or 20%, even at 200MPa) are far too small too account for the observed magnitude of variation in the leakage field. Ko and Francis' demonstration (10) that the leakage field increases with stress might provide an alternative explanation, but does not explain the initial decrease in signal with pressure.

Atherton and Daly (52) use the finite element technique to further model the leakage field from pits in pipelines. They point out that practical equipment often consists of a permanent magnet of which the flux is magnetically linked to the pipe wall by steel brushes. The apparatus then resembles Figure 4, where the wire rope is replaced by the pipe wall and magnetic excitation takes place from one side only. It is found as a first approximation that the flux leakage is roughly proportional to pit depth, for a reasonable range of pit diameters. However, more exact experiments using defects of known size show non-linearities. The pit diameter can be determined from the signal width.

Atherton and Daly modelled the leakage fields from rectangular grooves in a pipe as a 2D approximation to pits. Both internal and external grooves were modelled, with a permanent magnet excitation. With the detector on the interior of the pipe, the leakage field was modelled and found to increase linearly with increasing depth, for both farside and nearside penetrations, up to a penetration of 60% of the wall thickness. The latter was 9.5mm and the width of groove was set to a constant 5.25mm. For larger penetrations the increase in leakage signal was faster than linear.

This behaviour might be expected from the farside signal, since in this case large penetrations produce magnetic charge very close to the detector, which because of the inverse square law for fields from magnetic charges, should show a rapid increase in signal. However, the same phenomenon was modelled for the nearside grooves, i.e. a more than linear dependence of signal amplitude on groove depth for large penetration. This is in marked contrast to previous results (e.g. (28)) which suggest a tendency to saturation. Atherton and Daly suggest that the reason for this discrepancy is that previous work had considered constant H field excitation, whereas they have modelled a ferrite permanent magnet excitation. They argue that permanent magnets can be considered to work in a constant flux mode, in which increasing defect penetration leads to increasing magnetomotive force at only slightly lower flux density. The last bit of pipe wall to be removed still has a permeability significantly greater than air (and so takes a large portion of flux), so that its removal leads to a big increase in leakage signal. They conclude that assuming a linear relationship between leakage signal amplitude and pit depth would lead to a safe overestimate of the latter. In any case, pit depths of more than 60% penetration would normally be cause for immediate action to be taken.

Goebbels and Simkin (53) have further developed the finite element technique to predict the surface field of complicated steel parts upon magnetisation by an electromagnetic yoke. The agreement with experiment is good, and they suggest that the method could be used to eliminate much of the trial and error involved in determining whether there is sufficient field present in a particular complex part for MPI to take place, as required by standards such as BS6072 (8).

In a review of magnetic methods of NDT in 1990 Jiles (54) outlines the history of developments in MPI. He cites the work of many of the authors mentioned so far, and others besides. In particular, he recommends the work of Betz (55) as a standard reference work on the subject, and points out that MPI still has the considerable advantage over flux measurement techniques that large areas can be quickly inspected, eliminating the time consuming scanning of probes.

After describing several devices by Stumm (56) based on the leakage field method, Jiles reviews the state of development of the latter. The early work of Zatsepin and Shcherbinin (13) (29) is described, and the limitations of the model in adapting to complex shapes. The finite element work of Hwang and Lord (57) made possible the calculation of fields for such complex parts. When their method is applied to the slot of Figure 5 similar leakage profiles are obtained to that by Zatsepin and Shcherbinin. In particular, the finite element method gives lines of constant H in the leakage field as semicircles for sufficiently large stand off, as discovered by Förster (37) using a third independent method. Even using the finite element method, the level of excitation must be known, and the magnetic properties and history of the material play an important role in the development of the theory, as pointed out by Lord (58). Jiles reviews the work on semi-elliptic slots by Edwards and Palmer (41), concluding that the level of field recommended by BS6072 (8) is adequate for crack detection using MPI.

As Förster (42) points out, the state of understanding of magnetic flux leakage signals in recent times is still relatively poor. Early dipole modelling (13) (19) (24) indicated that there should be a saturation effect of the MFL signal with crack depth. Experiment (16) (19) showed that this was indeed the case with artificial flaws. The finite element modelling of Lord and Hwang (28) indicated a similar tendency to saturation with slot depth. However, Lord Bridges et al. (26) found that the active leakage field over a 3mm wide slot increased linearly with slot depth and such a linear increase was also found by Uetake and Ito (45). Clearly the method of magnetisation and individual geometries in the experiments are factors which must be taken into account, as there would appear to be a contradiction in the outcome of such experiments. Atherton and Daly (52) have shown, for example, that a permanent magnet excitation will lead to a faster than linear increase of MFL signal with crack depth, when the crack has only a small 'bottom' left to it. i.e. It is nearly a through crack. In addition, Förster (37) (42) has shown how the field inside a slot and the MFL signal depend on the geometry of the slot or crack, and indeed on the geometry of the magnetic circuit of which the crack forms a part. The results of his experiments with real cracks, using microprobes to record signal strengths in and around a crack, have no definitive explanation as yet.

Considerable progress has been made in Hall effect technology over the past twenty years; Hall probes of sensitivity 5mV/Gauss were available to the author. However, despite such advances, the understanding of MFL signals which can be measured by such Hall probes has not yet developed to the point where cracks can be routinely sized from their MFL signals. Whilst Hwang (30) has suggested a method for sizing, it is based on being able to use scan heights which are less than or of the same order as the crack width, and relies on a knowledge of the magnetic excitation and characteristics of the material in which the crack is situated. The method has not been generally adopted, and is not applicable to situations in which a linear dependence of the MFL signal on crack depth is observed. It is hoped that in the embodiment of the double probe system described in this thesis, such difficulties will be overcome and that the path to crack depth sizing will be shown.

CHAPTER 2

FUNDAMENTAL THEORY

2.1 **Fundamental theory**

Conventional magnetic particle inspection techniques rely on the leakage field produced at the surface of a ferromagnetic substance when it is magnetised. The technique relies on there being a flaw at or near the surface which will intercept the magnetisation in a specimen. Wherever there is a discontinuity in magnetisation in a substance, such as might arise from the face of a crack, the discontinuity acts as a source of magnetic field intensity. The precise vector relationship is given in simple form as:

$$d\underline{H} = \frac{\underline{M}.d\underline{S}\ \hat{\underline{r}}}{4\pi r^2} \qquad \text{Eqn. (18)}$$

where:

$d\underline{H}$ = An element of magnetic field intensity at position vector $\underline{r}$

$\underline{M}$ = Magnetisation

$d\underline{S}$ = An element of surface area at which the magnetisation terminates

r = Magnitude of position vector $\underline{r}$

$\hat{\underline{r}}$ = Unit vector in $\underline{r}$ direction

The field $\underline{H}$ at position $\underline{r}$ due to the discontinuity over surface S can then be found by integration of the elements $d\underline{H}$.

The quantity $\underline{M}$. $d\underline{S}$ plays a similar role to electric charge q in electrostatics, and is sometimes referred to as magnetic charge. Magnetic charge is not a physical reality, but a mathematical construct which may be treated as such, and will be spoken of as such hence forward.

Magnetic charge is a source of lines of intensity $\underline{H}$ in a similar way to which electric charge is a source of lines of electric field $\underline{E}$. Thus if we had a long and very thin magnetised rod, the discontinuity in $\underline{M}$ at one end would approximate to a point source of lines of $\underline{H}$ field. The field would then appear as in Figure 27.

It is important to realise that whilst such sources of $\underline{H}$ exist, there are no sources of magnetic induction field $\underline{B}$. The $\underline{B}$ field inside a specimen is given by

$$\underline{B} = \mu_o (\underline{H}+\underline{M}) \qquad \text{Eqn. (19)}$$

and where $\underline{M}$ falls to zero (e.g. in free space, or air to a very good approximation), $\underline{B}$ is given by $\mu_o \underline{H}$. Thus where a vector $\underline{M}$ terminates at an abrupt boundary between say steel and air, the $\underline{B}$ fields immediately inside and outside the specimen are given by $\underline{B}_{in} = \mu_o(\underline{H}_{in}+\underline{M})$ and $\underline{B}_{out} = \mu_o \underline{H}_{out}$, $\underline{H}_{in}$ and $\underline{H}_{out}$ being the field intensities just inside and outside the boundary. For the case of a large surface of magnetised steel exposed to the air we can calculate $\underline{H}_{out}$ from Eqn. (18). Consider the surface to be exposed as in Figures 28(a) and 28(b) and construct axes as in Figure 28(c).

The element of $\underline{H}$ produced by a small area $\delta z\ \delta y$ is given by

$$d\underline{H} = \frac{\sigma \delta z \delta y}{4\pi r^2}\ \hat{\underline{r}}$$

where σ is the magnetic charge per unit area on the surface. Since by symmetry when we integrate over an infinite (or at least very large) surface, the only component of $\underline{H}$ will be in the $\underline{x}$ direction in Figure 28(c), we need only consider $d\underline{H}_x$. This is given by

$$d\underline{H}_x = |d\underline{H}| \sin\theta \quad \cos\phi \quad \hat{\underline{x}}$$

$$= dH \frac{(x^2+y^2)^{½}}{(x^2+y^2+z^2)^{½}} \quad \frac{x}{(x^2+y^2)^{½}} \qquad \hat{\underline{x}}$$

The field $\underline{H}$ at a distance x from the surface is then given by

$$\underline{H}_{out} = \int d\underline{H}_x = \frac{\sigma}{4\pi} \int_{-\infty}^{\infty}\int_{-\infty}^{\infty} \frac{1}{(x^2+y^2+z^2)} \quad \frac{(x^2+y^2)^{½}}{(x^2+y^2+z^2)^{½}} \quad \frac{x}{(x^2+y^2)^{½}} \hat{\underline{x}} \; dzdy$$

This integral is readily evaluated, the result being

$$\underline{H}_{out} = \frac{\sigma}{2} \hat{\underline{x}} \quad = \frac{\sigma}{2} \hat{\underline{S}} \qquad \text{(Here S represents surface area)}$$

Since $\sigma = \frac{q}{S} = \frac{\underline{M}.\underline{S}}{S} = \underline{M}.\hat{\underline{S}}$ we have

$$\underline{H}_{out} = \frac{1}{2} \quad (\underline{M}.\hat{\underline{S}})\hat{\underline{S}}$$

and by symmetry $\underline{H}_{in} = -\underline{H}_{out} = -\frac{1}{2} \; (\underline{M}.\hat{\underline{S}}) \; \hat{\underline{S}}$

Thus the fields $\underline{B}_{in}$ and $\underline{B}_{out}$ on either side of the boundary are,

$$\underline{B}_{in} = \mu_o \; (- \frac{1}{2} \; (\underline{M}.\hat{\underline{S}}) \; \hat{\underline{S}} + \underline{M})$$

$$\underline{B}_{out} = \mu_o \frac{1}{2} (\underline{M}.\hat{\underline{S}}) \quad \hat{\underline{S}}$$

To show that the normal component of B is continuous over the boundary we need only take the dot products $\underline{B}_{in}.\hat{\underline{S}}$ and $\underline{B}_{out}.\hat{\underline{S}}$ to see if they are equal.

$$\underline{B}_{in}\cdot\hat{\underline{S}} = \mu_o\ (-\tfrac{1}{2}\ (\underline{M}\cdot\hat{\underline{S}}) + (\underline{M}\cdot\hat{\underline{S}})) = \tfrac{1}{2}\ \mu_o\ (\underline{M}\cdot\hat{\underline{S}})$$

$$\underline{B}_{out}\cdot\hat{\underline{S}} = \tfrac{1}{2}\ \mu_o(\underline{M}\cdot\hat{\underline{S}})$$

Thus Eqn. (18) is consistent with the view that no sources of B can exist, and there is no additional source of B field at the steel boundary.

When a crack is produced in a specimen of steel which has been magnetised, there may well be an open face which, depending on the relative orientations of the crack and the magnetisation, possesses 'magnetic charge'. Thus in Figure 29 cases (a) and (b) have cracks whose length has a component at right angles to M whereas (c) does not. Thus there is no possibility in case (c) of any magnetic charge being produced, and hence there can be no leakage field.

Evidently in the case of a crack there will be two faces, which if they interrupt a magnetisation M, will become equally and oppositely charged.

2.2 **The Vertical Field**

The calculation of the leakage field from a crack can be attempted by setting up a simplifying model, originally proposed by Zatsepin and Shcherbinin (13). The model consists of a long rectangular crack of depth h and width 2b and it is assumed that the crack interrupts the magnetisation at right angles. The situation then is depicted in Figure 30. We consider what element of vertical component of field $\underline{H}$ will be produced by a small element of area dzdy on the right hand face of the crack, at a height z_o above the surface and lateral distance x-b away from the right hand face of the crack, as in Figure 31.

The element d$\underline{H}$ of field has absolute magnitude

$$|d\underline{H}| = \frac{M\, dzdy}{4\pi(y^2+(z-z_o)^2+(x-b)^2)}$$

and the vertical component of this (coming away from the crack) is

$$dH_{vert} = \frac{M\, dzdy}{4\pi(y^2+(z-z_o)^2+(x-b)^2)} \; \frac{(z_o-z)}{(y^2+(z-z_o)^2+(x-b)^2\;)^{½}}$$

Thus the vertical component of $\underline{H}$ from the entirety of the right hand face will be given by

$$H_{vert}^{RH} = \frac{M}{4\pi}\int_{-h}^{0}\int_{-\infty}^{\infty}\frac{(z_o-z)}{(y^2+(z-z_o)^2+(x-b)^2\;)^{3/2}}\,dydz$$

This has an analytic solution, given by

$$H_{vert}^{RH} = \frac{M}{4\pi}\;\ln\left[\frac{(z_o+h)^2 + (x-b)^2}{z_o^2 + (x-b)^2}\right]$$

By symmetry, the contribution to $\underline{H}$ at the same point from the left hand face of the crack is given by

$$H_{vert}^{LH} = -\frac{M}{4\pi}\;\ln\left[\frac{(z_o+h)^2 + (x+b)^2}{z_o^2 + (x+b)^2}\right]$$

The minus sign arises because of the opposite sense of charge on the left hand face. Thus the vertical component of field from both faces considered together is

$$H_{vert} = H_{vert}^{RH} + H_{vert}^{LH}$$

Reversing the sense of magnetisation to coincide with that of Figure 5, we finally arrive at the expression

$$H_{vert} = \frac{M}{4\pi} \ln\left(\frac{[(h+z)^2+(x+b)^2]\,[z^2+(x-b)^2]}{[(h+z)^2+(x-b)^2]\,[z^2+(x+b)^2]} \right) \qquad \text{Eqn. (1)}$$

This is sketched in Figure 6 for the case h=10, z=10, 2b=1, in arbitrary units.

2.3 The Tangential Field

Referring back to Figure 31, an element of tangential field from the right hand face is given by

$$dH_T^{RH} = \frac{M\,dzdy}{4\pi(y^2+(x-b)^2+(z-z_0)^2)} \; \frac{(y^2+(x-b)^2)^{1/2}}{(y^2+(x-b)^2+(z-z_0)^2)^{1/2}} \; \frac{(x-b)}{(y^2+(x-b)^2)^{1/2}}$$

Thus

$$H_T^{RH} = \frac{M}{4\pi} \int_{-\infty}^{\infty} \int_{-h}^{0} \frac{(x-b)}{(y^2+(x-b)^2+(z-z_0)^2)^{3/2}}\, dzdy$$

This integral has solution

$$H_T^{RH} = \frac{M}{2\pi} \left[\arctan\left(\frac{h+z_0}{x-b}\right) - \arctan\left(\frac{z_0}{x-b}\right) \right]$$

Again, by symmetry, the field for both surfaces considered together (with the sense of magnetisation reversed) is

$$H_T = \frac{M}{2\pi} \left[\arctan\left(\frac{h+z}{x+b}\right) - \arctan\left(\frac{z}{x+b}\right) - \arctan\left(\frac{h+z}{x-b}\right) + \arctan\left(\frac{z}{x-b}\right) \right]$$

Eqn. (2)

This is sketched in Figure 7 for the case of h=10, z=10, 2b=1, again in arbitrary units.

2.4 Magnetic Particle Inspection

It has been seen that a crack in a magnetised specimen of steel can, under most circumstances, give rise to a leakage field near the crack. It is clear from Figure 6 and Figure 7 that this leakage field decreases, both in its tangential and horizontal components, as we move away from the crack. This changing aspect of the leakage field is made use of in magnetic particle inspection. In a region where the field $\underline{H}$ is changing in space, it can give rise to a force on a small magnetic particle. For a particle of volume V and susceptibility χ, it will experience a force (to first order) in free space of,

$$\underline{F} = \tfrac{1}{2} V \mu_o \chi \text{ grad } (H^2)$$

Figure 6 and Figure 7 show that the field changes most rapidly in the vicinity of the crack, and so magnetic particles will experience the greatest force in this region. The result is that particles conglomerate in the vicinity of the crack, and in this way the crack is made visible. The distribution of induction field lines B is approximately as in Figure 32, with the force on particles being directed towards the crack as indicated.

2.5 The Hall Effect

The method investigated in this project to detect the leakage field involved the use of Hall probes. The Hall effect is described in basic form in several texts (59) and a condensed description is given here for reference.

Imagine a sample of semiconductor (or indeed a metal) as in Figure 33, with associated axes as shown. Let the semiconductor have n electrons per unit volume and p holes per unit volume. This will be the general case, and for intrinsic samples we will have n=p. For the case of doped semiconductors we will not have this equality and the sample will be p or n type depending on whether the type of impurity introduced into the host lattice is from Group III or V of the periodic table. Even in this case, there will be minority carriers of the opposite type present, and for the case of light doping their numbers may be significant.

For the current discussion the convention that will be used is that mobilities of carriers, defined through the equation

$v_D = \mu E$ $\qquad$ v_D = Drift velocity

E = Electric field

are positive and that the charge on the electron is $-|e|$. Thus for electrons,

Force $\underline{F}_n = -|e|\,\underline{E}$ and velocity $\underline{v}_n = -\mu_n\,\underline{E}$

Now, since current per unit area $\underline{J} = n\,q\,\underline{v}$, with

n = no. of carriers per unit volume

q = charge on carriers

$\underline{v}$ = drift velocity of carriers

we obtain for electrons

$$\underline{J}_n = -|e|\,n\,\underline{v}_n$$

Thus

$$\underline{J}_n = -\,|e|\,n\,\left(-\mu_n\,\frac{\underline{F}_n}{-|e|}\right) = -\mu_n\,n\,\underline{F}_n$$

Similarly for holes we have

$$\underline{F}_p = |e| \; \underline{E}, \qquad \underline{v}_p = \mu_p \, \underline{E}$$

Thus

$$\underline{J}_p = p \; |e| \; \underline{v}_p = p \; |e| \, \mu_p \frac{\underline{F}_p}{|e|} = \mu_p \, p \, \underline{F}_p$$

In the basic Hall effect a field B_z is applied to a sample of material carrying a current (per unit area) J_x, as in Figure 33. The carriers of charge q will experience a Lorentz force $q(\underline{v} \times \underline{B}_z)$. If the carriers are electrons it can be seen that the direction of this force is in the $-\hat{\underline{y}}$ direction, since $\underline{v}$ is in the opposite direction to $\underline{J}_x$ and q is negative $(-|e|)$. Indeed a little thought will show that holes too are deflected in this same direction but for the moment we consider electrons as being the carriers e.g. n type semiconductors and most metals. The build up of electrons in this manner on the face of the sample nearest the observer in Figure 33 gives rise to a field $\underline{E}_y$ which will have a direction such that it opposes the Lorentz force, and tends to deflect electrons to the opposite side. It is this field $\underline{E}_y$ which gives rise to a Hall voltage, which may be measured by sensing the potential difference between the sides of the sample where there is a build up of charge, the shaded areas in Figure 33. Naturally, charge will only build up to the extent that $\underline{E}_y$ will exactly balance the Lorentz force $q\ (\underline{v} \times \underline{B}_z)$, when a state of equilibrium will exist. Exactly how $\underline{E}_y$ depends on the various factors involved shall be deduced here. In equilibrium there will be no current $\underline{J}_y$ so we obtain an expression for $\underline{J}_y$ due to the electrons and holes in the sample, and equate to zero.

The force in the $\hat{\underline{y}}$ direction on electrons is

$$\underline{F}_{yn} = -|e| \ (\underline{v}_n \times \underline{B}_z) - |e| \ \underline{E}_y$$

$$= -|e| \ (-\mu_n \ \underline{E}_x \times \underline{B}_z) - |e| \ \underline{E}_y$$

$$= -|e| \mu_n \ E_x \ B_z \ \hat{\underline{y}} - |e| \ E_y \ \hat{\underline{y}} = -|e| \ (\mu_n E_x B_z + E_y) \ \hat{\underline{y}}$$

The current density due to the electrons is therefore

$$\underline{J}_{ny} = -\mu_n \ n \ \underline{F}_{yn} = + \mu_n \ n \ |e| \ (\mu_n E_x B_z + E_y) \ \hat{\underline{y}}$$

The force in the $\hat{\underline{y}}$ direction on holes is $|e| \ (\underline{v}_p \times \underline{B}_z) + |e| \underline{E}_y$

$$\underline{F}_{yp} = |e| \ (\mu_p \underline{E}_x \times \underline{B}_z) + |e| \ \underline{E}_y$$

$$= |e| \ \mu_p \ E_x \ B_z \ (-\hat{\underline{y}}) + |e| \ E_y \hat{\underline{y}}$$

$$= (|e| \ E_y - |e| \ \mu_p \ E_x \ B_z) \ \hat{\underline{y}}$$

The current density due to the holes is therefore

$$\underline{J}_{py} = \mu_p p \ \underline{F}_{yp} = \mu_p p \ |e| \ (E_y - \mu_p \ E_x \ B_z) \ \hat{\underline{y}}$$

The total current in equilibrium in the $\hat{\underline{y}}$ direction must be zero. Thus

$$\underline{J}_y = \underline{J}_{py} + \underline{J}_{ny} = \underline{0}$$

$$J_y = \mu_n \ n |e| \ (\mu_n E_x B_z + E_y) + \mu_p \ p |e| \ (E_y - \mu_p E_x B_z) = 0$$

$$0 = \mu_n^2 \ n |e| E_x B_z + \mu_n \ n |e| E_y + \mu_p \ p |e| E_y - \mu_p^2 \ p |e| E_x B_z$$

This reduces to,

$$E_y = \frac{\mu_p^2 p - \mu_n^2 n}{\mu_n n + \mu_p p} E_x B_z \qquad \text{Eqn.(20)}$$

Now, the velocities of electrons and holes are

$\underline{v}_{xn} = -\mu_n \underline{E}_x$ and $\underline{v}_{xp} = \mu_p \underline{E}_x$

Also $\underline{J}_{xn} = n\,(-|e|)\underline{v}_{xn}$ and $\underline{J}_{xp} = p|e|\underline{v}_{xp}$

$= n|e|\mu_n \underline{E}_x$ $\quad$ $= p|e|\mu_p \underline{E}_x$

Thus $\underline{J}_x = \underline{J}_{xn} + \underline{J}_{xp} = n|e|\mu_n \underline{E}_x + p|e|\mu_p \underline{E}_x$

$= (n\mu_n + p\mu_p)\ |e|\,\underline{E}_x$

Thus from Eqn. (20)

$$E_y = \frac{\mu_p^2 p - \mu_n^2 n}{(\mu_n n + \mu_p p)^2} \frac{1}{|e|} B_z J_x \qquad \text{Eqn. (21)}$$

The Hall field is thus proportional to the field B_z and the current J_x. The constant of proportionality is called the Hall coefficient and is given by

$$R_H = \frac{1}{|e|} \frac{\mu_p^2 p - \mu_n^2 n}{(\mu_n n + \mu_p p)^2}$$

or with $\frac{\mu_n}{\mu_p} = b$

$$R_H = \frac{1}{|e|} \frac{(p - b^2 n)}{(bn + p)^2} \qquad \text{Eqn. (22)}$$

For pure electrons p=0 and $R_H = -\frac{1}{n|e|}$

For pure holes n=0 and $R_H = \frac{1}{p|e|}$

For intrinsic semiconductors of intrinsic hole and electron concentrations n_i

$$R_H = \frac{1}{|e|}\frac{1}{n_i}\frac{(1-b^2)}{(1+b)^2} = \frac{1}{|e|}\frac{1}{n_i}\frac{(1-b)}{(1+b)}$$

The existence of a Hall effect in the intrinsic case thus relies on there being a difference in mobilities of the holes and electrons. In all cases however the Hall coefficient will be large, and there will be a significant Hall voltage if the carrier concentration is low. As expected therefore, the experimentally determined Hall coefficient in metals is considerably smaller than it is in semiconductors. For example, the Hall coefficient for pure germanium is of the order $1 m^3C^{-1}$ whereas that of copper is about $5 \times 10^{-11} m^3C^{-1}$, a vast difference.

The linear dependence of the Hall voltage (given by $E_y w$ where w is the width of the specimen) on B_z through Eqn.(21) gives us a means of measuring magnetic fields, and it is this property which is utilised in the commercial Hall probes available.

CHAPTER 3

EXPERIMENTAL AND THEORETICAL INVESTIGATIONS

3.1 Relation of the leakage field equations to previous experimental work

Quantitative work was undertaken by Sharif (11) where a Hall probe was scanned over artificial cracks produced by joining together two pieces of mild steel, and using shims to keep the 'crack' surfaces at a known distance apart. The way in which the signal from the probe depended on the notch depth and width was quantified, as was the dependence on scan height. This was done by varying one parameter at a time, keeping the others constant. The vertical component signals produced from varying notch widths are indicated in Figure 34. Experimental results were available as follows:

1. Variation in maximum field value with scan height. Figure 35.
2. Variation in maximum field value with notch depth. Figure 36.
3. Variation in maximum field value with notch width. Figure 37.
4. Variation in signal width with notch width. Figure 38.

It was desired to correlate the results of Sharif (11) with the predictions of the leakage field Eqn. (1), and to this end a theoretical signal plotting program based on Eqn.(1) was written in AMSTRAD BASIC.

Using this program the following dependencies were investigated:

1.	As in case (1) above.	Figure 39.
2.	As in case (2) above.	Figure 40.
3.	As in case (3) above	Figure 41.

4. Variation in signal width with crack/notch width (see later).
5. Variation in signal width with scan height. Figure 42.
6. Variation in signal width with crack/notch depth. Figure 43.

In cases (1) to (3) above it can be seen that the agreement of experiment with theory is qualitatively good. In all three cases the theoretical and experimental curves are similar, with the possible exception of the region near the origin in Figure 36. However, in case (4), it was found theoretically that there should be little change in the signal width with varying notch width. For example, running the program with the parameters of scan height = 20, crack depth = 20, and with the crack width varying from 0.25 to 7 (all in arbitrary but comparable units to experiment), it was found that the signal width varied from 15.35 to 15.65. This represents a 2% change in signal width for almost a 30-fold (or 3000%) change in the crack or notch width. This result is in stark contrast to Figure 38, the result of experiment. This discrepancy is investigated further in the following section.

3.2 Initial Experimental Work

The object of the initial experiments in this project was to try and confirm the relationships predicted by computer plotting. The dependence of the field strength (maximum field value) on notch width, depth and scan height were shown to be experimentally and theoretically compatible. It was desired to produce experimental results which could be compared with cases (4)-(6) in Section 3.1, the theoretical dependence of signal width on crack/notch width, depth and scan height. Sharif (11) had observed a linear dependence of signal width on notch width which was not predicted in theory. It was thus important to test the reproducibility of this result.

Hall effect probes were obtained for this series of experiments, type 634SS2. This is a four terminal device, which has characteristics as shown in Appendix A, and a sensitivity of about 1mV/Gauss. A circuit suitable for amplification of the probe output was designed which gave an output suitable for a chart recorder. This circuit is shown in Figure 44. It was found in practice that the zero point of the amplifier (i.e. the output indication for no field) tended to drift somewhat, and so needed frequent adjustment of the zero control. Various possible causes of this drift were investigated.

Two blocks of 15mm x 100mm x 40mm 50D steel were cut, each having an upper, lower and side face ground flat, as in Figure 45. These blocks were somewhat smaller than those used by Sharif (11). The two blocks were used together with permanent magnets to produce an almost complete magnetic circuit. The blocks were separated by aluminium shims of varying thickness as in Figure 46, the gap between the blocks forming the artificial defects. The two blocks were clamped together, thus allowing a tight fit for the shims in the gap. This method of magnetisation was more direct than that used by Sharif, who relied on a field being induced in the specimen by a nearby cable carrying a large current.

In order to vary the depth of the artificial defect, a nickel shim was used, 200μm thick and 15 x 110mm^2 in area. It was to be hoped that the high susceptibility of the nickel ensured a high degree of magnetic continuity in the region underneath the 'crack' and any leakage field from this region was assumed to be negligible. When the nickel shim was positioned flush with the surface, so that a zero depth crack was simulated (a non-existent crack), there was still found to be a significant leakage field. However, this was small in comparison to the fields produced when the shim was lowered to allow a genuine steel-air notch interface to occur. This is as would be expected since a high magnetic charge depends on an abrupt discontinuity in magnetisation (see Section 2.1). When this discontinuity is softened, such as for example, in a steel nickel interface, the magnetic charge produced is not as great. This is because the difference between the susceptibilities of the steel and nickel is not as great as that of steel and air. Both nickel and steel are ferromagnetic with susceptibilities of about 480 and 700 respectively, and hence the magnetisation on going from steel to nickel will just drop to a lower value, whereas from steel to air it will drop to zero, a much more abrupt change.

The probe was scanned over the defect at a height determined by non-magnetic plastic shims which were placed over the defect. Normally this was set at 1.5mm.

3.2.1 Results of initial experimental work

Amplifier Performance

The probe/amplifier system was found to be reasonably sensitive, and could detect fields down to that of the earth quite readily. Thus rotating the probe through 180° in a north-south direction produced a trace on the chart recorder as in Figure 47. Since the earth's field here is 0.18 Gauss, the probe can detect a field of 0.36 Gauss with a signal to noise ratio of about 3. With no signal applied the noise trace was as in Figure 48. However, there was found to be a considerable problem with the drift of the zero point of the amplifier. This necessitated sufficiently rapid scanning of the probe to prevent sizeable drift. Experiment showed that the drift was mainly due to thermal effects and that significant variation could be seen for as little as 1-2°C change in probe temperature. Thus while simultaneously detecting the earth's field (this time at the dip angle to obtain a larger signal) and placing the hand as a heat source a few centimetres near the probe, a trace was produced as in Figure 49. This represents a drift in the zero point of about 0.9 to 1.7 Gauss $°C^{-1}$, a figure in agreement with the calibration curves of the probe in Appendix A. Increasing temperature will enable more electrons on average to traverse the energy gap of the semiconductor and so an increase in the number of conduction electrons per unit volume n would be expected. Not only does this increase the conductivity but inspection of Eqn. (22) shows that the Hall coefficient will be changed (in fact it will be reduced). Thus a temperature effect on the performance of the probe is not to be altogether unexpected.

The probe was also found to be sensitive to nearby static charges, which is an expected occurrence since an external static charge can cause the deflection of electrons and holes within the specimen, so changing the Hall voltage. On removal of the external charge the probe output returned immediately to its previous level, again as would be expected.

3.2.2 Experimental Procedures

Using the probe system, blocks of steel and shims, set up as in Figure 46, the probe was scanned in unison with the chart recorder paper in three experimental cases.

1. To investigate the dependence of signal width on notch width the probe was scanned with the following parameters: notch depth = 15mm, scan height = 1.5mm, notch width varying from 25μm to 100μm, by use of 25μm shims.

2. To investigate the dependence of signal width on notch depth the probe was scanned with the following parameters: notch width = 200μm, scan height = 1.5mm, notch depth varying from 1mm to 5mm, by lowering the nickel shim.

3. To investigate the dependence of signal width on scan height the probe was scanned with the following parameters: notch width = 50μm, notch depth = 15mm, scan height varying from 0.2mm to 1mm, by means of 0.2mm thick plastic shims.

In all cases the probe was kept in unison with the chart recorder paper by attaching the probe to the paper and keeping it taught as the paper unfurled. As a control, using a constant velocity scanning arm and computer interface described in Section 5.5, it was possible at a later date to generate the background signal (i.e. with no notch present) on the screen of the Amstrad CPC6128 computer, using an appropriately sized metal block (80mm × 100mm × 15mm). This was then transferred to a printer using an appropriate screen dump program.

3.2.3 **Results**

The signals resulting in cases (1) and (3) are shown in Figures 50 and 51. If the signal height is plotted as a function of notch width we obtain a straight line, as indicated in Figure 52. This demonstrates the reproducibility of the same result obtained by Sharif (11) in Figure 37. However, plotting the signal width as a function of notch width we obtain the resulting graph given in Figure 53. This shows little change in signal width for varying notch width, a result contradictory to that obtained by Sharif, Figure 38, but in agreement with the prediction of computer plotting. In fact, although in qualitative agreement, there is a discrepancy since computer plotting predicts a total signal width of 2.95mm, whereas the observed signal width was about 4.2mm (Figure 53). The lack of quantitative agreement is dealt with in Section 3.3.1 and as we shall see can be accounted for by the finite extent of the probe. It is clear in Sharif's experiment that the noise in Figure 34 is considerable, especially for the smaller notch widths: This leaves Figure 38 open to interpretation.

When the signal width is plotted as a function of scan height we obtain the result in Figure 54. This is a very different result to the linear dependence approximately through the origin predicted by computer plotting also in Figure 54.

This discrepancy can again be accounted for by the finite size of the probe.

The observed dependence of signal width on notch depth was as shown in Figure 55, together with the theoretical prediction of computer plotting. Again, we have qualitative agreement, in that the signal width is not strongly dependent on notch depth, but again the agreement is not quantitative.

3.2.4 The effect of the background signal

It is apparent from Figures 50 and 51 that in addition to the signal predicted by Eqn.(1), there is a background signal not observed by Sharif (11) in Figure 34. This background signal is thought to be due to the proximity of the magnet/steel interfaces of Figure 46, which effectively form large width gaps with associated leakage fields. As these interfaces are approached by the probe, the field increases rapidly. This is indicated in Figure 56, which is the background signal with no crack or notch present. It can be seen that the background signal is not a simple spatially linear bias, and that there is a region in the centre of about 2cm over which the background bias becomes relatively flat. The bias was found to be largely independent of scan height, providing this was not greater than about 7mm.

The bias observed with no notch present is clearly affected by the presence of a notch. This is most evident in Figure 50, where for the case of a 25μm wide notch there is a definite bias even within the previously measured 2cm flat region. The background bias therefore is itself a function of the notch parameters, as well as the magnetisation in the specimen. The exact shape of the bias however is unclear. Kalwa and Piekarski (49) concluded only that the background signal was spatially antisymmetric, whereas Oehl and Swartzendruber (27) approximated the bias by a spatially linear term. Oehl and Swartzendruber had however observed a bias in the opposite sense to Figures 50 and 51, which show 'positively' biased signals.

It is unclear whether or not there is a spatially linear bias in the region near the origin of the signals in Figures 50 and 51. If a linear bias is assumed, bias lines may be drawn into the signals as shown, and the effect of the bias may be accounted for by adding the bias signal near the origin to the main signal peaks. Such corrected signal amplitudes are shown in Figure 52 as a function of notch width, where the linear correlation of the points (0.9968) was found to increase slightly over the uncorrected case (0.9944). This correlation is however somewhat dependent upon the exact way in which the bias lines are drawn. The best fit straight line for the corrected case does not go through the origin, but intercepts the abscissa at about -11μm. This indicates that the surface roughness of each steel block must have been of the order 5-6μm, and that the effective width of notch when using an xμm shim was actually (x+11)μm. The good linear correlation observed for both the corrected points and uncorrected points arises because the ratio of the bias coefficient D (Am^{-1} per m) to the magnetisation M (Am^{-1}) is generally very small (about $2\times10^{-2}m^{-1}$) so that the correction is relatively minor.

No clear conclusion can be drawn from the experimental results as to the nature of the bias, which may well have a slope at the origin which is rather less than that indicated by the bias lines drawn into Figures 50 and 51. In this case the bias lines may be treated as a worst case situation.

3.2.5 Remarks on the initial results

While the linear dependence of signal height on notch width was readily demonstrable and reproducible, the experiments to determine the signal width dependency on the three factors of notch width, depth and scan height were only qualitatively in concord with theory in two cases, and for the scan height dependence, not even qualitative agreement could be seen. It was clear that either the experiments were badly done (something the author might be willing to admit) or else something had been overlooked. The factor that was injected into the theory to try and account for the discrepancies was the effect of the finite extent of the probe. This aspect has been dealt with to some extent by Ko and Francis (10) where they considered the signal that would be produced from a rectangular Hall probe of uniform sensitivity. Edwards and Palmer (41) have also used such probe averaging techniques to account for the signals produced from relatively large probes.

3.3 Finite probe theory and signal width dependence

Consider a probe of width 2K being scanned at a height z over a notch or crack of width 2b and depth h, at a lateral distance x away from the centre of the crack, as in Figure 57. It has been shown that the vertical field around the crack is given by

$$H_V = \frac{M}{4\pi} \ln \left(\frac{[(x+b)^2 + (z+h)^2]\ [(x-b)^2 + z^2]}{[(x+b)^2 + z^2]\ [(x-b)^2 + (z+h)^2]} \right) \qquad \text{Eqn.(1)}$$

To determine the value of x at which the maxima/minima occur, it is necessary to differentiate this function with respect to x, equate to zero, and solve the resulting equation. This operation was carried out by Zatsepin and Shcherbinin (13), with the result that the values of x, x_{max}, for which the function is at an extremity are given by

$$x_{max} = \pm \left(\frac{(B^2-4AC)^{½} - B}{2A} \right)^{½} \qquad \text{Eqn.(23)}$$

where

$A = 3h(2z+h)$

$B = (z+h)^4 - z^4 - 2hb^2\ (2z+h)$

$C = (b^2+z^2)\ (b^2z^2-(z+h)^4) + (z+h)^2\ (z^4-b^4)$

This signal width predicting equation produces results which are not quantitatively in agreement with the practical dependence of x_{max} on b and h, and not even qualitative agreement with the experimental dependence of z. The width of the probe must come into the theory.

For the probe of width 2K as indicated in Figure 57 and of normalised sensitivity s(t) at a distance t along the probe surface (Figure 58), the average field picked up by the probe at a position x_o will be given by

$$\overline{H}_V\ (x_o) = \frac{1}{2K} \int_{x_o-K}^{x_o+K} s(x-(x_o-K))\, H_V(x)\, dx$$

For a probe of uniform sensitivity s(t)=1 and so

$$\bar{H}_v\ (x_o) = \frac{1}{2K} \int_{x_o-K}^{x_o+K} H_v(x)\ dx$$

This integral has been performed by Ko and Francis (10) using the expression for H_v given in Eqn.(1). The result is

$$\bar{H}_v\ (x) = \frac{M}{8\pi K}\left(I_1 + I_2 - I_3 - I_4\right) \qquad \text{Eqn.(24)}$$

where

$$I_i = (b_i + K)\ln\left((b_i+K)^2 + a_i^2\right) - (b_i-K)\ln\left((b_i-K)^2 + a_i^2\right)$$
$$+ 2a_i\left[\ \arctan\left(\frac{b_i + K}{a_i}\right) - \arctan\left(\frac{b_i - K}{a_i}\right)\right]$$

with $a_1 = a_4 = z+h$ $\qquad a_2 = a_3 = z$

$b_1 = b_3 = x+b$ $\qquad b_2 = b_4 = x-b$

This result provides us with a means of finding signal widths by, for example, writing a computer program to plot the resultant field $\bar{H}_v(x)$ and observing where the maxima occur. However, it was desired to find a faster analytic solution to this problem, and produce an algebraic expression such as Eqn.(23), this time with an added parameter K to account for the finite probe size. This was not attempted by Ko and Francis (10).

The same procedure was taken as with the infinitesimal probe case. Namely, Eqn.(24) was differentiated, equated to zero and the resultant equation solved for $\bar{X}_{max}$. This is carried out in Appendix B, with the result

$$\bar{X}_{max} = \pm\left(\frac{A + (A^2 + 12B)^{½}}{6}\right)^{½} \qquad \text{Eqn.(25)}$$

where

$A = 2K^2 + 2b^2 - a_1^2 - a_2^2$

$B = (a_1\ a_2)^2 + (a_1^2 + a_2^2)\ (b^2 + K^2) + (b^2 - K^2)^2$

with $a_1 = z+h$, $a_2 = z$

3.3.1 Effect of finite probe on vertical component signal

Figure 53 shows the variation in signal width with notch width when the finite 634SS2 probe was scanned over a 15mm deep notch at a scan height of 1.5mm. Using the infinitesimal Eqns. (1) and (23), with the parameters h=15mm, z=1.5mm and 2b=0.025mm, theory predicts a signal width $2x_{max} = 2.95$mm. Varying 2b from 25μm to 100μm makes virtually no difference to the signal width, so we should have expected a straight horizontal line to be produced in experiment in Figure 53 at around 3mm on the ordinate.

The refined theory of Eqn. (25) permits us to inject the finite size of the probe into the problem. The actual dimension of the probe was 5.3mm (see Appendix A) but it is stated by the manufacturer that the probe is more sensitive towards its centre. We have some leeway therefore in what we choose for the parameter 2K, providing of course that it is less than 5.3mm. There should be a value of 2K which, via Eqn. (25), will give better credence to the experimental results of Figure 53. Choosing by trial and error a parameter 2K=3mm together with h=15mm, z=1.5mm and 2b varying from 25μm to 100μm, the signal width $2\bar{x}_{max}$ is found to be virtually constant at 4.18mm. This is qualitatively and quantitatively compatible with the result obtained. Note that the effect of a finite probe is to widen the signal, a result obtained by Ko and Francis (10) using computer plots.

Referring to Figure 54 it is seen that Eqn. (23) does not predict the observed dependence of signal width on scan height. Having already chosen the parameter 2K=3mm this is now used in Eqn.(25) to see how the finite probe will alter this theoretical dependence. The other parameters in the experiment were 2b=0.05mm, h=15mm with z varying from 0.2mm to 1mm. Figure 54 includes the theoretical finite probe result. It can be seen that agreement with experiment is improved both qualitatively and quantitatively by taking into account the parameter K.

Figure 55 shows how infinitesimal probe theory is not in quantitative agreement with experiment when we consider the variation of signal width with notch depth. However, using Eqn.(25), again with the parameter 2K=3mm, and with b,h and z values appropriate to the experiment, the agreement is seen in Figure 59 to be qualitatively and quantitatively much better.

The general dependencies of signal amplitude on crack/notch width and depth are little affected by the finite probe. To illustrate this a signal plotting program based on Eqn.(24) was written. Using this program the theoretical signal amplitude is plotted as functions of crack width and depth in Figures 60 and 61, for the case of 2K=3mm, z=1.5mm. By comparison with Figures 41 and 40 for the infinitesimal case it can be seen that the shape of the dependencies is very similar in both cases. The detailed signal amplitudes are however different.

3.4 <u>An attempt at defect characterisation</u>

Whilst much of the literature predicts what a signal should look like from a given defect and then compares with experiment, there seems to have been few attempts to start from a signal and arrive at the defect dimensions. This was attempted for the signal derived from Eqn.(24).

The first step in the procedure is differentiation of Eqn.(24). We find

$$\frac{dI_i}{dx} = \ln\left(\frac{(b_i+K)^2 + a_i^2}{(b_i-K)^2 + a_i^2}\right) = \ln\ [i], \quad \begin{array}{ll} a_1=a_4=z+h, & a_2=a_3=z \\ b_1=b_3=x+b, & b_2=b_4=x-b \end{array}$$

so that

$$\frac{8\pi K}{M} \quad \frac{d\bar{H}_v}{dx} = \ln\ [1] + \ln[2] - \ln[3] - \ln[4]$$

Evaluating at x=o and putting $p=\exp\left\{\frac{-8\pi K}{M} \left| \left(\frac{d\bar{H}_v}{dx}\right)_{x=0} \right|\right\}$ (M>0)

$$p^{1/2} = \frac{[(b+K)^2 + (z+h)^2]\ [(b-K)^2 + z^2]}{[(b-K)^2 + (z+h)^2]\ [(b+K)^2 + z^2]}$$

putting $B = \frac{(b+K)^2 + z^2}{(b-K)^2 + z^2}$ we get

$$h = \left[\frac{(b+K)^2 - p^{1/2}B(b-K)^2}{p^{1/2}\ B-1}\right]^{1/2} - z \qquad \text{Eqn.(26)}$$

Eqn.(26) suggests that given a value of b (with z and K known), a corresponding h may be found by measuring $(d\bar{H}/dx)_{x=0}$ and M. The essential part of the procedure is to guess at a value of b, work out the corresponding h from Eqn.(26), and using these values together with the measured $\bar{x}_{max}$, predict a value of $\bar{H}_{max}$ from Eqn.(24). We keep systematically guessing at b in this way until the predicted $\bar{H}_{max}$ agrees with the measured $\bar{H}_{max}$.

A program was written to carry out this procedure, plotting the modulus of $\bar{H}_{max}$ (measured) - $\bar{H}_{max}$ (calculated) against b. The modulus becomes zero when the correct values of b and h are attained. Given consistent values of $\bar{H}_{max}$, $\bar{x}_{max}$, $(d\bar{H}/dx)_{x=0}$ and M, (for example from a signal plotting program; not all combinations are necessarily consistent), it was found that the program could successfully locate the correct values of b and h. However, a little experiment showed that small variations (2-3%) in the measured $\bar{x}_{max}$ and M^{-1} $(d\bar{H}/dx)_{x=0}$, representing small inaccuracies in measurement, would produce large errors in the width prediction (10%) and a very large error in depth measurement (45%). This prohibitive need for accurate measurement renders the method ineffective. The problem arises because several pairs of crack dimensions [2b,h] can give rise to similar signals. For example, Figure 62 shows the fields produced from two theoretical cracks or notches of significantly different crack parameters, and yet the fields are very similar.

Using the signal plotting program based on Eqn. (24), Figures 60 and 61 can be expanded to show the signal amplitude produced for varying widths and depths of notch. For example, Figure 63 shows how the signal amplitude against notch width dependence has a slope which depends on notch depth. A given signal amplitude s indicates various possible combinations of notch depth and width as shown in Figure 63. However, some useful information is obtained when we consider the $h=\infty$ line, and realise that the signal will indicate a minimum 'crack' width w_s as shown.

Since a measure of crack width may not be as useful as a measure of crack depth we can adopt a slightly different approach. The information in Figure 63 can be alternatively displayed as in Figure 64. We assume a value of crack width of about 10μm below which it would not be possible to detect the crack by, for example, magnetic particle inspection. Assuming a value for the magnetisation M and knowing the leakage field H we see that for an ordinate in Figure 64 above about 50×10^{-4} the possibility of a through crack $h=\infty$ is indicated. For lower values of ordinate we can get a measure of the crack depth.

Above a depth of about 2 or 3mm it is clear that small inaccuracies in the measured H_{max}/M would produce large errors in crack depth measurement. If a wider crack is assumed, say 30µm, it would be possible to go to slightly larger depths before the measurements would become inaccurate. It is worth exploring what leakage fields are actually represented in the ordinate of Figure 64. If we assume an induction field in the body of the steel of 0.72 Tesla, as prescribed in BS6072 (8) we will have a magnetisation given by $B=\mu_o(H+M)$ i.e. $0.72 = \mu_o\ (\chi^{-1} + 1)\ M \approx \mu_o M$ since the susceptibility $\chi >> 1$. The leakage field B_{max} when $H_{max}/(\frac{M}{4\pi} \times 10^{-4}) = 100$ is

$$B_{max} = \mu_o H_{max} = \mu_o x100 \times \frac{M}{4\pi} \times 10^{-4} = \frac{100 \times 0.72}{4\pi} \times 10^{-4} = 5.73 \text{ gauss}$$

The peak to peak field is twice this amount (10 or 11 gauss) and since, as we have seen, the 634SS2 probe can detect fields down to about 0.5 gauss with a signal to noise ratio above 3, it is clear that we can work in the region close to the origin in Figure 64.

This proposed method of defect characterisation has two distinct disadvantages. Firstly, in order to get a measurement of the depth of the crack, it is necessary to assume a value for the width of the crack. Secondly, it assumes that we can measure the value of M, which in reality is a very difficult thing to do, particularly for the case of M being invariant with time. As we shall see, a method of crack depth measurement shall be proposed which overcomes both of these difficulties.

3.5 The field from a more realistic tapered crack

The rectangular shaped crack of Figure 30 is only an approximation to a real fatigue crack. Indeed, it is likely that any model will only be an approximation. Nevertheless, an improved model was investigated, that of the tapered crack in Figure 65.

The mathematics of the solution for the vertical component of field at the point P in Figure 65 is presented in Appendix C. The result is that the vertical component is given by

$$H = \frac{M}{4\pi\left(1+\frac{b^2}{h^2}\right)}\left[\ln \frac{z^2+(x+b)^2}{z^2+(x-b)^2} + 2\,[L(b) - L(-b)]\right] \quad \text{Eqn.(27)}$$

where

$$L(b) = -\frac{b}{h}\left[\arctan\left(\frac{h^2+hz+bx}{hx-bh-bz}\right) - \arctan\left(\frac{hz+bx-b^2}{hx-hb-bz}\right)\right]$$

As a comparison with the result given by Eqn.(1) for the equivalent rectangular crack, Eqns.(27) and (1) are plotted together for the case of 2b=10μm, h=1mm and z=1.5mm in Figure 66. It is seen that the signal width x_{max} is left virtually unchanged and that the strength of the signal is roughly halved. These two statements may not be true for all values of b,z and h and it is left as future work for Eqns.(27) and (1) to be investigated further. The values of b, z and h chosen were for a typical inspection situation. The reduction in signal is intuitively as expected, since the crack becomes less visible than in the rectangular crack case at deeper regions of the specimen. It would be expected that the lessening of the signal becomes less apparent for deeper cracks. After all, there is no difference between an infinite tapered and an infinite rectangular crack. The simple example shown in

Figure 66 however, shows that if the possibility of a tapered crack is to be allowed for, somewhat more caution in the interpretation of the leakage field is needed.

3.6 Practical hand scans on a welded Y-joint

To get some idea of what practical magnetic signals might look like from a real welded tubular Y-joint and so investigate the use of Hall probes in the non-destructive testing of welded tubulars, scans were made by hand on a cracked welded Y-joint which had been used for experiments involving acoustic emissions (60).

3.6.1 Experimental Procedures

The cracked and welded Y-joint, as illustrated in Figure 67, was magnetised in a rather crude manner. This involved stroking the pole of a fairly strong permanent magnet laterally across the weld. Scans were made with the 634SS2 probe at distances measured along the weld from the saddle point (at x=0mm) of 0mm, 50mm, 130mm and 170mm. The stand off was made as small as practicable, which was of the order 2-3mm directly above the crack taking into account the thickness of the plastic protective covering (1mm). Just to the side of the crack a stand off of 1mm was possible. At the saddle point the weld had a 2mm thick smooth plastic covering. The signal from the probe was amplified by the circuit of Figure 44 and fed to a chart recorder.

3.6.2 Results

The resultant signals from the Y-joint are as indicated in Figures 68 and 69.

3.6.3 Discussion of Results

The x=0mm position was a relatively wide portion of the crack with a smooth 2mm thick covering. Consequently the leakage field is smooth in appearance. The x=50mm position was scanned at a smaller stand off and so the signal is somewhat larger. It can be seen that the weld material produces a stepped signal (the weld itself has a stepped appearance) which it might be expected would interfere with the main signal if the crack had small enough dimensions. At x=100mm the signal has reduced in magnitude, indicating that the crack is getting smaller, but we can still see the characteristic shape. At x=130mm the crack is sufficiently small to make the signal more difficult to detect. However, increasing the stand off slightly by means of small plastic shims (0.5mm thick) the characteristic shape returns. At x=170mm there is no crack indicated, and all that can be seen is the signal due to the irregularity of the weld.

The crack length had previously been measured using acoustic emissions as being about 150mm long from the saddle point, so the results of the scans made with the Hall probe are consistent with at least one other method of non-destructive testing.

3.7 An investigation into the use of the tangential component of leakage field

Having investigated some of the features of the vertical component of magnetic signal, it was decided to investigate the use of the tangential signal. As we have seen, this is given by, in the usual notation for a crack of width 2b and depth h, scan height z:

$$\frac{2\pi}{M} H_T = \arctan\left(\frac{h+z}{x+b}\right) - \arctan\left(\frac{z}{x+b}\right) - \arctan\left(\frac{h+z}{x-b}\right) + \arctan\left(\frac{z}{x-b}\right) \qquad \text{Eqn. (2)}$$

This is sketched in Figure 70. It is clear that the maximum H_T^{max} occurs at x=0. In this case

$$\frac{2\pi}{M} H_T^{max} = 2\left[\arctan\left(\frac{h+z}{b}\right) - \arctan\left(\frac{z}{b}\right)\right]$$

Since in most cases we will have z>>b we can make use of the relationship

$$\tan\left(\frac{\pi}{2} - \frac{1}{x}\right) = \cot\left(\frac{1}{x}\right) \approx x \qquad \text{when } x >> 1$$

Thus $\arctan(x) \approx \frac{\pi}{2} - \frac{1}{x}$ when x>>1

Thus

$$\frac{2\pi}{M} H_T^{max} = 2\left[\frac{\pi}{2} - \frac{b}{h+z} - \frac{\pi}{2} + \frac{b}{z}\right] = \frac{2hb}{z(h+z)} \qquad \text{Eqn.(28)}$$

The field H_T^{max} is thus dependent on a combination of b, h, z and M, as we might expect. This result has been obtained from a slightly different viewpoint by Förster (37), the result there being expressed in terms of the field inside the crack rather than the magnetisation M. It shows that, as for the vertical component case, there are many pairs of [2b,h] values which will produce a given signal amplitude, and so unique width or depth characterisation is not possible using the signal amplitude measurement of a single scan.

The minima of Figure 70 occur where Eqn.(2) is differentiated and equated to zero. This process is done in Appendix D. The result is a cubic equation for which one solution is zero, as expected and the other two values are given by, when z>>b,

$$x^2_{min} = z(h+z) + [z^2(h+z)^2 + z(h+z)(h^2+3hz+3z^2)]^{\frac{1}{2}} \quad \text{Eqn. (29)}$$

If we evaluate x_{min} for the parameters used in the direct plot in Figure 70 where 2b=0.1mm, h=13mm, z=6mm we obtain the result $x_{min} = \pm 19.5$mm, in good agreement with the the theoretical plot in Figure 70.

The solutions for x_{min} are plotted as a function of h and z in Figure 71. These graphs are potentially useful as they show a possible method of getting at the crack's most important parameter, its depth, simply by measuring the width of the tangential signal. This signal width is independent of the crack width for all practical purposes (z>>b), unlike the signal strength of Eqn. (28). Moreover, the signal width is independent of the magnetisation (which merely affects signal amplitude) and can be approximately found from the graphs as

$$x_{min} \approx \sqrt{3}z + Ah$$

where A is of the order 0.6-0.7.

The only parameter that would need to be known is the scan height z which would be easily measurable and the depth of crack could then simply be read off by reading off the appropriate line in Figure 71.

Before testing this theory by experiment however, it was decided to try and predict the effect of a finite probe on the measurement of signal width. As we have seen, the width of the vertical component signal can be considerably changed by a large probe.

3.7.1 Finite probe theory for the tangential signal

Consider the probe of width 2K whose centre is at height z_0 above a flat plate with a rectangular crack of width 2b and depth h as in Figure 72.

It is known that the field detected by a probe of infinitesimal K size is given by Eqn.(2). For a probe of uniform sensitivity and of finite K we must integrate Eqn. (2) over the face of the probe and divide by 2K to find the mean value of signal detected in the position shown i.e.

$$\bar{H}_T = \frac{1}{2K}\int_{z_0-K}^{z_0+K} H_T \, dz$$

Note that whereas with the vertical component we integrated with respect to x we must now do so with respect to z. The result is presented in Appendix E. To find the values of x for which the stationary values of $\bar{H}_T$ occur we must next differentiate $\bar{H}_T$ with respect to x, equate to zero and solve the resulting equation for x. This also is done in Appendix E, with the result (assuming z-K>>b)

$$\bar{x}_{min}^{2} = (z^2 - K^2 + hz)$$
$$+ \left\{(z^2-K^2+hz)^2 - \frac{1}{h}\Big[(z+h)\ (z^2-K^2)^2 - z(z+K+h)^2\ (z-K+h)^2\Big]\right\}^{1/2}$$

Eqn. (30)

It is noted in Appendix E that when we set K=0 in Eqn. (30) the infinitesimal result Eqn.(29) is produced. This is indeed as the case should be.

The finite probe values of $\bar{x}_{min}$ are plotted for the case K=1.5mm (corresponding to the value of K used in the vertical component case) as a function of z and h in Figure 73. Comparing with Figure 71, we see that the effect of the finite probe is to shift the line for any particular z value down slightly. This is what we would intuitively expect from the following argument. From Figure 71 the general trend as z decreases is for the width of the signal to go down. From Eqn. (28) the signal also becomes stronger for smaller z. Thus a uniformly sensitive probe of width 2K whose centre is at height z_0 as in Figure 72 will give greater weighting to the field below the central line than above it, because of the stronger field there. Hence the tendency of the probe is to give greater weighting to the narrowing influences of the field below the centre line than the opposing widening influences of the field above the centre line.

The theory indicates that the finite size of the probe should present no fundamental problem to the method proposed to gauge the depth of the crack. The only difference is that the graphs in Figure 73 are used rather than Figure 71.

3.7.2 A practical attempt at justifying the finite probe theory for the tangential component

Experimental Procedures

To test the theory of the finite probe two blocks of steel 35mm x 120mm x 13mm were acquired and placed together to form an artificial crack as in Figure 46. The width of the notch was set to 100μm by appropriate 25μm thick aluminium shims, the depth of notch being 13mm. The magnets were set in place, and by means of plastic shims the height of the centre point of the probe above the notch opening was set to 6mm, as in Figure 72. The probe was then attached to the paper from the chart recorder and as the paper unfurled the probe was scanned across the notch. The resultant chart recorder signal thus had a 'real distance' abscissa.

3.7.3 Results

The resultant signal is as indicated in Figure 74.

3.7.4 Comments

The general shape of the signal in Figure 74 is much as expected (compare with Figure 70). The total width of the signal is measured to be 55mm. However, the prediction of Eqn.(30) for the appropriate parameters of z, K and h is that the signal should have a width of 39mm. This is a considerable discrepancy, and unfortunately the author cannot offer an explanation. It was thought at first that the signal could have been widened by the effect of interference from the permanent magnet poles in Figure 46. However, closer examination reveals that if there was any interference from this source, then it would have had the effect of narrowing the signal and would have been revealed by a general superimposed curvature on the signal. (Indeed, this was the case when the smaller $40\times100\times15\text{mm}^3$ blocks were used). As this was not observed, no explanation of the discrepancy can be offered. There was evidently an additional field present in the experiment which was overlooked by the theory.

3.7.5 The use of the tangential field applied to a Y-joint

It was decided to abandon the possible use of the tangential signal to measure the depth of a crack in a welded Y-joint for two main reasons. Firstly, the minima in the signal occur at small signal strengths, typically 1/10th of the main signal peak (see Figure 70). For cracks of the order 20μm wide and 3 or 4mm deep, the tangential minima would occur at approximately 0.2 gauss signal strength (5mm stand off, 0.72 Tesla magnetisation). Since any scanning device would inevitably have to follow a curve as it passed over the weld, there would be significant interference from the earth's field of 0.18 gauss, which would tend to misplace the signal minima. Secondly, the use of the tangential signal would require that the scanning device kept a record of the distance it had travelled as it scanned laterally across the crack, to get a measure of the signal width. The curvature of the lateral scan itself would distort the shape of the signal which would have its 'ideal' shape only along a line perpendicular to the crack, along the line AB in Figure 75. In examining a point on the weld, such as at x in Figure 75, the whole idea breaks down because the pipe itself would get in the way of the signal before we could record it. i.e. the minima would be in the pipe itself, overshadowed by the immensely greater field due to the magnetisation of the pipe.

In short,the tangential signal could be of very considerable use on flat plates but not for the practical situation of a welded tubular Y-joint. The theoretical graphs in Figure 71 remain as a potentially useful method of gauging crack depth, and despite the setback of the single experiment carried out to investigate their validity, they invite further experiments to be undertaken.

3.8 Characterisation of the vertical component peak

Having focused attention back to the vertical component, a simple expression was sought for which would describe the peak signal strength, a vertical component equivalent of Eqn.(28).

When $h \rightarrow \infty$, the expression for the vertical component

(Eqn. (1)) becomes

$$H_{Vert} = \frac{M}{4\pi} \ln \left[\frac{(x-b)^2 + z^2}{(x+b)^2 + z^2} \right]$$

Differentiating with respect to x and equating to zero,

$$2(x-b)\ [(x+b)^2 + z^2] - 2(x+b)\ [(x-b)^2 + z^2\ ] = 0$$

This has solutions,

$$x_{max} = \pm\ (b^2 + z^2)^{½}$$

It is known from computer plotting of Eqn.(1) that x_{max} does not vary enormously with varying depth h (see Figure 43) Therefore we use the value $x_{max} = (b^2 + z^2)^{½}$ in the original full Eqn. (1) in order to get an approximate expression for the maximum in H_{Vert}. This process is carried out in Appendix F with the result

$$\frac{4\pi}{M} H_{max} = \frac{2b}{z} \left(\frac{h^2 + 2hz}{2z^2 + h^2 + 2hz} \right) \quad (z>>b) \quad \text{Eqn.(31)}$$

This equation has desirable properties, as shall be shown in Section 4.1.

If the signal given by Eqn.(1) has in addition a linear bias as has been modelled by Oehl and Swartzendruber (27) the situation is rather more complicated. The signal can then be modelled by the expression

$$H_{Vert} = \frac{M}{4\pi} f(x,z,b,h) + Dx + C \qquad \text{Eqn.(32)}$$

where the function f takes its meaning from Eqn.(1). In order to try and characterise the crack from such a model, the coefficient D is taken at first to be positive (Oehl and Swartzendruber observed a negative coefficient). This reproduces the general sense of bias in Figures 50 and 51. If H_{Vert} becomes zero at distances $x=x_o$ from the origin of the signal (ignoring C), then

$$D = -\frac{M}{4\pi}\frac{f(x_o,z,b,h)}{x_o} \qquad \text{Eqn.(33)}$$

The gradient at the origin is

$$G = \left(\frac{dH_V}{dx}\right)_{x=0} = \frac{M}{4\pi}\Big[f'(x,z,b,h)\Big]_{x=0} + D$$

so that

$$G-D = \frac{M}{4\pi} f'(0,z,b,h) \qquad \text{Eqn.(34)}$$

The left hand sides of Eqns.(33) and (34) are fixed by experiment, while x_o and z will generally be measurable. There are three unknown variables, namely M, b and h. Since there are only two equations, it is impossible using this method to deduce anything about the width or depth of the notch, without assuming a value for M. If M could be measured, it might then be possible to find unique values of b and h to fit both Eqns.(33) and (34). Otherwise there is a whole range of solutions to the problem. In Section 3.4 it has been shown that when D=0 (so that $x_o=\infty$), there is a whole range of solutions to Eqn.(34) based on pairs [b, h] when M is known. (Indeed, Eqn.(31), which is based on Eqn.(1), shows how solutions in pairs occur even more clearly, based on the requirement to fit the theoretical signal amplitude to the measured amplitude). If M is not known (as will generally be the case), the method becomes ineffective. It was found also in Section 3.4 that small inaccuracies in the measurement of $M^{-1}(dH_V/dx)_{x=0}$ led to greatly inaccurate solutions for b and h. This is therefore a poor parameter on which to base calculations, and is likely to remain so even when $D \neq 0$.

It is likely that the coefficient D will increase roughly in direct proportion to M in any given situation. Oehl and Swartzendruber (27) note a linear correlation between D and their applied field of greater than 0.95 over a twelve-fold increase in applied field. In the double probe system described in Section 4.1, the ratio of signal amplitudes at two different scan heights is taken, and shown to be independent of the magnetisation M. If the signals are corrected to remove the effect of the bias as in Figures 50 and 51, this bias itself is proportional to M, implying that the ratio of signals will remain independent of M even for the corrected case. The linear biases observed are in any case small compared to the signal amplitudes.

3.8.1 Comments on the characterisation of the peak vertical component

It can be seen immediately from Eqn.(31) that the well known result of linear dependence of H_{max} on b (e.g. Figure 52) has a sound theoretical basis. Not only that but Eqn.(31) gives the decreasing dependence of H_{max} on z, being proportional to z^{-2} for small h and proportional to z^{-1} for large h. In practice, h will be of the same order as z so that the dependence is intermediate between z^{-1} and z^{-2}. The equation also gives the dependence of H_{max} on h. It is instructive to compare the predicted dependence on h given by Eqn.(31) with the previously produced computer plot in Figure 40. This comparison is shown in Figure 76, and it can be seen that the approximation is quite good.

To test the predicted dependence of H_{max} on z the experimental results of Figure 51 can now be used. For these signals the parameters $2b=50\mu m$, $h=15mm$ were used, with the scan height of the probe varying from 0.2mm to 1.0mm. If the signal strength of each of the signals is plotted against its corresponding scan height the result in Figure 77 is obtained. By using the appropriate values of b, z and h in Eqn.(31) and choosing a value of M which will normalise H_{vert} to coincide with, say, the z=0.2 datum, we obtain the simple theory curve also shown in Figure 77. Choosing a value for M in this way is allowable since it is an unknown quantity and we are only interested in the dependence of H_{max} on z, rather than detailed amplitudes. It is clear that the theory predicts a sharper fall off than is observed, and the difference is by a large factor of 3. The finite size of the probe might explain the discrepancy but even so we would not expect it to be so large. A more fundamental factor was suspected.

At this point it was decided to take a closer look at the 634SS2 probe. Consequently one of the probes was broken open and the active area sought out. It was found that there was a 1mm thickness of plastic separating the active face of semiconductor from the outside surface, and that the active element appeared to be a 1mm square section.

This information could be put to use in the assessment of the predicted values of H_{max} via Eqn.(31). Clearly the range of values for z must be amended for the theoretical plot of Figure 77. Instead of having z ranging from 0.2mm to 1mm one should use z=1.2mm to 2mm to account for the plastic covering of the probe proper. With this modification, and again choosing a value of M to normalise the z=1.2 datum to 53 arbitrary experimental units, the prediction given by Eqn.(31) is also plotted in Figure 77. This time the agreement is seen to be excellent.

As in Section 3.2.4, the possibility of a linear bias in the signals of Figure 51 must be considered. Once again, it is unclear whether or not there is a spatially linear bias in the region near the origin of the signals in Figure 51. Assuming a linear bias as shown in Figure 51, the bias near the origin of the signals can be added to the main signal peaks. The z=1.2 datum can be normalised to the previous value of 53 units by adding the observed 1.5 units of bias to the 53 units of raw signal and then multiplying by a constant factor of 0.9725. A similar procedure is carried out for each of the other data points, namely adding the estimated bias to the raw signal and then multiplying by 0.9725. The results of such a corrected signal dependence on scan height are also shown in Figure 77, where it can be seen that the correlation with the prediction given by Eqn.(31) is still very good. By plotting the observed signal amplitude against the signal amplitude predicted by Eqn.(31) for each scan height, the corrected signals were found to have a linear correlation of 0.994 as opposed to the figure of 0.996 for the uncorrected case. This is only a small difference, which reflects the fact that the bias is small in comparison to the main signal peak.

3.9 A review of experimental results

It was pointed out in Section 3.3.1 that in order to give quantitative agreement to the experimental results of Figures 53, 54 and 55, we should assume a probe width of 2K=3mm, scan heights being measured from the test specimen surfaces to the probe surface. These assumptions have just been disproved by discovering that the probe is only approximately 1mm square, and that it is buried beneath 1mm of plastic. How do these realisations effect the credibility of the results? Well, this is easily tested. Eqn.(25) is used just as before. In the case of Figure 53 we substitute z=2.5mm and 2K=1mm into Eqn.(25), instead of the previous values z=1.5mm and 2K=3mm. (h=15mm as before).

The result is that the total signal width is invariant with notch width, the signal width being 4.9mm. This is still in fair numerical agreement with the observed value of 4.2-4.3mm (see Figure 78).

In the case of Figure 54 we again put $2b=0.05$mm, $h=15$mm into Eqn.(25) but change the now measured parameter 2K to 1mm and change the range of variation of z to 1.2mm to 2.0mm. It is seen that the resultant theory (Figure 79) is in at least as good agreement with experiment as that in Figure 54.

Making the appropriate changes in z and K values in Eqn.(25) for the case of the experiment conducted in Figure 59, we see that if anything the agreement of the theory has been enhanced by the change (see Figure 80).

The fact that there are two (or even more) sets of [z,K] values which will produce similar results for x_{max} is not to be altogether unexpected. This is because, as we have seen, increasing z or K will increase x_{max}. Thus reducing K whilst increasing z will have combined effects which will partially cancel each other out.

CHAPTER 4

THE LOHET II, CRACK DEPTH MEASUREMENT AND THE DOUBLE PROBE SYSTEM

4.1 A proposed method of crack depth measurement using the vertical component

The double probe system

Faced with the relationship Eqn.(31), a method was proposed by which crack depth measurement might be possible without the need for the accurate tracking of probe movement that would be necessary in the tangential component use. Moreover, the method has the advantages that the precise magnetisation M of the specimen need not be known, and also that we would not need to make any assumptions as to the width of the crack. The latter two conditions were both serious drawbacks to the method proposed in Section 3.4.

The idea is to have two probes, one on top of the other, and to record the ratio of the magnitudes of the two signals produced. If the lower probe is at a height z_1 and the upper probe at a height Z_2, then from Eqn.(31) the two signals will be given by

$$\frac{4\pi}{M} H_{max1} = \frac{2b}{z_1} \frac{(h^2 + 2hz_1)}{(2z_1^2 + h^2 + 2hz_1)}$$

$$\frac{4\pi}{M} H_{max2} = \frac{2b}{z_2} \frac{(h^2 + 2hz_2)}{(2z_2^2 + h^2 + 2hz_2)}$$

Taking the ratio r of these signals we find

$$r = \frac{H_{max1}}{H_{max2}} = \frac{z_2}{z_1} \frac{(h+2z_1)\ (2z_2^2+h^2+2hz_2)}{(h+2z_2)\ (2z_1^2+h^2+2hz_1)} \qquad \text{Eqn.(35)}$$

We find immediately that r is independent of the magnetisation. Moreover, since H_{max1} and H_{max2} are both proportional to b, their ratio r remains independent of b, depending only on h, z_1 and z_2. Obviously z_1 and z_2 should be as different as possible to get a fair spread in values of r as h changes. In practice it would be necessary to make a compromise between how small z_1 can be made, limited by such factors as local specimen geometry, probe dimensions and robotic scanning tolerance, and how large z_2 can be made, limited by the sensitivity of the probe, magnetisation employed and how small a width of crack it is required to detect. z_1 and z_2 must also be kept much greater than b for Eqn.(35) to apply.

Choosing, for the sake of simplicity and compromise, z_1=2.5mm, z_2=5mm, r is plotted as a function of h in Figure 81. The graph is of such a shape that useful depth measurement should be possible to depths of 10 to 11mm or so, but beyond that small variations in r would produce large variations in h. However, this problem occurs anyway with the method proposed in Section 3.4. It is a natural consequence of the fact that the further away from the surface that an additional depth of crack is placed, the smaller will be the effect at the surface. It is intuitively clear that there would be more effect going from 4mm to 5mm depth than from 10mm to 11mm, such intuition is borne out in Figure 81 and Figure 76. Even so, it should still be possible to say that the crack is greater than 10mm deep, which is useful information.

4.1.1 The range of cracks detectable

The relation given by Eqn.(31) allows us to plot the areas in the b-h plane where detection would be possible and where it would not, given the criterion of what is the minimum signal we can reliably detect. If we choose a value of 0.36 gauss as this minimum value (so far detectable with a signal to noise ratio of 3), the range of cracks detectable for 0.72 Tesla internal field and 5mm scan height is as indicated in Figure 82. Also included in Figure 82 is the range of b, h values detectable for a minimum detectable field of 0.54 gauss (3 x earth's field), corresponding to a higher signal to noise ratio in the field measured by the probe.

The circuit of Figure 44 used to amplify the probe output under quiescent conditions, illustrated in Figure 48, had been powered by a mains derived power supply, and it was thought that the inevitable ripple on the supply lines might well be contributing to the noise. The circuit was powered by batteries for comparison and the earth's field detected. The result is shown in Figure 83 and it can be seen that the noise has been significantly reduced, but that there is still a considerable problem with thermal drift. Sufficiently fast scanning was thus necessary.

4.1.2 The suitability of the 634SS2 probe to the double probe system

Figure 47 illustrates the level of noise present with the 634SS2 probe when detecting a field of 0.36 gauss, a signal to noise ratio of about 3, and the range of cracks detectable at 5mm stand off using this S/N ratio is indicated in Figure 82. For simple detection purposes therefore the 634SS2 probe should be quite adequate. However, when we consider their use in the proposed double probe system, we encounter a problem when it comes to sizing using this S/N ratio. For example, suppose a ratio of signal strengths from the probes of 2.5 is measured, subject to each probe having an S/N ratio of 3. The possible values for the true ratio could be thus anywhere within a range:

$$\frac{2.5 - \frac{1}{2}(1/3 \times 2.5)}{1 + \frac{1}{2}(1/3 \times 1)} < \text{true value} < \frac{2.5 + \frac{1}{2}(1/3 \times 2.5)}{1 - \frac{1}{2}(1/3 \times 1)}$$

i.e. $1.79 < \text{true value} < 3.5$

From Figure 81 this would indicate the depth of crack as anything from 1.5mm to infinity, hardly a reliable measure of crack depth. The best we could do under such circumstances would be to say that the crack was at least

1.5mm deep. It should be noted however that for large crack width, say 50µm and over, we would generally be working well within the detectable region of Figure 82, so that we would have higher S/N ratios and hence a more precise value for the ratio of signals detected by the probes. The crack depth measurement would thus be correspondingly more precise, (and hopefully accurate).

The 634SS2 probe has been shown to have a thermal drift of about 1.5 gauss °C^{-1}. For sufficiently fast scanning, this drift would have little effect on the signals produced, but it would be very difficult for a data logger which accepted a fixed input signal range to follow such a large zero drift and maintain a reasonable resolution in the signal magnitude.

4.2 The Lohet II probe

Early in 1989 a probe of 5mV $gauss^{-1}$ sensitivity was made available by Honeywell. The characteristics of the device are given in Appendix G. It is a 3-terminal device unlike most Hall probes, requiring a supply voltage of 8 volts. Two terminals are for the 0-8V supply, with the third terminal displaying a voltage which varies from 2V to 6V as the applied field varies from -400 gauss to +400 gauss i.e. 5mV/gauss. The fact that only three terminals are present led to a design of amplifier for the probe which largely eliminates zero drift. This circuit is shown in Figure 84. For a supply voltage V_s, the Lohet II displays an output of $\frac{V_s}{2}$ ± 5mV $Gauss^{-1}$. The potential divider in parallel with the probe is designed so that the tapping point leading to IC1 can be accurately tailored to $V_s/2$. IC1 then inverts this, and the result, $-V_s/2$, is combined together with the output of the Lohet II by summing amplifier IC2. The output of IC2 is therefore $V_s/2$ ± 5mV $gauss^{-1}$ - $V_s/2$ = 5mV $gauss^{-1}$. IC3 then amplifies the result to a convenient level for a chart recorder or data logger. In fact the two stages of summing and amplification could be combined into one, and this approach was taken in a later design.

For 'perfect' components the effect of falling battery voltage should result only in a slight loss of sensitivity of the probe, as the current through the active element reduces slightly. The zero point however should remain fixed.

4.2.1 Lohet II amplifier performance

Having powered the circuit of Figure 84 with standard PP3 alkaline cells, the practical zero drift obtained was as indicated in Figure 85. On the same vertical scale the detection of the earth's field by rotation of the probe in a North-South direction is as illustrated in Figure 86. The steps represent a field of 0.36 Gauss. From Figure 85, apart from an initial surge lasting a minute or so, the amplifier is seen to drift 0.25 gauss in the first hour of operation, 0.1 gauss in the second, and 0.04 gauss in the third. This stability is quite adequate for a data logger, keeping the zero in range. The ICs used in Figure 84 incidentally were the ubiquitous and cheap industry standard type 741.

It is clear from Figure 86 that a considerable improvement in signal to noise ratio has also been achieved over the 634SS2 (c.f. Figure 47). There is no apparent noise present at this level of amplification. Increasing the chart recorder gain by a factor of ten to 20mV f.s.d. resulted in the appearance of some noise. This noise is indicated in Figure 87, and it can be seen that a field of 0.36 gauss can be detected with a signal to noise ratio of about 20, a considerable improvement on the value of 3 for the 634SS2 probe.

By comparison with Figure 83 it is clear from Figure 86 that the thermal properties of the Lohet II are also far superior to the 634SS2. Figure 88 shows the effect of placing the probe near to a naked flame for nearly half a minute at an amplification of 200mV f.s.d. Comparing this with the steps of 0.36 gauss of Figure 86 and estimating the probe to have heated up by at least 10°C, we observe a thermal drift of not more than 0.012 gauss $^{o}C^{-1}$, over a hundred times better than the 634SS2. The maximum temperature drift quoted for the output in Appendix G of 0.02%$^{o}C^{-1}$ indicates a practical drift of 0.16 gauss $^{o}C^{-1}$, so we are working well within this limit. This thermal stability is certainly adequate for a data logger.

4.2.2 **The suitability of the Lohet II to the double probe system**

Referring to Figures 81 and 82, and reasoning along the same lines as in section 4.1.2, a measured signal ratio of 2.5 from a double probe system, subject to each probe having a S/N ratio of 20 would indicate a true value in the range

$$\frac{2.5 - \frac{1}{2}(1/20 \times 2.5)}{1 + \frac{1}{2}(1/20 \times 1)} < \text{true value} < \frac{2.5 + \frac{1}{2}(1/20 \times 2.5)}{1 - \frac{1}{2}(1/20 \times 1)}$$

i.e. $2.38 < \text{true value} < 2.63$

From Figure 81 the crack depth is given as between 5mm and 8mm, a much improved estimate over the equivalent 634SS2 information which indicates the crack depth observed as between 1.5mm and ∞ . Figure 82 shows that for a field of only 0.36 gauss to be produced from a 5-8mm deep crack, it would be less than 10µm wide. As before, a wider crack would give a more precise value for the depth, since the signal to noise ratio would be increased.

4.2.3 Scans made with the Lohet II

It was desired to see what sort of signals would be produced from the Y-joint as in section 3.6. Scans were made at a fairly small stand off of 1mm over a cracked portion of the weld. The expected shape of signal was produced, a typical example of which is indicated in Figure 89. The method of magnetisation was once again to stroke the pole of a fairly strong magnet laterally across the weld, and so it was anticipated that the actual magnetisation level was quite low.

A robotic arm was being developed during the course of this project at University College, London. It was hoped and anticipated that the arm should be capable of tracking and scanning around the weld to within 5mm scan height around the weld toe. Consequently, it was desired to see what sort of signal would be produced from the crack at a height of 5mm. Such a scan height was arranged with the aid of a 5mm thick plasticine covering, and the Lohet II was scanned over the same portion of crack for which Figure 89 had been produced, (at a 1mm scan height). The resultant signal is indicated in Figure 90. It can be seen that there has been an expected fall in amplitude of the signal, but in addition a considerable asymmetry has been introduced. In fact there is a slight asymmetry in Figure 89 but this was not at first thought to be of much significance.

Work has been done on the effect on the magnetic signal of a crack which has not propagated at right angles to the surface, but at an angle (13) (30). The result of such an analysis is that the ideal antisymmetric picture of Figure 6 becomes increasingly asymmetric as the angle increasingly departs from the $\pi/2$ ideal i.e. the peaks become unequal in size. In view of the type of scan seen in Figure 90, the possibility of the crack in the tubular having propagated at an asymmetric angle presented itself.

4.3 Comparison of the probe with magnetic particle inspection

A graticule was fixed to the Y-joint weld along the length of the crack, and the weld was magnetised to BS6072 using an Emcol MF10 direct current mode unit. Magnetic particle inspection was carried out using a U.V. sensitive magnetic particle spray. The crack length was indicated as being 168mm long from the saddle point. With the same level of magnetisation maintained, the Lohet II probe was scanned with a 1mm stand off at various positions over the crack. The signals obtained at various distances along the graticule are as indicated in Figure 91. At this level of magnetisation the signals achieved are not the expected shape, nor is there a clear indication of where the crack ends. It would seem that there is considerable stray flux from the electromagnets which is interfering with the measurement of the flux leakage from the crack. It was decided therefore to scan the crack at a lower level of magnetisation, as had been used previously. This was achieved simply by stroking the pole of a fairly strong magnet over the crack. The signals obtained in this case are indicated in Figure 92. A clear signal is obtained up to about 146mm, which is as far as the visible crack extends, but beyond that the signal becomes difficult to interpret. Using the Hall probe signals in this manner would seem to indicate that MPI would be a better method of determining crack length.

4.4 Testing of the double probe system

Experimental procedures

In order to test the double probe system, blocks of 50D steel were cut from which artificial cracks of varying depth could be formed. The specimens were cut in pairs and as it was desired initially to minimise edge effects, one dimension of the block was made quite large. The dimensions of the block used were 300mm x 100mm x xmm where x determined the depth of the crack, and took on the values x = 4, 6, 8, 10, 12 and 14.

The specimen edges were ground flat and artificial cracks were formed as in Figure 93 with aluminium shims of about 40μm thickness. The actual width of the shims, and hence the notch, was not too important. The blocks were not clamped tightly together and indeed, the evidence was that there could have been some variation in the notch width to within a factor of 2 or 3.

The double probe system was constructed from two Lohet II probes, as in Figure 94, and an amplifier for the two probes was built, based on a stereo version of Figure 84. Each artificial crack was magnetised to two different levels using the Emcol MF10 unit as in Figure 93. One level was that of the British Standard, and the other a somewhat lower level. The double probe was scanned manually over the crack at each level of magnetisation, the extreme positions of the scan being about 5cm on each side of the crack. The signals from the amplifier were fed into two channels of a 4 channel data logger, type Vela Mark 2. Each channel was capable of storing 1024 data points which could be examined at leisure and also transferred to a chart recorder to give a permanent record.

4.4.1 Results and discussion

The general shape of signal produced from the probes using the 300mm long plates is an indicated in Figure 95. This shape of signal is not quite as expected from theory. Whereas the classic leakage field dies away to zero on both sides of the crack, it is seen in practice that at some distance from the crack the field tends to a local minimum value, of the same polarity as the main signal peak on that particular side of the crack. This 'biased' type of signal, with the apparent additional vertical components providing the bias, has been encountered by Oehl and Swartzendruber (27). They were observing the field from small subsurface cylindrical shaped holes and found that the signals obtained from a Hall probe could be least squares fitted to an equation of the form

$$H_{\mathrm{vert}} = \frac{-2mzx}{[z^2+x^2]^2} + Dx + C \qquad \text{Eqn.(36)}$$

with z being the height above the defect, m related to the magnetisation, D and C fitted constants, and x the distance along the line of scan. This curve is sketched in Figure 96 where the bias in the signal becomes evident. It is worth noting that if we take the classical Eqn.(1)

$$H_{\mathrm{Vert}} = \frac{M}{4\pi} \ln \frac{[(x+b)^2 + (z+h)^2]\ [(x-b)^2 + z^2]}{[(x+b)^2 + z^2]\ [(x-b)^2 + (z+h)^2]}$$

with the symbols having their usual meaning and work under the assumption that the dimensions of the slit are small compared to the scan height (i.e. b,h<<z, simulating the small defects observed by Oehl and Swartendruber), then Eqn.(1) can be shown to reduce to

$$H_{\mathrm{Vert}} \approx \frac{-2M(bh)\ zx}{\pi[z^2+x^2]^2} \qquad \text{Eqn.(37)}$$

The similarity with Eqn. (36) becomes apparent, the only difference being the absence of a term Dx + C. It is suggested by Oehl and Swartzendruber (27) that the origin of this linear field is the fact that the specimens of steel are not magnetised exactly parallel to the surface. The magnetisation then could be envisaged as having a component perpendicular to the surface, as illustrated in Figure 97, which suddenly drops to zero at the surface and consequently acts as a source of H field. The observed signals, of which Figure 95 is typical, would then be a combination of the defect leakage field given by Eqn.(1) and the linear field Dx + C having the above origin. The linearity of this field is, of course, empirical and approximate. In fact it is shown in Appendix H that an accurate linear field can be explained if we assume a surface charge density which changes linearly with distance i.e. the vertical component of magnetisation reaching the surface varies linearly with distance. The details of the bias field are however not well understood.

It was desired to take the ratio of signal amplitudes from the two probes and plot this as a function of crack depth. The general relationship sought for was as in Figure 81. The signal amplitude was taken as the distance between the extremal points of the biased signal, the distance A in Figure 96. The signal from the crack alone would have an amplitude somewhat less than A due to the above effect of the linear bias field, but this correction was ignored initially to see what sort of results would be obtained.

Using the measured amplitudes A, ratios r of the signals from the near and far probes were calculated for each notch depth at a magnetising current of 1.6A, which was sufficient for the standard 0.72 Tesla to be present. The process was repeated for a lower electromagnet current of 0.5A. A plot of signal ratio r against notch depth for the two magnetisation levels used is given in Figure 98. It is immediately apparent that the desired trend of Figure 81 has not been achieved. The ratio shows no increase as we move to smaller depths of notch, and in fact appears to remain constant at a value of about 2.6.

In order to take the negative bias in the signals into account, lines were drawn into the signals as indicated in Figure 95, to represent an assumed linear bias as had been suggested by Oehl and Swartzendruber (27). By subtracting the bias near the origin from the signal amplitude A in Figure 96, it was hoped to isolate the signals due to the notch alone. Signal ratios could again be taken with these new signals, the result appearing as in Figure 99. It is seen that the desired trend of Figure 81 has still not been achieved, and no obvious pattern has emerged. One possible reason for the scattered results is that the resolution in the signals is not particularly good (see Figure 95); the A/D converter of the data logger only has 8 bit resolution which under this particular circumstance has led to rather coarse steps in the signal.

Figures 100 and 101 show the expected and observed individual amplitudes A from the long plates, both with the bias present and removed. While the theoretical curve is not accurately traced out by experiment, variations are easily attributable to variation in notch width 2b (or indeed magnetisation). The ordinate of any individual unbiased point in Figures 100 and 101 is directly proportional to 2b so that, for example, the notch could well have been about 60μm wide in the case of the 12mm and 14mm notch depth. It was not possible to accurately control the notch width because of the difficulty in clamping together such long and thin plates. The fact remains however, that the ratio of results from Figures 100 and 101, indicated in Figure 99, does not behave as we would like.

The plates had been made long to avoid edge effects, and yet it was felt that it was the bias in the signal which was responsible for the disappointing result.

Previous specimens in earlier work (See Section 3.2) had been rather shorter so that, for example, the 300mm edge in Figure 93 would be about 40mm in length. In the latter case the 'tail ends' of the signal from the probe behaved as in Figure 102 with the signal diverging from the zero far from the crack in the opposite sense to the long plates. This background signal is attributable to the proximity of the spare edges of the plates which are in contact with the electromagnets and which have opposite magnetic polarity with respect to their corresponding notch faces. Nevertheless, this type of signal was shown experimentally to behave quite well when compared with theoretical behaviour, despite an apparent bias in the signal. For example, the clear and well documented linear dependence of signal amplitude on notch width was observed. In addition, the dependence of signal amplitude on scan height in Figure 77 was found to follow Eqn.(31), which is based on an unbiased signal. It was this feature which led to the repetition of the experiments in Section 4.4 with smaller samples, measuring 60mm x 100mm x xmm. An additional value of x=1.8mm was included, which it was not possible to machine with a 300mm long sample. The two levels of magnetisation current used in this case were 1.6A (giving the British standard field) and 1A.

Typical signals from the probes using these shorter samples appear as in Figure 103 where the field away from the notch now has the previous form. i.e. The field far from the notch is biased as in the initial experiments (Section 3.2.2). Figures 104 and 105 show the variation in peak to peak output voltage with notch depth for the near and far probes at the two different magnetisation levels. Also indicated are the theoretical variations for a constant notch width of 50µm and British standard magnetisation. There is apparently not much correlation and bearing in mind the previous comment that the ordinate of each experimental point is proportional to the width of the notch, it was clear that there was considerable variation in the latter. The specimens were not clamped to purposely introduce such a random variation in notch width for each notch depth and magnetisation level considered. This was desirable since the signal ratio r sought for is theoretically independent of notch width. When ratios are deduced they should ideally eliminate the random variation in notch width indicated in Figures 104 and 105, providing evidence for the independence of r on notch width.

Each ordinate in Figures 104 and 105 is also proportional to the magnetisation which may vary in some unknown way with the thickness of the plates (the depth x) presented between the electromagnets. We assume for the moment that any background signal is negligible. Since for any individual scan the near and far probes pass over the same width of notch magnetised to the same level, the signals S_{near} and S_{far} must appear as $S_{near}(M,2b)=K_1Mb$ and $S_{far}(M,2b)=K_2Mb$. (K_1 and K_2 depend on notch depth and scan height). If the magnetisation between scans changes from $M_{1.6}$ to $M_{1.0}$ and the width changes slightly from $2b_{1.6}$ to $2b_{1.0}$, the signals from the scans in both cases should be:

$$S_{near}^{1.6} = K_1\, M_{1.6}\, b_{1.6} \qquad S_{far}^{1.6} = K_2\, M_{1.6}\, b_{1.6}$$

$$S_{near}^{1.0} = K_1\, M_{1.0}\, b_{1.0} \qquad S_{far}^{1.0} = K_2\, M_{1.0}\, b_{1.0}$$

i.e. whatever the slight variation in crack width or magnetisation between scans, we should always have

$$\frac{S_{near}^{1.6}}{S_{near}^{1.0}} = \frac{S_{far}^{1.6}}{S_{far}^{1.0}} \qquad \text{Eqn.(38)}$$

The ratios on the left and right hand sides of Eqn.(38) are plotted in Figure 106 for the various notch depths and it can be seen that the correlation is excellent. For the case of constant notch width the ratio is simply the factor by which the magnetisation at the higher level is greater than that at the lower level. In most cases this appears to be about 1.3.

Re-arranging Eqn.(38):

$$r = \frac{S_{near}^{1.6}}{S_{far}^{1.6}} = \frac{S_{near}^{1.0}}{S_{far}^{1.0}}$$

The ratio r is of course the ordinate in Figure 81 and r should vary with notch depth in a manner which depends only on the scan heights employed. The ratio r is plotted for the two different magnetisation levels in Figure 107. Evidently the magnetisation and notch width variations indicated in Figures 104 and 105 have been elegantly eliminated when we consider the correlation of the points. Moreover, the desired trend indicated in Figure 81, one of increasing r with decreasing notch depth, is also apparent.

If it is assumed that the signals such as in Figure 103 have a linear bias near the origin, bias lines may be drawn in to the signals as in Figure 95, except this time with a positive slope. The contribution to the signal amplitude of the bias in this case is a negative one, so that the true amplitude of the signal due to the notch alone is slightly greater than that in Figure 103. Unfortunately only the extreme values of the peaks in the pairs of signals were recorded from the double probe system, with Figure 103 being taken as an example of a full signal pair. Thus it was not possible to try and correct for any possible bias in the signals. The likely effect of any bias would be to slightly depress the picture in Figure 107, with a possible decrease in the range of variation in signal ratio r. For example, with the bias lines drawn as shown into Figure 103, which shows the signals from an 8mm deep notch, the author estimated r to fall from 2.943 to 2.722 when taking into account the bias. The corrected ratio of 2.722 is more appropriate to a 10mm deep notch, so that an error of 2mm has been introduced. For smaller depth notches, the error would be less than this since the measured depth h becomes less critically dependent on the measured value of r. (See for example Figure 81).

It should be noted that the bias in Figure 103 appears to be increasing in magnitude as we move further out from the origin of the signal. Another way of looking at this is to say that the bias appears to be decreasing as we move towards the origin. This indicates the possibility of a background signal roughly of the form in Figure 56, with a region of relative flatness near the origin where the peaks are measured. The bias lines in Figure 103 in this case are likely to overestimate the extent of the bias, providing a worst case scenario.

Further evidence for the presence of a background signal of the form in Figure 56, or at least the absence of a simple linear bias, is the fact that the lines far from the origin in Figure 103 are not colinear. It could be argued that non-colinearity is consistent with a linear bias, as shown in Figure 107(a). This is however only looking at two (full) signal widths from the origin, where not even the unbiased signal shows colinearity in its signals on either side of the origin! The appropriate number of signal widths for the near probe in Figure 103 is more like eleven or twelve. Figure 107(b) shows the classical signal given by Eqn.(1) (with parameters 2b=0.04mm, z=2.2mm, h=8mm, as in the experiment) together with a linear bias $D/(M/4\pi) = 2.5\times10^{-4}$ mm^{-1}. Clearly if the bias were purely linear, colinearity would be seen in the signals far from the crack at a distance of ten signal widths from the origin of the signal. This is not observed in experiment. Non-colinearity is however consistent with the type of background signal measured in Figure 56.

The precise nature of the curve in Figure 81 is determined by the relation:

$$r = \frac{n_1}{n_2} \; \frac{z_2}{z_1} \; \frac{(h + 2z_1) \quad (2z_2^2 + h^2 + 2hz_2)}{(h + 2z_2) \quad (2z_1^2 + h^2 + 2hz_1)} \qquad \text{Eqn.(39)}$$

This relation has been derived previously where z_1 and z_2 are the near and far probe scan heights respectively, and h is the notch depth. Since we are measuring voltages in practice rather than fields, the ratio (n_1/n_2) has been included in the expression. n_1 and n_2 are merely the sensitivities of the near and far probe/amplifier circuits. In fact a simple measurement indicated that $n_1 = n_2$ very closely.

The actual scan heights used were subject to some speculation. It was assumed that the active element of the probe was somewhere in the plane p of Figure 94 so that the nominal scan heights would have been 2mm and 5.05mm. Assuming scan heights of 2.2mm and 5.1mm seemed to give a reasonable agreement with experiment given that $(n_1/n_2)=1$. Admittedly, these values were chosen to provide the best fit, but they differ from the nominal values by only 50µm and 200µm, which is quite a reasonable manufacturing tolerance for the probes. The agreement is indicated in Figure 108, where the theoretical curve is compared with the mean of the curves in Figure 107. An alternative display of the data in Figures 107 and 108 is given in Figure 109 where the depth of notch as measured by the probes (using the appropriate theoretical curve of Figure 108) is plotted against the actual true depth of notch. The result is not quite a straight line at a 45° angle, but approximately so. Figure 109 might well be used to refine the measurements of depth made, which would seem to be overestimated by 1mm or so at notch depths of the order 1 or 2mm.

The overall accuracy of the technique is seen to be a depth measurement to within ± 1mm to a depth of 12mm or so. The r.m.s. error over the whole of the range 0-14mm in Figure 109 is 0.64mm for the British standard magnetisation, and 0.97mm for the lower level. Figure 106 indicates this lower level to be about 75% of the British standard.

Unfortunately, a complete equivalent assessment of the theory which takes into account any possible bias was not possible, mainly due to a lack of data. In any case, the measurement of any bias near the origin of signals such as in Figure 103 is not a simple matter. Assuming a simple linear bias introduces an error of 2mm in the measurement of an 8mm depth notch, from Figure 103. This error is likely to be less severe for smaller notch depths, as discussed previously. Figure 107(b) clearly shows however, that a simple linear bias drawn through the signal is not really appropriate, since Figure 103 does not show colinearity in the signals far from the crack. The simple linear bias assumption is thus likely to give an overestimate of the effect of the bias, and the 2mm error introduced for the specific case above is also an overestimated error. The assumption has been made in the double probe theory that there is no bias at the point of measurement of the signal peaks, as would be the case for pure signals given by Eqn.(1) of Zatsepin and Shcherbinin. With the risk present of comparing a theory without bias with experimental signals which contain bias, it is acknowledged that this assumption remains open to criticism. In this case the double probe theory presented here remains a novel theoretical technique by which crack depth measurement might be made in the future, and the experiments are inconclusive.

4.4.2 Precision of the double probe measurements

The near and far probe signals were available for inspection on the data logger, the actual extremes of the signal from the short specimens appearing as in Figure 110. Since the measurements were taken with a precision of ± 0.01mV in this table, it was possible to account for the error introduced in the observed ratio of signals by the following method. Four measurements are used to obtain a ratio at a particular notch depth so that the ratio appears as,

$$r = \frac{(V_{max} - V_{min})_{near}}{(V_{max} - V_{min})_{far}}$$

Clearly the possible spread in measured values due to errors in the A/D converter lies within the range,

$$\frac{(V_{max} - V_{min})_{near} - 0.02\text{mV}}{(V_{max} - V_{min})_{far} + 0.02\text{mV}} < r < \frac{(V_{max} - V_{min})_{near} + 0.02\text{mV}}{(V_{max} - V_{min})_{far} - 0.02\text{mV}}$$

This range of values leads to error bars on the points in Figures 107 and 109. Such error bars for the use of a 1.6A magnetising current appear in Figures 111 and 112, again assuming scan heights of 5.1mm and 2.2mm.

4.5 Effects of misalignment of the probe

It was desired to investigate how the effect of misaligning the double probe in height would modify the measurement of 'crack' depth obtained. Naturally a sensible specification for the acceptable tolerance in scan height is needed, and to this end it was necessary to investigate the matter, at least in theory. If the nominal scan heights are 2.2mm and 5.1mm, and the entire double probe is misaligned by a height Δzmm, then naturally the actual probe scan heights will be 2.2 + Δzmm and 5.1 + Δzmm. Several misalignment heights Δz were investigated. The theoretical ratio of signals from probes at scan heights of 2.2 + Δzmm and 5.1 + Δzmm were calculated via Eqn.(35), and this value read off the 'perfect alignment' curve in Figure 111. In practice the problem was solved by a short computer program which took in values for Δz and a 'true' h and gave a returned value for the 'measured' h. The result of this investigation is summarised in Figure 113. Clearly the error in measured notch depth increases with $|\Delta z|$, this error being worse for large values of notch depth h. In practice the graphs are such that we would not want the misalignment to be any more than ± 0.1mm, which may be quite a harsh constraint for many applications.

4.6 Refinement of the double probe theory

The calibration curve in Figure 111 is based on the approximate theory which led to Eqn.(35). An attempt to improve on the theory was made in which such a calibration curve was exact rather than approximate. Information from the manufacturers of the Lohet II, Honeywell, was used. The Hall element was located at the ceramic/board interface in Appendix G, and of size 0.178x 0.178mm^2.

Using this information, and taking the probe width 2K=0.178mm, the precise location of the minima and maxima $\overline{x}_{max}$ of signals at scan heights of 2.2mm and 5.1mm were calculated via Eqn.(25). These values of $\overline{x}_{max}$ were then put into the finite probe Eqn.(24) to find values for $\overline{H}_{max}$. The larger value for $\overline{H}_{max}$ could then be divided by the smaller value to give our precise ratio r. Such a calibration curve, assuming a crack width 2b=0.1mm (though in fact the result is independent of 2b providing 2b<<z), is given in Figure 114. It was hoped that the experimental points would give a better fit to this curve than to the curve of Figure 111 which was based on an approximation.

In order to calculate 'measured' values of notch depth h from the experimental points it was necessary to read values by a straight graphical method rather than by calculation, since there is no simple equation describing the curve of Figure 114 as a function of h. Measured values of h appear in Figure 115 for the British Standard magnetisation, and the r.m.s. error in this case was calculated as 0.835mm. (For the lower magnetisation level used the r.m.s. error was found to be 1.03mm). This is slightly worse than the 0.64mm r.m.s. error given from the simple theory, but it must be remembered that in the latter case values for z_1 and z_2 were chosen so as to improve errors to an extent. We have effectively allowed for small tolerances in the manufacturing process of the probes. It could well be that by adjusting z_1 and z_2 slightly in the precise theory, we would end up with a figure better than 0.64mm for the r.m.s. error. This is left as future work.

4.7 An attempt at characterising a genuine fatigue crack with the double probe system

A bar of steel of dimensions 300mm x 19mm x 64mm with a real fatigue crack at its mid point was scanned with the double probe system to try and characterise the crack. The resultant signals from the probes appeared as in Figure 116. The signals are seen to be of the linearly biased type, which we have already seen are not easily decipherable as far as the crack depth is concerned. However, the signal from the near probe (2.2mm height) clearly indicates the presence of a crack, so that at least it is being detected. The signal from the far probe (5.1mm height) is less informative and is overshadowed by the magnitude of the coefficient D in Eqn.(36). Given that the crack appeared to be a through crack (19mm deep), on visual examination of the specimen, the small amplitude of the signal from the near probe (0.15V peak to peak) showed that the crack could not have been more than 6μm in width.

CHAPTER 5

5.1 A novel differentiating probe

Having had some (limited) degree of success in actually sizing notches with the double probe system, a device was sought for which could be easily used either by an operator or a robotic arm, which would simply alert the user as to the presence of a crack. In this respect such a device would give no additional information that MPI would not give, but it may offer certain advantages such as increased sensitivity etc.

Returning to the ideal signal shape such as in Figure 6, it was decided to make use of the relatively large spatial slope of the signal directly over the crack. The idea was to scan a probe over the crack at a known constant velocity, and differentiate the signal from the probe in time so as to get a spike at the point of crossing the crack. If this spike exceeded a preset amount, it would sound a buzzer so as to alert the user to the presence of a crack.

After a mixture of theoretical and experimental design work, the final instrument built had a circuit diagram as in Figure 117. The probe amplifier gives an output of $\frac{500}{11}$mV/gauss to the differentiater, which in turn gives an output of $RC\,\frac{5}{110}\,\frac{dG}{dt}$ volts where R=47K, C=0.47μF and $\frac{dG}{dt}$ is is the rate of change of field in gauss per second. Another amplifier follows which has a maximum gain of 50, and this is followed by a rectifier and comparator. The signal from the comparator triggers a monostable/astable pair which sounds a buzzer for a quarter of a second each time the output from the rectifier exceeds 0.5 volts. The rectifier allows both increasing and decreasing field changes to be detected. Imperfections in this rectifier introduced a small asymmetry into the system but this was negligible and not greater than 2%.

5.1.1 Calibration of the differentiating probe

With a maximum gain of 50, the circuit triggers at a rate of change of field

$$\frac{dG}{dt} > \frac{0.5}{50} \times \frac{100}{5} \times \frac{1}{47\times10^{3} \times 0.47\times10^{-6}} \approx 10 \text{ gauss sec}^{-1}$$

What range of cracks is detectable using this trigger level? The answer can be found by using finite probe theory once more. We need to find the value of dH/dx directly above the crack when scanning at a height z with a probe of width 2K. To this end we differentiate Eqn.(24) with respect to x and evalute the resulting expression at x=0. This process is carried out in Appendix I, with the result,

$$\left(\frac{d\bar{H}}{dx}\right)_{x=0} = \frac{Mb}{\pi}\left[\frac{1}{(z+h)^2+K^2} - \frac{1}{z^2+K^2}\right]$$

With a probe velocity $v = \frac{dx}{dt}$, we find

$$\left(\frac{d\bar{H}}{dt}\right)_{x=0} = \frac{Mbv}{\pi}\left[\frac{1}{(z+h)^2+K^2} - \frac{1}{z^2+K^2}\right] \quad \text{Eqn.(40)}$$

Eqn.(40) allows us to plot areas in the b-h plane where detection is possible and where it is not with any given values for the appropriate variables. Such plots are given in Figure 118 for four different conditions. It is seen that the shape of the curves is similar to Figure 82, which is not to be altogether unexpected since we are essentially using the same curve to derive these b-h plots.

5.1.2 Use of differentiating probe on a welded Y-joint

See section 5.3

5.2 A differential probe

While the differentiating probe was found to work very well on the welded Y-joint, it was felt that the velocity sensitive nature of the probe was rather a disadvantage, especially since the Hall probe itself gives a velocity independent signal. To this end a tried and trusted method of NDT was employed, that of the differential probe. A differential probe consists of two probes side by side as in Figure 119, and the output from the combination is taken as the difference in signals from the two probes. Such an arrangement has been used by Kalwa and Piekarski (48) in the non-destructive testing of steel ropes. Naturally, for maximum signal output the Hall elements should be placed at the two peaks of the vertical component signal in Figure 119, which we have seen would indicate an ideal separation of 2z for most practical cases, where z is the scan height. The nearest separation that the physical outlay of the Lohet II probes will allow is 7.6mm, which might at first indicate that a smaller stand off than 3.8mm should not be used. However, it is apparent that moving to smaller stand offs will increase the signal strength in any case, which compensates to some extent for the shift away from the peaks that would result.

Such a differential probe was built, the previous design of amplifier being employed in the circuit. The actual design used was an indicated in Figure 120. Not shown in Figure 120 are two 0.1μF decoupling capacitors across the power supply lines, which were found necessary to achieve an accurate difference voltage.

5.2.1 Differential probe performance

One potential drawback with the differential probe was zero drift. Figure 85 shows that over 3 hours the total zero drift from switch on for each amplifier is of the order of 1 gauss, although a great deal of this is over within a couple of minutes. It was hoped and anticipated that the differential probe drift should be rather less than this, since it was expected that both probes would meander in the same sense, keeping the difference in drifts less than each individual drift. The practical drift obtained was as indicated in Figure 121. After a drift of 0.29 gauss in the first five minutes there appeared to be very little change in the zero point, even after an hour. Notice that one advantage of the differentiating probe discussed in section 5.1 is that this slow meandering of the zero point is irrelevant and has no practical effect on the operation of the system, which is thus ready to use at switch on.

5.3 Use of the differential and differentiating probe on a welded Y-joint

For the differentiating probe it is necessary to move the probe at right angles to the length of the crack at a known speed to see if the buzzer sounds to indicate the presence or absence of a crack at that particular point of the weld. The differential probe however is scanned along the line of the weld, with the probes straddling the crack. The output from the amplifier indicates the strength of the leakage field from the crack at each position that the probes adopt along the line of the weld.

5.3.1 Initial experimentation with the differentiating probe

The differentiating probe was tested initially in a rather crude but surprisingly effective manner. The cracked welded Y-joint was brushed with the pole of a reasonably strong magnet, at right angles to the line of the crack. The probe was then scanned in a similar manner and found to successfully indicate the presence of the crack with the sounding of the buzzer. Moreover, it would detect the crack at rather less than full instrument sensitivity and with a stand off of as much as 5mm. The probe was scanned at a rate of 10-15cms^{-1} and the length of crack was measured as 30.6cm. This is compared with the technique of MPI in Section 5.3.3.

5.3.2 Experimental procedures with the differentiating and differential probe/comparison with MPI

Having built two probes to be tested on the Y-joint, each was tested so that a comparison could be made between them under various operating conditions and with the technique of MPI. First of all a coil consisting of 3 turns of thick insulated cable was placed 30cm from the node of the Y-joint, just as in a typical MPI preparation. A gradually decreasing A.C. current was passed through the cable to demagnetise the joint as far as possible. Under these conditions the differentiating probe would not indicate the presence of the crack.

A D.C. current of 310A was then passed through the coil to magnetise the weld in what shall be called the forward direction. The sensitivity of the differentiating probe was reduced to the point where it would not trigger in the strong field from the coil in the vicinity of the weld. This was necessary to prevent the probe from triggering even in the absence of a crack. The reduced level of sensitivity was 65 gauss sec^{-1}, and the probe was scanned at a height of 5mm across the crack with a speed of about 10-15cm sec^{-1}. The differentiating probe was scanned at various positions along the line of the weld to establish the length of the crack.

With 310A D.C. present in the cable, it was found that a Burmah-Castrol strip indicated the presence of at least 0.72 Tesla in the pipe, so that conditions were suitable for magnetic particle inspection. Consequently a fluorescent ink was sprayed on to the weld and the Y-joint was viewed under an ultra-violet light. The length of the indication gave a measurement of the length of crack as given by MPI, which could then be compared with the differentiating probe indication.

Under the same level of magnetisation, the differential probe was scanned along the line of the weld in synchronisation with the chart recorder used to monitor the output of the amplifier. This gave a direct indication of the leakage field present at various positions along the weld. The scan height in this case was 3mm.

The differentiating and differential probes were tested in the same manner as above in the residual field in the forward direction, which was achieved by simply turning off the current. In this case the full sensitivity of 10 gauss sec^{-1} was used for the differentiating probe. The procedures were then repeated in the reverse direction of field, which was achieved by passing 310A D.C. in the opposite direction through the coil.

As a final experiment, the differentiating probe was scanned in the residual field at very low stand off (i.e. direct contact with the tubular) and at the maximum sensitivity of a 10 gauss sec^{-1} trigger level.

5.3.3 Resulting practical indications from the Y-joint with the differentiating and differential probes

The active leakage field produced in the forward direction of magnetisation is indicated in Figure 122.

This field was as indicated by the differential probe. The zero error shown is due to the strong field from the coil about 10cm away from the weld. It represents the extreme error in the zero point that would be produced due to possible variations in the orientation of the weld with respect to the coil. It is a pessimistic indication obtained by rotating the probe so as to produce maximum variation in the signal at some distance (about 10cm) from the weld. The length of crack as indicated by the differentiating probe was 30.9cm at a 65 gauss sec^{-1} trigger level, while the MPI indication extended as far as 34.2cm.

The residual leakage field as indicated by the differential probe is given in Figure 123. Here the differentiating probe measured the crack as being 30.6cm long at a 5mm scan height and sensitivity of 10 gauss sec^{-1}. It is seen that compared with the full magnetisation the signal level has dropped to about half its previous level. Also indicated in Figure 123 are the results of an experiment on the Y-joint which involved acoustic emmissions (60). This experiment indicated the crack to be 29cm long.

The leakage field in the reverse direction is shown in Figure 124. In this case the differentiating probe would not detect any part of the crack with a 65 gauss sec^{-1} trigger level. Finally with a 10 gauss sec^{-1} trigger level used at very low stand off in residual field, the crack was measured as being 31.8cm long.

5.3.4 Discussion of differentiating and differential probe results

The differentiating probe was found to give a crack indication which was not quite as long as the MPI result.

This might indicate the method to be inferior, and indeed this is true if our overriding concern is the detection of the full extent of the crack. However, the probe offers three distinct advantages over MPI. Firstly, the method is fairly easily adapted to use by a robotic arm. Secondly, and more importantly, the system will work with a considerable stand off which would allow, for example, a degree of marine growth to be present on the weld during inspection. Thirdly, and most importantly, the system can be made sensitive enough to allow a significantly lower level of magnetisation to be present than is required by BS6072. It was demonstrated on several occasions that after demagnetising, the mere stroking of a magnet over the weld was sufficient to allow an indication of a crack. Over sound areas of the weld such a process resulted in a null indication.

Thus it is not recommended that such a differentiating probe should be used to measure the length of a crack in a weld. This process is better left to MPI. However, it is felt that there is great potential for such a probe to be used by an underwater robotic arm as a structural integrity monitoring device. One can envisage a robot which periodically strokes the weld in an appropriate fashion with a magnet, and then scans it with a differentiating probe at various positions along the weld. At some point nearing the end of the useful life of the weld a crack will develop which may not immediately be detected by the probe. However, the crack will gradually grow to a size which can be detected, so that the probe will give a warning as to a potential failure. It is at this point that divers could be sent down to make a thorough investigation using MPI. Up to this point however there would be no need for extensive cleaning, ultra violet lights magnetising coils or video equipment. Not even a diver. The entire process could be done by ROV.

In some ways the differential probe is superior to the differentiating probe. It is not velocity dependent, can be scanned in a simpler manner and gives an analogue output as opposed to the 'digital' sounding of a buzzer. The size of the signal gives an indication in a general sense as to the severity of the crack. It would be feasible to draw detection curves such as in Figure 82 for the analogue outputs corresponding to each position along the weld. This would give some idea as to the regions in the b-h plane in which the crack might lie at different points along the weld. For example, if we assumed for a moment that the crack was of constant depth, then Figures 122, 123 and 124 would be giving direct indications of the width of the crack, since the signal is directly proportional to the width as has been discussed. However, the crack is almost certain to vary in both depth and width along the length in practice, so that this simple interpretation should not be taken literally. If it were known that the crack is a through crack at one particular point, then measuring the leakage field at that point will enable the width to be determined, and so fix a point in the b-h plane. A straight line between this point and the origin will cut through all the detection curves corresponding to lower leakage fields than at the point at which there is a through crack, as in Figure 125. In a crude sort of way, width and depth measurement can be made on the crack by looking at the intersecting point of this line with the leakage field detection curve at any point along the weld. Unfortunately, the presence of a through crack would mean that the joint would have failed.

5.4 A differential probe with comparator

Despite the inferior crack length determining properties of the differentiating probe, it is seen that the analogue output of the differential probe corresponds well with the results of MPI, i.e. the output becomes very low when the MPI indication ceases. This property was used in a device which was to give similar 'yes/no' indications of a crack. The idea was to have an l.e.d. at the probe head which would light in the presence of a crack and go out when there was no crack. The circuit diagram of the device is given in Figure 126, and is essentially the same as Figure 120 but with an additional amplifier, rectifier and comparator. The prototype device was battery operated, and so a degree of compensation for falling battery voltage was required. This was achieved in practice by returning the 39K resistor, which feeds the non-inverting terminal of the comparator with a reference voltage, to the -ve terminal of the Lohet II probes. Thus decreasing magnetic sensitivity due to falling battery voltage is compensated in a simple way by the smaller threshold voltage required for triggering.

5.4.1 Use of the differential probe with comparator on the Y-joint

The combined circuits of Figures 120 and 126 give an output to the comparator of $5 \times \frac{100}{11} \times \frac{100}{7.5} = 0.606\ \mathrm{Vgauss}^{-1}$. The total drift after switch on is of the order 190mV at the comparator. By introducing a judicious offset at the early amplifier stages the rectifier can effectively reduce this drift by half, so that the effective zero drift is about 95mV. This introduces an asymmetry into the detection of fields. The trigger level of 1.2V (corresponding to 2 gauss) is a compromise between sensitivity and ability to detect fields symmetrically.

The asymmetry in this case is (0.095/1.2)x100 = 8%, and means that the length of crack detected will be slightly different depending on which way round the probes straddle the crack.

In practice the length of crack over which the l.e.d. remained lit on the Y-joint was 31.1cm at a trigger level of 2 gauss, and a scan height of 2mm. This was with simple residual magnetism.

5.4.2 Discussion of use of differential probe with comparator

The differential probe of Figures 120 and 126 has been successfully used to detect a crack in the specimen Y-joint. The length of crack detected is still not as good as that given by MPI (34.2cm). However, the threshold level of detection could easily be set lower than the 2 gauss actually used, and in any case the device was not tested under identical magnetisation conditions to that present for MPI. With the Lohet II probes used, some time would be required to elapse before inspection could begin if a significantly lower threshold level were used. This would be to allow for drift. Alternatively a control pot and meter could be fitted into the circuit, together with a mumetal container in which the probes could be inserted periodically, to zero the probe accurately. This would make the operation of the system slightly more complicated, but the circuit would then be ready for use immediately after turn on and the sensitivity could be made rather higher.

The circuit as it stands is still useful, and could be used by a diver as a precursor to a full MPI inspection. For robotic arm use, there would be little point in using a comparator as a form of signal processing, this could be done on the surface with the full analogue signal. The l.e.d.. indicator gives an immediate indication at source as to the presence of a crack; a truly 'electronic' magnetic particle indicator.

5.5 Structural integrity monitoring

The idea occured that it might not be necessary to use a robotic arm to scan the weld at all. Since it is known approximately where the line of the crack will be, this can be taken advantage of by simply placing differential pairs of Hall probes at strategic positions along the weld. With several probes in position, the leakage field can be continously monitored as the crack develops.

Equipment to perform this task was designed and built. Eleven pairs of probes were positioned as desired along the weld of the specimen Y-joint. Amplifiers were built for each pair of probes, following the design of Figure 120. The amplifier outputs were fed through an array of low pass filters having a 3dB point of 5Hz. This was to eliminate a degree of high frequency noise that was found to be present. The eleven signals were fed through a multiplexer followed by an A/D converter and interfaced to an Amstrad CPC6128 computer. A short piece of software enabled the computer to control the interface circuit of Figure 127 using the appropriate address decoding also indicated in Figure 127. A bar chart style display enabled all eleven channels to be simultaneously displayed.

Each channel was updated at a rate of about 4Hz. This should be quite adequate to enable the opening and closing of the crack under wave action to be detected and measured in a typical underwater monitoring situation. More importantly, continuous real time monitoring of the leakage field is possible.

A typical display of the leakage field from the residually magnetised cracked Y-joint is given in Figure 128. In this case the probes were positioned at 4cm intervals to monitor a section of weld ± 20cm from the saddle point. Five or ten minutes were required to elapse before taking readings to allow for zero drift. Whilst for most probes this was less than 0.75 gauss, it was in one case as much as 1.5 gauss. Even so, all the probes eventually settled to within 0.5 gauss of the zero point with no applied field. The leakage field profile is seen to follow that of Figure 123. The crack is clearly shown not to extend as far as ± 20cm but at ± 16cm there is a small indication and at less than ± 16cm there is a definite indication. The display would suggest a crack having developed which was between 32cm and 40cm in length, in agreement with the MPI indication of 34.2cm.

CHAPTER 6

CONCLUSIONS AND RECOMMENDATIONS FOR FUTURE WORK

6.1 Conclusions

6.2 Recommendations for future work

6.1 Conclusions

The main conclusions of this thesis can be summarised as follows:

1. A double probe theory has been developed. Using the theory it is possible in principle to size the depths of notches in steel specimens up to 14mm in depth,to within an accuracy of ±1mm, from their magnetic flux leakage signals. No knowledge of notch width or magnetisation level is required. In order for the theory to be applied to experimental signals, proper account must be taken of any bias effects in the signals.

2. A novel differentiating probe has been designed and built which offers the following advantages over magnetic particle inspection:

   a) The probe does not require the high level of magnetisation necessary for MPI or the use of the associated bulky magnetising equipment. Indeed, remanent magnetism from a few strokes of a strong magnet across the crack is sufficient to produce crack indications.
   b) The probe does not require thorough cleaning of the inspection area. A scan height of up to 5mm is permissible, which will allow for a degree of marine growth or paint to be present during inspection.
   c) The probe is more suited to automated inspection using a robotic scanning arm.

3. A scanning differential probe may be used at a scan height of 3mm to give a crack indication consistent and comparable with MPI. In addition to the advantages

over MPI described in (2) the probe requires a much simpler scanning system than the differentiating probe.

4. Structural integrity monitoring is possible using multiple differential probes. The leakage field from a growing crack in the weld of a Y-joint may be continuously monitored in real time, giving an indication of the severity and length of the crack.

5. The width of the signal produced from the interaction of the vertical component leakage signal with a Hall probe of width 2K has been shown to follow the relationship:

$$x_{max} = \pm \left(\frac{A + (A^2 + 12B)^{1/2}}{6} \right)^{1/2}$$

where

$$A = 2K^2 + 2b^2 - a_1^2 - a_2^2$$

$$B = (a_1 a_2)^2 + (a_1 + a_2)^2 (b^2 + K^2) + (b^2 - K^2)^2$$

with $a_1 = z+h$, $a_2 = z$

Here 2b is the crack width, h is the crack depth and z the scan height.

6.2 Recommendations for future work

An alternative double probe system

As shown in Section 5.1.1., the rate of change of field H over a probe of width 2K scanned with velocity v at a height z over a crack of width 2b and depth h is given by, in the absence of any background bias,

$$H' = \left(\frac{dH}{dt}\right)_{x=0} = \frac{Mbv}{\pi} \left[\frac{1}{(z+h)^2+K^2} - \frac{1}{z^2+K^2} \right]$$

Here M is the magnetisation in the specimen. By using a physical arrangement of probes as in the double probe system discussed in Section 4.1, the ratio of time differentiated signals H' from probes at scan heights z_2 and z_1 ($z_2>z_1$) is given by

$$r = \frac{H_1'}{H_2'} = \frac{\left[\dfrac{1}{(z_1+h)^2+K^2} - \dfrac{1}{z_1^2+K^2}\right]}{\left[\dfrac{1}{(z_2+h)^2+K^2} - \dfrac{1}{z_2^2+K^2}\right]} \qquad \text{Eqn. (41)}$$

As in the case of the original double probe proposal, the ratio r of such signals depends only upon the scan heights z and the crack depth h, using infinitesimal probes. The general shape of the r-h curve for K=0mm, z_1=2.5mm and z_2=5mm follows that of Figure 81 with a change of scale in the ordinate. There is still a factor of 2 by which r changes as h varies from 0 to infinity. For a non-zero K value the range of r is decreased slightly but for the size of probe present in the Lohet II this is not significant.

It is recommended therefore that experiments are carried out with Hall probes to try and justify Eqn(41). This would then provide an alternative method of crack depth sizing.

6.2.1 **The bias problem**

It was pointed out in Section 4.4.1 that for cracked samples of practical size the ideal shaped signal of Figure 6 takes on a linear bias as in Figures 95 and 96. This linear bias renders the double probe method ineffective. At the time of writing, an MSc project has been proposed in which the aim is to artificially eliminate this linear bias. The idea is to use two channels of the interface circuit of Figure 127 to record the raw biased signals from the double probe into two arrays on the Amstrad CPC6128.

Given that the system was capable of gathering and displaying eleven channels, each at a rate of about 4Hz (see Section 5.5), it is reasoned that a pair of probe data points should be displayed within at least 2/44 seconds or at a rate of 22Hz. With its horizontal display of 640 pixels the computer should finish displaying the near and far probe signals in 640/22 ≈ 30 seconds. Indeed, the single channel display indicated in Figure 56 took about 15 seconds to produce. This is a reasonable time in which to scan the double probe a distance of 0.5 metres or so, representing a practical size of specimen. Unfortunately the spatial resolution between points in this case would be as much as 0.5/640m = 0.78mm, which is rather higher than ideal. A sensible solution would be to increase the size of the computer arrays and assign several adjacent array members to a particular pixel. The form of the PLOT command on the Amstrad makes this a simple procedure. The time of scan and consequent resolution could thus be increased.

Since the bias is linear with distance, it is important to record the latter faithfully. Thus a constant velocity robotic arm is recommended, such as that used to produce Figure 56. Having obtained the two signals on the screen (such as Figure 116) superimposed on top of each other, two points distant from and on either side of the defect can be chosen. A straight line between these two points represents the extent of the bias as suggested by the model of Oehl and Swartzendruber (27) for the reverse bias case. All that is needed therefore to obtain the signal due to the crack alone is to superimpose an exact negative of this straight line (i.e one of opposite slope) into the computer arrays. This is easily done on the computer and it is these resulting signals that could be used in ratiometric mode to try and gauge crack depth. The trend of Figure 81 might then be reproducible for specimens of practical size, allowing crack depth measurement for the general case.

6.2.2 A triple probe system

Figure 113 illustrates the effect of a misalignment Δz in the double probe scan height. It was recommended in Section 4.5 that this should be kept below ± 0.1mm, which constitutes a fairly harsh constraint in certain applications. The idea occurred that it might be possible to compensate in some way for a misalignment using a third probe. Using probes at scan heights z_1, z_2 and z_3 ($z_3>z_2>z_1$), and following the method of Section 4.1, the three signals are found to be given by (in usual notation):

$$\frac{4\pi}{M} H_{maxn} = \frac{2b}{z_n} \frac{(h^2 + 2hz_n)}{(2z_n^2 + h^2 + 2hz_n)} \qquad n=1,2,3$$

If the triple probe is made rigid the probe separations can be designated as $\Delta z_1 = z_2 - z_1$ and $\Delta z_2 = z_3 - z_1$. The distances Δz_1 and Δz_2 can be measured accurately and kept constant. Taking ratios of probe signals, we find

$$r_1 = \frac{H_{max1}}{H_{max2}} = \frac{z_1 + \Delta z_1}{z_1} \frac{(h+2z_1)\ (2(z_1+\Delta z_1)^2 + h^2 + 2h\ (z_1 + \Delta z_1))}{(h+2(z_1+\Delta z_1))\ (2z_1^2 + h^2 + 2hz_1)}$$

$$r_2 = \frac{H_{max1}}{H_{max3}} = \frac{z_1 + \Delta z_2}{z_1} \frac{(h+2z_1)\ (2(z_1+\Delta z_2)^2 + h^2 + 2h\ (z_1 + \Delta z_2))}{(h+2(z_1+\Delta z_2))\ (2z_1^2 + h^2 + 2hz_1)}$$

In brief we have $r_1 = f(z_1, h, \Delta z_1)$, $r_2 = f(z_1, h, \Delta z_2)$. Since r_1 and r_2 can be measured and Δz_1, Δz_2 and the function f are known, we are faced with two equations in two unknowns. These equations can in principle therefore be solved for z_1 and h, although it is not a trivial solution. In this way it might be possible to overcome the necessity for the precise scan heights of the double probe system to be known.

There is another important case in which such a triple probe would prove useful. Hwang (30) has stated that it would be impossible to characterise subsurface defects from their leakage fields. From a single scan this is indeed the case. However, using the triple probe system as described above, it should be possible to find both the depth of the defect h, and the distance of its uppermost point from the lowest point of the three probes (i.e. z_1). By measuring the scan height of the lowest probe above the surface, the depth of the defect below the surface could be simply deduced.

ACKNOWLEDGEMENTS

The author wishes to thank his supervisors during the SIM project. Particular thanks to Brian Hockenhull for his willingness to engage in discussion and for his encouraging words.

REFERENCES

1. Honeycombe, R.W.K., "The plastic deformation of metals", Edward Arnold, 2nd ed., 1983, p416

2. Gaythwaite, J., "The marine environment and structural design", New York, Van Nostrand Reinhold Co., 1981

3. Booth, G.S. and Wylde, J.G., Met. Sci. 1977, Vol.11, p308

4. Brebbia, C.A. and Walker, S., "Dynamic analysis of offshore structures", Newnes-Butterworths, 1979

5. Evans, U.R., "An introduction to metallic corrosion", London, Arnold, 3rd ed., 1981

6. Uhlig, H.H., "The corrosion handbook", Wiley, 1948

7. Tuthill, A.H. and Schillmoller, C.M., "Guidelines for selection of marine materials", International Nickel Co., New York, 1966

8. British Standard 6072, "Method for magnetic particle flaw detection", British Standards Institution, 1981

9. Bleaney, B.I. and Bleaney, B., "Electricity and magnetism", Oxford University Press, 3rd ed., 1976

10. Ko, W.L. and Francis, P.H., "Magnetic field leakage due to a surface crack", British Jnl. of NDT, September 1975, pp141-144

11. Sharif, T., "Defect sizing using magnetic flux techniques", MSc Thesis, Cranfield, 1983

12.Marchant, B.G., "An instrument for the non-destructive testing of wire ropes", Systems Technology, August 1978, No.29, pp26-32

13.Zatsepin, N.N. and Shcherbinin, V.E., "Calculation of the magnetostatic field of surface defects, I. Field topography of defect model", Defektoskopiya, Sept./Oct. 1966, No.5, pp50-59

14.Lord, W. and Oswald, D.J., "Leakage field methods of defect detection", International Jnl. of NDT, 1972, Vol.4, pp249-274

15.Stumm, W., "Nondestructive testing of ferrous tubes and rods with a new magnetic test unit", presented at the ASNT Spring Conference, Los Angeles, California, March 1971

16.Lord, W. and Oswald, D.J., "The generated reaction field method of detecting defects in steel bars", Materials Evaluation, 1971, Vol.29 No.2, pp21-27

17.McMaster, R.C. and Sisson, E.C., "Magnetic reaction analyser - theory and applications", publication no. MRA 1265, F.W. Bell Inc., (No more information in original citation from Ref.14)

18.Lankford, J. and Francis, P.H., "Magnetic field perturbation due to metallurgical defects", International Jnl. of NDT, 1971, Vol.3, pp77-94

19.Novikova, A. and Miroshin, N.V., "Investigation of the fields of artificial open flaws in a uniform constant magnetic field", Defektoskopiya, July/August 1973, No.4, pp95-101

20.Akrad'ev, V.N., Izv. AN SSSR, OTN 2, 233 (1937)

21.Bol'Shakov, P.N., Candidate's dissertation, Siberian Physicotechnical Institute, Tomsk (1949)

22.Subbotina, Z.S., Shturkin, D.A. and Yanus, R.I., Fiz Met. i Metalloved., 13 529 (1962)

23.Sapozhnikov, A.B. and Bol'Shakov, P.N., Trudy Sib. Fizikotekh. Inst., No.24, Tomsk (1947) p245

24.Burtsev, G.A. and Fedorishcheva, E.E., "Simple approximation for the magnetostatic fields of surface defects and inhomogeneities", Defektoskopiya, March/April 1974, No.2, pp111-119

25.Francis, P.H. and Davidson, D.L., "Experimental characterisation of yield induced by surface flaws"; The surface crack: Physical problems and computational solutions, ASME publication H29, Edit. J.L. Swedlow, 1972, pp63-78

26.Lord, W., Bridges, J.M., Yen, W. and Palanisamy, R., "Residual and active leakage fields around defects in ferromagnetic materials", Materials Evaluation, July 1978, Vol.36 No.7, pp47-54

27.Oehl, C.L. and Swartzendruber, L.J., "On the optimum applied field for MPI using direct current", Jnl. of Nondestructive Evaluation, 1982, Vol.3 No.3, pp125-136

28.Lord, W. and Hwang, J.H., "Defect characterisation from magnetic leakage fields", British Jnl. of NDT, January 1977, Vol.19 No.1, pp14-18

29.Shcherbinin, V.E. and Zatsepin, N.N., "Calculation of the magnetostatic field of surface defects, II.

Experimental verification of the principal theoretical relationships", Defektoskopiya, Sept./Oct. 1966, No.5, pp59-65

30.Hwang, J.H., "Defect characterisation by magnetic leakage fields", PhD Thesis, Colorado State University, Ft. Collins, Colorado, 1975

31.Francis, P.H. and Moseley, T.K., "A model for diagnosis of surface cracks by magnetic flux leakage", British Jnl. of NDT, March 1979, Vol.21 No.2, pp 79-83

32.Lord, W. and Palanisamy, R., "Magnetic probe inspection of steam generator tubing", Materials Evaluation, May 1980, Vol.38 No.5, pp38-40

33.Bainton, K.F., "Characterising defects by determining magnetic leakage fields", NDT International, 1977, Vol.10 No.5, pp253-257

34.Beissner, R.E., Matzkanin, G.A. and Teller, C.M., "NDE applications of magnetic leakage field methods", NTIAC-80-1, Southwest Research Institute, San Antonio, Texas, 1980

35.Holler, P. and Dobmann, G., "Physical analysis methods of magnetic flux leakage", in 'Research techniques in NDT', ed R.S. Sharpe, Academic Press, New York, 1980, Vol.4, p39

36.Shcherbinin, V.W. and Pashagin, A.E., Defektoskopiya, 1972, Vol.8 No.4, pp74-82

37.Forster, F., "Nondestructive inspection by the method of magnetic leakage fields. Theoretical and experimental foundations of the detection of surface cracks of finite and infinite depth", Soviet Jnl. of NDT, July

1983, Vol.18 No.11

38.Dobmann, G. and Munnich, H., "Eine Integralgleichungsnaherung zur Berechnung von magnetischen Streufeldern in der Umgebung von Oberflachenrissen", Europaische Vortragstagung Zerstorungsfreie Materialprufung, 1978

39.Munnich, H., "Experimentelle und numerische Untersuchungen zum magnetischen Streuflussverfahren", Diplomarbeit, Saarbrucken, 1978

40.McIntire, P., "Electromagnetic testing. Nondestructive testing handbook", (American society for NDT), Columbus OH, 2nd ed., 1986, Vol.4, pp622-624

41.Edwards, C. and Palmer, S.B., "The magnetic leakage field of surface breaking cracks", J.Phys. D: Appl. Phys., 1986, Vol.19, pp657-673

42.Forster, F., "New findings in the field of nondestructive magnetic leakage field inspection", NDT International, February 1986, Vol.19 No.1, pp3-14

43.Forster, F., "Computer controlled magnetic field research installation - examples and possibilities", Proc. X World Conf. NDT, Moscow, 1982, Vol.2, Plenary address pp172-186

44.Forster, F., "Nondestructive inspection by the method of magnetic leakage fields", Defektoskopiya, 1982, No.11, pp3-25

45.Uetake, I. and Ito, H., "Lift-off effect and its application to the defect size estimation in the magnetic leakage flux method", Transactions of National

Research Institute for metals, June 1986, Vol.28 No.2, pp177-187

46.Shiraiwa, T. and Hiroshima, T., J. Japan. Soc. Nondestr. Inspec., 1972, Vol.21 No.3, pp166-176 (In Japanese)

47.Owston, C.N., British Jnl. of NDT, 1974, Vol.16 No.6, pp162-168

48.Kalwa, E. and Piekarski, K., "Design of Hall effect sensors for magnetic testing of steel ropes", NDT International, October 1987, Vol.20 No.5

49.Kalwa, E. and Piekarski, K., "Abrasion of wire ropes - their models and the magnetic testing method", Can. Soc. NDT Jnl., March/April 1987, Vol.8 No.2, pp46-49

50.Kalwa, E., "Detection and measurement of faults in steel cable by magnetic testing method", Doctoral dissertation, University of mining and metallurgy, Cracow, December 1982

51.Atherton, D.L. and Czura, W., "Finite element calculations on the effects of permeability variation on magnetic flux leakage signals", NDT International, August 1987, Vol.20 No.4, pp239-241

52.Atherton, D.L. and Daly, M.G., "Finite element calculation of magnetic flux leakage detector signals", NDT International, August 1987, Vol.20 No.4, pp235-238

53.Goebbels, K. and Simkin, J., "Modelling and measurement of field and flux of MPI", Review of progress in quantitative nondestructive evaluation, ed Thompson, D. and Chimenti, D., Plenum Press, New York and London, 1988, Vol.8B, pp2141-2148

54.Jiles, D.C., "Review of magnetic methods for nondestructive evaluation (Part 2)", NDT International, April 1990, Vol.23 No.2, pp83-92

55.Betz, C.E., "Principles of magnetic particle testing", Magnaflux Corporation, Chicago, 1966

56.Stumm, W., "Tube testing by electromagnetic NDT methods", Nondestructive testing, 1974, Vol.7, p251

57.Hwang, J.H. and Lord, W., "Finite element modelling of magnetic field - defect interactions", J. Test. and Eval., 1975, Vol.3, p21

58.Lord, W., "Applications of numerical field modelling to electromagnetic methods of nondestructive testing", IEEE Trans. Magn., 1983, MAG-19, p2437

59.Kip, A.F., "Fundamentals of electricity and magnetism", McGraw-Hill Kogakusha, 2nd ed., 1969

60.Mathieson, P.A.R., Hockenhull, B.S. and Billingham, J., "Monitoring corrosion fatigue cracks in an offshore structural steel by acoustic emissions", 21st Annual British Conference on NDT (NDT 86)

Appendix A

Linear Hall effect ic (304-267)

A miniature linear output Hall effect sensor in a moulded 4-pin dil plastic package. This device features a differential output stage. One output increases linearly in voltage whilst the other decreases for a linear increase in magnetic flux density over a ±40mT range.

Typical applications for this versatile ic include magnetic field investigation in the vicinity of transformers and cables, current sensors with high isolation, linear feedback elements in analogue control systems, etc. The sensor is immune from damage by high values of flux density.

Absolute maximum ratings

Supply voltage	+12Vdc
Output current	20mA
Operating frequency	100kHz
Operating temperature	−40°C to +100°C
Storage temperature	−55°C to +150°C

Electrical characteristics

Supply voltage (Vdc)	Supply current (mA)	Output type	Output voltage	Sensitivity
4 to 10	3.5 typ.	Differential outputs, linear	1.75 to 2.25V at 5V & 0 Gauss	(−400 to +400 Gauss) 0.75 to 1.06mV/Gauss

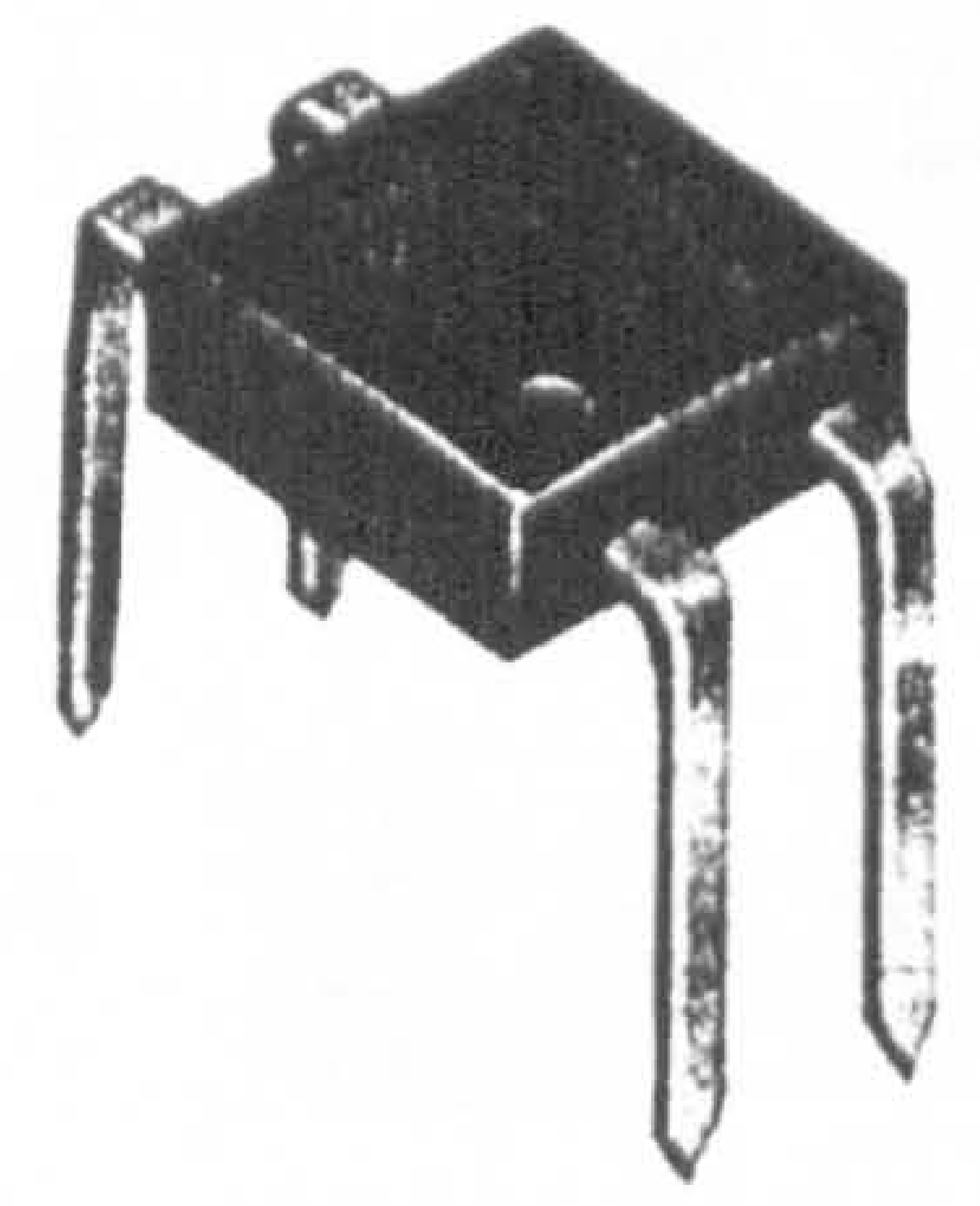

Figure 11 **Dimensions**

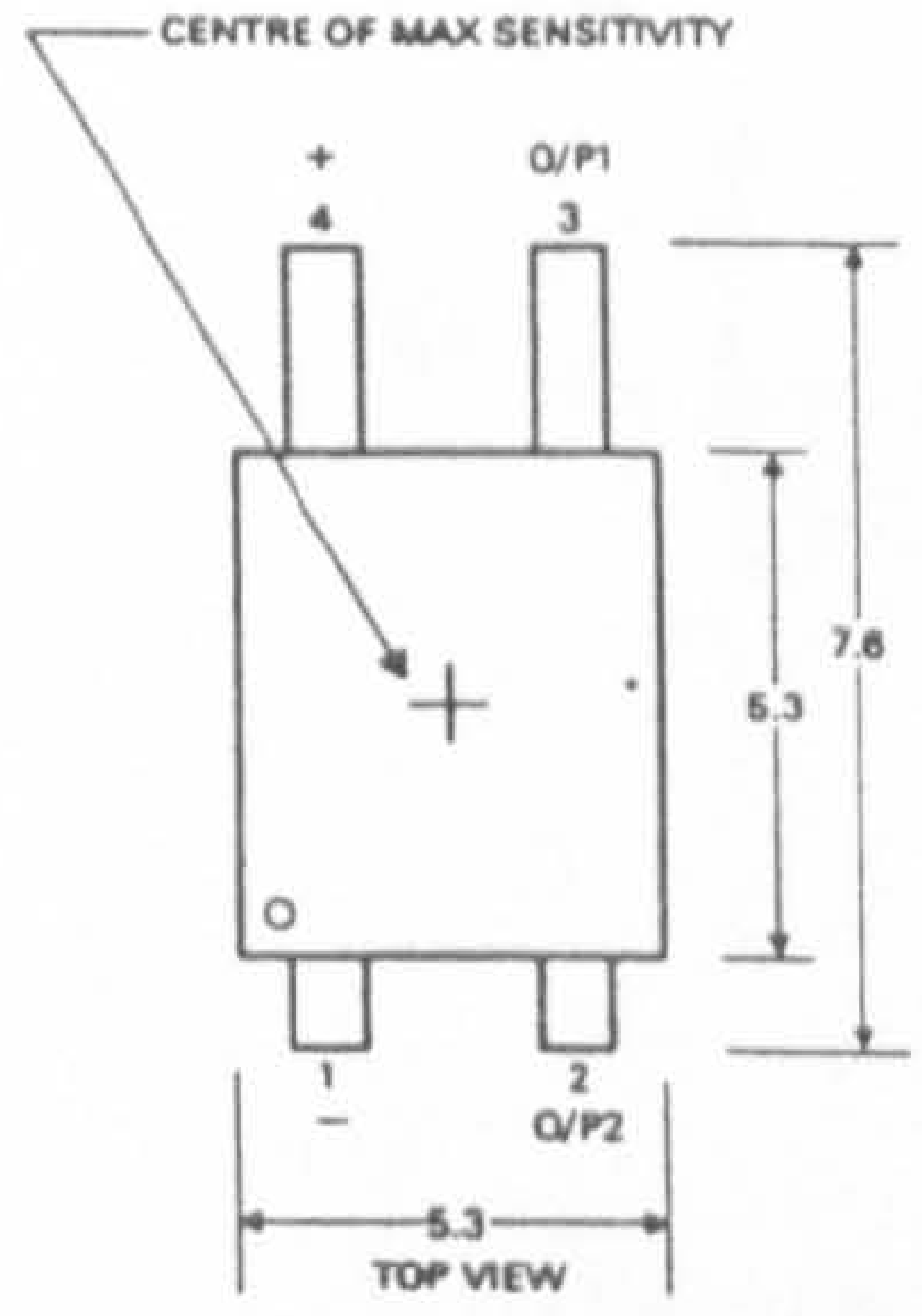

Typical linear output characteristics

The linear Hall effect ic features differential outputs. One output increases, whilst the other output decreases with an increase in Gauss.

Figure 12 **Typical output characteristics as a function of supply voltage**

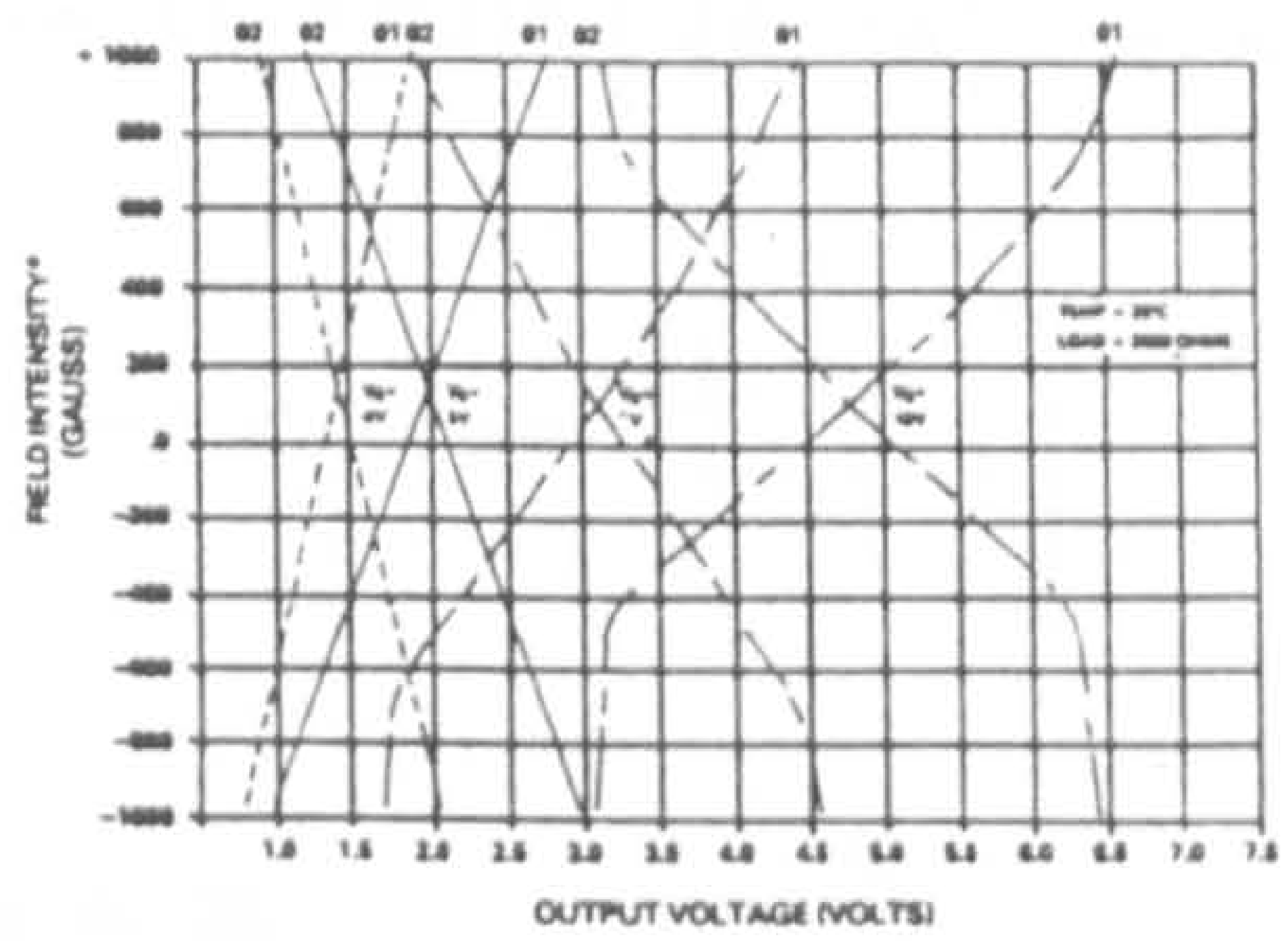

Figure 13 **Typical output characteristics as a function of temperature**

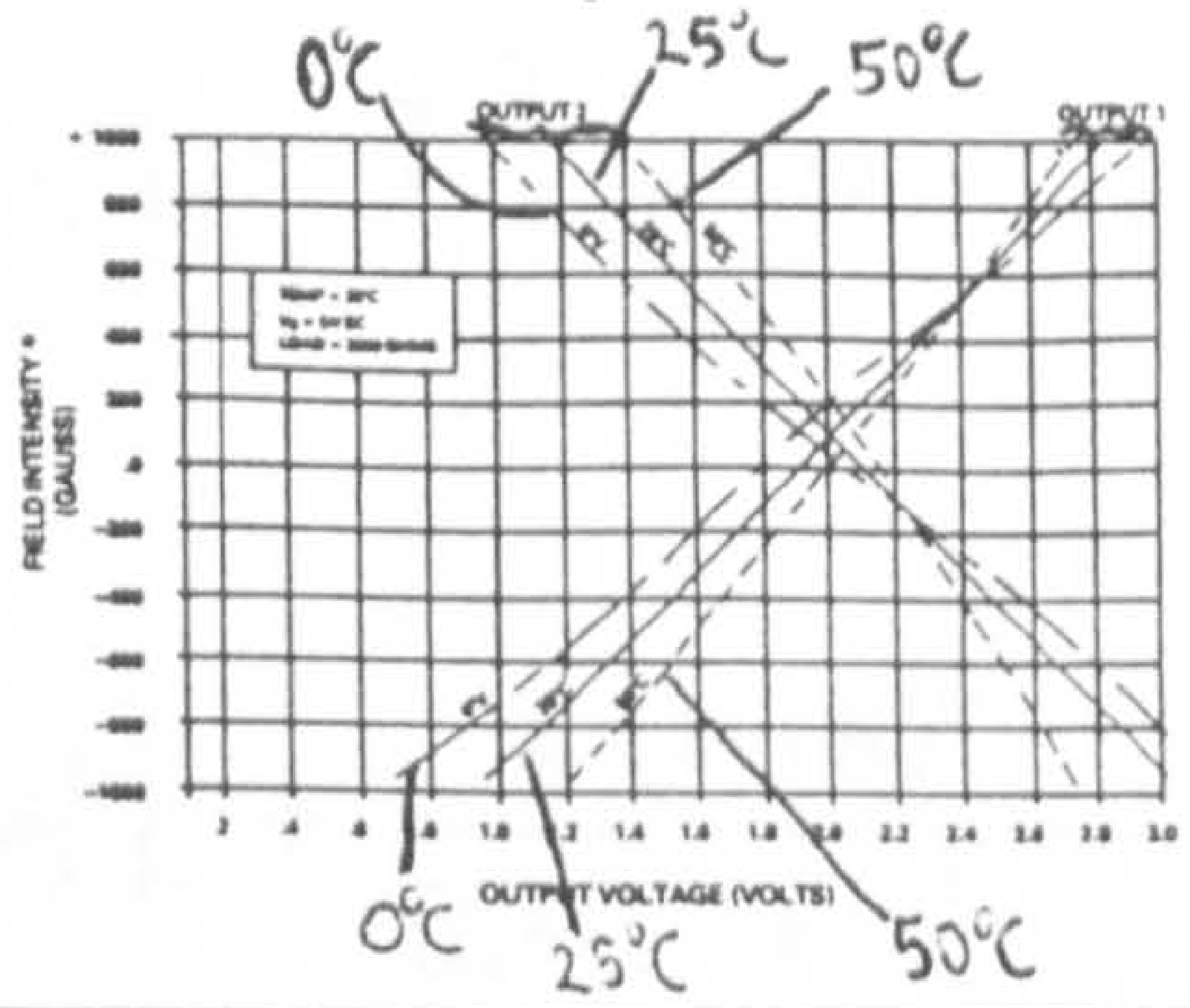

*Positive Gauss represents the south pole of the magnet facing the sensing area. Negative Gauss represents the north pole of the magnet facing the sensing area.

Appendix B

Calculation of the signal width with a finite probe

We have

$$\bar{H}_v(x) = \frac{M}{8\pi K}\left[I_1 + I_2 - I_3 - I_4\right]$$

Where

$$I_i = (b_i+K)\ln\left\{(b_i+K)^2+a_i^2\right\} - (b_i-K)\ln\left\{(b_i-K)^2+a_i^2\right\}$$

$$+\,2a_i\left[\arctan\left(\frac{b_i+K}{a_i}\right) - \arctan\left(\frac{b_i-K}{a_i}\right)\right]$$

with

$$\left.\begin{array}{ll} a_1 = a_4 = z+h & a_2 = a_3 = z \\ b_1 = b_3 = x+b & b_2 = b_4 = x-b \end{array}\right\} \qquad \text{Eqn.(B1)}$$

We require

$$\frac{d\bar{H}_v(x)}{dx} = \frac{d}{dx}\left[I_1 + I_2 - I_3 - I_4\right] = 0$$

Since $db_i = dx$ we consider

$$\frac{dI_i}{dx} = \frac{dI_i}{db_i} = \ln\left\{(b_i+K)^2+a_i^2\right\} + \frac{2\,(b_i+K)^2}{(b_i+K)^2+a_i^2}$$

$$-\left[\ln\left\{(b_i-K)^2+a_i^2\right\} + \frac{2\,(b_i-K)^2}{(b_i-K)^2+a_i^2}\right]$$

$$+\,2\left[\frac{a_i^2}{(b_i+K)^2+a_i^2} - \frac{a_i^2}{(b_i-K)^2+a_i^2}\right]$$

$\therefore$

$$\frac{dI_i}{db_i} = \ln\left\{\frac{(b_i+K)^2+a_i^2}{(b_i-K)^2+a_i^2}\right\}$$

We must solve

$$\ln\left\{\frac{(b_1+K)^2+a_1^2}{(b_1-K)^2+a_1^2}\right\}+\ln\left\{\frac{(b_2+K)^2+a_2^2}{(b_2-K)^2+a_2^2}\right\}-\ln\left\{\frac{(b_3+K)^2+a_3^2}{(b_3-K)^2+a_3^2}\right\}$$

$$-\ln\left\{\frac{(b_4+K)^2+a_4^2}{(b_4-K)^2+a_4^2}\right\}\equiv 0$$

Using Eqn.(B1) we get

$$\left\{(b_1+K)^2+a_1^2\right\}\left\{(b_2+K)^2+a_2^2\right\}\left\{(b_1-K)^2+a_2^2\right\}\left\{(b_2-K)^2+a_1^2\right\}\qquad\text{(LHS)}$$

$$=\left\{(b_1-K)^2+a_1^2\right\}\left\{(b_2-K)^2+a_2^2\right\}\left\{(b_1+K)^2+a_2^2\right\}\left\{(b_2+K)^2+a_1^2\right\}\qquad\text{(RHS)}$$

Expanding slightly, we get

$$LHS=\left\{(b_1^2-K^2)^2+a_2^2(b_1+K)^2+a_1^2(b_1-K)^2+(a_1a_2)^2\right\}\times\left\{(b_2^2-K^2)^2+\right.$$
$$\left.a_1^2(b_2+K)^2+a_2^2(b_2-K)^2+(a_1a_2)^2\right\}$$

$$RHS=\left\{(b_1^2-K^2)^2+a_2^2(b_1-K)^2+a_1^2(b_1+K)^2+(a_1a_2)^2\right\}\times\left\{(b_2^2-K^2)^2+\right.$$
$$\left.a_1^2(b_2-K)^2+a_2^2(b_2+K)^2+(a_1a_2)^2\right\}$$

Expanding,

$$LHS=\overset{\textcircled{1}}{(b_1^2-K^2)^2(b_2^2-K^2)^2}+\overset{L_1}{a_1^2(b_2+K)^2(b_1^2-K^2)^2}+\overset{L_2}{(b_1^2-K^2)^2a_2^2(b_2-K)^2}$$
$$+\overset{\textcircled{2}}{(b_1^2-K^2)^2(a_1a_2)^2}+\overset{L_3}{a_2^2(b_1+K)^2(b_2^2-K^2)^2}+\overset{\textcircled{3}}{a_2^2(b_1+K)^2a_1^2(b_2+K)^2}$$
$$+\overset{L_4}{a_2^2(b_1+K)^2a_2^2(b_2-K)^2}+\overset{L_5}{a_2^2(b_1+K)^2(a_1a_2)^2}+\overset{L_6}{a_1^2(b_1-K)^2(b_2^2-K^2)^2}$$
$$+\overset{L_7}{a_1^2(b_1-K)^2a_1^2(b_2+K)^2}+\overset{\textcircled{4}}{a_1^2(b_1-K)^2a_2^2(b_2-K)^2}+\overset{L_8}{a_1^2(b_1-K)^2(a_1a_2)^2}$$
$$+\overset{\textcircled{5}}{(a_1a_2)^2(b_2^2-K^2)^2}+\overset{L_9}{(a_1a_2)^2a_1^2(b_2+K)^2}+\overset{L_{10}}{(a_1a_2)^2a_2^2(b_2-K)^2}+\overset{\textcircled{6}}{(a_1a_2)^4}$$

$$
\begin{aligned}
\text{RHS} = {} & \overset{\textcircled{1}}{(b_1^2-K^2)^2(b_2^2-K^2)^2} + \overset{R_1}{(b_1^2-K^2)^2 a_1^2(b_2-K)^2} + \overset{R_2}{(b_1^2-K^2)^2 a_2^2(b_2+K)^2} \\
& + \overset{\textcircled{2}}{(b_1^2-K^2)^2(a_1a_2)^2} + \overset{R_3}{a_2^2(b_1-K)^2(b_2^2-K^2)^2} + \overset{\textcircled{4}}{a_2^2(b_1-K)^2 a_1^2(b_2-K)^2} \\
& + \overset{R_4}{a_2^2(b_1-K)^2 a_2^2(b_2+K)^2} + \overset{R_5}{a_2^2(b_1-K)^2(a_1a_2)^2} + \overset{R_6}{a_1^2(b_1+K)^2(b_2^2-K^2)^2} \\
& + \overset{R_7}{a_1^2(b_1+K)^2 a_1^2(b_2-K)^2} + \overset{\textcircled{3}}{a_1^2(b_1+K)^2 a_2^2(b_2+K)^2} + \overset{R_8}{a_1^2(b_1+K)^2(a_1a_2)^2} \\
& + \overset{\textcircled{5}}{(a_1a_2)^2(b_2^2-K^2)^2} + \overset{R_9}{(a_1a_2)^2 a_1^2(b_2-K)^2} + \overset{R_{10}}{(a_1a_2)^2 a_2^2(b_2+K)^2} + \overset{\textcircled{6}}{(a_1a_2)^4}
\end{aligned}
$$

After cancelling the ringed terms from both sides, and labelling the remaining left and right hand terms as indicated,

$$\sum_{n=1}^{10} L_n = \sum_{n=1}^{10} R_n \qquad \text{or} \qquad \sum_{n=1}^{10}(L_n - R_n) = 0$$

We take terms in pairs:

$$L_1 - R_1 = a_1^2(b_1^2-K^2)^2\left[(b_2+K)^2-(b_2-K)^2\right] = 4Kb_2a_1^2(b_1^2-K^2)^2 \qquad [5]$$

$$L_2 - R_2 = -4Kb_2a_2^2(b_1^2-K^2)^2 \qquad [5]$$

$$L_3 - R_3 = 4Kb_1a_2^2(b_2^2-K^2)^2 \qquad [4]$$

$$L_4 - R_4 = a_2^4\left\{\left[(b_1+K)(b_2-K)\right]^2-\left[(b_1-K)(b_2+K)\right]^2\right\} = 4a_2^4(b_1b_2-K^2)(b_2-b_1)K \qquad [3]$$

$$L_5 - R_5 = 4Kb_1a_1^2a_2^4 \qquad [1]$$

$$L_6 - R_6 = -4Kb_1a_1^2(b_2^2-K^2)^2 \qquad [4]$$

$$L_7 - R_7 = -4a_1^4(b_1b_2-K^2)(b_2-b_1)K \qquad [3]$$

$$L_8 - R_8 = -4Kb_1a_1^4a_2^2 \qquad [2]$$

$$L_9 - R_9 = 4Kb_2a_1^4a_2^2 \qquad [2]$$

$$L_{10} - R_{10} = -4Kb_2a_1^2a_2^4 \qquad [1]$$

$[n],[n]$ denote associated pairs

Adding together associated pairs,

$$0 = 4Ka_1^2a_2^4(b_1-b_2) - 4Ka_1^4a_2^2(b_1-b_2)$$
$$+ 4(a_2^4 - a_1^4)(b_1b_2 - K^2)(b_2-b_1)K - 4Kb_1(b_2^2-K^2)^2(a_1^2-a_2^2)$$
$$+ 4Kb_2(b_1^2-K^2)^2(a_1^2-a_2^2)$$

Factorising slightly,

$$0 = 4K(b_1-b_2)a_1^2a_2^2(a_2^2-a_1^2) + 4(a_2^2-a_1^2)(a_2^2+a_1^2)(b_1b_2-K^2)(b_2-b_1)K$$
$$- 4K(a_2^2-a_1^2)\left[b_2(b_1^2-K^2)^2 - b_1(b_2^2-K^2)^2\right]$$

Getting rid of the common factor $4K(a_2^2 - a_1^2)$

$$0 = (b_1-b_2)a_1^2a_2^2 + (a_2^2+a_1^2)(b_1b_2-K^2)(b_2-b_1)$$
$$+ b_1[b_2^4 - 2b_2^2K^2 + K^4] - b_2[b_1^4 - 2b_1^2K^2 + K^4]$$

$$0 = (b_1-b_2)[a_1^2a_2^2 - (a_2^2+a_1^2)(b_1b_2-K^2)] + b_1b_2^4 - b_2b_1^4$$
$$-2b_1b_2^2K^2 + 2b_2b_1^2K^2 + K^4(b_1-b_2)$$

Now $b_1b_2^4 - b_2b_1^4 = -b_1b_2(b_1-b_2)(b_1^2+b_2^2+b_1b_2)$

and $-2b_1b_2^2K^2 + 2b_2b_1^2K^2 = 2b_1b_2K^2(b_1-b_2)$

So, dividing through by (b_1-b_2)

$$0 = a_1^2a_2^2 - (a_2^2+a_1^2)(b_1b_2-K^2) - b_1b_2(b_1^2+b_2^2+b_1b_2) + 2b_1b_2K^2 + K^4$$

We now substitute from Eqn.(B1)

$$b_1 = x + b \qquad b_2 = x - b$$

or $$b_1b_2 = x^2 - b^2 \qquad b_1^2 + b_2^2 = 2(x^2+b^2)$$

Our equation becomes

$$0 = a_1^2 a_2^2 - (a_2^2 + a_1^2)(x^2 - b^2 - K^2) - (x^2 - b^2)(3x^2 + b^2) + 2(x^2 - b^2)K^2 + K^4$$

This is a quadratic in x^2, and hence is solvable easily. Examining the coefficients,

Coefficient of $x^4 : -3$
$x^3 : 0$
$x^2 : -(a_2^2 + a_1^2) - b^2 + 3b^2 + 2K^2 = 2K^2 + 2b^2 - a_1^2 - a_2^2$
$x : 0$
Cnst. coefficient $: a_1^2 a_2^2 + (a_1^2 + a_2^2)(b^2 + K^2) + (b^2 - K^2)^2$

On writing this in the form

$$-3x^4 + Ax^2 + B = 0$$

with A and B coming from above

We get

$$x^2 = \frac{-A \pm (A^2 + 12B)^{1/2}}{-6} = \frac{A \pm (A^2 + 12B)^{1/2}}{6}$$

We choose the +ve sign since $B > 0$ and x must be real.

Our final result is

$$\bar{x}_{max} = \pm \left\{ \frac{A + (A^2 + 12B)^{1/2}}{6} \right\}^{1/2}$$

Where $A = 2K^2 + 2b^2 - a_1^2 - a_2^2$
$B = (a_1 a_2)^2 + (a_1^2 + a_2^2)(b^2 + K^2) + (b^2 - K^2)^2$

with $a_1 = z + h$
$a_2 = z$

We again obtain an antisymmetric result, reflecting the antisymmetry of the physical system described.

Appendix C

The tapered crack leakage field

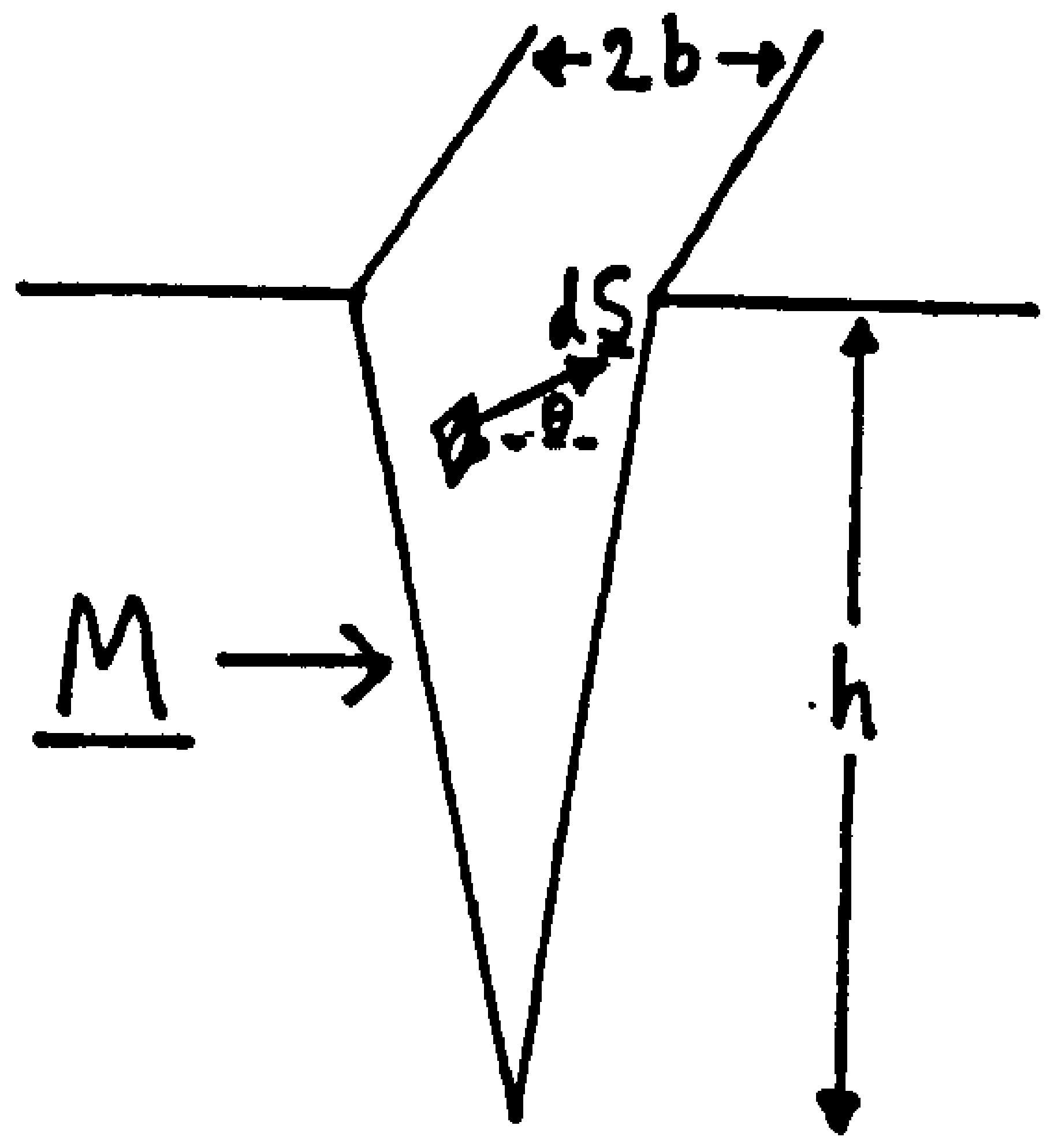

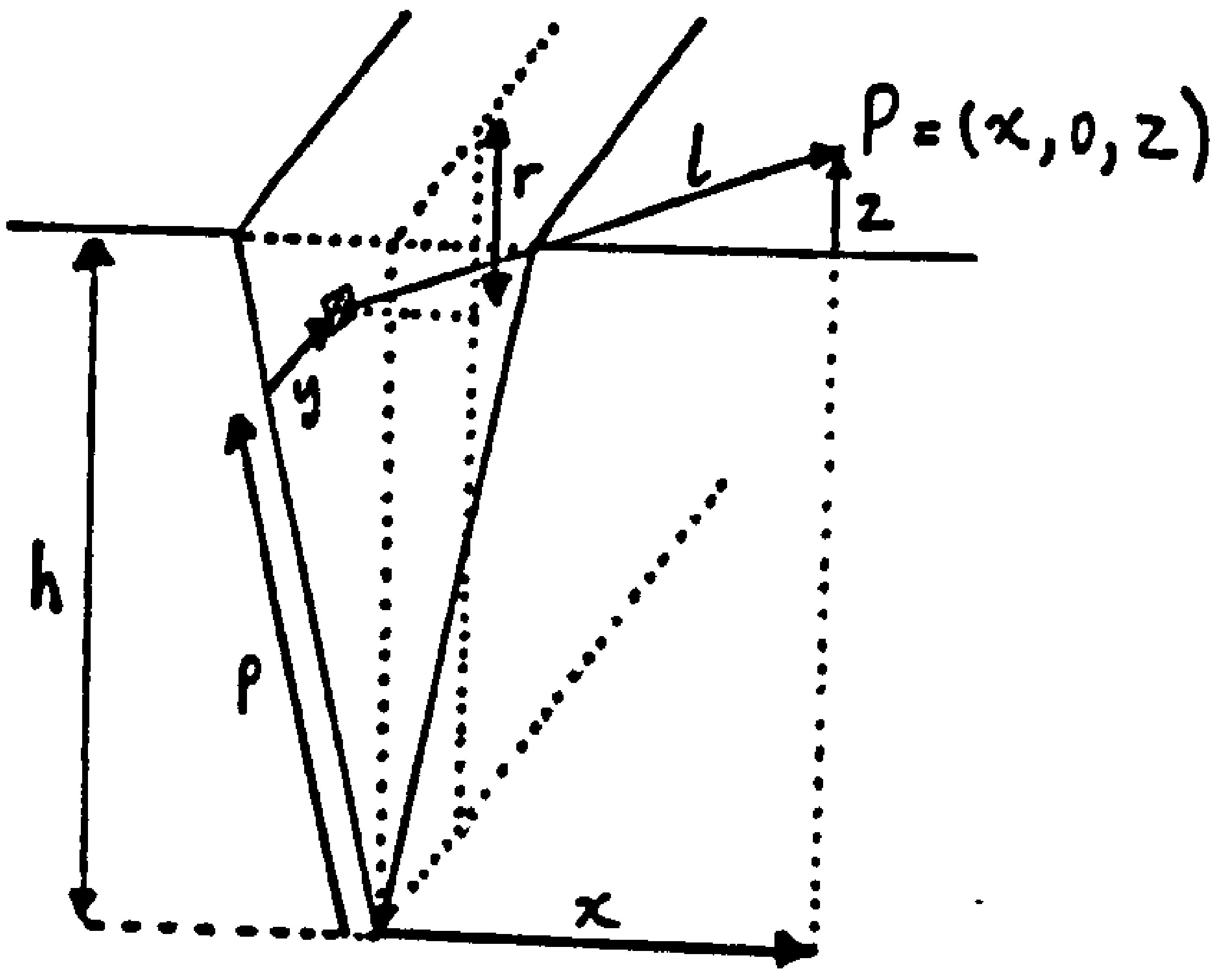

$\underline{M}$ is the magnetisation

$\underline{dS}$ is an area element

From the above diagrams

$$l^2 = (z+r)^2 + y^2 + \left(x+b\left(1-\frac{r}{h}\right)\right)^2$$

Charge element $dq = \underline{M}.d\underline{S} = M\,dS\cos\theta = M\,dS\dfrac{h}{(h^2+b^2)^{\frac{1}{2}}}$

$$dS = dy\,d\rho \qquad \frac{\rho}{h-r} = \frac{(h^2+b^2)^{\frac{1}{2}}}{h} \; ; \; d\rho = \frac{-(h^2+b^2)^{\frac{1}{2}}}{h}\,dr$$

Element of $\underline{H}$ at point P is given by

$$d\underline{H} = \frac{dq}{4\pi l^2}\,\hat{\underline{l}} = \frac{M\,dy\,d\rho\,h\,(h^2+b^2)^{-\frac{1}{2}}}{4\pi\left[(z+r)^2+y^2+\left(x+b\left(1-\frac{r}{h}\right)\right)^2\right]}\,\hat{\underline{l}}$$

Vertical component of $d\underline{H}$ is given by

$$dH_z = (d\underline{H}.\hat{\underline{z}}) = |d\underline{H}|\,(\hat{\underline{l}}.\hat{\underline{z}}) = |d\underline{H}|\,\frac{z+r}{l}$$

Vertical component is thus

$$dH_z = \frac{-M\, dy\, h^{-1}(h^2+b^2)^{\frac{1}{2}}\, dr\; (z+r)\, h\, (h^2+b^2)^{-\frac{1}{2}}}{4\pi\left[(z+r)^2 + y^2 + (x+b-\frac{br}{h})^2\right]^{3/2}}$$

$$= \frac{-M\,(z+r)\; dy\, dr}{4\pi\left[(z+r)^2 + y^2 + \left(x+b-\frac{br}{h}\right)^2\right]^{3/2}}$$

Our summation to find the total field must cover $y: -\infty \to \infty$ and $r: 0 \to h$

i.e.

$$H_z^{LH} = -\frac{M}{4\pi}\int_0^h \int_{-\infty}^{\infty} \frac{(z+r)}{\left[(z+r)^2 + y^2 + \left(x+b-\frac{br}{h}\right)^2\right]^{3/2}}\, dy\, dr$$

Putting $(z+r)^2 + \left(x+b-\frac{br}{h}\right)^2 = f^2$ and making use of

the result $\displaystyle\int_{-\infty}^{\infty} \frac{1}{(y^2+f^2)^{3/2}}\, dy = \frac{2}{f^2}$

we obtain

$$H_z^{LH} = -\frac{M}{2\pi}\int_0^h \frac{(z+r)}{(z+r)^2 + \left(x+b-\frac{br}{h}\right)^2}\, dr$$

We write the integral in the form $\int \frac{N}{D}\, dr$ (N and D denoting numerator and denominator).

$$\frac{dD}{dr} = 2(z+r) + 2\left(x+b-\frac{br}{h}\right)\left(-\frac{b}{h}\right)$$

$$= 2\left(1+\frac{b^2}{h^2}\right)r + 2z - 2(x+b)\frac{b}{h}$$

$$N = z+r = z + \frac{\frac{dD}{dr} - 2z + 2(x+b)\frac{b}{h}}{2\left(1+\frac{b^2}{h^2}\right)}$$

$$\int \frac{N}{D}\,dr = \frac{1}{2\left(1+\frac{b^2}{h^2}\right)} \ln D + \int \frac{q}{D}\,dr$$

where $q = z + \dfrac{(x+b)\frac{b}{h} - z}{\left(1+\frac{b^2}{h^2}\right)}$

Now

$$\int \frac{q}{D}\,dr = \int \frac{q}{\left(1+\frac{b^2}{h^2}\right)r^2 + \left(2z - 2(x+b)\frac{b}{h}\right)r + (x+b)^2 + z^2}\,dr$$

Write the denominator in the form $D = Ar^2 + Br + C$, where the coefficients A, B, C have the obvious values from above.

$$D = A\left(r^2 + \frac{Br}{A} + \frac{C}{A} + \frac{B^2}{4A^2} - \frac{B^2}{4A^2}\right)$$

$$= A\left[\left(r + \frac{B}{2A}\right)^2 + \frac{C}{A} - \frac{B^2}{4A^2}\right]$$

$$\therefore \quad \int \frac{q}{D}\,dr = \frac{q}{A}\int \frac{1}{\left(r+\frac{B}{2A}\right)^2 + \left(\frac{C}{A} - \frac{B^2}{4A^2}\right)}\,dr$$

$$= \frac{q}{A}\int \frac{1}{\left(\frac{C}{A} - \frac{B^2}{4A^2}\right)}\left[\frac{1}{1 + \frac{\left(r+\frac{B}{2A}\right)^2}{\left(\frac{C}{A} - \frac{B^2}{4A^2}\right)}}\right] dr$$

Put $\dfrac{C}{A} - \dfrac{B^2}{4A^2} = f^2$

$$\int \frac{q}{D}\,dr = \frac{q}{Af^2}\int \frac{1}{1+\left(\frac{r}{f} + \frac{B}{2Af}\right)^2}\,dr = \frac{q}{Af}\arctan\left(\frac{r}{f} + \frac{B}{2Af}\right)$$

Thus

$$H_z^{LH} = -\frac{M}{2\pi}\left[\frac{1}{2A}\ln\left[(z+r)^2+\left(x+b-\frac{br}{h}\right)^2\right]+\frac{q}{Af}\arctan\left(\frac{r}{f}+\frac{B}{2Af}\right)\right]_0^h$$

$$= -\frac{M}{2\pi}\left[\frac{1}{2A}\ln\left[(z+h)^2+x^2\right] + \frac{q}{Af}\arctan\left(\frac{h}{f}+\frac{B}{2Af}\right)\right]$$

$$+\frac{M}{2\pi}\left[\frac{1}{2A}\ln\left[z^2+(x+b)^2\right] + \frac{q}{Af}\arctan\left(\frac{B}{2Af}\right)\right]$$

$$\therefore$$

$$H_z^{LH} = -\frac{M}{2\pi A}\left[\frac{1}{2}\ln\frac{\left[(z+h)^2+x^2\right]}{\left[z^2+(x+b)^2\right]} + \frac{q}{f}\left\{\arctan\left(\frac{h}{f}+\frac{B}{2Af}\right)-\arctan\left(\frac{B}{2Af}\right)\right\}\right]$$

Where $A = 1+\frac{b^2}{h^2}$, $B = 2z - 2(x+b)\frac{b}{h}$

$$q = z + \frac{(x+b)\frac{b}{h}-z}{A}, \quad f = \left\{\frac{(x+b)^2+z^2}{A} - \frac{B^2}{4A^2}\right\}^{\frac{1}{2}}$$

The evaluation of the contribution to H_z from the right hand face of the tapered crack follows exactly the same pattern. In fact the only difference is that we must replace b everywhere by $-b$ and M everywhere by $-M$. We find

$$H_z^{RH} = \frac{M}{2\pi A}\left[\frac{1}{2}\ln\frac{\left[(z+h)^2+x^2\right]}{\left[z^2+(x-b)^2\right]} + \frac{q'}{f'}\left\{\arctan\left(\frac{h}{f'}+\frac{B'}{2Af'}\right)-\arctan\left(\frac{B'}{2Af'}\right)\right\}\right]$$

with $B' = 2z + 2(x-b)\frac{b}{h}$

$$q' = z - \frac{(x-b)\frac{b}{h}+z}{A}$$

$$f' = \left[\frac{(x-b)^2+z^2}{A} - \frac{B'^2}{4A^2}\right]^{\frac{1}{2}}$$

Evaluating

$$f = \frac{1}{2A}\left\{4A\left[(x+b)^2 + z^2\right] - B^2\right\}^{\frac{1}{2}}$$

$$= \frac{1}{2A}\left\{4\left(1+\frac{b^2}{h^2}\right)\left[(x+b)^2+z^2\right]-\left(4z^2 + 4(x+b)^2\frac{b^2}{h^2} - 8z(x+b)\frac{b}{h}\right)\right\}^{\frac{1}{2}}$$

$$= \frac{1}{A}\left\{(x+b)^2 + \frac{z^2b^2}{h^2} + 2z(x+b)\frac{b}{h}\right\}^{\frac{1}{2}}$$

$$= \frac{1}{A}\left(x+b+\frac{zb}{h}\right)$$

Thus

$$\frac{h}{f} + \frac{B}{2Af} = \frac{Ah}{\left(x+b+\frac{zb}{h}\right)} + \frac{2z-2(x+b)\frac{b}{h}}{2\left(x+b+\frac{zb}{h}\right)} = \frac{h^2+hz-xb}{hx+hb+zb}$$

and $$\frac{B}{2Af} = \frac{hz-xb-b^2}{xh+bh+zb}$$

After a little manipulation we find : $\frac{q}{f} = \frac{b}{h}$
The total field H_z is then given by

$$H_z = H_z^{LH} + H_z^{RH}$$

$$H_z = \frac{M}{4\pi A}\ln\left\{\frac{z^2+(x+b)^2}{z^2+(x-b)^2}\right\}$$

$$- \frac{M}{2\pi A}\frac{b}{h}\left\{\arctan\left(\frac{h^2+hz-xb}{hx+hb+bz}\right) - \arctan\left(\frac{hz-xb-b^2}{hx+hb+bz}\right)\right\}$$

$$- \frac{M}{2\pi A}\frac{b}{h}\left\{\arctan\left(\frac{h^2+hz+xb}{hx-hb-bz}\right) - \arctan\left(\frac{hz+xb-b^2}{hx-hb-bz}\right)\right\}$$

i.e.

$$H_z = \frac{M}{4\pi\left(1+\frac{b^2}{h^2}\right)}\left[\ln\left\{\frac{z^2+(x+b)^2}{z^2+(x-b)^2}\right\} + 2\left(L(b)-L(-b)\right)\right]$$

where

$$L(b) = -\frac{b}{h}\left[\operatorname{arctan}\left(\frac{h^2+hz+xb}{hx-hb-bz}\right)-\operatorname{arctan}\left(\frac{hz+xb-b^2}{hx-hb-bz}\right)\right]$$

Appendix D

Solution for the extremal values of the tangential signal

$$\frac{2\pi}{M} H_T = \arctan\left(\frac{h+z}{x+b}\right) - \arctan\left(\frac{z}{x+b}\right) - \arctan\left(\frac{h+z}{x-b}\right) + \arctan\left(\frac{z}{x-b}\right)$$

We must have

$$\frac{dH_T}{dx} = 0 = \frac{1}{1+\left(\frac{h+z}{x+b}\right)^2} \times (h+z)(-1)(x+b)^{-2} \quad \text{+ three other similar terms}$$

$$0 = \frac{-(h+z)}{(x+b)^2+(h+z)^2} + \frac{z}{(x+b)^2+z^2} + \frac{(h+z)}{(x-b)^2+(h+z)^2} - \frac{z}{(x-b)^2+z^2}$$

$$\left\{(h+z)\left[(x+b)^2+z^2\right] - z\left[(x+b)^2+(h+z)^2\right]\right\}\left[(x-b)^2+(h+z)^2\right]\left[(x-b)^2+z^2\right] \qquad (LHS)$$

$$= \left\{(h+z)\left[(x-b)^2+z^2\right] - z\left[(x-b)^2+(h+z)^2\right]\right\}\left[(x+b)^2+(h+z)^2\right]\left[(x+b)^2+z^2\right] \qquad (RHS)$$

Expanding left and right hand sides (LHS and RHS), we get

$$\begin{aligned}
LHS = {} & (h+z)(x+b)^2(x-b)^4 + \overset{①}{(h+z)(x+b)^2 z^2 (x-b)^2} \\
& + \overset{②}{(h+z)(x+b)^2 (h+z)^2 (x-b)^2} + \overset{③}{(h+z)(x+b)^2 z^2 (h+z)^2} \\
& + (h+z) z^2 (x-b)^4 + (h+z) z^2 z^2 (x-b)^2 + \overset{④}{(h+z) z^2 (h+z)^2 (x-b)^2} \\
& + \overset{⑤}{(h+z) z^2 z^2 (h+z)^2} - z(x+b)^2(x-b)^4 - \overset{⑥}{z(x+b)^2 z^2 (x-b)^2} \\
& - \overset{⑦}{z(x+b)^2(h+z)^2(x-b)^2} - \overset{⑧}{z(x+b)^2 z^2 (h+z)^2} - z(h+z)^2(x-b)^4 \\
& - \overset{⑨}{z(h+z)^2 z^2 (x-b)^2} - z(h+z)^2(h+z)^2(x-b)^2 - \overset{⑩}{z(h+z)^2 z^2 (h+z)^2}
\end{aligned}$$

$$\begin{aligned}
RHS = {} & (h+z)(x-b)^2(x+b)^4 + \overset{①}{(h+z)(x-b)^2 z^2 (x+b)^2} \\
& + \overset{②}{(h+z)(x-b)^2(h+z)^2(x+b)^2} + \overset{④}{(h+z)(x-b)^2 z^2 (h+z)^2} + \ldots
\end{aligned}$$

P.T.O.

$$\ldots + z^2(h+z)(x+b)^4 + z^2(h+z)z^2(x+b)^2 + z^2(h+z)\overset{\textcircled{3}}{(h+z)^2}(x+b)^2$$

$$+ z^2(h+z)\overset{\textcircled{5}}{z^2}(h+z)^2 - z(x-b)^2(x+b)^4 - z(x-b)^2\overset{\textcircled{6}}{z^2}(x+b)^2$$

$$- z(x-b)^2\overset{\textcircled{7}}{(h+z)^2}(x+b)^2 - z(x-b)^2\overset{\textcircled{9}}{z^2}(h+z)^2 - z(h+z)^2(x+b)^4$$

$$- z(h+z)^2\overset{\textcircled{8}}{z^2}(x+b)^2 - z(h+z)^2(h+z)^2(x+b)^2 - z(h+z)^2\overset{\textcircled{10}}{z^2}(h+z)^2$$

Cancelling the ringed terms and bringing together the remaining terms,

$$\begin{aligned} \text{LHS} &= h(x+b)^2(x-b)^4 + (h+z)z^2(x-b)^4 + (h+z)z^4(x-b)^2 \\ &\quad - z(h+z)^2(x-b)^4 - z(h+z)^4(x-b)^2 \\ \text{RHS} &= h(x-b)^2(x+b)^4 + (h+z)z^2(x+b)^4 + (h+z)z^4(x+b)^2 \\ &\quad - z(h+z)^2(x+b)^4 - z(h+z)^4(x+b)^2 \end{aligned}$$

Expanding again

$$\begin{aligned} \text{LHS} &= h(x^2-b^2)^2(\overset{\textcircled{1}}{x^2} - 2bx + \overset{\textcircled{2}}{b^2}) + (h+z)z^2(x^2-2bx+b^2)^2 \\ &\quad + (h+z)z^4(\overset{\textcircled{3}}{x^2} - 2bx + \overset{\textcircled{4}}{b^2}) - z(h+z)^2(x^2-2bx+b^2)^2 \\ &\quad - z(h+z)^4(\overset{\textcircled{5}}{x^2} - 2bx + \overset{\textcircled{6}}{b^2}) \\ \text{RHS} &= h(x^2-b^2)^2(\overset{\textcircled{1}}{x^2} + 2bx + \overset{\textcircled{2}}{b^2}) + (h+z)z^2(x^2+2bx+b^2)^2 \\ &\quad + (h+z)z^4(\overset{\textcircled{3}}{x^2} + 2bx + \overset{\textcircled{4}}{b^2}) - z(h+z)^2(x^2+2bx+b^2)^2 \\ &\quad - z(h+z)^4(\overset{\textcircled{5}}{x^2} + 2bx + \overset{\textcircled{6}}{b^2}) \end{aligned}$$

Cancelling the ringed terms and expanding further,

$$\begin{aligned} \text{LHS} &= -2bxh(x^2-b^2)^2 + (h+z)z^2\left[\overset{\textcircled{1}}{x^4} + (b^2-2bx)^2 + 2x^2\overset{\textcircled{2}}{(b^2-2bx)}\right] \\ &\quad - 2bx(h+z)z^4 - z(h+z)^2\left[\overset{\textcircled{3}}{x^4} + (b^2-2bx)^2 + 2x^2\overset{\textcircled{4}}{(b^2-2bx)}\right] \\ &\quad + 2bxz(h+z)^4 \end{aligned}$$

$$RHS = 2bxh(x^2-b^2)^2 + (h+z)z^2\left[\overset{\textcircled{1}}{x^4} + (b^2+2bx)^2 + 2x^2\,\overset{\textcircled{2}}{(b^2+2bx)}\right]$$

$$+ 2bx(h+z)z^4 - z(h+z)^2\left[\overset{\textcircled{3}}{x^4} + (b^2+2bx)^2 + 2x^2\overset{\textcircled{4}}{(b^2+2bx)}\right]$$

$$- 2bxz(h+z)^4$$

Cancelling ringed terms and expanding a little further,

$$LHS = -2bxh(x^2-b^2)^2 + (h+z)z^2\left[\overset{\textcircled{1}}{b^4} + \overset{\textcircled{2}}{4b^2x^2} - 4b^3x - 4bx^3\right]$$

$$-2bx(h+z)z^4 - z(h+z)^2\left[\overset{\textcircled{3}}{b^4} + \overset{\textcircled{4}}{4b^2x^2} - 4b^3x - 4bx^3\right]$$

$$+ 2bxz(h+z)^4$$

$$RHS = 2bxh(x^2-b^2)^2 + (h+z)z^2\left[\overset{\textcircled{1}}{b^4} + \overset{\textcircled{2}}{4b^2x^2} + 4b^3x + 4bx^3\right]$$

$$+2bx(h+z)z^4 - z(h+z)^2\left[\overset{\textcircled{3}}{b^4} + \overset{\textcircled{4}}{4b^2x^2} + 4b^3x + 4bx^3\right]$$

$$-2bxz(h+z)^4$$

After cancelling the ringed terms we notice that the LHS is the negative of the RHS so that each side must equal zero. Dividing the RHS by 2, we obtain

$$bxh(x^2-b^2)^2 + 2z^2(h+z)(b^3x + bx^3) + bx(h+z)z^4$$

$$-2z(h+z)^2(b^3x+bx^3) - bxz(h+z)^4 = 0$$

Evidently $x=0$ is a root of this equation, corresponding to the maximum in Figure 70. Removing this root and the common factor b, we obtain

$$h(x^4 + b^4 - 2x^2b^2) + 2z^2(h+z)(b^2+x^2) + (h+z)z^4$$

$$- 2z(h+z)^2(b^2+x^2) - z(h+z)^4 = 0$$

$$h x^4 + \left[2z^2(h+z) - 2hb^2 - 2z(h+z)^2\right]x^2 + hb^4 + 2z^2(h+z)b^2$$
$$+ (h+z)z^4 - 2z(h+z)^2 b^2 - z(h+z)^4 = 0$$

The coefficient of x^2 is: $2\left[z^2h + z^3 - hb^2 - zh^2 - 2z^2h - z^3\right]$

$$= 2\left[-z^2h - hb^2 - zh^2\right]$$
$$= -2h\left[z(h+z) + b^2\right]$$

The constant coefficient is:

$$hb^4 + (h+z)\left[2z^2b^2 + z^4 - 2zhb^2 - 2z^2b^2 - z(h^3 + 3h^2z + 3hz^2 + z^3)\right]$$
$$= hb^4 + (h+z)\left[-2zhb^2 - zh(h^2 + 3hz + 3z^2)\right]$$

Cancelling the common factor h in the coefficients,

$$x^4 - 2\left[z(h+z) + b^2\right]x^2 - z(h+z)\left[2b^2 + h^2 + 3hz + 3z^2\right] + b^4 = 0$$

Written in this form it is clear that when $z \gg b$, the width of the crack $2b$ has little effect on the solution. We then have

$$x^4 - 2z(h+z)x^2 - z(h+z)(h^2 + 3hz + 3z^2) = 0$$

To which the two solutions for x are given by

$$x^2_{min} = z(h+z) + \left[z^2(h+z)^2 + z(h+z)(h^2 + 3hz + 3z^2)\right]^{1/2}$$

Once again, the symmetrical nature of the problem results in equal and opposite values for x_{min}.

Appendix E

The effect of the finite probe on the detected tangential signal

We have

$$\frac{2\pi}{M} H_T = \arctan\left(\frac{h+z}{x+b}\right) - \arctan\left(\frac{z}{x+b}\right) - \arctan\left(\frac{h+z}{x-b}\right) + \arctan\left(\frac{z}{x-b}\right)$$

We need to evaluate $\bar{H}_T = \frac{1}{2K}\int_{z_0-K}^{z_0+K} H_T \, dz$

Consider first the integral

$$I = \int \arctan\left(\frac{h+z}{x+b}\right) dz = z \arctan\left(\frac{h+z}{x+b}\right) - \frac{1}{(x+b)}\int \frac{z}{1+\left(\frac{h+z}{x+b}\right)^2} dz$$

Now

$$\frac{d}{dz}\left[1+\left(\frac{h+z}{x+b}\right)^2\right] = 2\left(\frac{h+z}{x+b}\right)\frac{1}{(x+b)}$$

so that $\frac{1}{2}(x+b)^2 \frac{d}{dz}\left[1+\left(\frac{h+z}{x+b}\right)^2\right] - h = z$

and

$$\int \frac{z}{1+\left(\frac{h+z}{x+b}\right)^2} dz = \int \frac{\frac{1}{2}(x+b)^2 \frac{d}{dz}\left[1+\left(\frac{h+z}{x+b}\right)^2\right] - h}{\left[1+\left(\frac{h+z}{x+b}\right)^2\right]} dz$$

$$= \frac{1}{2}(x+b)^2 \ln\left[1+\left(\frac{h+z}{x+b}\right)^2\right] - h(x+b)\arctan\left(\frac{h+z}{x+b}\right)$$

Thus the integral

$$I = (z+h)\arctan\left(\frac{h+z}{x+b}\right) - \frac{1}{2}(x+b)\ln\left[1+\left(\frac{h+z}{x+b}\right)^2\right]$$

The other three terms arising from the integration of H_T may be found by substituting z for $h+z$ and $x-b$ for $x+b$ as appropriate, taking care to preserve the negative sign of the two middle terms.

Evaluating the integral between the two limits, we find, dropping the subscript on z_0,

$$\frac{2\pi}{M}\int_{z_0-K}^{z_0+K} H_T\, dz = \frac{4\pi K}{M}\bar{H}_T$$

$$= (z+K+h)\,\mathrm{arctan}\left(\frac{z+K+h}{x+b}\right) - \frac{1}{2}(x+b)\ln\left[1+\left(\frac{z+K+h}{x+b}\right)^2\right]$$

$$-(z+K)\,\mathrm{arctan}\left(\frac{z+K}{x+b}\right) + \frac{1}{2}(x+b)\ln\left[1+\left(\frac{z+K}{x+b}\right)^2\right]$$

$$-(z+K+h)\,\mathrm{arctan}\left(\frac{z+K+h}{x-b}\right) + \frac{1}{2}(x-b)\ln\left[1+\left(\frac{z+K+h}{x-b}\right)^2\right]$$

$$+(z+K)\,\mathrm{arctan}\left(\frac{z+K}{x-b}\right) - \frac{1}{2}(x-b)\ln\left[1+\left(\frac{z+K}{x-b}\right)^2\right]$$

$$-(z-K+h)\,\mathrm{arctan}\left(\frac{z-K+h}{x+b}\right) + \frac{1}{2}(x+b)\ln\left[1+\left(\frac{z-K+h}{x+b}\right)^2\right]$$

$$+(z-K)\,\mathrm{arctan}\left(\frac{z-K}{x+b}\right) - \frac{1}{2}(x+b)\ln\left[1+\left(\frac{z-K}{x+b}\right)^2\right]$$

$$+(z-K+h)\,\mathrm{arctan}\left(\frac{z-K+h}{x-b}\right) - \frac{1}{2}(x-b)\ln\left[1+\left(\frac{z-K+h}{x-b}\right)^2\right]$$

$$-(z-K)\,\mathrm{arctan}\left(\frac{z-K}{x-b}\right) + \frac{1}{2}(x-b)\ln\left[1+\left(\frac{z-K}{x-b}\right)^2\right]$$

This must now be differentiated with respect to x , and equated to zero.

Differentiating the first two terms,

$$0 = -(z+K+h)\frac{1}{\left[1+\left(\frac{z+K+h}{x+b}\right)^2\right]}(z+K+h)(x+b)^{-2}$$

$$-\frac{1}{2}\ln\left[1+\left(\frac{z+K+h}{x+b}\right)^2\right]$$

$$+\frac{1}{2}(x+b)\frac{1}{\left[1+\left(\frac{z+K+h}{x+b}\right)^2\right]}\,2\left(\frac{z+K+h}{x+b}\right)(z+K+h)(x+b)^{-2}$$

+ seven other similar such terms substituting appropriately for $z+K+h$ and $x+b$. The differential of the first two terms is seen to simplify as do the other terms. Eventually we get,

$$0 = -\frac{1}{2}\ln\left[1+\left(\frac{z+K+h}{x+b}\right)^2\right] + \frac{1}{2}\ln\left[1+\left(\frac{z+K}{x+b}\right)^2\right]$$

$$+\frac{1}{2}\ln\left[1+\left(\frac{z+K+h}{x-b}\right)^2\right] - \frac{1}{2}\ln\left[1+\left(\frac{z+K}{x-b}\right)^2\right]$$

$$+\frac{1}{2}\ln\left[1+\left(\frac{z-K+h}{x+b}\right)^2\right] - \frac{1}{2}\ln\left[1+\left(\frac{z-K}{x+b}\right)^2\right]$$

$$-\frac{1}{2}\ln\left[1+\left(\frac{z-K+h}{x-b}\right)^2\right] + \frac{1}{2}\ln\left[1+\left(\frac{z-K}{x-b}\right)^2\right]$$

or

$$\frac{\left[1+\left(\frac{z+K}{x+b}\right)^2\right]\left[1+\left(\frac{z+K+h}{x-b}\right)^2\right]\left[1+\left(\frac{z-K+h}{x+b}\right)^2\right]\left[1+\left(\frac{z-K}{x-b}\right)^2\right]}{\left[1+\left(\frac{z+K+h}{x+b}\right)^2\right]\left[1+\left(\frac{z+K}{x-b}\right)^2\right]\left[1+\left(\frac{z-K}{x+b}\right)^2\right]\left[1+\left(\frac{z-K+h}{x-b}\right)^2\right]} = 1$$

$$\left[(x+b)^2+(z+K)^2\right]\left[(x-b)^2+(z+K+h)^2\right]\left[(x+b)^2+(z-K+h)^2\right]\left[(x-b)^2+(z-K)^2\right]$$

$$=\left[(x+b)^2+(z+K+h)^2\right]\left[(x-b)^2+(z+K)^2\right]\left[(x+b)^2+(z-K)^2\right]\left[(x-b)^2+(z-K+h)^2\right]$$

Expanding partially, left and right hand sides become

LHS

$$=\left[(x+b)^2(x-b)^2+(z+K+h)^2(x+b)^2+(z+K)^2(x-b)^2+(z+K)^2(z+K+h)^2\right]\times$$
$$\left[(x+b)^2(x-b)^2+(z-K)^2(x+b)^2+(z-K+h)^2(x-b)^2+(z-K+h)^2(z-K)^2\right]$$

RHS

$$=\left[(x+b)^2(x-b)^2+(z+K)^2(x+b)^2+(z+K+h)^2(x-b)^2+(z+K+h)^2(z+K)^2\right]\times$$
$$\left[(x+b)^2(x-b)^2+(z-K+h)^2(x+b)^2+(z-K)^2(x-b)^2+(z-K)^2(z-K+h)^2\right]$$

Expanding further,

$$\text{LHS} = \overset{\textcircled{1}}{\left[(x+b)^2(x-b)^2\right]^2} + \overset{\textcircled{A}}{(z-K)^2(x-b)^2(x+b)^4} + \overset{\textcircled{B}}{(z-K+h)^2(x+b)^2(x-b)^4}$$
$$+ \overset{\textcircled{2}}{(z-K+h)^2(z-K)^2(x+b)^2(x-b)^2} + \overset{\textcircled{C}}{(z+K+h)^2(x+b)^4(x-b)^2}$$
$$+ \overset{\textcircled{D}}{(z+K+h)^2(z-K)^2(x+b)^4} + \overset{\textcircled{3}}{(z+K+h)^2(z-K+h)^2(x+b)^2(x-b)^2}$$
$$+ \overset{\textcircled{E}}{(z+K+h)^2(z-K+h)^2(z-K)^2(x+b)^2} + \overset{\textcircled{F}}{(z+K)^2(x+b)^2(x-b)^4}$$
$$+ \overset{\textcircled{4}}{(z+K)^2(z-K)^2(x-b)^2(x+b)^2} + \overset{\textcircled{G}}{(z+K)^2(z-K+h)^2(x-b)^4}$$
$$+ \overset{\textcircled{H}}{(z+K)^2(z-K+h)^2(z-K)^2(x-b)^2} + \overset{\textcircled{5}}{(z+K)^2(z+K+h)^2(x+b)^2(x-b)^2}$$
$$+ \overset{\textcircled{I}}{(z+K)^2(z+K+h)^2(z-K)^2(x+b)^2} + \overset{\textcircled{J}}{(z+K)^2(z+K+h)^2(z-K+h)^2(x-b)^2}$$
$$+ \overset{\textcircled{6}}{(z+K)^2(z+K+h)^2(z-K+h)^2(z-K)^2}$$

$$\begin{aligned}
\text{RHS} = {} & \overset{\textcircled{1}}{\left[(x+b)^2(x-b)^2\right]^2} + \overset{\textcircled{B}}{(z-K+h)^2(x+b)^4(x-b)^2} + \overset{\textcircled{A}}{(z-K)^2(x+b)^2(x-b)^4} \\
& + \overset{\textcircled{2}}{(z-K)^2(z-K+h)^2(x+b)^2(x-b)^2} + \overset{\textcircled{F}}{(z+K)^2(x+b)^4(x-b)^2} \\
& + \overset{\textcircled{G}}{(z+K)^2(z-K+h)^2(x+b)^4} + \overset{\textcircled{4}}{(z+K)^2(z-K)^2(x+b)^2(x-b)^2} \\
& + \overset{\textcircled{H}}{(z+K)^2(z-K)^2(z-K+h)^2(x+b)^2} + \overset{\textcircled{C}}{(z+K+h)^2(x+b)^2(x-b)^4} \\
& + \overset{\textcircled{3}}{(z+K+h)^2(z-K+h)^2(x+b)^2(x-b)^2} + \overset{\textcircled{D}}{(z+K+h)^2(z-K)^2(x-b)^4} \\
& + \overset{\textcircled{E}}{(z+K+h)^2(z-K)^2(z-K+h)^2(x-b)^2} + \overset{\textcircled{5}}{(z+K+h)^2(z+K)^2(x+b)^2(x-b)^2} \\
& + \overset{\textcircled{J}}{(z+K+h)^2(z+K)^2(z-K+h)^2(x+b)^2} + \overset{\textcircled{I}}{(z+K+h)^2(z+K)^2(z-K)^2(x-b)^2} \\
& + \overset{\textcircled{6}}{(z+K+h)^2(z+K)^2(z-K)^2(z-K+h)^2}
\end{aligned}$$

The NUMBERED ringed terms cancel and we are free to examine the coefficients of the various powers of x on each side of the equation.

Coefficient of x^6:

$$\text{LHS}: (z-K)^2 + (z-K+h)^2 + (z+K+h)^2 + (z+K)^2$$

$$\text{RHS}: (z-K+h)^2 + (z-K)^2 + (z+K)^2 + (z+K+h)^2$$

These coefficients cancel so that there is no term in x^6

Coefficient of x^4:

$$\begin{aligned}
\text{LHS}: {} & \overset{\textcircled{1}}{-b^2(z-K)^2} \overset{\textcircled{2}}{- b^2(z-K+h)^2} \overset{\textcircled{3}}{- b^2(z+K+h)^2} \\
& \overset{\textcircled{4}}{+ (z+K+h)^2(z-K)^2} \overset{\textcircled{5}}{- b^2(z+K)^2} \overset{\textcircled{6}}{+ (z+K)^2(z-K+h)^2}
\end{aligned}$$

$$\begin{aligned}
\text{RHS}: {} & \overset{\textcircled{2}}{-b^2(z-K+h)^2} \overset{\textcircled{1}}{- b^2(z-K)^2} \overset{\textcircled{5}}{- b^2(z+K)^2} \\
& \overset{\textcircled{6}}{+ (z+K)^2(z-K+h)^2} \overset{\textcircled{3}}{- b^2(z+K+h)^2} \overset{\textcircled{4}}{+ (z+K+h)^2(z-K)^2}
\end{aligned}$$

These coefficients cancel so that there is no term in x^4

Coefficient of x^2:

$$\text{LHS}: -b^4\overset{①}{(z-K)^2} - b^4\overset{②}{(z-K+h)^2} - b^4\overset{③}{(z+K+h)^2}$$

$$+ \overset{④}{6b^2(z+K+h)^2(z-K)^2} + \overset{⑤}{(z+K+h)^2(z-K+h)^2(z-K)^2}$$

$$-\overset{⑥}{b^4(z+K)^2} + \overset{⑦}{6b^2(z+K)^2(z-K+h)^2} + \overset{⑧}{(z+K)^2(z-K+h)^2(z-K)^2}$$

$$+ \overset{⑨}{(z+K)^2(z+K+h)^2(z-K)^2} + \overset{⑩}{(z+K)^2(z+K+h)^2(z-K+h)^2}$$

$$\text{RHS}: -\overset{②}{b^4(z-K+h)^2} - \overset{①}{b^4(z-K)^2} - \overset{⑥}{b^4(z+K)^2}$$

$$+ \overset{⑦}{6b^2(z+K)^2(z-K+h)^2} + \overset{⑧}{(z+K)^2(z-K)^2(z-K+h)^2}$$

$$- \overset{③}{b^4(z+K+h)^2} + \overset{④}{6b^2(z+K+h)^2(z-K)^2} + \overset{⑤}{(z+K+h)^2(z-K)^2(z-K+h)^2}$$

$$+ \overset{⑩}{(z+K+h)^2(z+K)^2(z-K+h)^2} + \overset{⑨}{(z+K+h)^2(z+K)^2(z-K)^2}$$

These terms cancel so that there is no term in x^2.

Constant coefficient :

$$\text{LHS}: \overset{①}{(z-K)^2b^6} + \overset{②}{(z-K+h)^2b^6} + \overset{③}{(z+K+h)^2b^6}$$

$$+ \overset{④}{(z+K+h)^2(z-K)^2b^4} + \overset{⑤}{(z+K+h)^2(z-K+h)^2(z-K)^2b^2}$$

$$+ \overset{⑥}{(z+K)^2b^6} + \overset{⑦}{(z+K)^2(z-K+h)^2b^4} + \overset{⑧}{(z+K)^2(z-K+h)^2(z-K)^2b^2}$$

$$+ \overset{⑨}{(z+K)^2(z+K+h)^2(z-K)^2b^2} + \overset{⑩}{(z+K)^2(z+K+h)^2(z-K+h)^2b^2}$$

$$\text{RHS}: \overset{②}{(z-K+h)^2b^6} + \overset{①}{(z-K)^2b^6} + \overset{⑥}{(z+K)^2b^6} + \overset{⑦}{(z+K)^2(z-K+h)^2b^4}$$

$$+ \overset{⑧}{(z+K)^2(z-K)^2(z-K+h)^2b^2} + \overset{③}{(z+K+h)^2b^6}$$

$$+ \overset{④}{(z+K+h)^2(z-K)^2b^4} + \overset{⑤}{(z+K+h)^2(z-K)^2(z-K+h)^2b^2}$$

$$+ \overset{⑩}{(z+K+h)^2(z+K)^2(z-K+h)^2b^2} + \overset{⑨}{(z+K+h)^2(z+K)^2(z-K)^2b^2}$$

These terms cancel so that there is no constant coefficient. Consequently our equation LHS = RHS can be written in the form $ax^5 + bx^3 + cx = 0 = x(ax^4 + bx^2 + c) = 0$

Clearly one solution is $x = 0$ which we would expect since this corresponds to the maximum in H_T at any given scan height z. Moreover, the other two solutions for $\bar{x}_{min}$ are evidently equal and opposite. This too must be so because of the symmetry of the situation. The lettered terms in LHS and RHS are identical except that in RHS the corresponding lettered term in LHS has had b replaced by $-b$. Thus we aim to determine the coefficients of LHS, knowing that those for RHS are identical except with b replaced by $-b$.

Coefficient of x^5:

$$\text{LHS}: 2b(z-K)^2 + (z-K+h)^2(-2b) + 2b(z+K+h)^2 - 2b(z+K)^2$$

$$= (-2b)(2h(z-K)+h^2) + 2b(2h(z+K)+h^2) = 8bhK$$

Coefficient of x^3:

$$\text{LHS}: -4b^3(z-K)^2 + 4b^3(z-K+h)^2 - 4b^3(z+K+h)^2$$

$$+4b(z+K+h)^2(z-K)^2 + 4b^3(z+K)^2 - 4b(z+K)^2(z-K+h)^2$$

Coefficient of x:

$$\text{LHS}: 2b^6(\overset{①}{z}-K)^2 - 2b^5(z-\overset{②}{K}+h)^2 + 2b^5(\overset{②}{z}+K+h)^2$$

$$+4b^3(z+\overset{③}{K}+h)^2(z-K)^2 + 2b(z+K+h)^2(z-\overset{④}{K}+h)^2(z-K)^2$$

$$-2b^5(\overset{①}{z}+K)^2 - 4b^3(z+K)^2(\overset{③}{z}-K+h)^2 - 2b(z+K)^2(\overset{⑤}{z}-K+h)^2(z-K)^2$$

$$+2b(z+K)^2(\overset{⑤}{z}-K)^2(z+K+h)^2 - 2b(z+K)^2(\overset{④}{z}+K+h)^2(z-K+h)^2$$

It is noted that, since only odd powers of b occur in the coefficients of x^5, x^3 and x, the corresponding coefficients in RHS will be equal and opposite. We factorise our equation $ax^5+bx^3+cx=0$ to obtain the form $ax^4+bx^2+c=0$. It is noted that each of the coefficients has a common factor $2b$, so that we divide by $2b$ to obtain,

Coefficient of x^4: $4hK$

Coefficient of x^2: $2b^2\left[(z+K)^2-(z-K)^2\right] + 2b^2\left[(z-K+h)^2-(z+K+h)^2\right]$

$$+2\left[(z+K+h)^2(z-K)^2 - (z+K)^2(z-K+h)^2\right]$$

$$= 2b^2(2z)(2K) + 2b^2\left[2(z+h)\right]\left[-2K\right] + 2\left[2(z^2-K^2+hz)\right]\left[-2hK\right]$$

$$= 8K\left[b^2 z - b^2(z+h) - h\,(z^2 - K^2 + hz)\right]$$

$$= -8hK\left[b^2 + z^2 - K^2 + hz\right]$$

Constant coefficient; we consider the ringed pairs of terms:

① $b^4\left[(z-K)^2 - (z+K)^2\right] = -4Kzb^4$

② $b^4\left[(z+K+h)^2 - (z-K+h)^2\right] = 4b^4(z+h)K$

③ $2b^2\left[(z-K)^2(z+K+h)^2 - (z+K)^2(z-K+h)^2\right] = -8b^2(z^2+hz-K^2)Kh$

④ $(z+K+h)^2(z-K+h)^2\left[(z-K)^2 - (z+K)^2\right] = -4Kz(z+K+h)^2(z-K+h)^2$

⑤ $(z+K)^2(z-K)^2\left[(z+K+h)^2 - (z-K+h)^2\right] = 4K(z+h)(z+K)^2(z-K)^2$

Having obtained the coefficients of x^4, x^2 and the constant coefficient, we are in a position to solve for $\bar{x}_{min}$. Before we do this however we can use the result of Appendix D that when $z \gg b$ we can ignore b. This condition must be modified in the present case however since the lower end of the probe is at a height $z-K$ and not z. The modified restriction on ignoring b is thus $z-K \gg b$. Assuming this to be the case, as it will be for many practical situations, we obtain:

Coefficient of x^4: $4hK$

Coefficient of x^2: $-8hK\left[z^2 - K^2 + hz\right]$

Constant coefficient : $4K(z+h)(z^2-K^2)^2 - 4Kz(z+K+h)^2(z-K+h)^2$

Dividing by the common factor $4K$, our equation reduces to,

$$hx^4 - 2h(z^2-K^2+hz)x^2 + (z+h)(z^2-K^2)^2 - z(z+K+h)^2(z-K+h)^2 = 0$$

To which the solutions for $\bar{x}_{min}$ are

$$\bar{x}^2_{min} = (z^2 - K^2 + hz)$$
$$\pm\left\{(z^2-K^2+hz)^2 - \frac{1}{h}\left[(z+h)(z^2-K^2)^2 - z(z+K+h)^2(z-K+h)^2\right]\right\}^{1/2}$$

It is worth noting that if we let $K=0$ we must obtain the result of Appendix D for the infinitesimal probe. Putting $K=0$ into the equation for $\bar{x}_{min}$,

$$\bar{x}^2_{min}(K=0) = z^2+hz+\left\{(z^2+hz)^2-\frac{1}{h}\left[(z+h)z^4-z(z+h)^4\right]\right\}^{1/2}$$

$$= z(h+z)+\left\{z^2(h+z)^2-\frac{z(h+z)}{h}\left[z^3-(z^3+3z^2h+3h^2z+h^3)\right]\right\}^{1/2}$$

$$= z(h+z)+\left\{z^2(h+z)^2+z(h+z)\left[3z^2+3zh+h^2\right]\right\}^{1/2}$$

This indeed reproduces the result of Appendix D.

Appendix F

An approximation for the peak vertical field

We have

$$\frac{4\pi}{M} H_{vert} = \ln \frac{\left[(x+b)^2+(z+h)^2\right]\left[(x-b)^2+z^2\right]}{\left[(x+b)^2+z^2\right]\left[(x-b)^2+(z+h)^2\right]}$$

We use our approximate value for $x_{max} = (b^2+z^2)^{\frac{1}{2}} \approx z$ when $z \gg b$

Thus

$$\frac{4\pi}{M} H_{max} = \ln \left[\frac{(z^2+2zb+b^2+z^2+2hz+h^2)(z^2-2bz+b^2+z^2)}{(z^2+2zb+b^2+z^2)(z^2-2bz+b^2+z^2+2zh+h^2)}\right]$$

We discount the terms in b^2 as negligible.

$$\frac{4\pi}{M} H_{max} = \ln\left[\frac{2z^2-2bz}{2z^2+2bz}\right] + \ln\left[\frac{2z^2+2hz+h^2+2bz}{2z^2+2hz+h^2-2bz}\right]$$

$$= \ln\left[\frac{1-\frac{b}{z}}{1+\frac{b}{z}}\right] + \ln\left[\frac{1+\frac{2bz}{2z^2+2hz+h^2}}{1-\frac{2bz}{2z^2+2hz+h^2}}\right].$$

Each of the terms is now in the form $\ln\left[\frac{1+x}{1-x}\right]$ where x is small.

When x is small, $\ln\left[\frac{1+x}{1-x}\right] \approx 2x$

so that

$$\frac{4\pi}{M} H_{max} = -\frac{2b}{z} + \frac{4bz}{2z^2+2hz+h^2} = \frac{4bz^2-2b(2z^2+2hz+h^2)}{(2z^2+2hz+h^2)z}$$

$$\frac{4\pi}{M} \left|H_{max}\right| = \frac{2b}{z}\left(\frac{h^2+2hz}{2z^2+h^2+2hz}\right)$$

(We have taken the modulus of H_{max}).

Appendix G

LOHET II (650-548)

The LOHET II high performance Hall effect analogue position sensor is affected by the magnetic field of either permanent magnets or electro-magnets. The output voltage varies in proportion to the strength of the magnetic field. The transducer is constructed on a thin ceramic substrate and the actual chip is protected by a ceramic cap. The device has three in-line pcb terminals on standard 0.1 in mounting centres, and utilises a new Hall effect integrated circuit which provides increased temperature stability and performance with a temperature drift almost ten times better than the LOHET I. The laser trimmed thick film resistors on the ceramic substrate, and the thin film resistors on the integrated circuit reduce null and gain shifts against temperature and provide consistent sensitivity from one device to another. The transducer operates from an 8Vdc supply, and the linear output can be either current sinking or current sourcing. The output from the transducer, which is a ratiometric device, varies from 25% to 75% of the supply voltage as the magnetic flux varies from −400 to +400 Gauss. The output voltage from the device will increase linearly with the magnetic field until a +400 Gauss level is reached, at which point the typical output voltage will be 6V. The output voltage at 0 Gauss is typically 4.0V.

Specification

Parameter	Min.	Typ.	Max.	Units
Supply voltage	7.6	8.0	8 4	Vdc
Supply current	-	13	20	mA
Output	-	-	1	mA
Response time		20		µs
Magnetic characteristics Span (−400 to +400 Gauss)	-	Vs/2	-	V
Sensitivity (@ 25°C)	4.40	5.0	6.0	mV/Gauss
Linearity	-	-	1.0	% span
Null (offset at 0 Gauss)	3 960	4.000	4.040	V
Temperature errors Null	−0.02	-	+0.02	% per °C
Gain	−0.02	-	+0.02	% per °C

Features

- Single, current sinking or current sourcing, linear output
- Improved temperature stability
- Three pin in-line pcb terminals
  Standard 0.1 in mounting centres
- Laser trimmed thin film and thick film resistors minimise variations in sensitivity and compensate for temperature variations
- Flux range of −400 to +400 Gauss.

Mounting dimensions

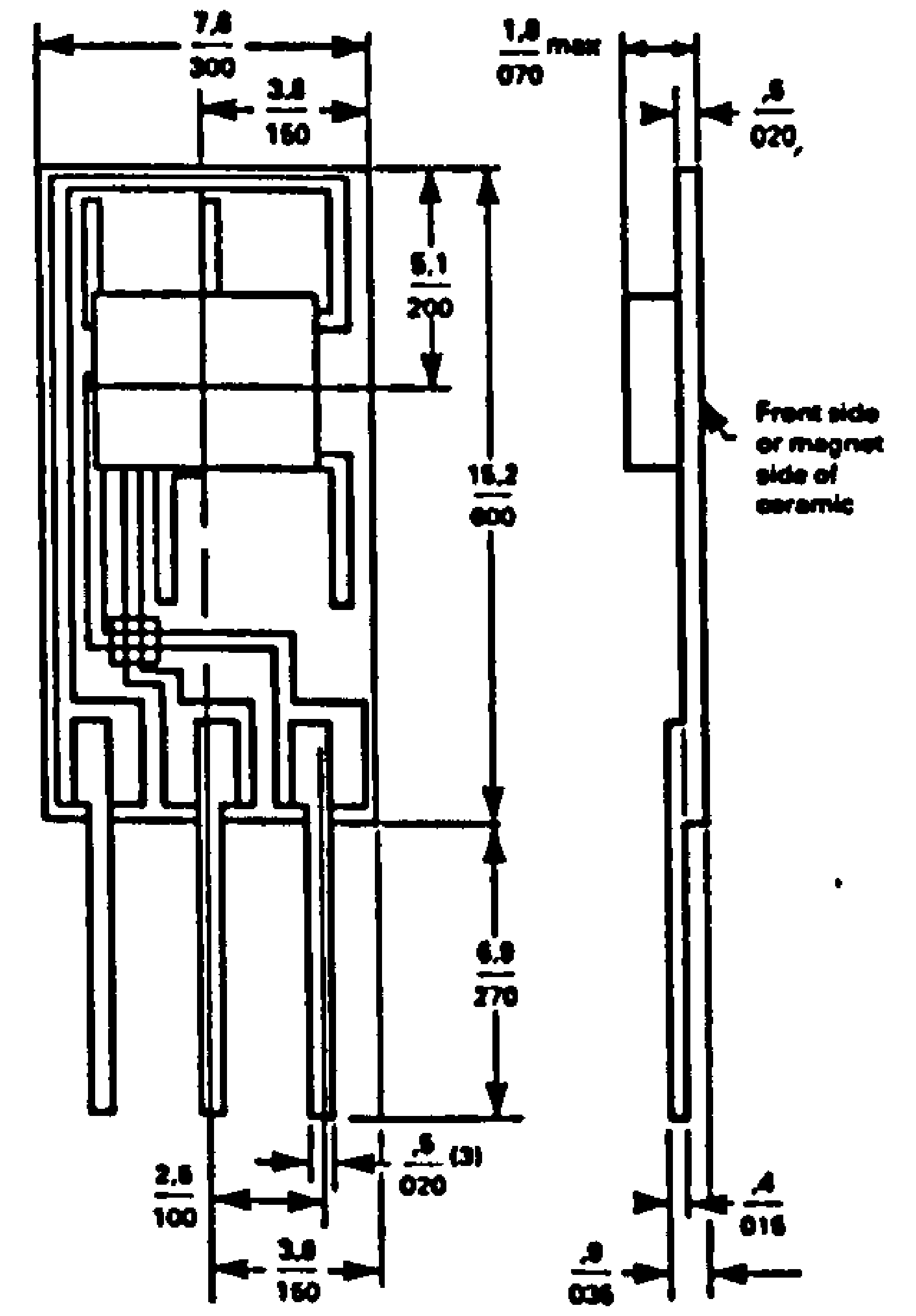

Figure 15 Transfer characteristics

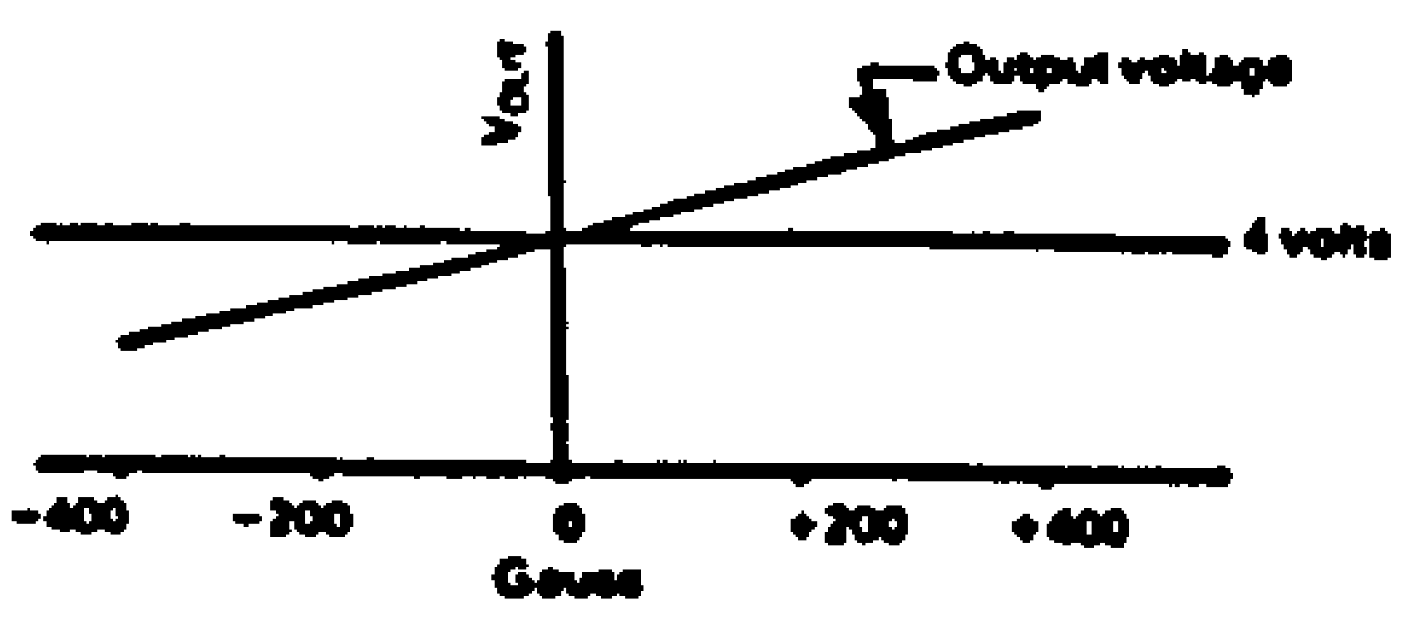

Appendix H

A possible origin of the linear bias field

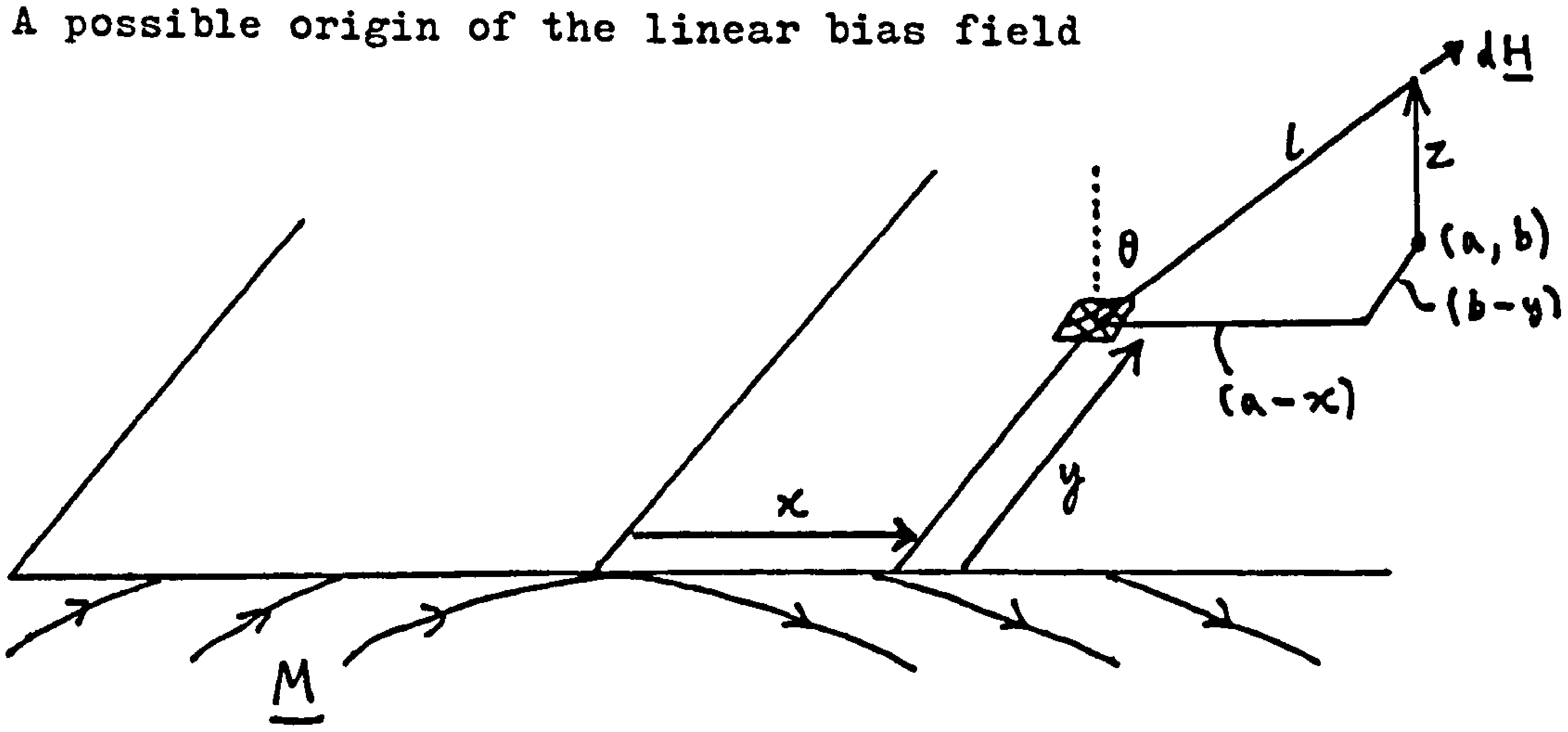

Assume a charge density variation $\rho(x) = -Kx$, the charge per unit area.

Take an element of area $\delta x \delta y$, having a charge $dq = \rho\,\delta x \delta y$. Since

$$d\underline{H} = \frac{dq}{4\pi r^2}\,\hat{\underline{r}} \qquad , \quad l^2 = (b-y)^2 + (a-x)^2 + z^2$$

We have in the above diagram

$$d\underline{H} = \frac{\rho\,\delta x \delta y}{4\pi l^2}\,\hat{\underline{l}} \quad , \quad dH_z = \frac{\rho\,\delta x\delta y}{4\pi l^2}\cos\theta = \frac{\rho\,\delta x\delta y}{4\pi l^2}\,\frac{z}{l}$$

$$H_z(a,b,z) = \int dH_z = \int_{-\infty}^{\infty}\int_{-\infty}^{\infty}\frac{-Kxz\,dx\,dy}{4\pi\left[(b-y)^2+(a-x)^2+z^2\right]^{3/2}}$$

Now

$$\left[(a-x)^2+z^2+(b-y)^2\right]^{3/2} = \left[(a-x)^2+z^2\right]^{3/2}\left[1 + \frac{(b-y)^2}{(a-x)^2+z^2}\right]^{3/2}$$

Put $\dfrac{(b-y)}{\left[(a-x)^2+z^2\right]^{1/2}} = \tan t$, $\dfrac{-dy}{\left[(a-x)^2+z^2\right]^{1/2}} = \sec^2 t\,dt$

The integrand becomes

$$-\frac{Kz}{4\pi}\,\frac{x}{\left[(a-x)^2+z^2\right]^{3/2}}\,\frac{1}{\sec^3 t}\,dx\,(-)\left[(a-x)^2+z^2\right]^{1/2}\sec^2 t\,dt$$

So that

$$H_z(a,b,z) = \frac{Kz}{4\pi}\int_{-\infty}^{\infty}\int_{\frac{\pi}{2}}^{-\frac{\pi}{2}}\frac{x}{[(a-x)^2+z^2]}\cos t\,dt\,dx = -\frac{Kz}{2\pi}\int_{-\infty}^{\infty}\frac{x}{(a-x)^2+z^2}\,dx$$

We have,

$$a+\frac{1}{2}\,\frac{d}{dx}\left[(a-x)^2+z^2\right] = x$$

So that the integral

$$I = \int_{-\infty}^{\infty}\frac{a}{[(a-x)^2+z^2]}\,dx + \frac{1}{2}\Big[\ln\left[(a-x)^2+z^2\right]\Big]_{-\infty}^{\infty}$$

Thus

$$H_z(a,b,z) = -\frac{Kz}{2\pi}\left[-\frac{a}{z}\left[\arctan\left(\frac{a-x}{z}\right)\right]_{-\infty}^{\infty} + \lim_{R\to\infty}\left[\frac{1}{2}\ln[(a-x)^2+z^2]\right]_{-R}^{R}\right]$$

$$= -\frac{Kz}{2\pi}\left[-\frac{a}{z}\left(-\frac{\pi}{2}-\frac{\pi}{2}\right)+\frac{1}{2}\lim_{R\to\infty}\left(\ln\frac{[(a-R)^2+z^2]}{[(a+R)^2+z^2]}\right)\right]$$

$$= -\frac{Kz}{2\pi}\,\frac{\pi a}{z} = -\frac{Ka}{2}$$

Hence the field above such a surface at a point (x,y,z) is given by

$$H_z(x,y,z) = -\frac{Kx}{2}$$

a linear field as observed by Oehl and Swartzendruber.

Appendix I

Evaluation of the gradient at the origin of the vertical component signal with a finite probe

From Section 3.3,

$$2K\frac{\bar{H}}{\left(\frac{M}{4\pi}\right)} = A_1 + A_2 - A_3 - A_4$$

With

$$A_i = (b_i+K)\ln\left[(b_i+K)^2+a_i^2\right] - (b_i-K)\ln\left[(b_i-K)^2+a_i^2\right]$$
$$+2a_i\left[\arctan\left(\frac{b_i+K}{a_i}\right) - \arctan\left(\frac{b_i-K}{a_i}\right)\right]$$

where $a_1 = a_4 = z+h$ $\quad b_1 = b_3 = x+b$

$a_2 = a_3 = z$ $\quad b_2 = b_4 = x-b$

We find

$$\frac{dA_i}{dx} = \ln\left[\frac{(b_i+K)^2+a_i^2}{(b_i-K)^2+a_i^2}\right] = \ln[i]$$

So that

$$\frac{2K}{\left(\frac{M}{4\pi}\right)}\left(\frac{d\bar{H}}{dx}\right) = \ln[1] + \ln[2] - \ln[3] - \ln[4]$$
$$= \ln\left[\frac{(b+K)^2+(z+h)^2}{(b-K)^2+(z+h)^2}\right] + \ln\left[\frac{(b-K)^2+z^2}{(b+K)^2+z^2}\right]$$
$$-\ln\left[\frac{(b+K)^2+z^2}{(b-K)^2+z^2}\right] - \ln\left[\frac{(b-K)^2+(z+h)^2}{(b+K)^2+(z+h)^2}\right] \quad \text{at } x=0$$

$$K\left(\frac{4\pi}{M}\right)\left(\frac{d\bar{H}}{dx}\right)_{x=0} = \ln\frac{\left[(b+K)^2+(z+h)^2\right]\left[(b-K)^2+z^2\right]}{\left[(b-K)^2+(z+h)^2\right]\left[(b+K)^2+z^2\right]}$$

Now

$$\ln\left[(b+K)^2+(z+h)^2\right] = \ln\left[(z+h)^2+K^2+b^2+2bK\right]$$

$$= \ln\left[(z+h)^2+K^2+b^2\right] + \ln\left[1+\frac{2bK}{(z+h)^2+K^2+b^2}\right]$$

$$\approx \ln\left[(z+h)^2+K^2+b^2\right] + \frac{2bK}{(z+h)^2+K^2+b^2}$$

Thus

$$K\left(\frac{4\pi}{M}\right)\left(\frac{d\bar{H}}{dx}\right)_{x=0} \approx \ln\left[(z+h)^2+K^2+b^2\right] + \frac{2bK}{(z+h)^2+K^2+b^2}$$

$$+ \ln\left[z^2+K^2+b^2\right] - \frac{2bK}{z^2+K^2+b^2}$$

$$- \ln\left[(z+h)^2+K^2+b^2\right] + \frac{2bK}{(z+h)^2+K^2+b^2}$$

$$- \ln\left[z^2+K^2+b^2\right] - \frac{2bK}{z^2+K^2+b^2}$$

$$\approx 4bK\left[\frac{1}{(z+h)^2+K^2} - \frac{1}{z^2+K^2}\right] \qquad (z \gg b)$$

Thus

$$\left(\frac{d\bar{H}}{dx}\right)_{x=0} = \frac{Mb}{\pi}\left[\frac{1}{(z+h)^2+K^2} - \frac{1}{z^2+K^2}\right]$$

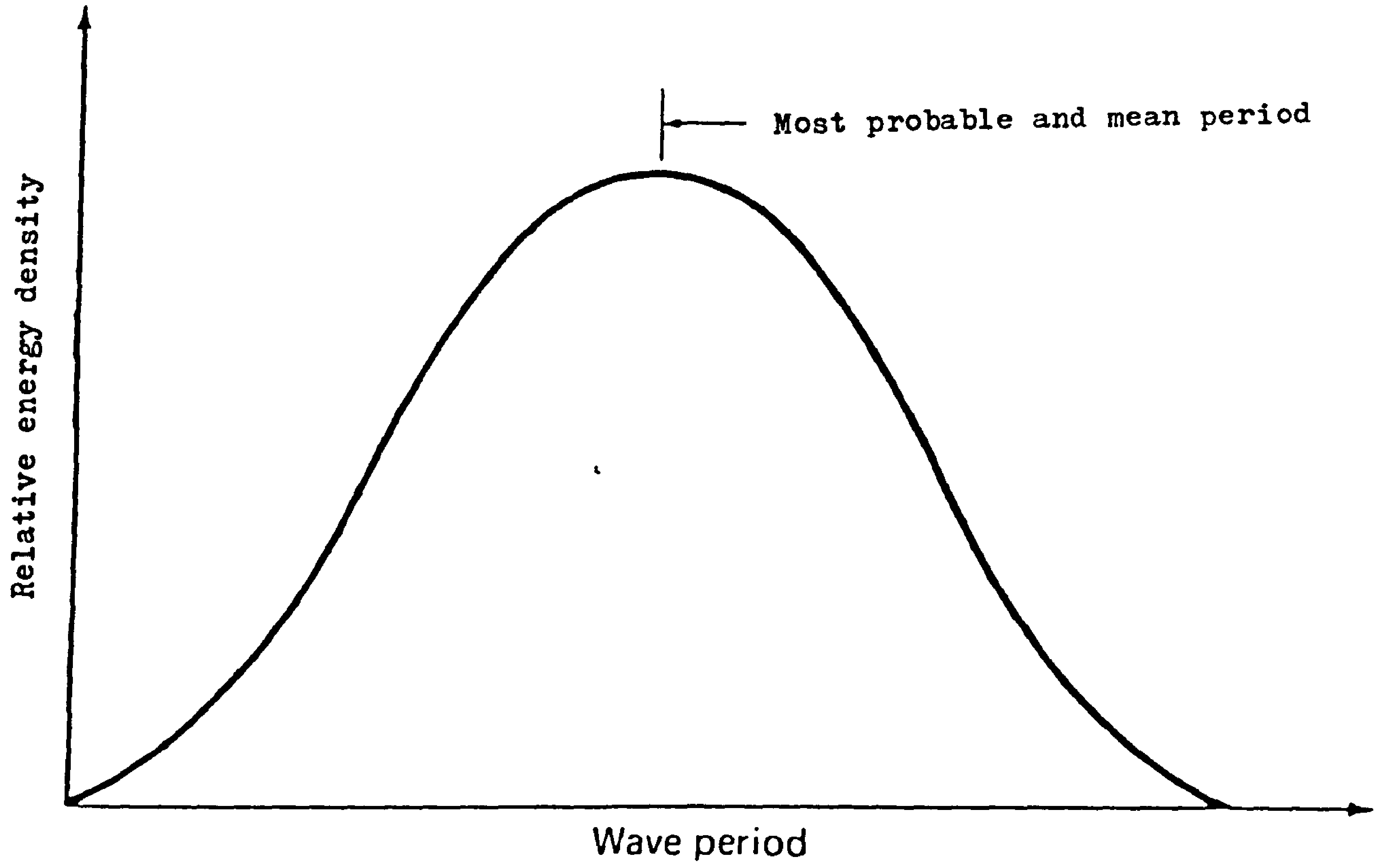

Figure 1. Wave period spectrum of the sea state.

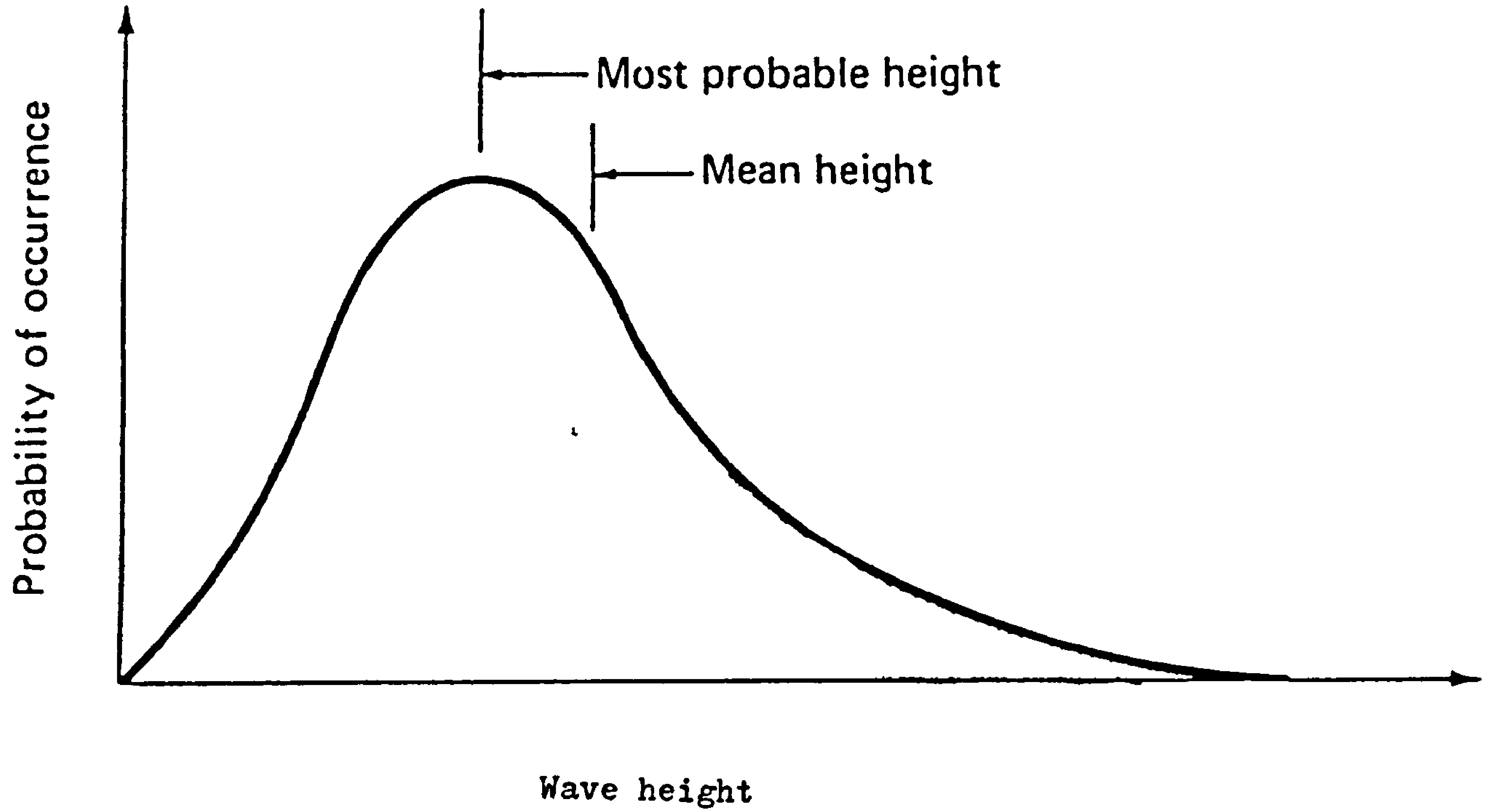

Figure 2. Wave height probability distribution of the sea state.

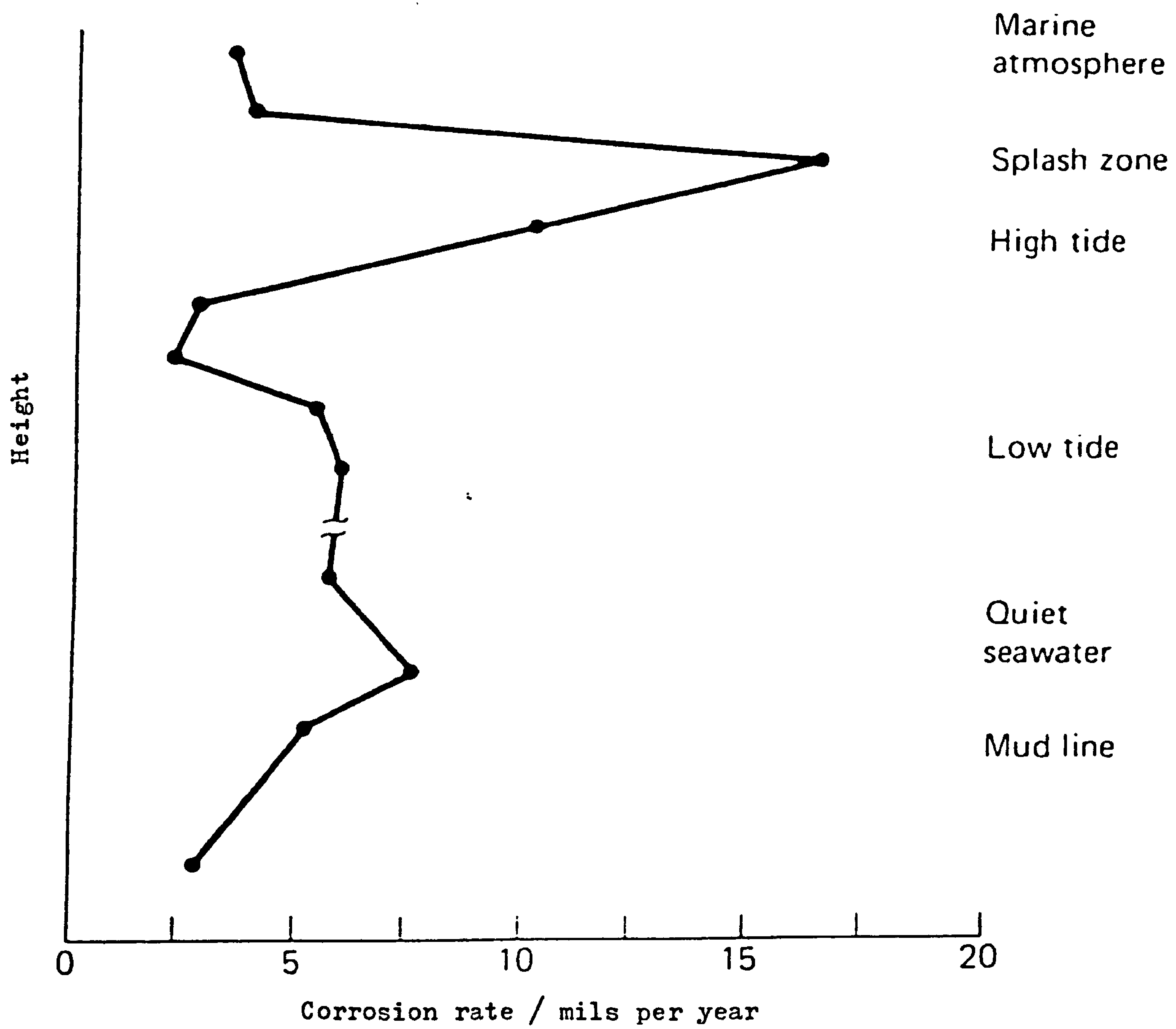

Figure 3 . Generalised vertical profile of corrosion of steel in seawater.

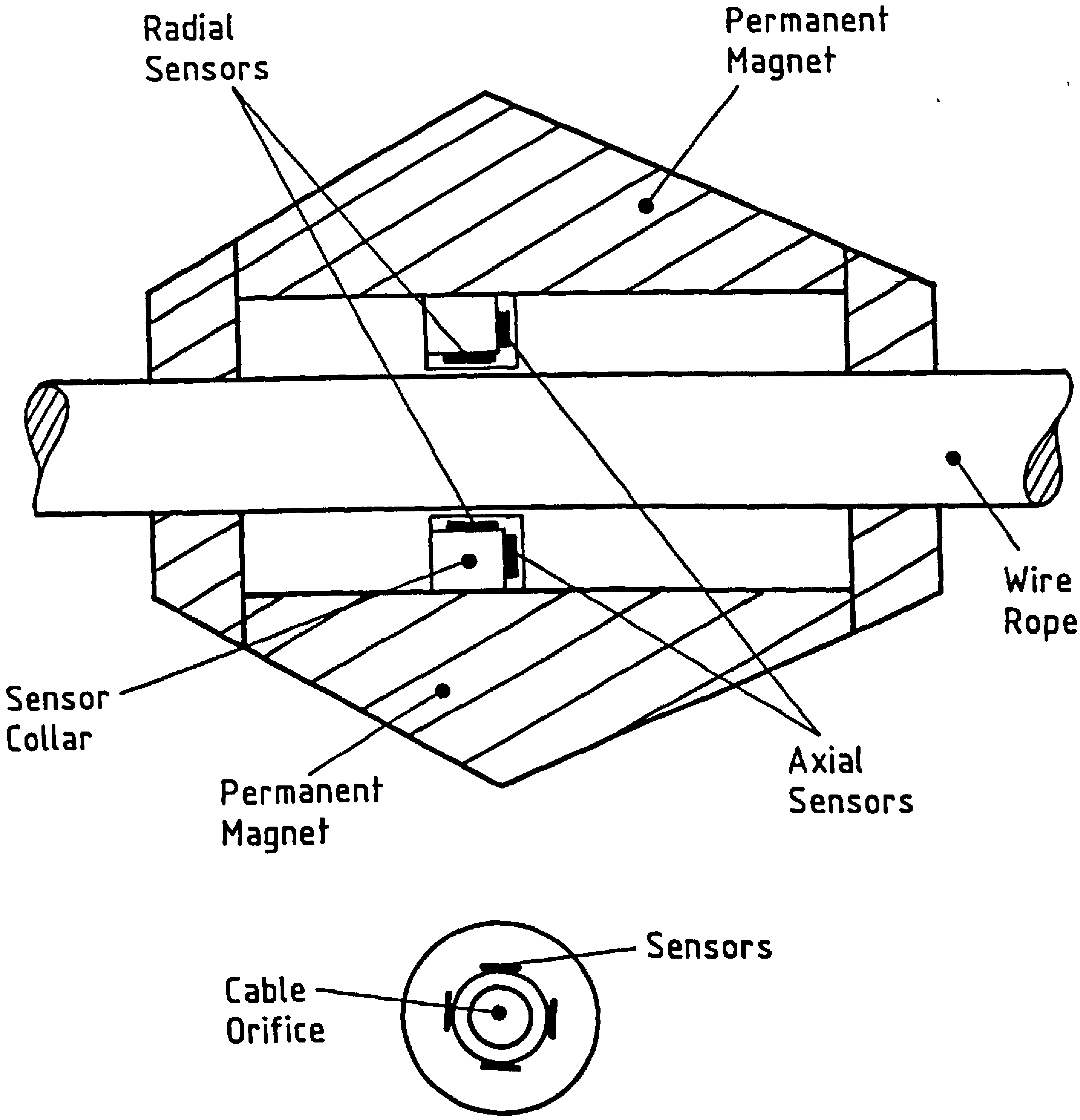

Sensor Collar

Figure 4. The use of Hall effect probes in the non destructive testing of wire ropes.

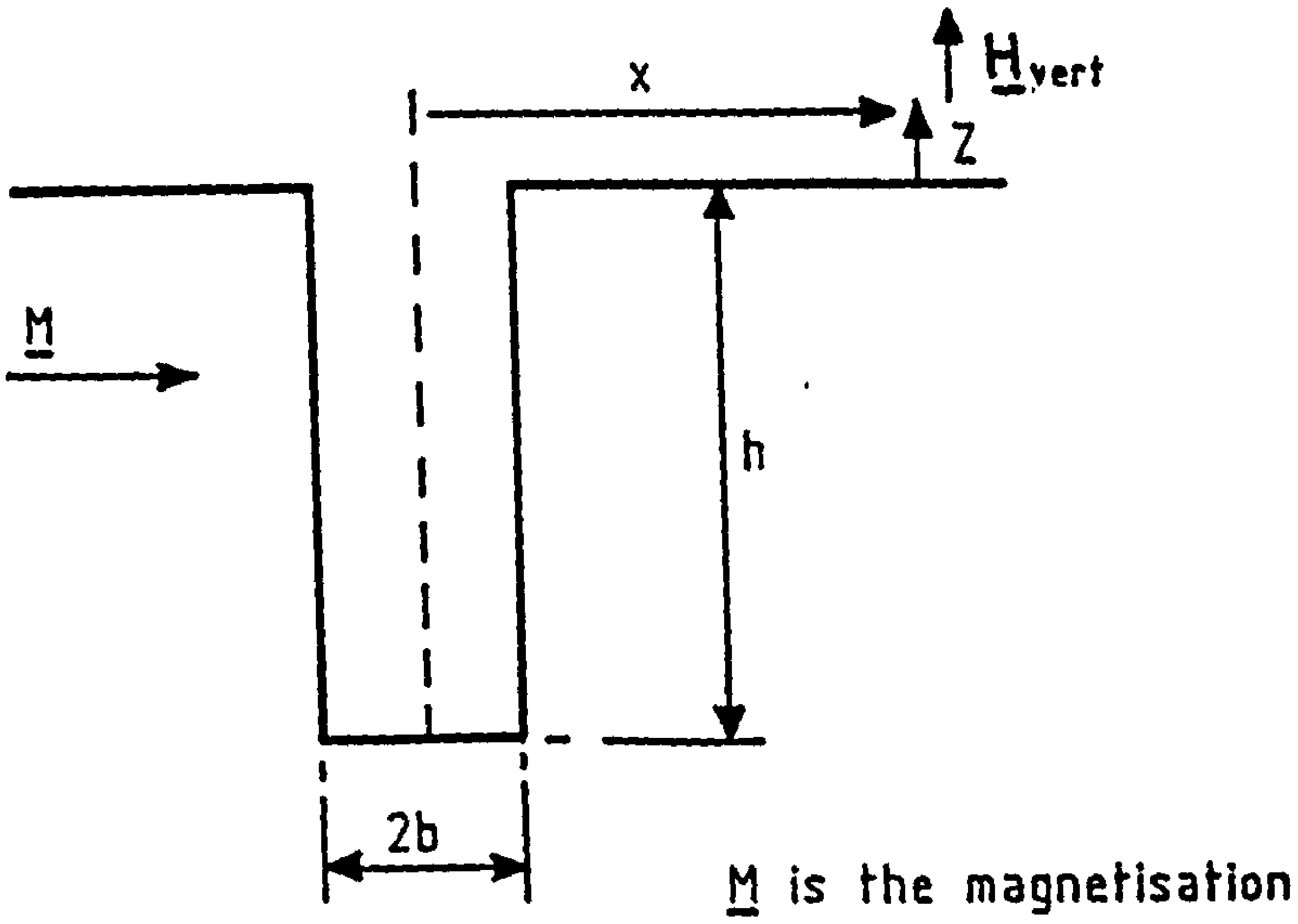

Figure 5. Standard crack notation.

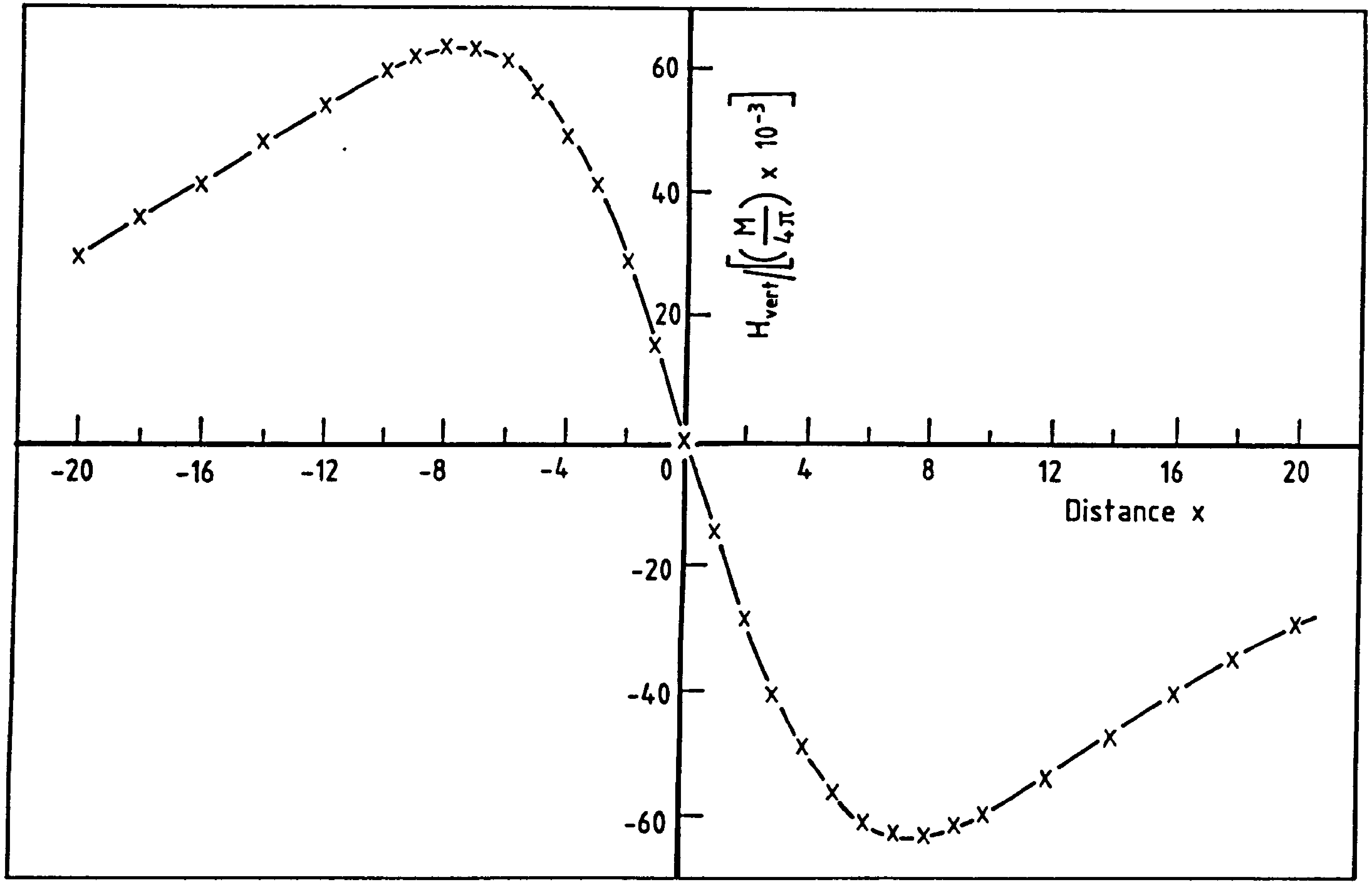

FIGURE 6. THEORETICAL VERTICAL COMPONENT OF FIELD OVER A CRACK FOR WHICH 2b = 1, h = 10, Z = 10, (arbitrary units)

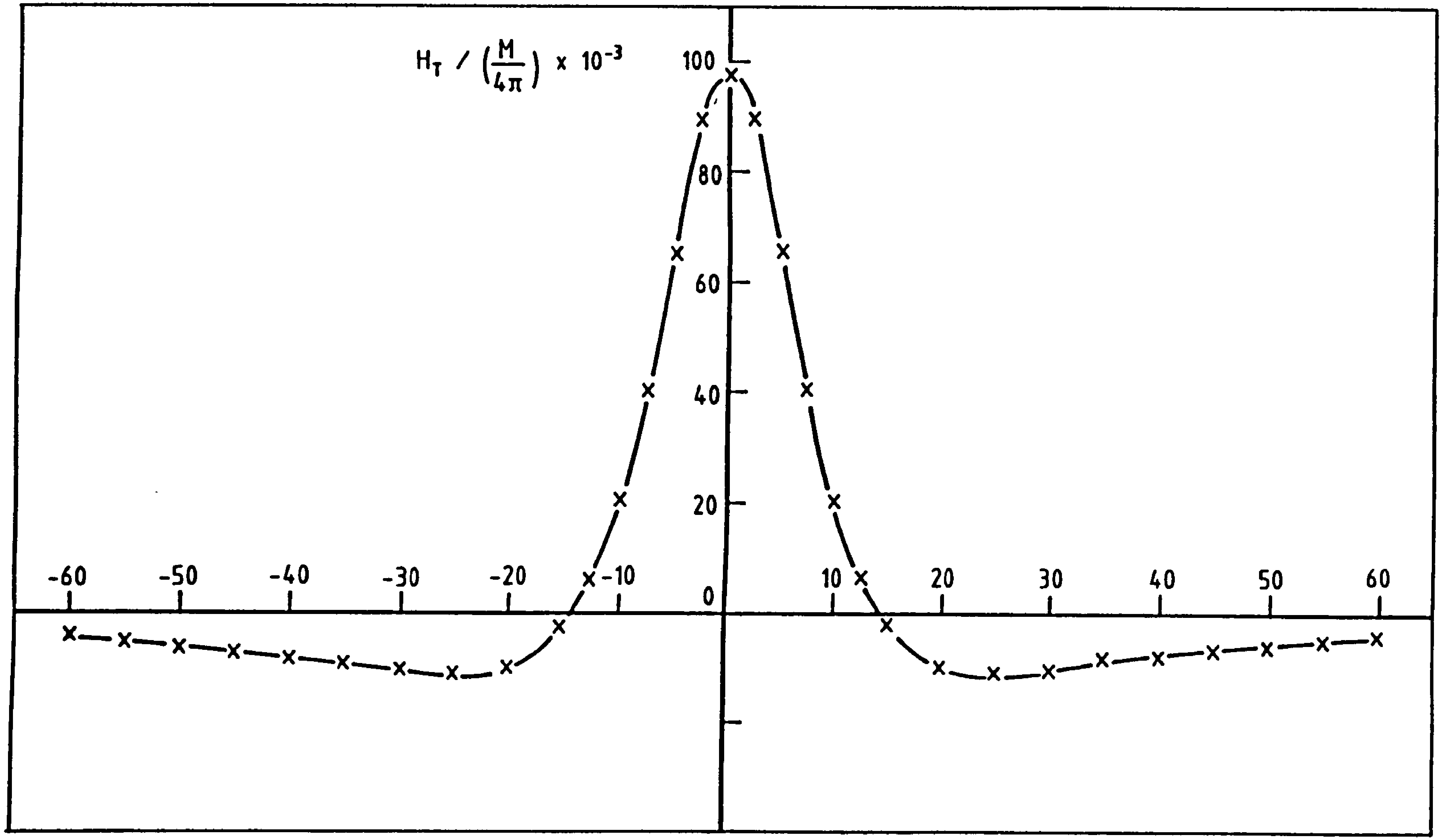

FIGURE 7. THEORETICAL TANGENTIAL COMPONENT OF FIELD OVER A CRACK FOR WHICH 2b = 1, h = 10, z = 10. (ARBITRARY UNITS)

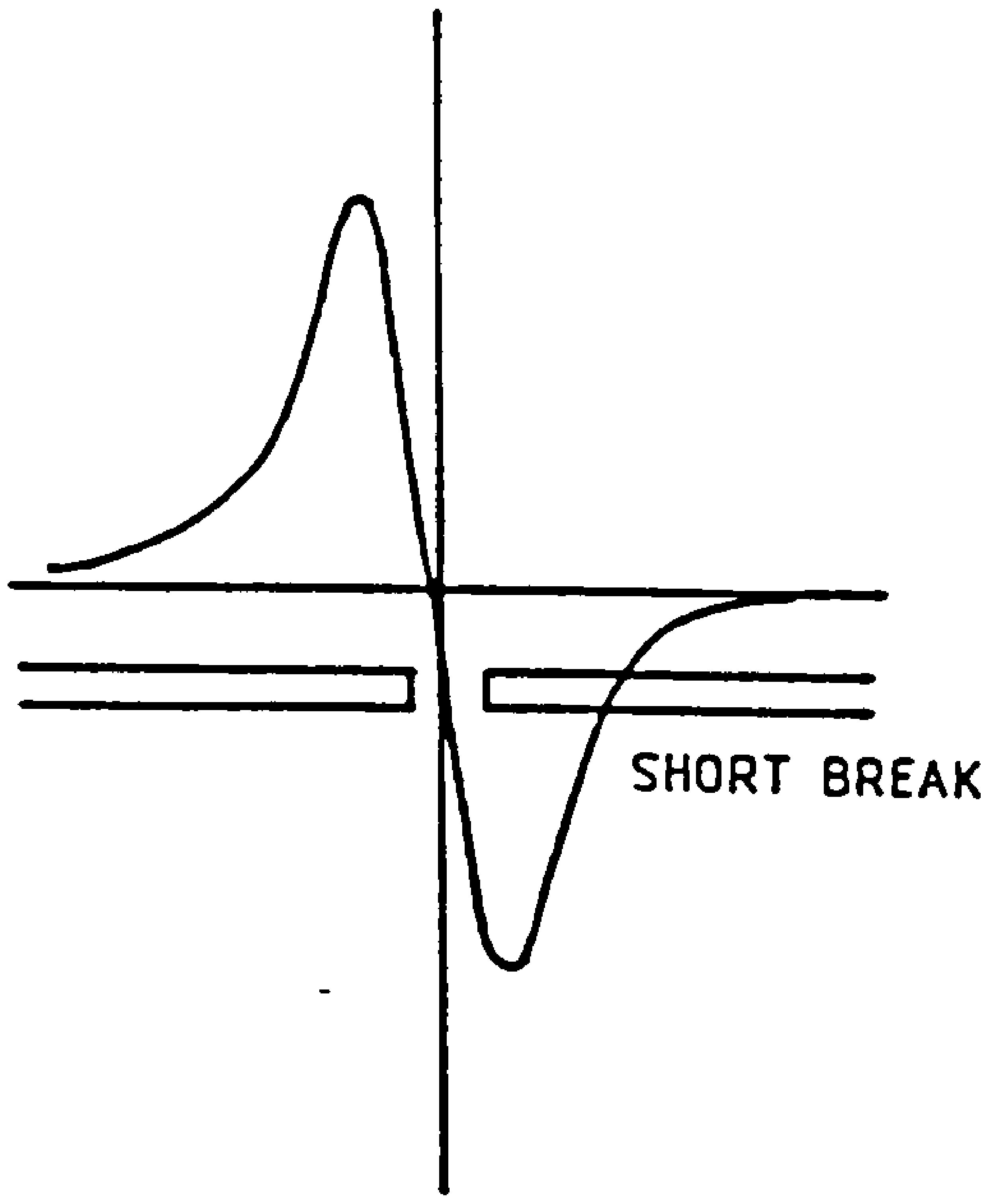

Figure 8. Transient signal from a broken wire, detected by the radial (vertical component) sensors.

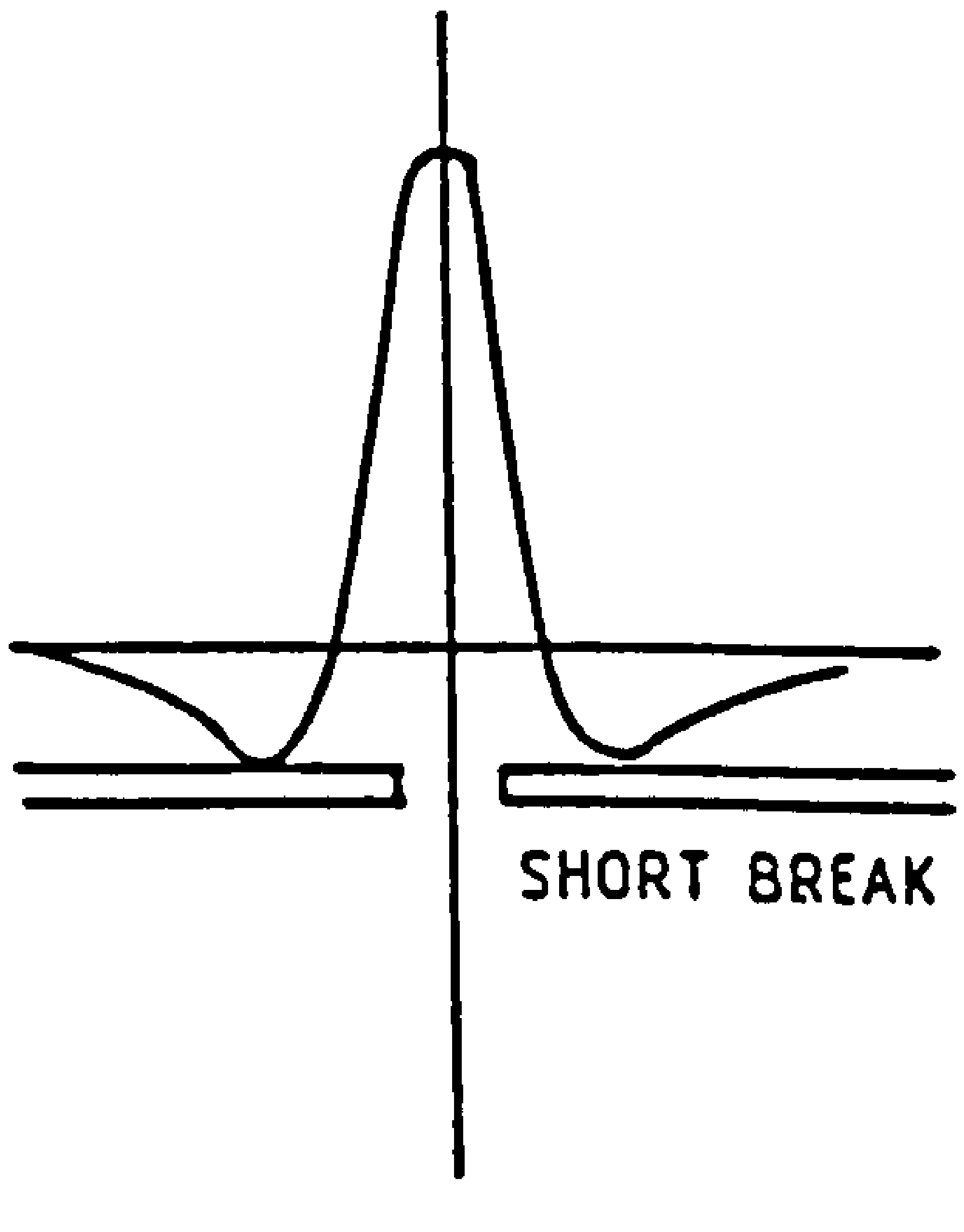

Figure 9. Transient signal from a broken wire, detected by the longitudinal (tangential) magnetic sensors.

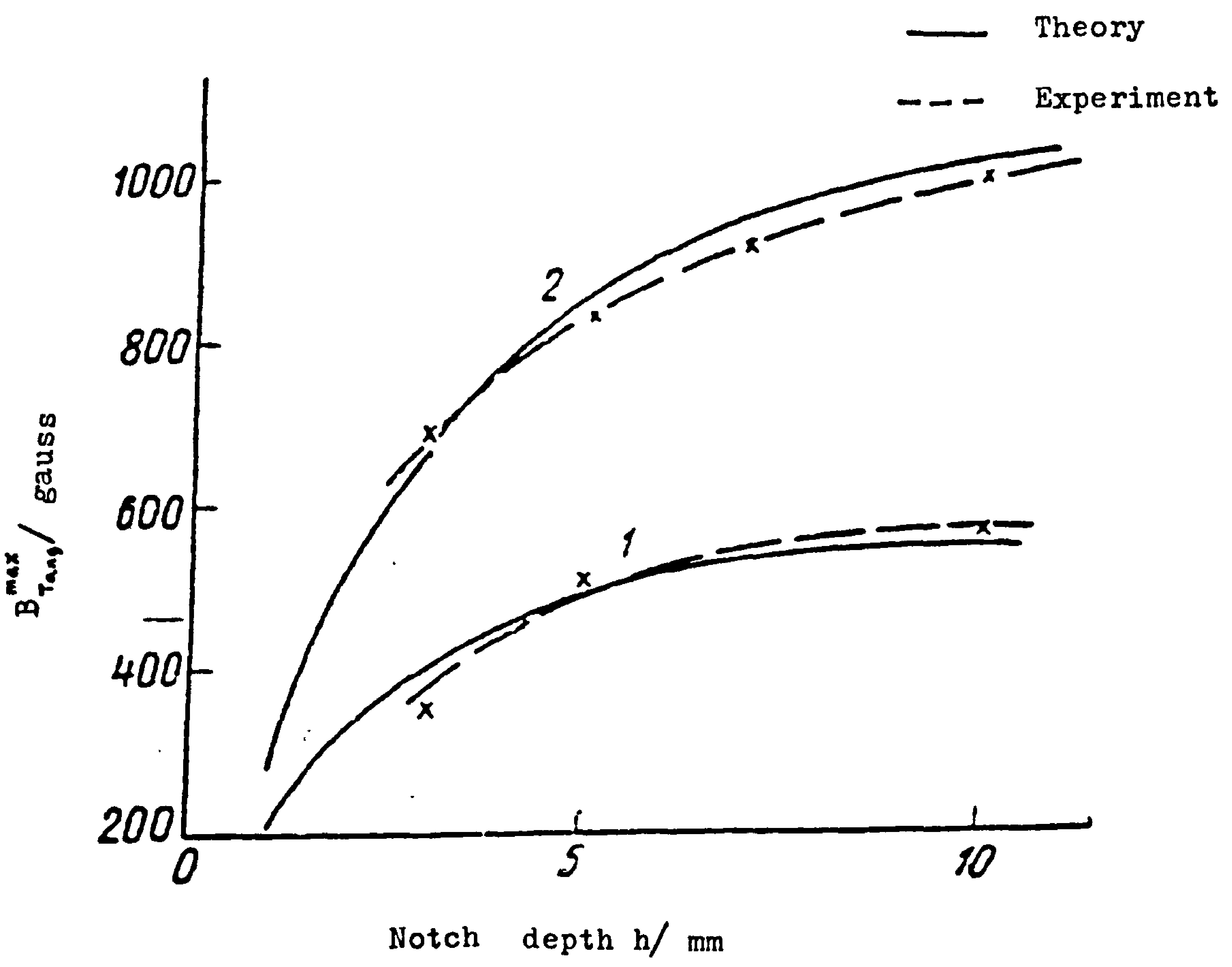

Figure 10. Tangential field maximum as a function of notch depth. (Scan height=0.9mm).1) Notch width 2b=0.108mm 2) 2b=0.216mm

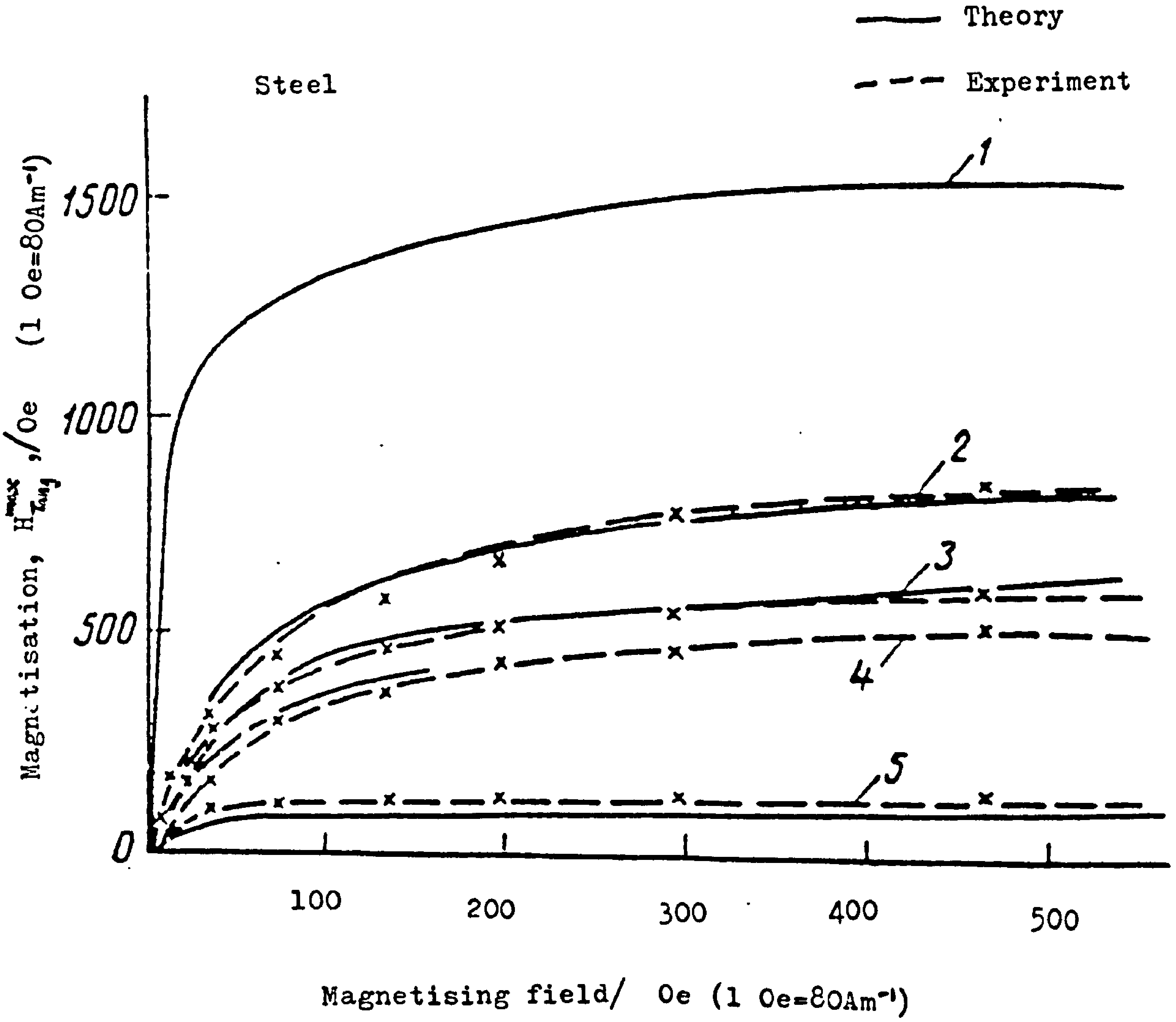

Figure 11. Dependence of magnetisation (curve 1) and tangential maximum field value on the magnetising field. 2) Notch width 2b=0.216mm, notch depth h=5mm. 3) 2b=0.108mm, h=7mm. 4) 2b=0.162mm, h=3mm. 5) 2b=0.036mm, h=3mm.

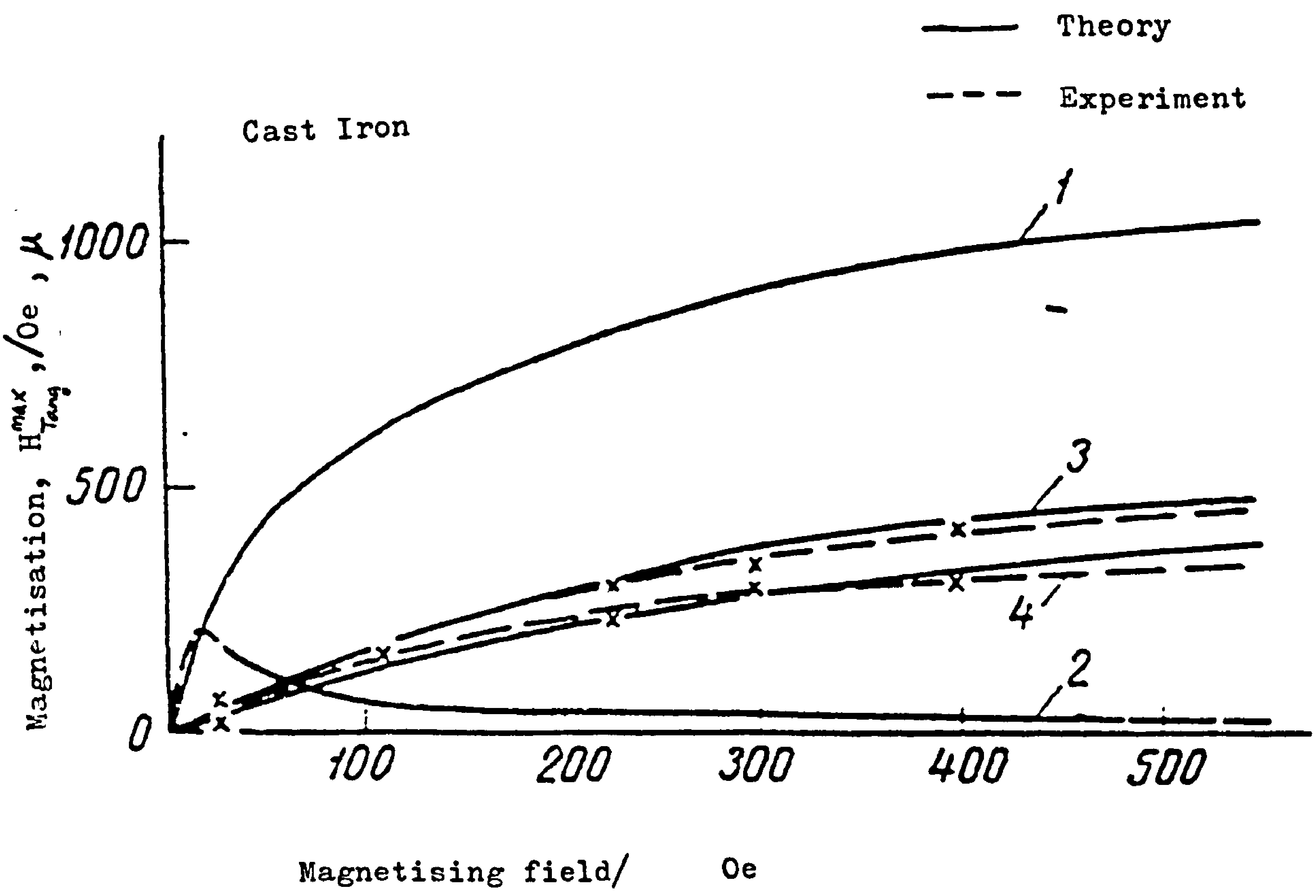

Figure 12. Dependence of magnetisation (curve 1) and tangential maximum field value on the magnetising field. 2) Permeability μ. 3) Notch width 2b=0.230mm, notch depth h=5mm. 4) 2b=0.230mm, h=3mm.

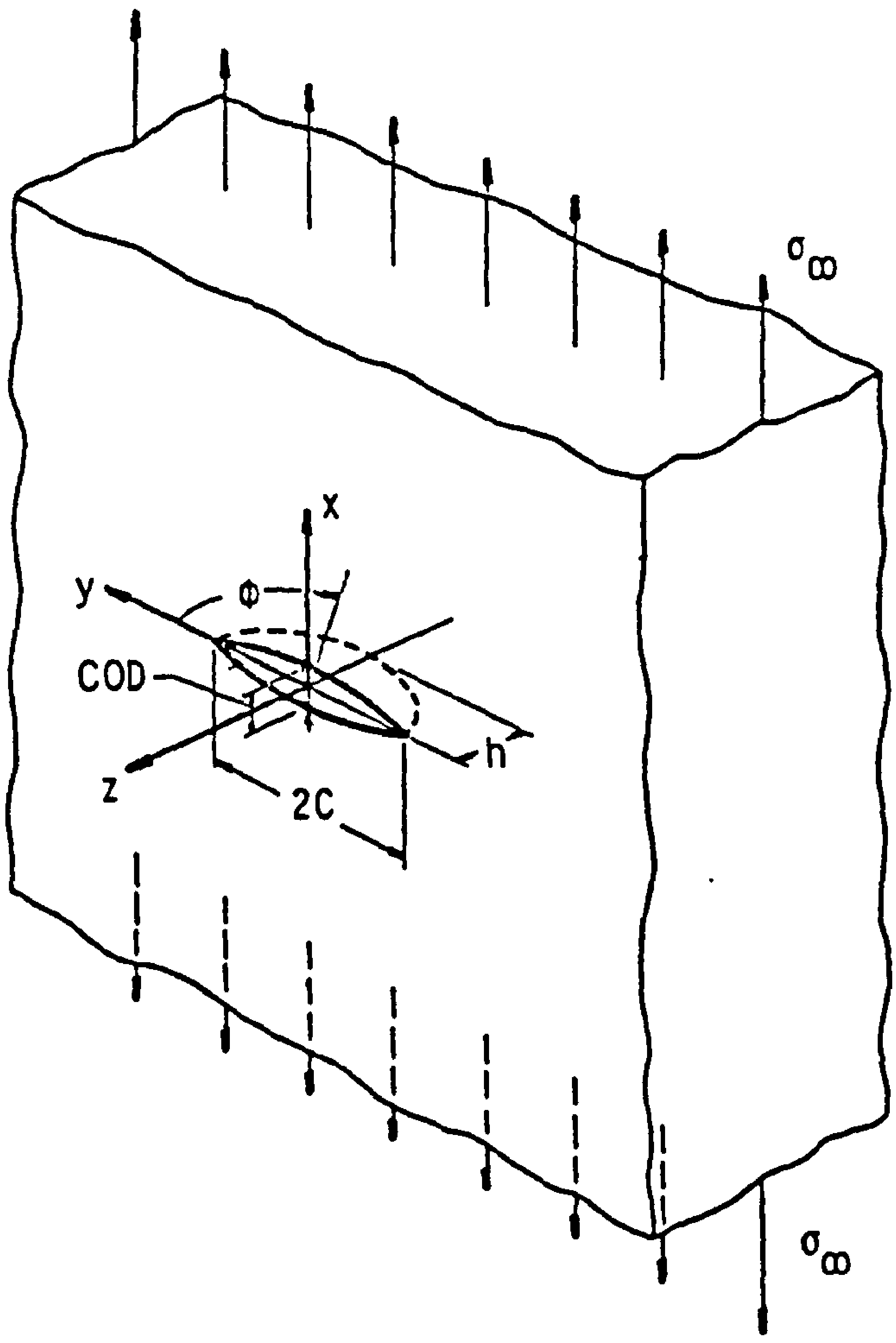

Figure 13. A semi-elliptical surface crack.

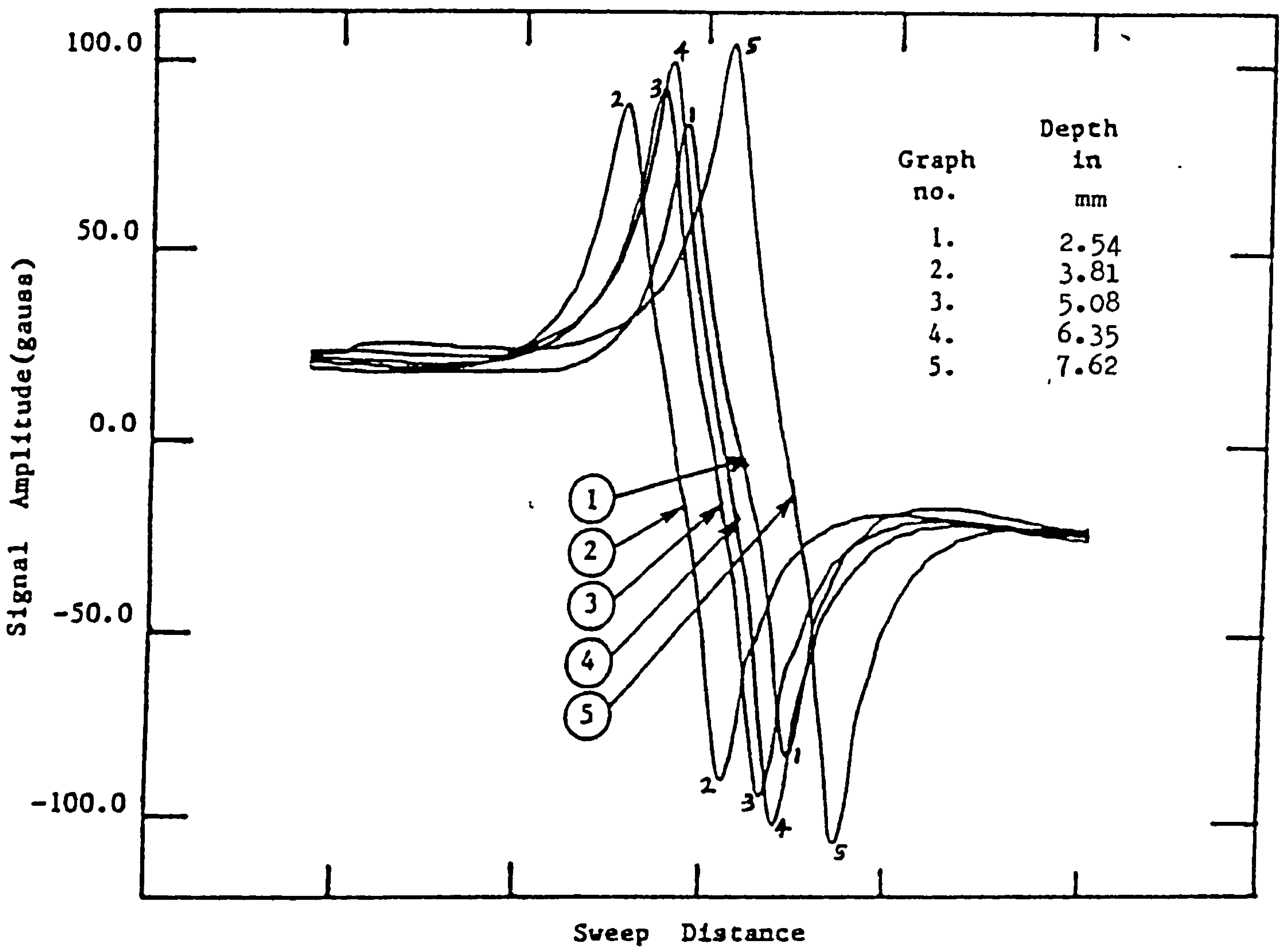

Figure 14. Variation of vertical component signal with notch depth.

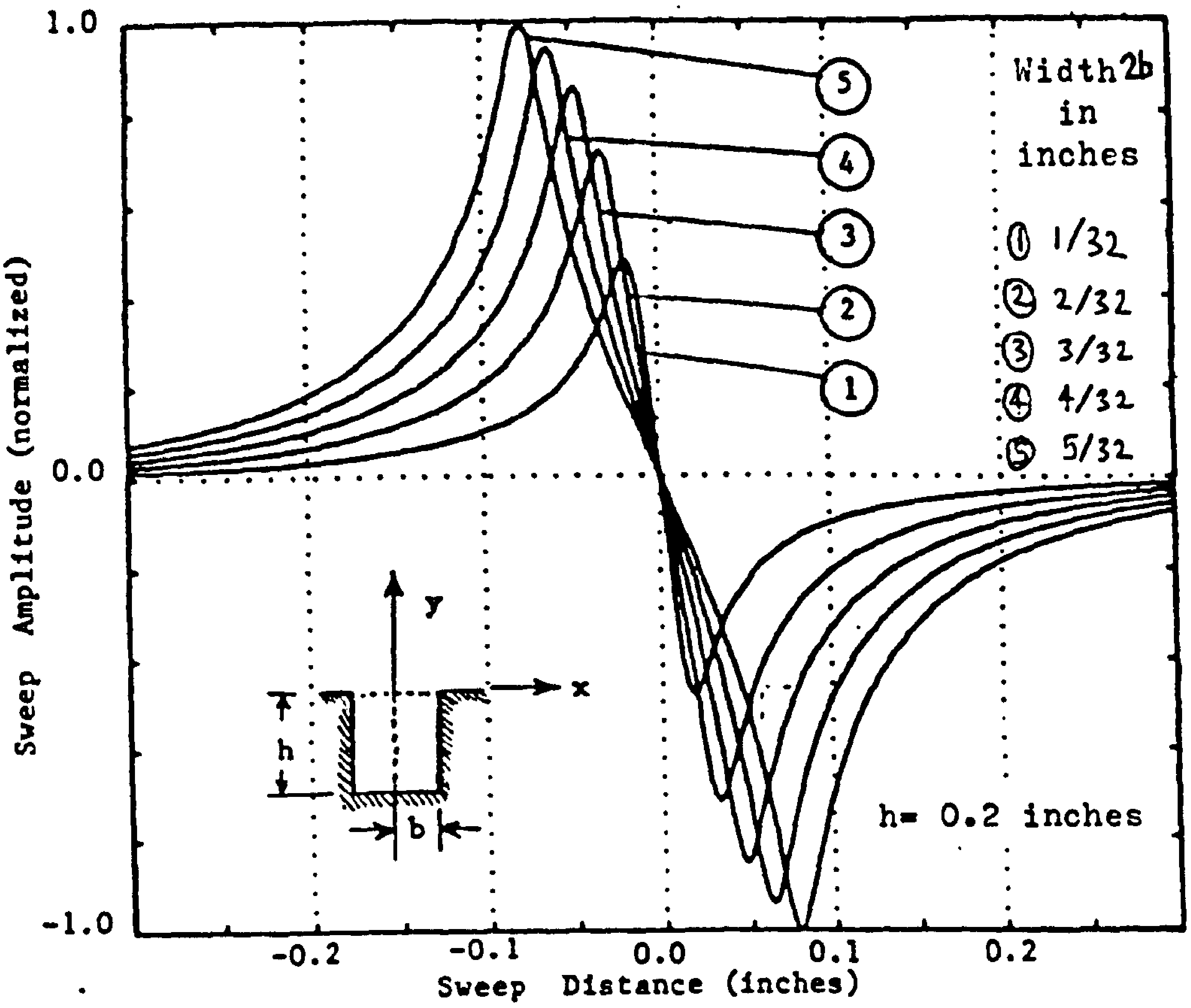

Figure 15. Plots of Eqn.(1) with varying width 2b,

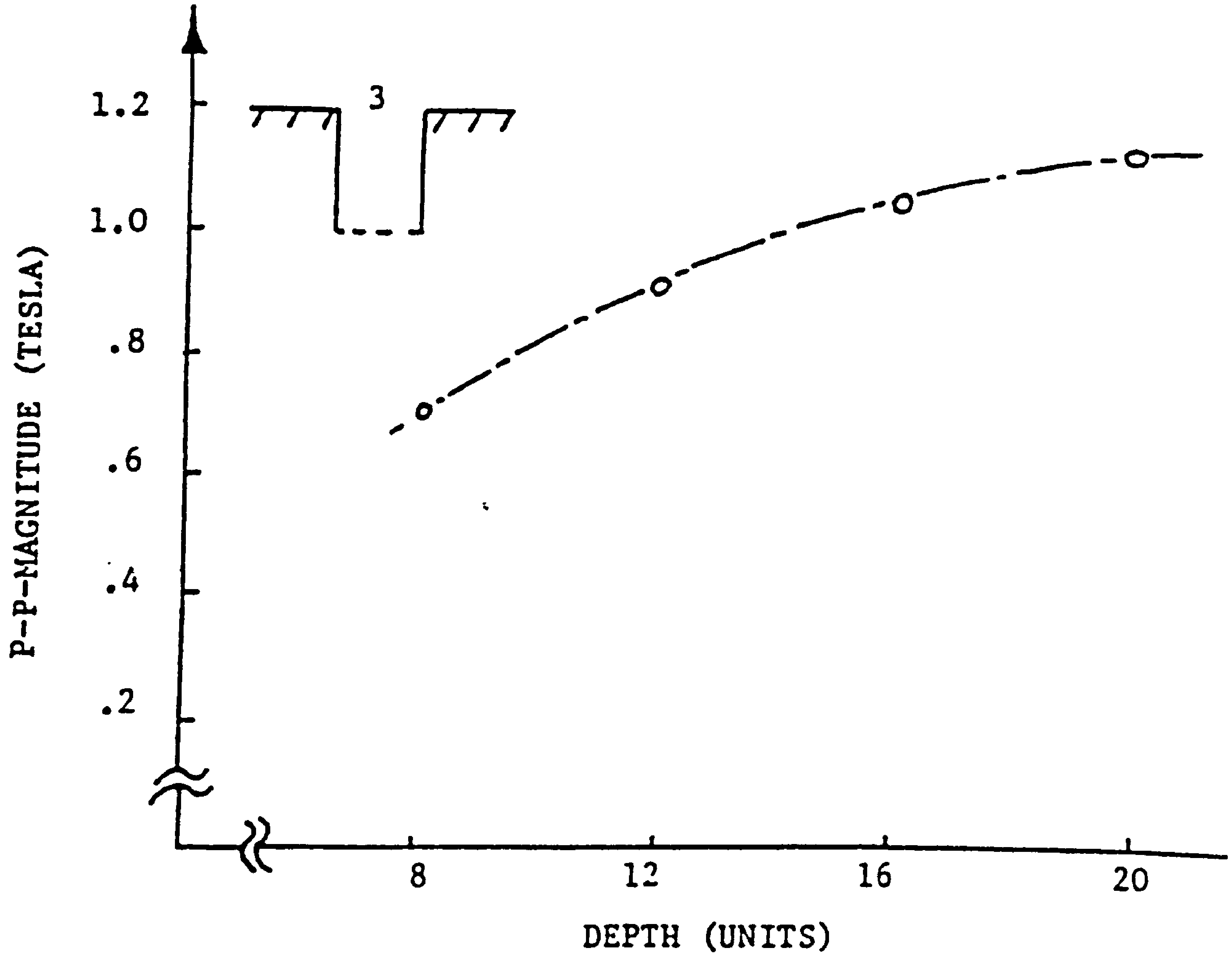

Figure 16. Defect signal magnitude as a function of defect depth (1 unit=0.127mm)

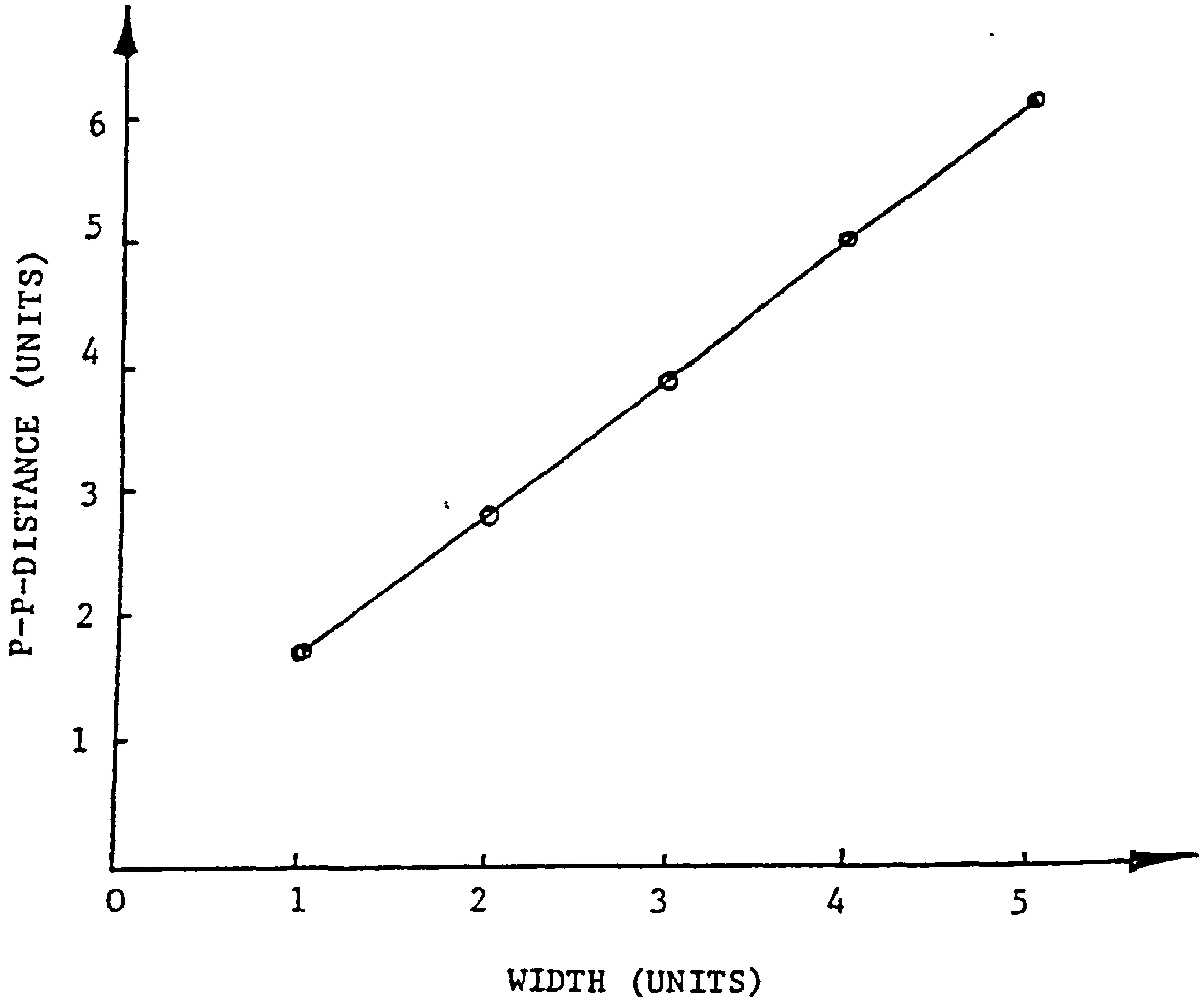

Figure 17. Spreading of vertical component signal as a function of defect width (1 unit=0.127mm)

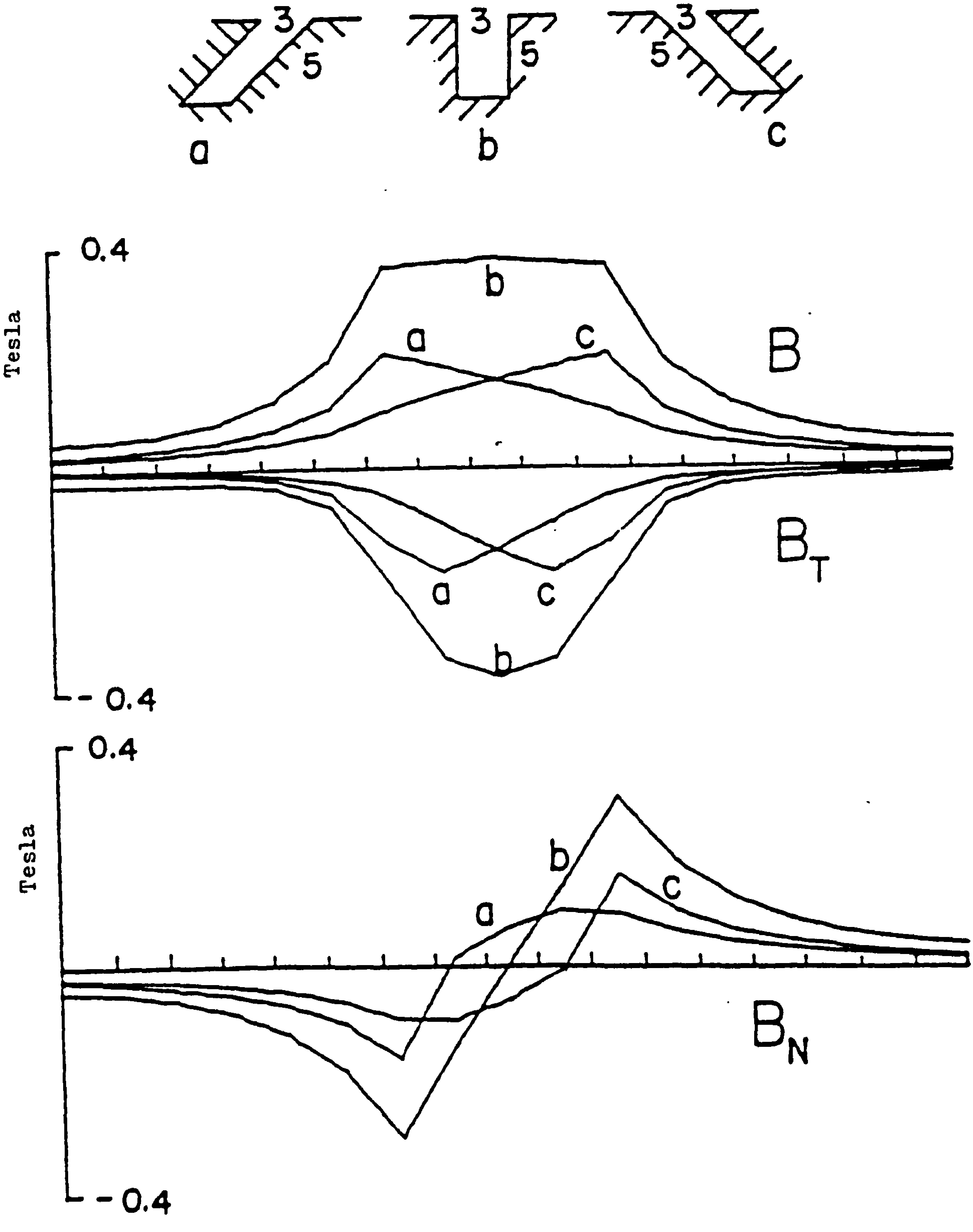

Figure 18. Effect of oblique defect on normal, tangential and total leakage fields.

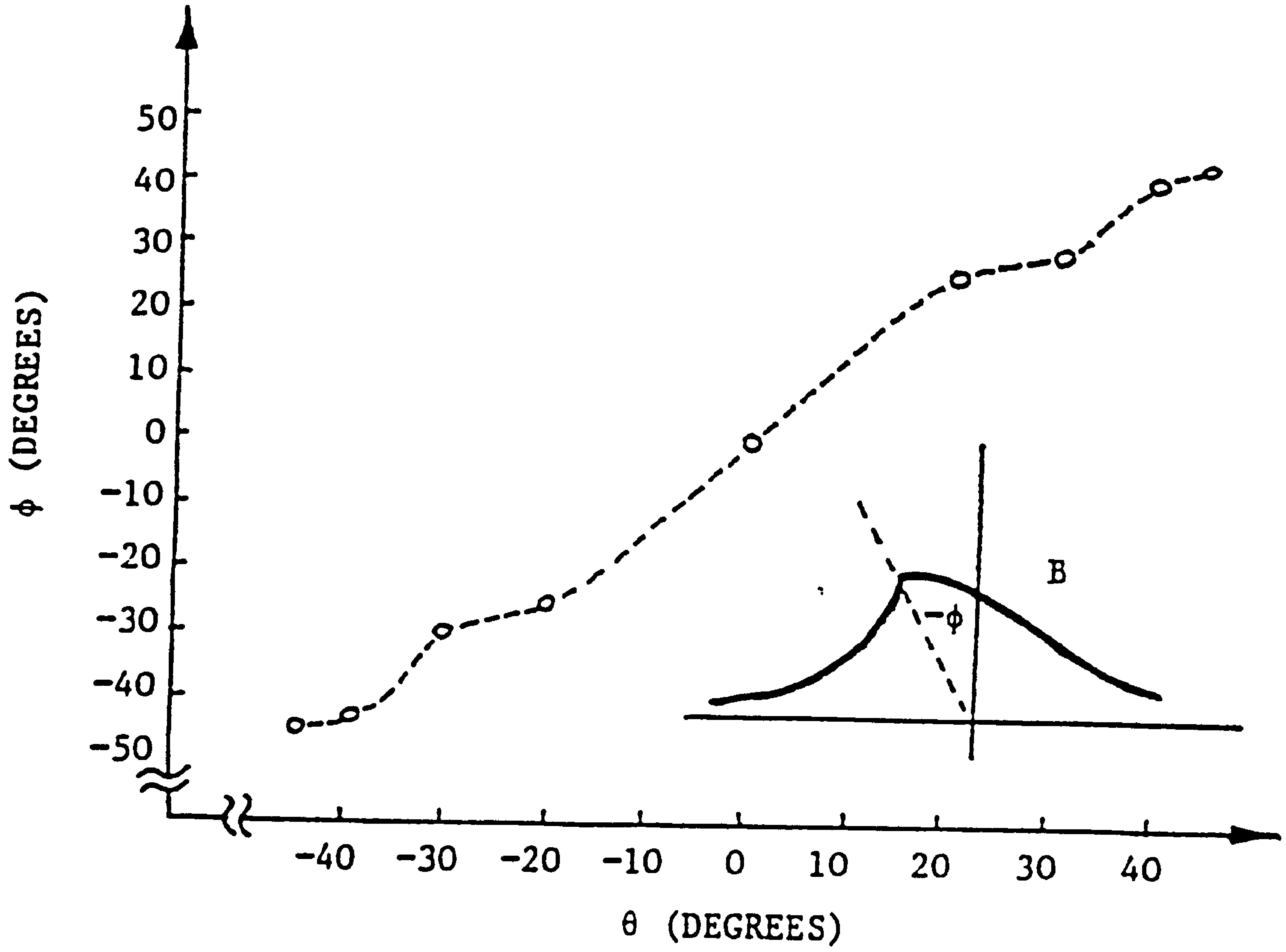

Figure 19. ϕ versus θ characteristic for an oblique surface defect.

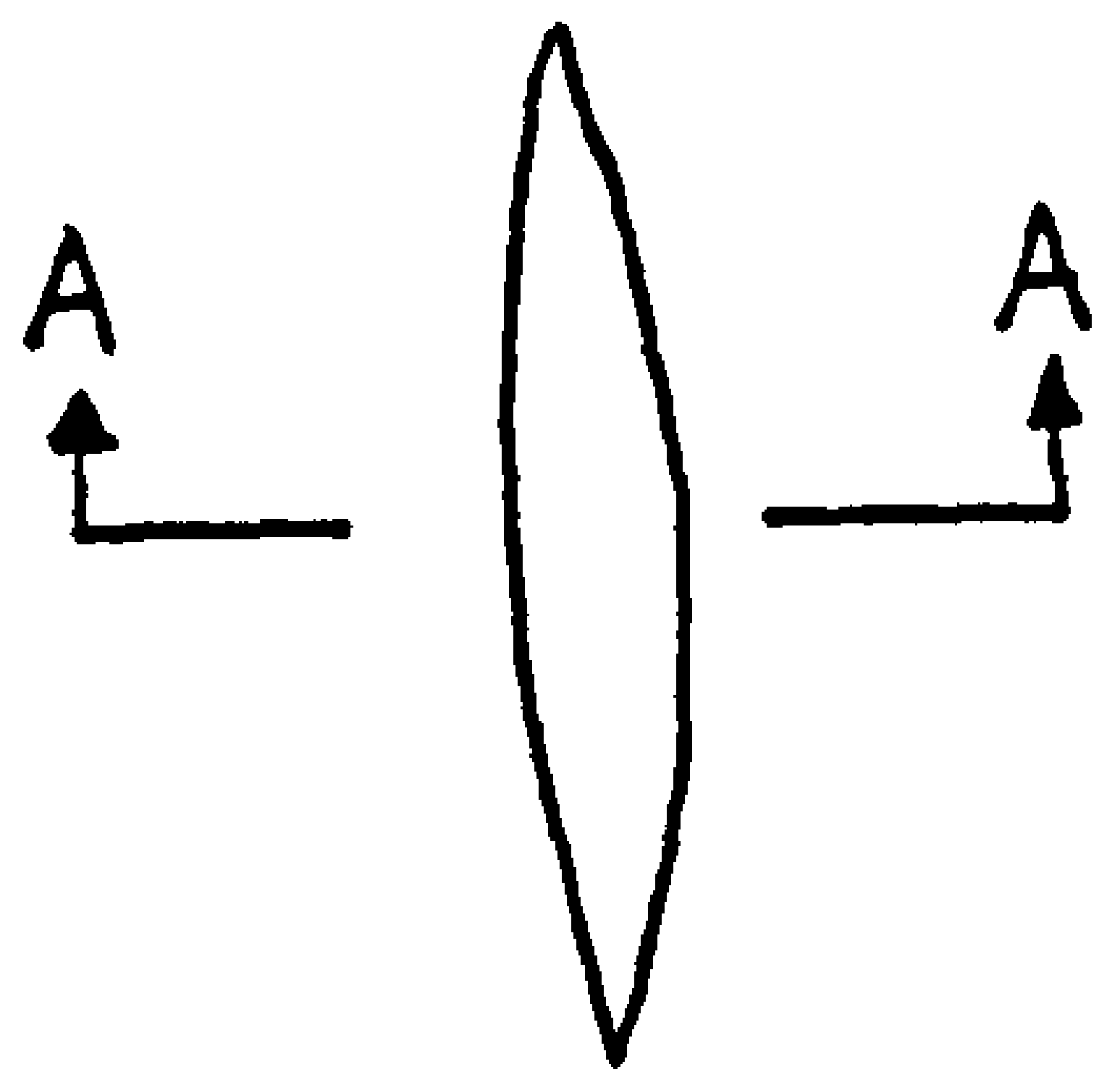

Top view

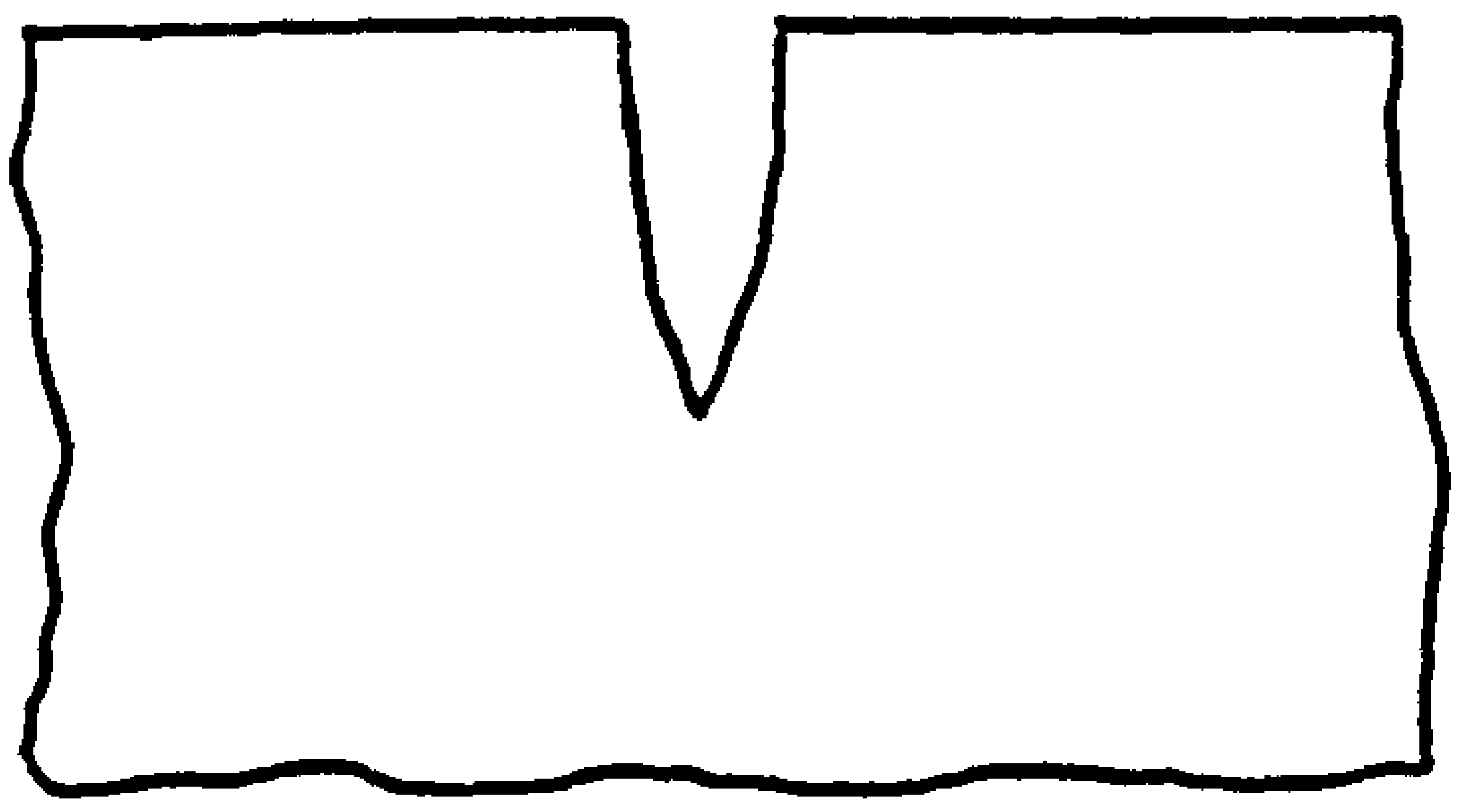

Section "A-A"
(Side view)

Figure 21. A half penny shaped crack

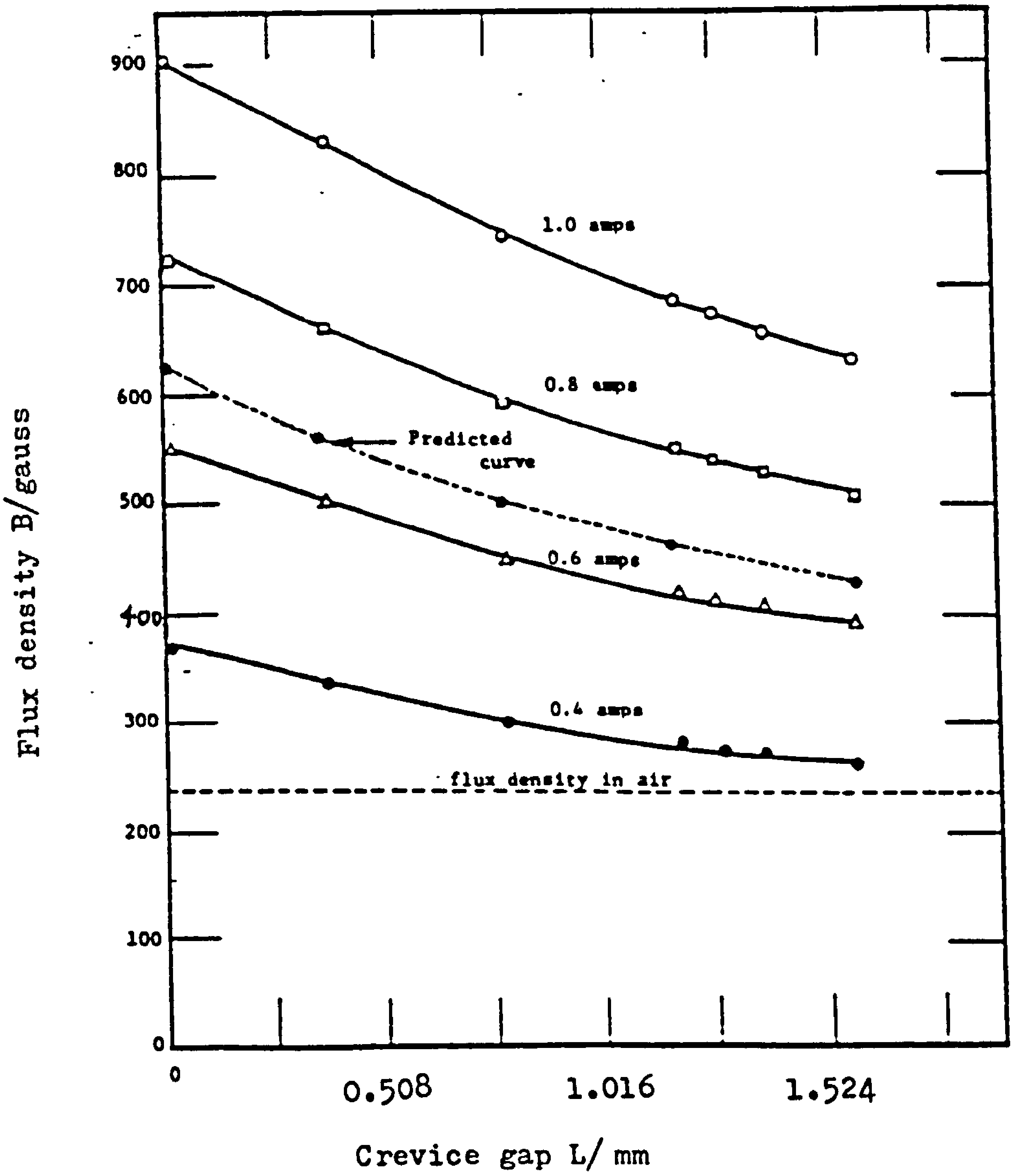

Figure 22. Peak flux density B as a function of crevice gap clearance L for four different probe currents.

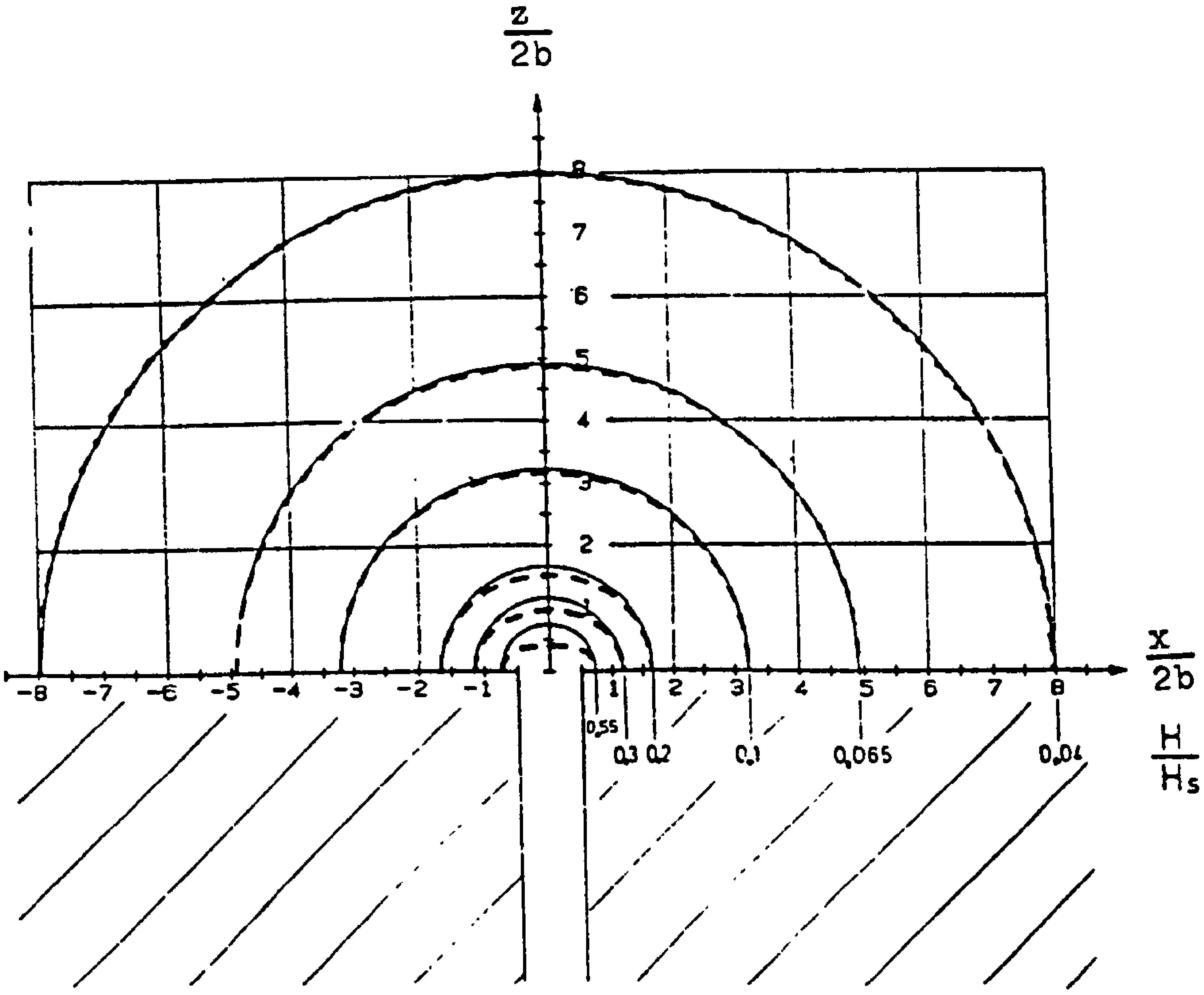

Figure 23. Transition of lines of constant field intensity (dashed lines) into circles (solid lines) with increasing distance from the crack mouth. H_s is the field deep in the slot; 2b is the crack width.

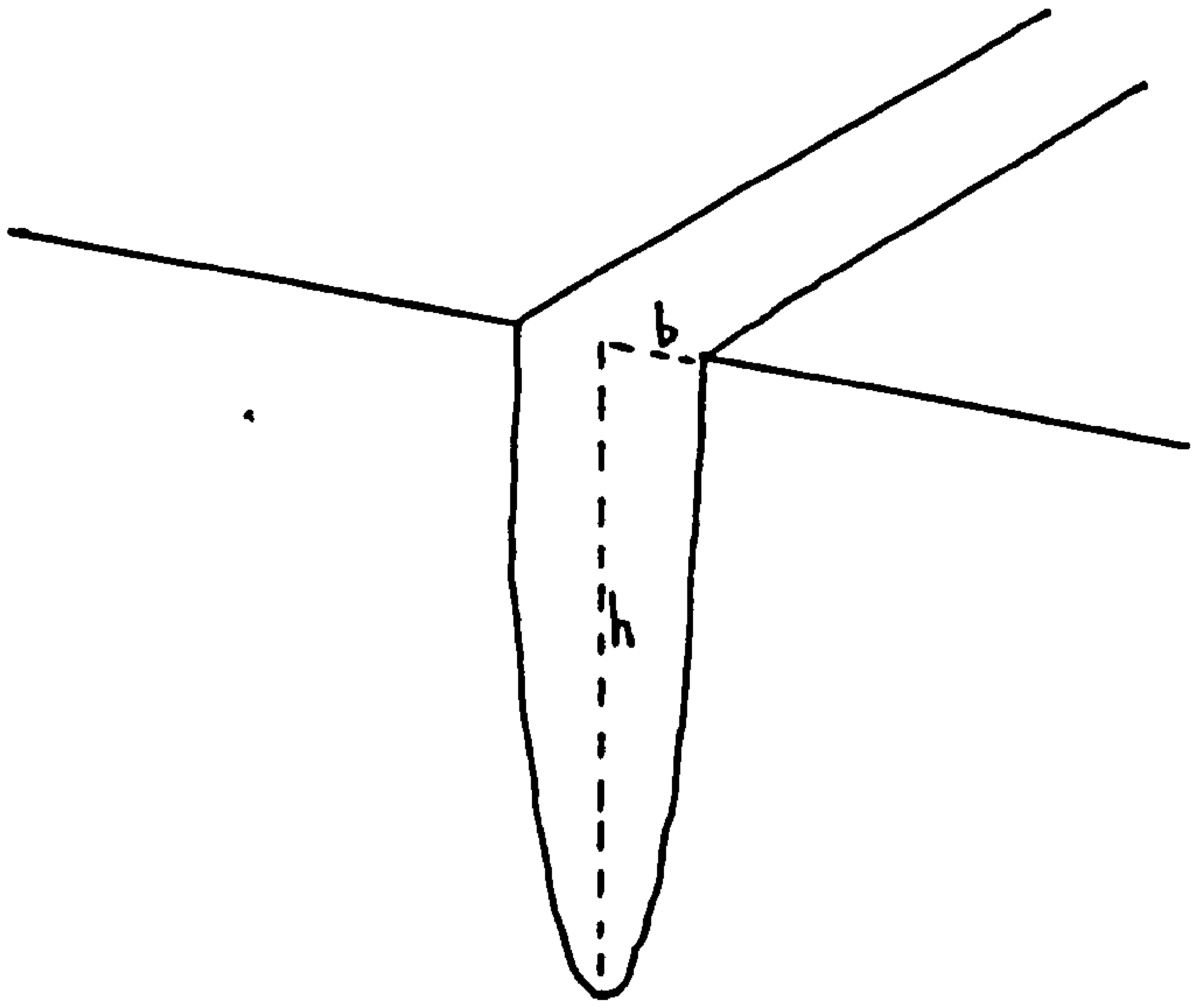

Figure 24. A semi-elliptic slot.

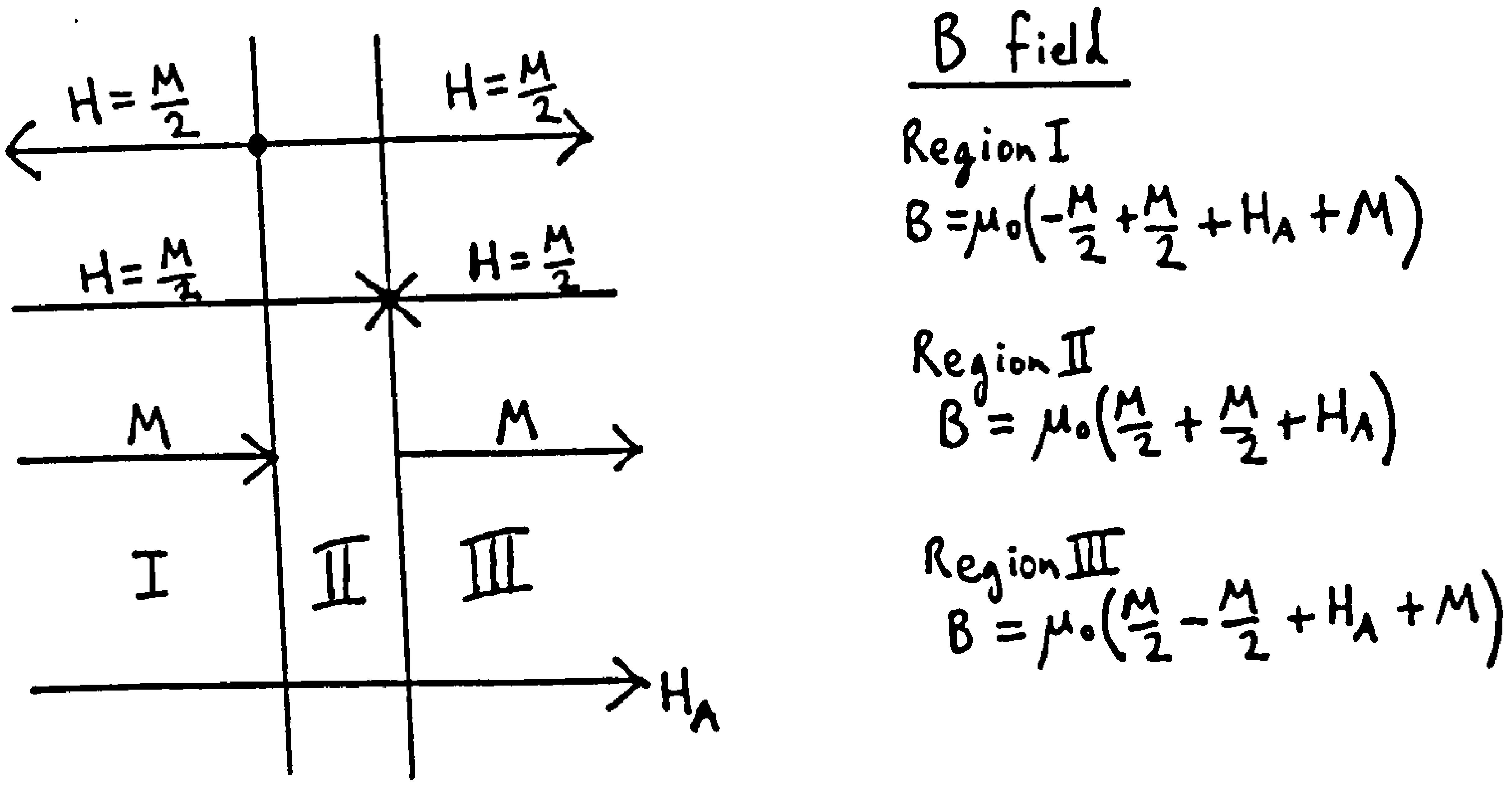

Figure 25. B, H and M fields present near a deep slot.

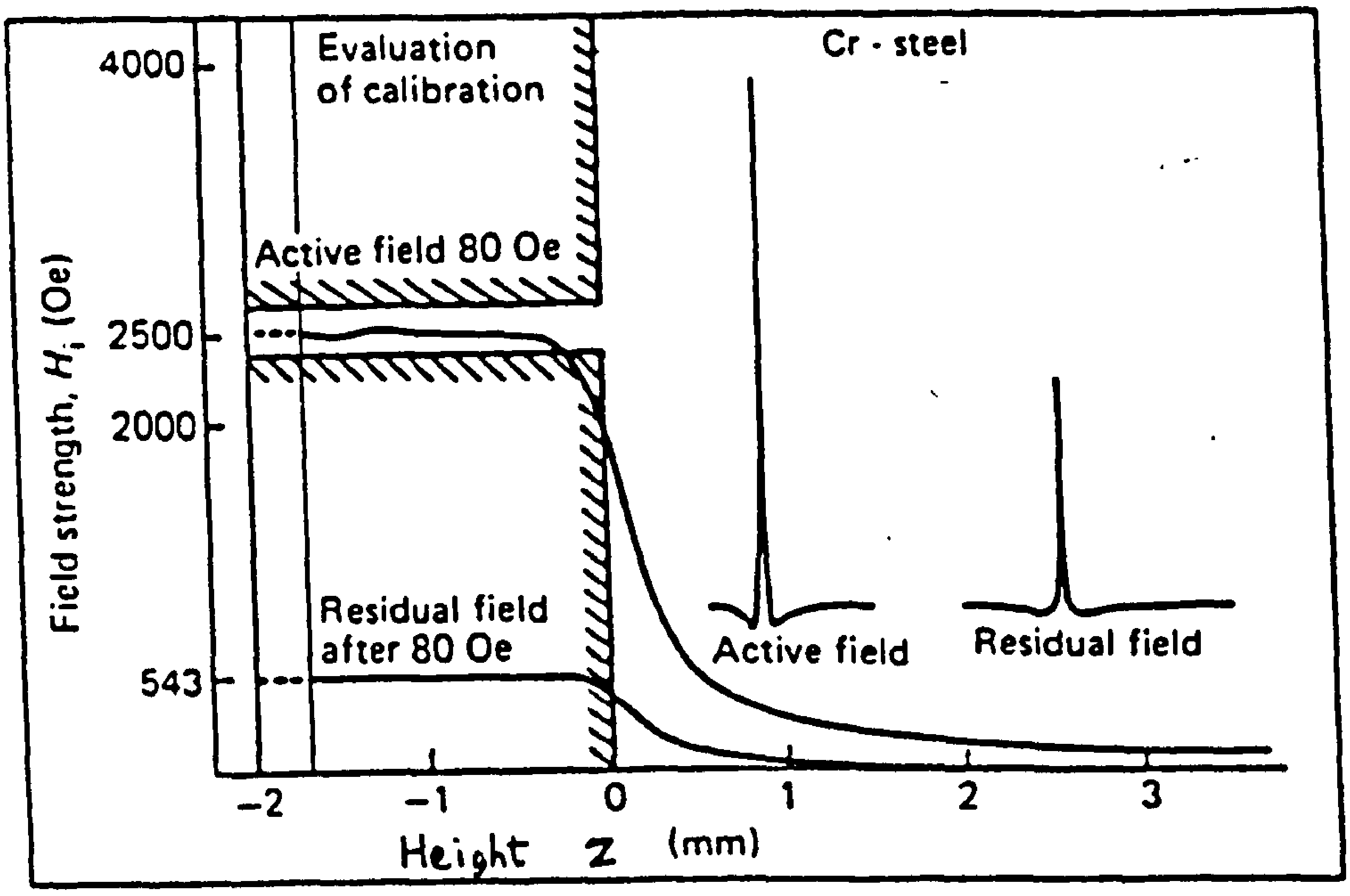

Figure 26. The tangential field in and above a genuine crack, 2mm deep and 0.3mm wide.

(1Oe = 80Am^{-1})

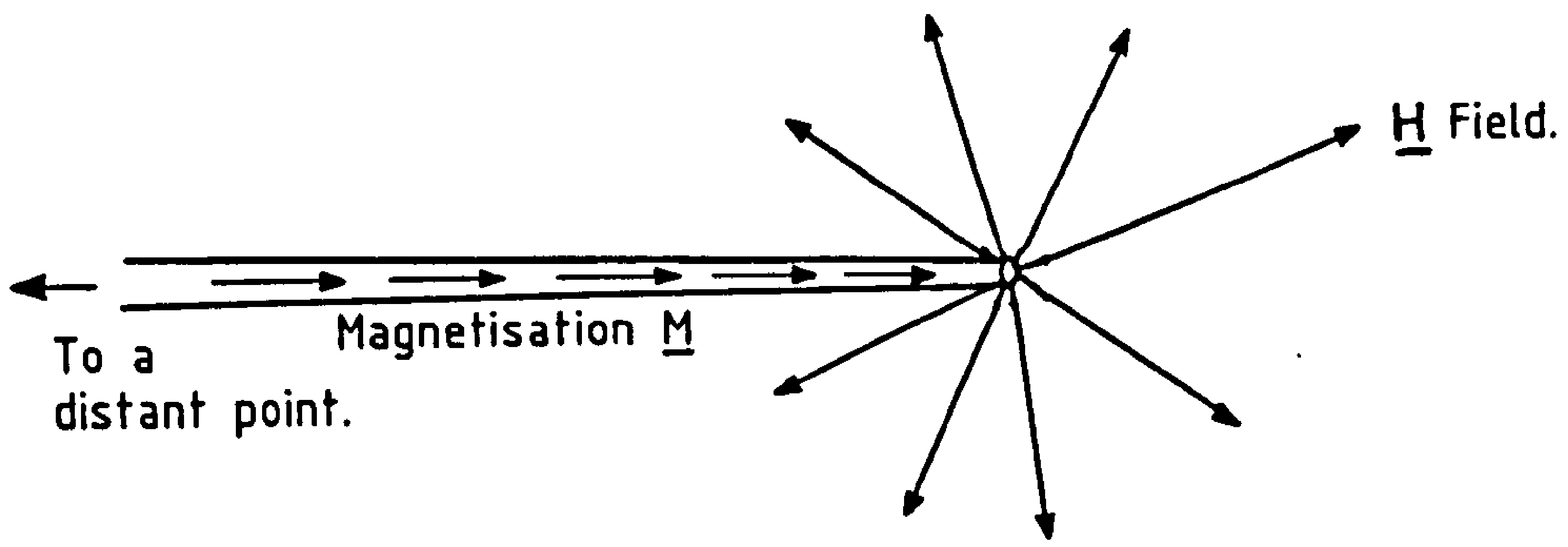

FIGURE 27. AN INFINITESIMAL SOURCE OF H FIELD.

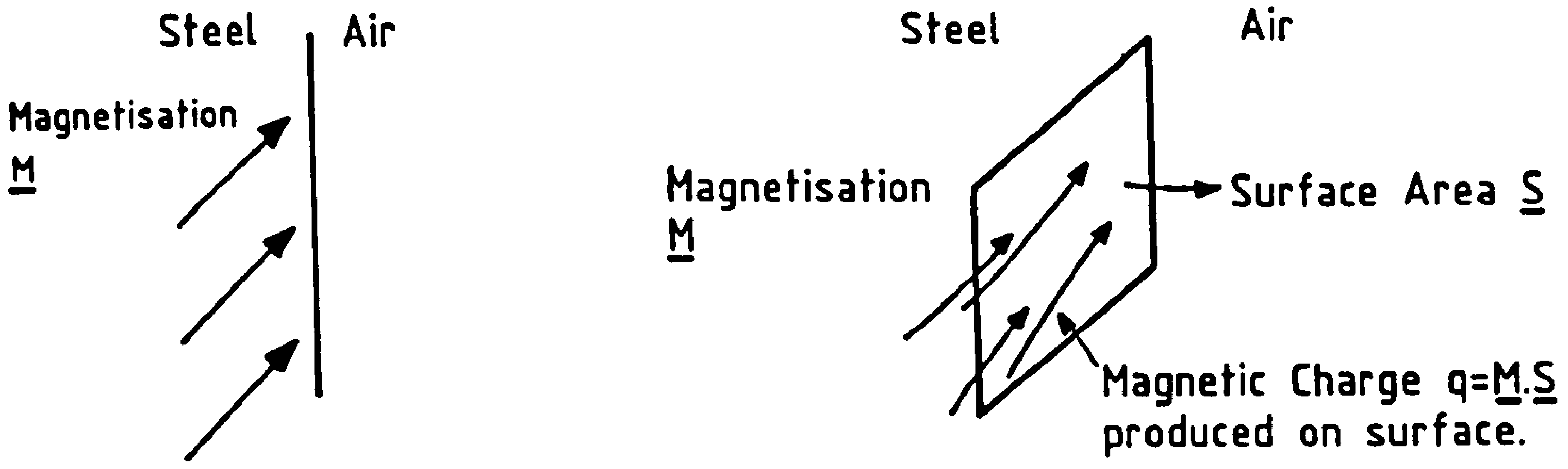

(a) Side View

(b) Angled View

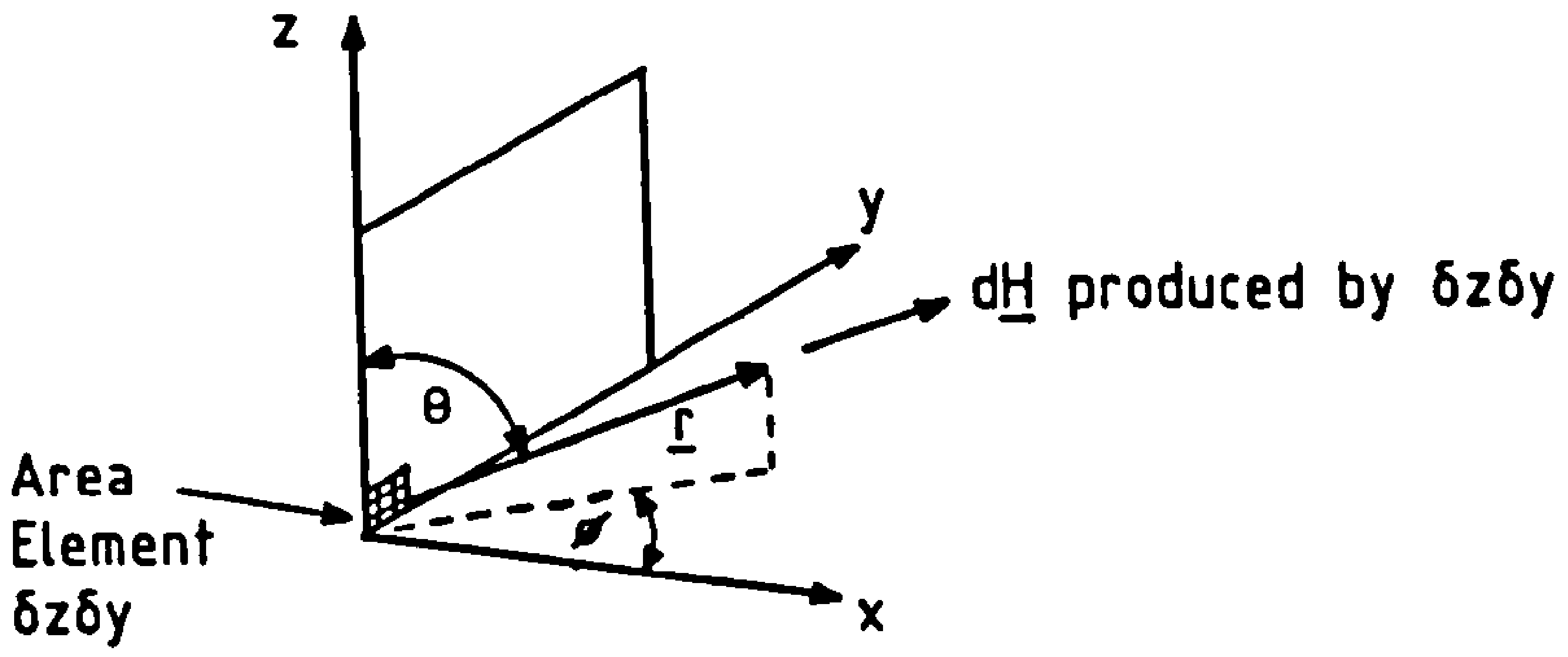

(c) Constructing Co-ordinate Axes

FIGURE 28. CALCULATION OF THE H FIELD FROM A STEEL/AIR INTERFACE.

<u>M</u> The Magnetisation.

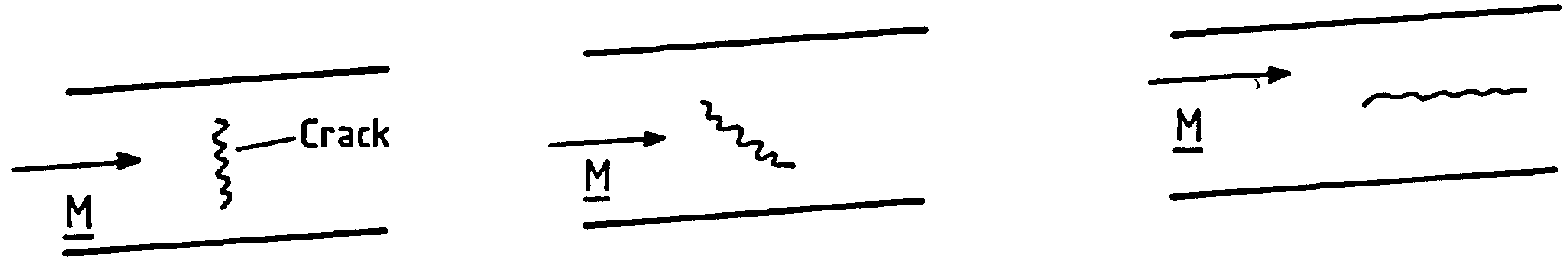

(a) A lot of charge. (b) Less charge. (c) No charge.

FIGURE 29. MAGNETIC CHARGE PRODUCTION DEPENDENCE ON CRACK ORIENTATION.

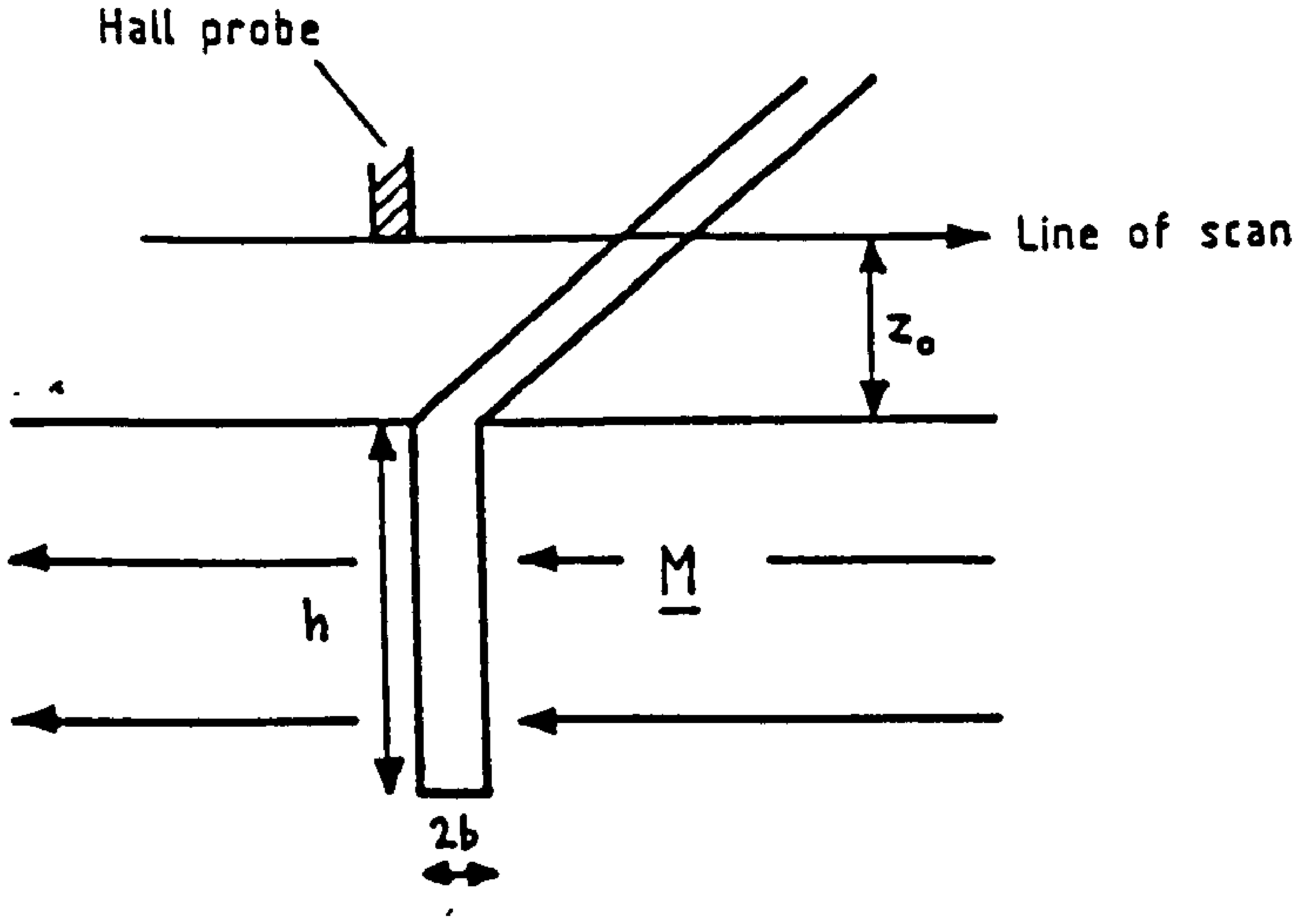

Figure 30. Calculation of the vertical component of leakage field.

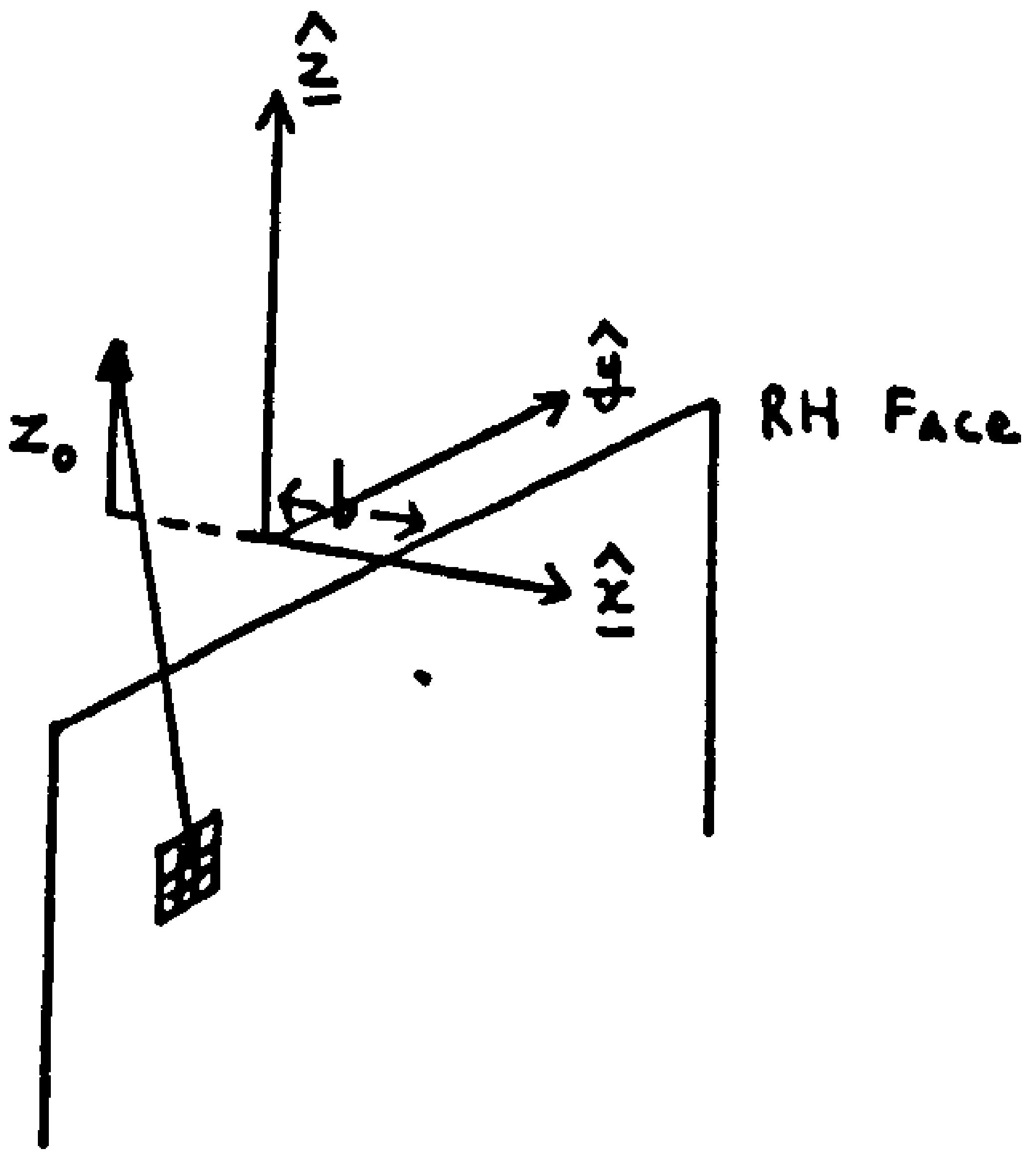

Figure 31. The right hand face of the crack in Figure 30.

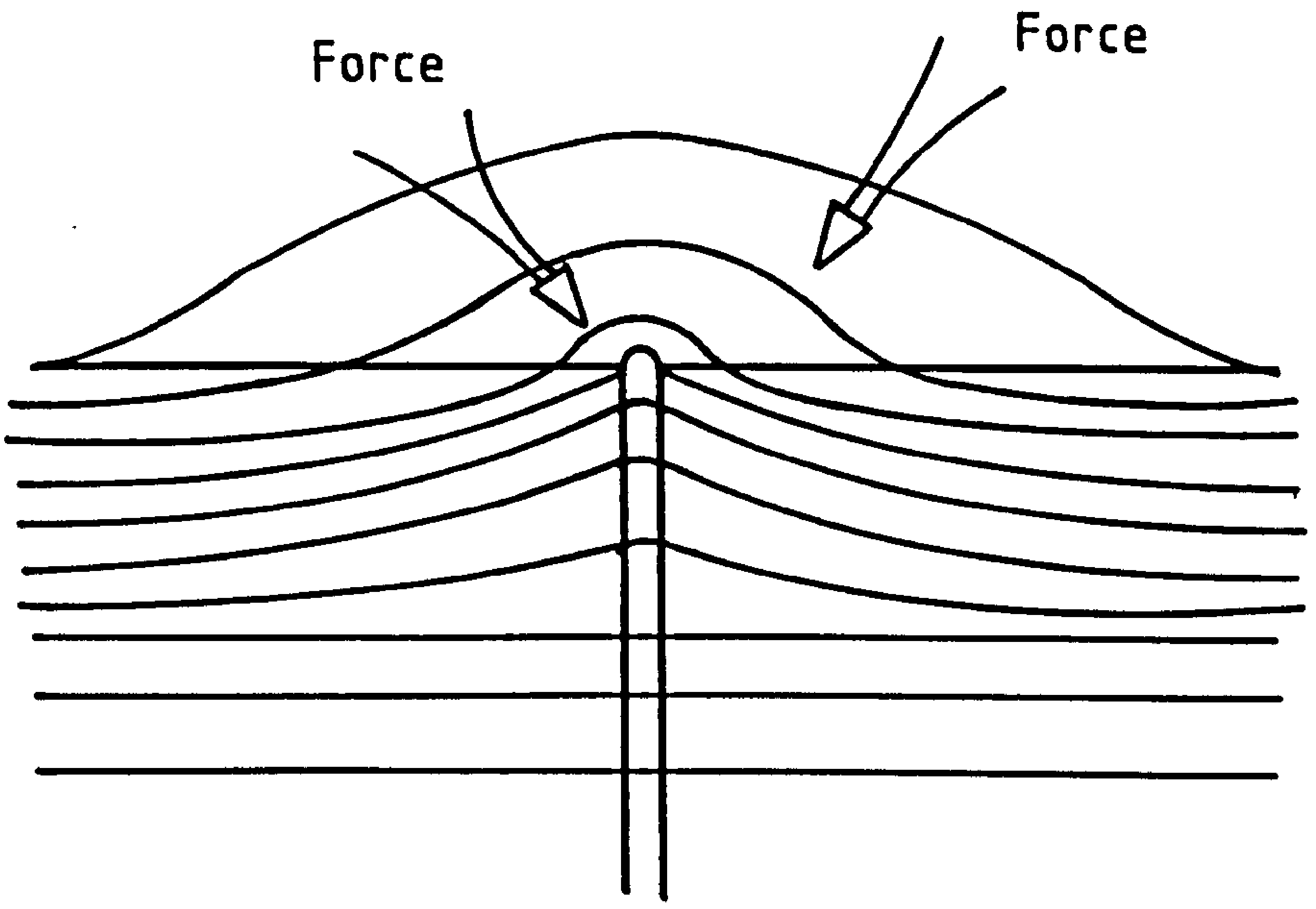

FIGURE 32. APPROXIMATE DISTRIBUTION OF B FIELD AROUND A CRACK, SHOWING DIRECTION OF FORCE ON MAGNETIC PARTICLES.

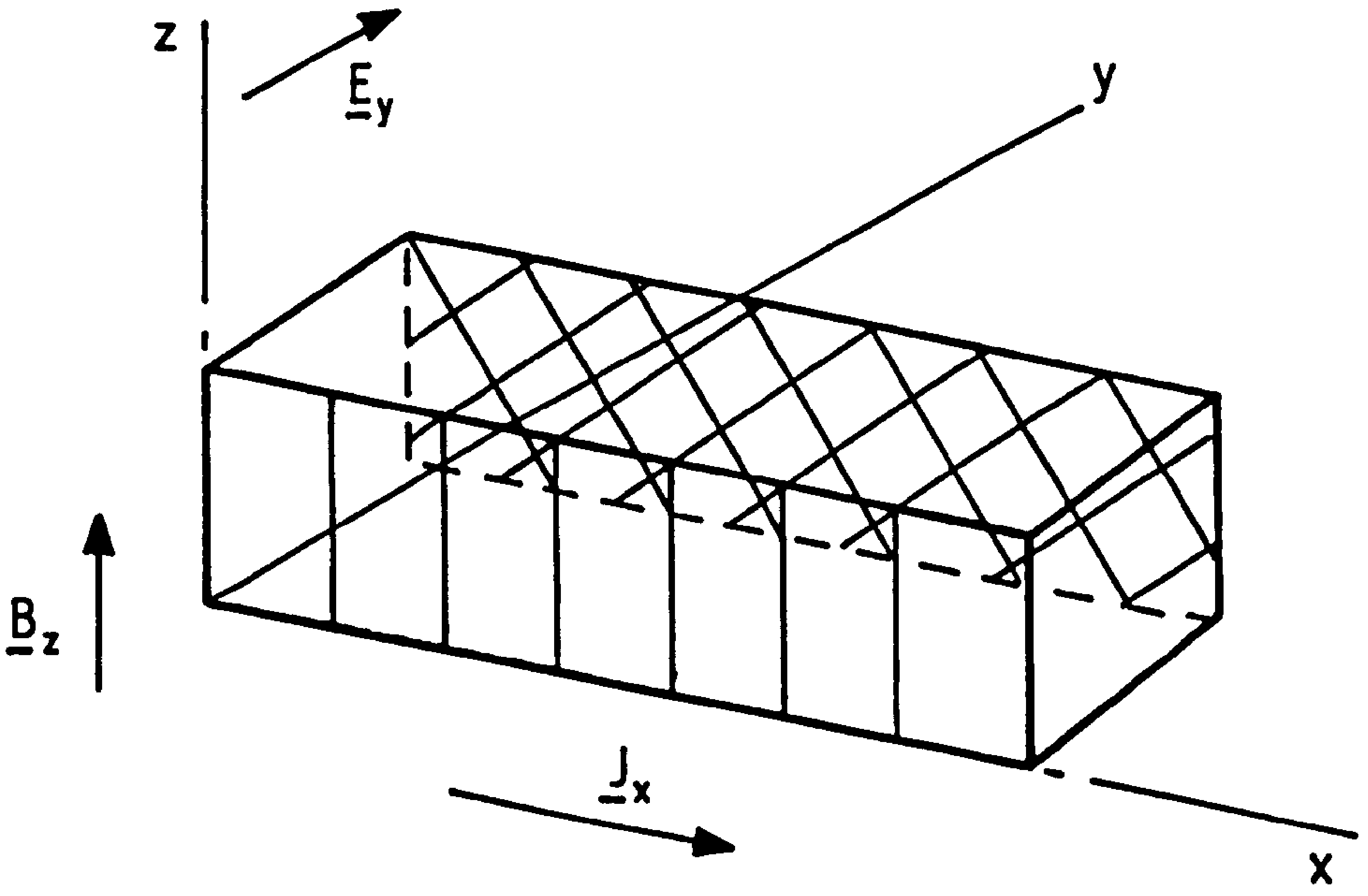

FIGURE 33. DERIVATION OF THE HALL EFFECT.

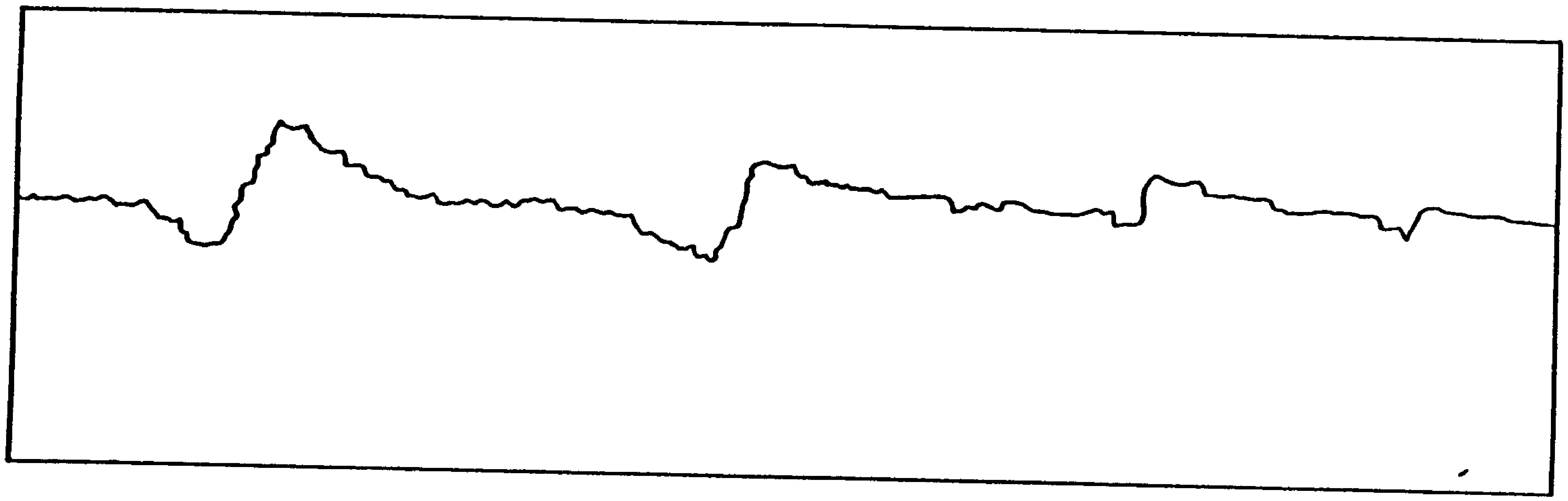

Figure 34. Stray flux signals showing the variation of stray flux amplitude and signal width with varying notch widths.

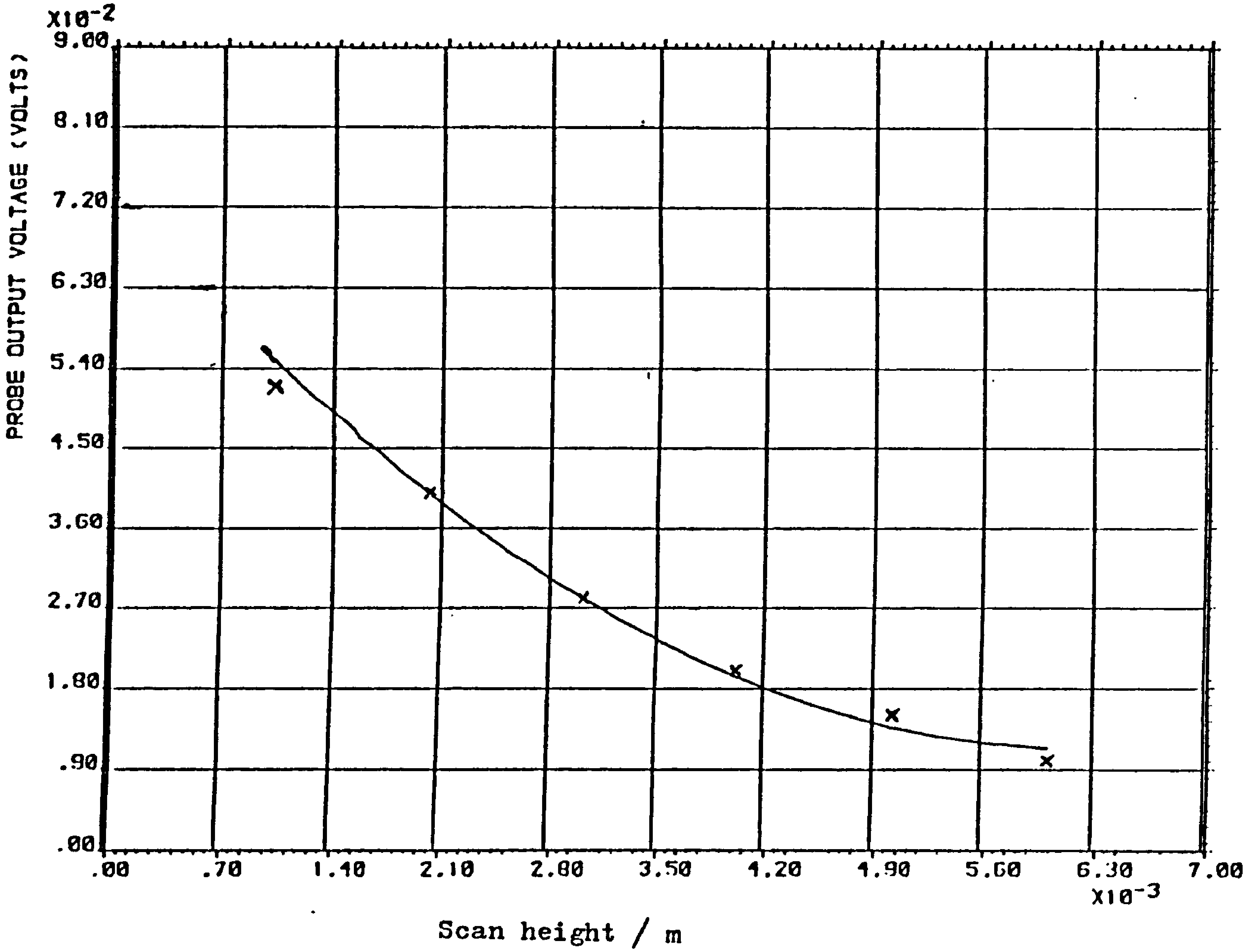

Figure 35. Probe output voltage versus scan height above 2mm wide notch.

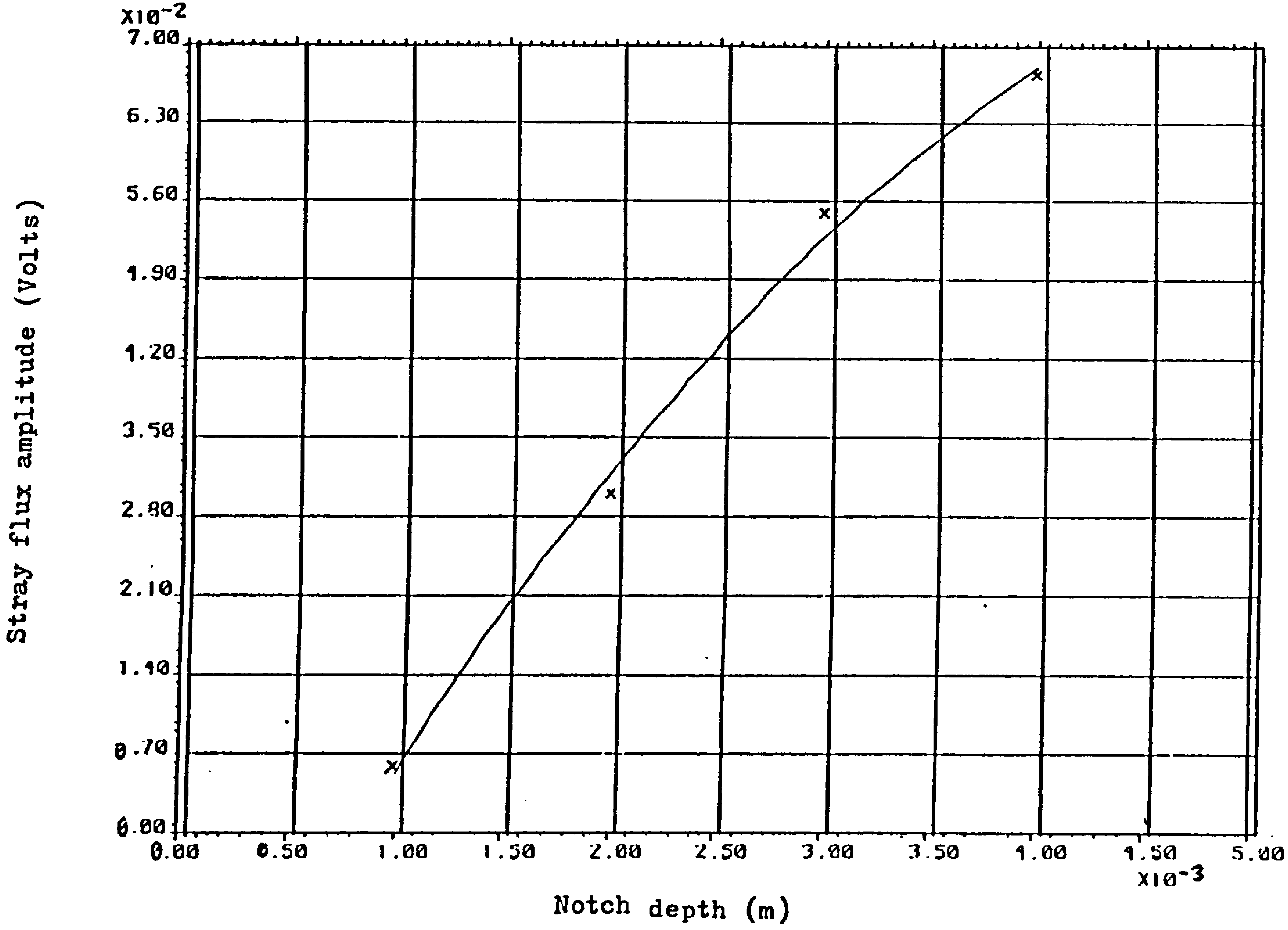

Figure 36. Variation of stray flux amplitude with notch depth.

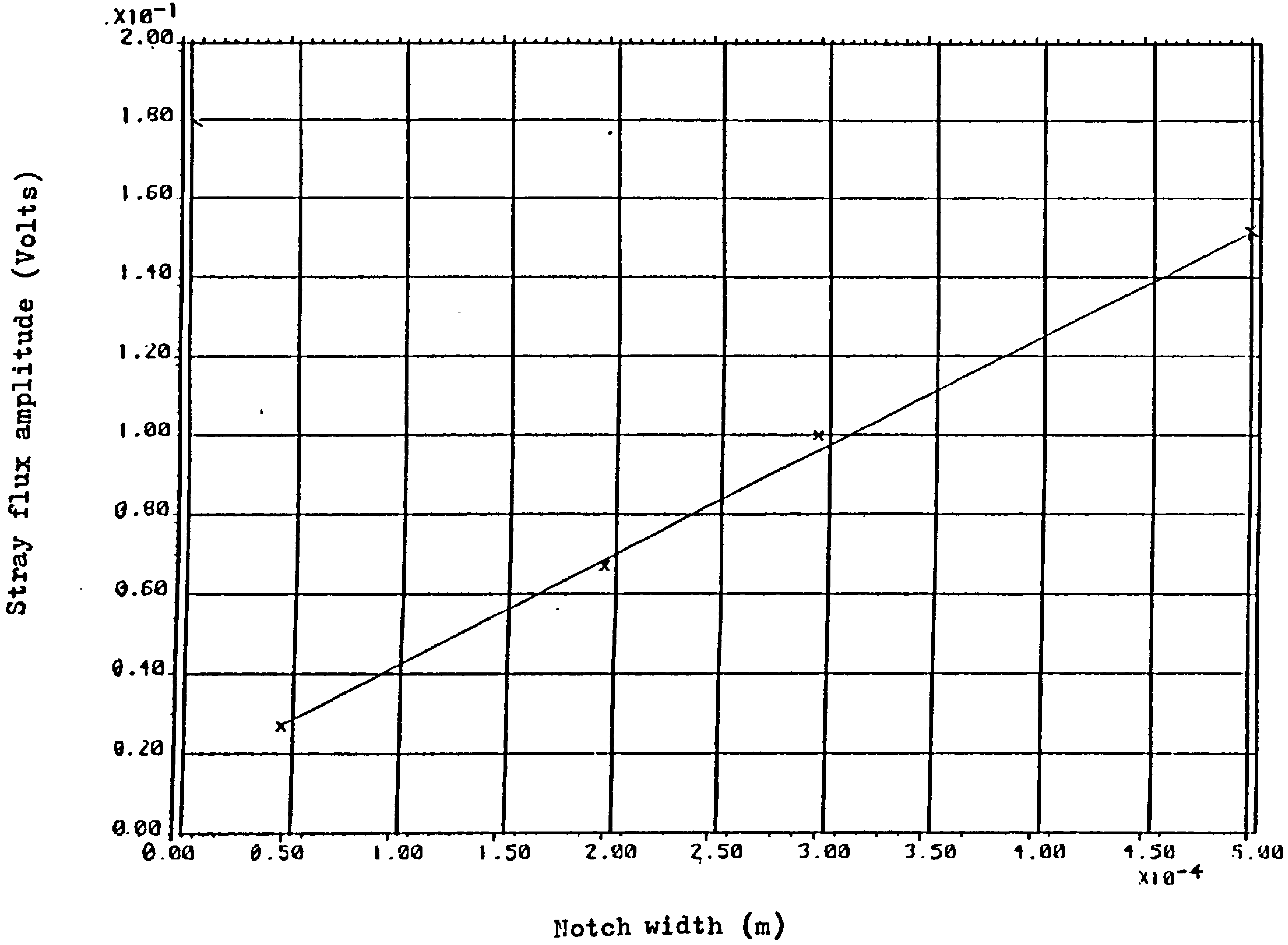

Figure 37. Variation of stray flux amplitude with notch width.

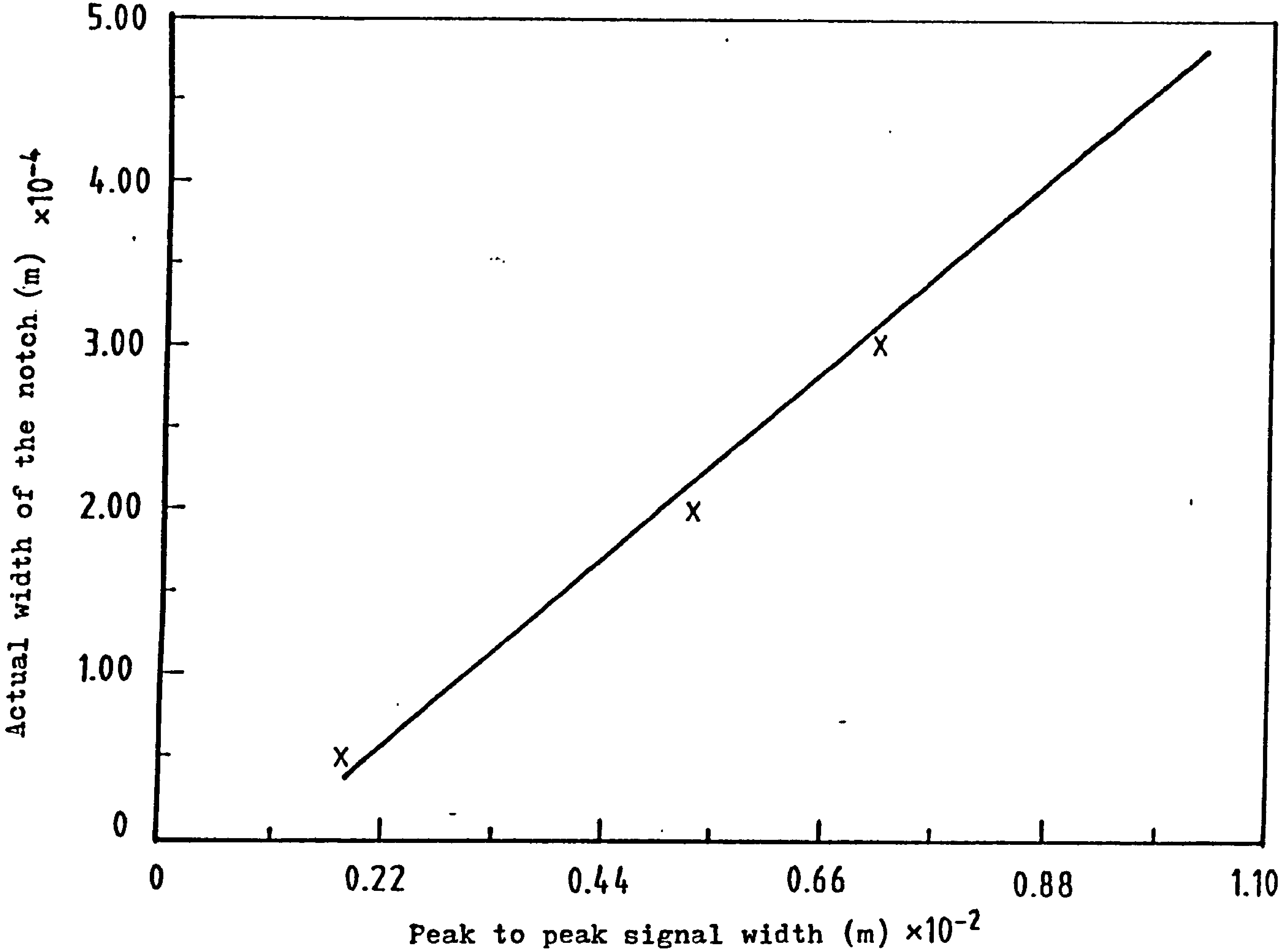

Figure 38. Variation of actual notch width with peak to peak signal width.

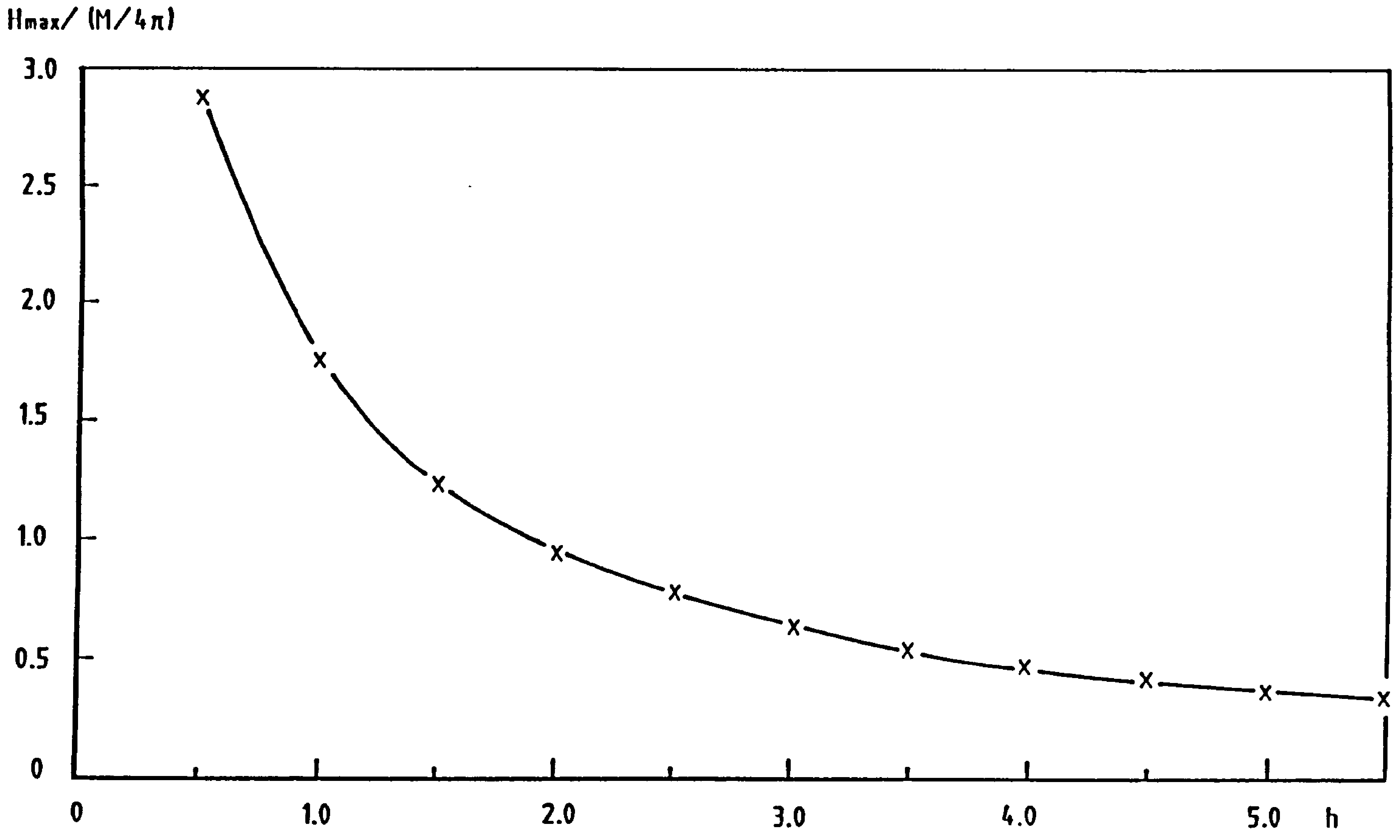

Figure 39. Graph to show drop in maximum field value with scan height h for an artificial crack of width w=2, depth d=20 (Arbitrary units).

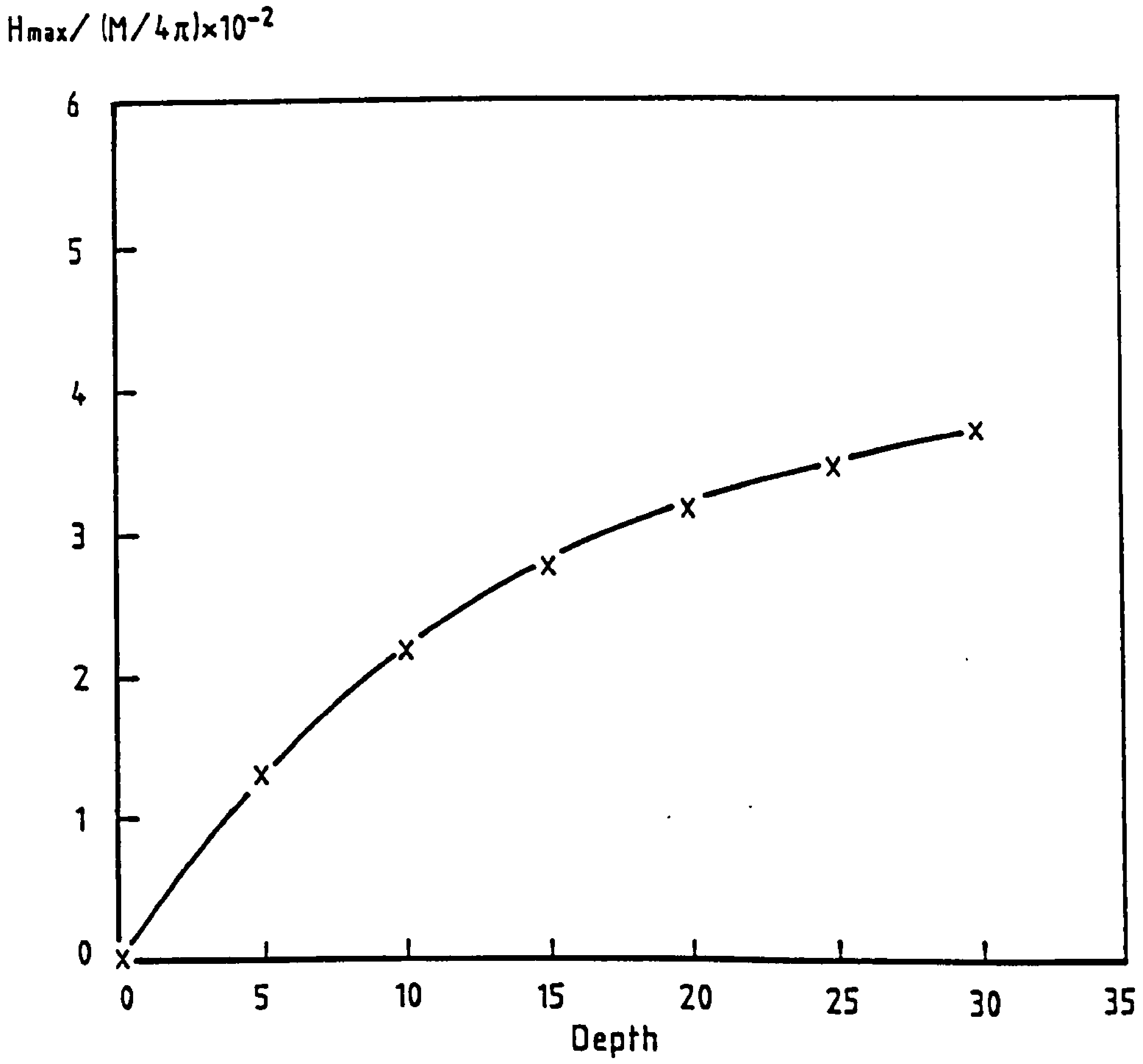

Figure 40. Variation in Hmax as a function of notch depth for scan height=20, notch width=1 (Arbitrary units).

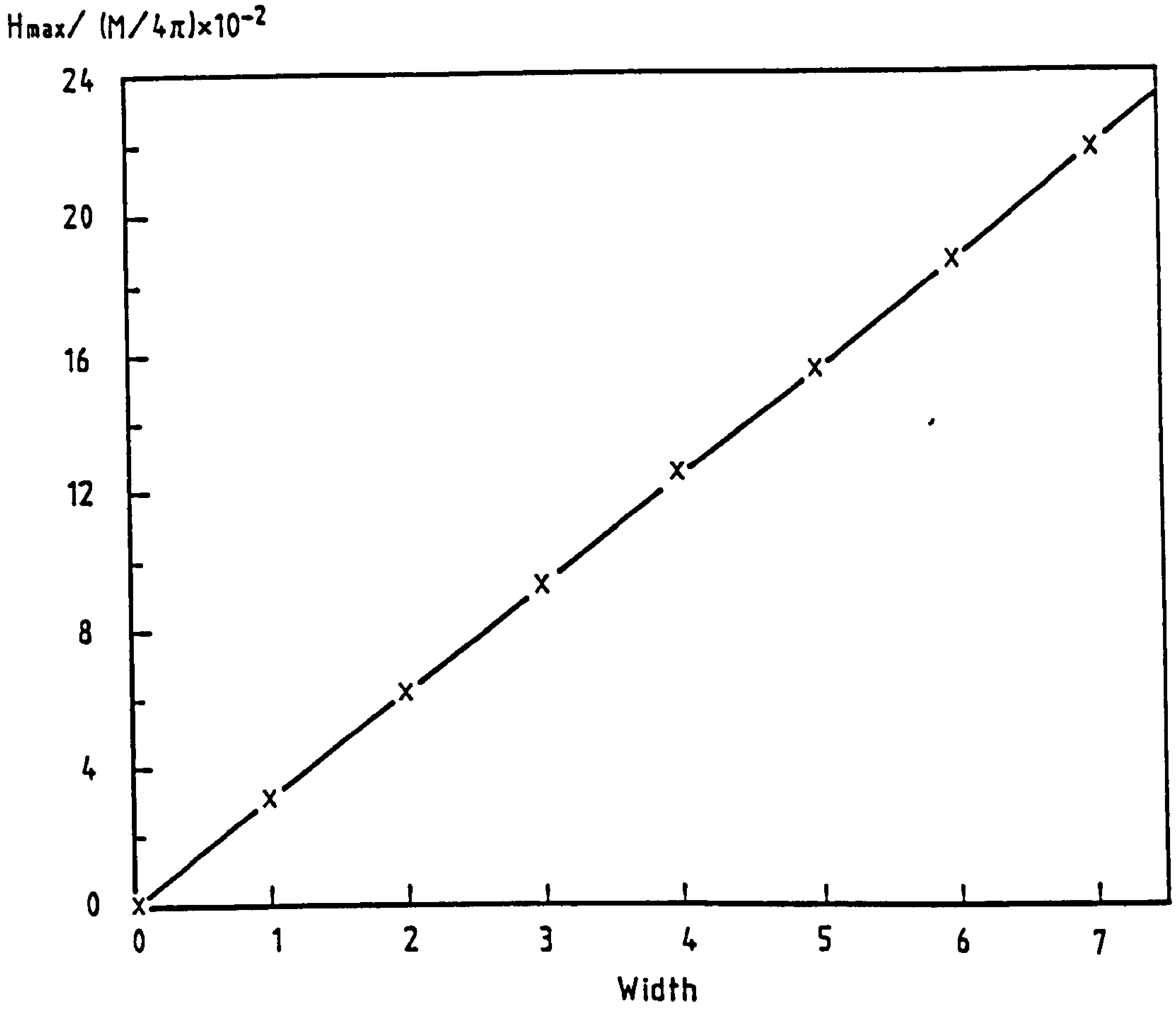

Figure 41. Stray flux maximum amplitude as a function of notch width for scan height=20, notch depth=20 (Arbitrary units).

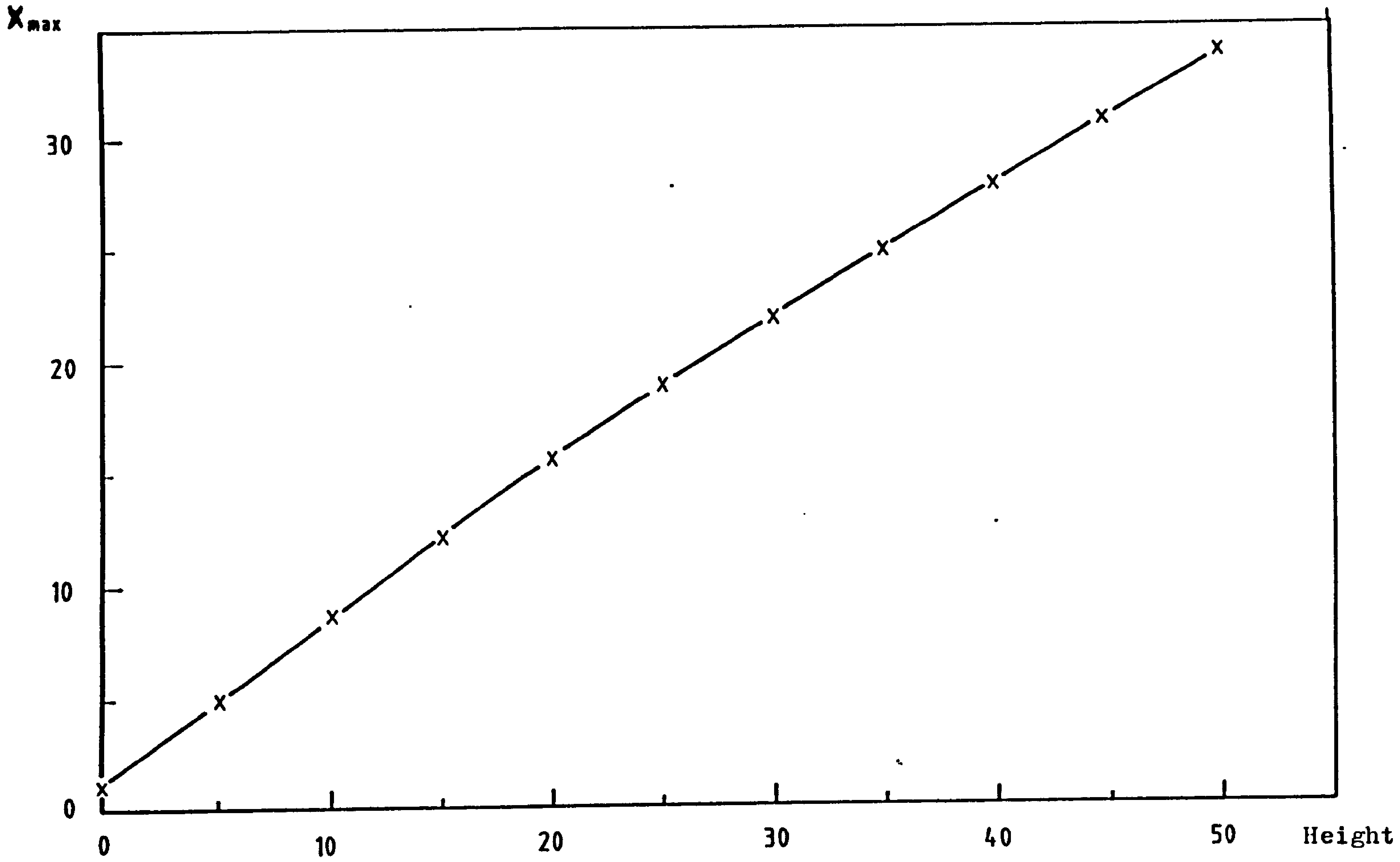

Figure 42. Graph to show half width of signal with varying scan height for notch width=2, notch depth=20 (Arbitrary units).

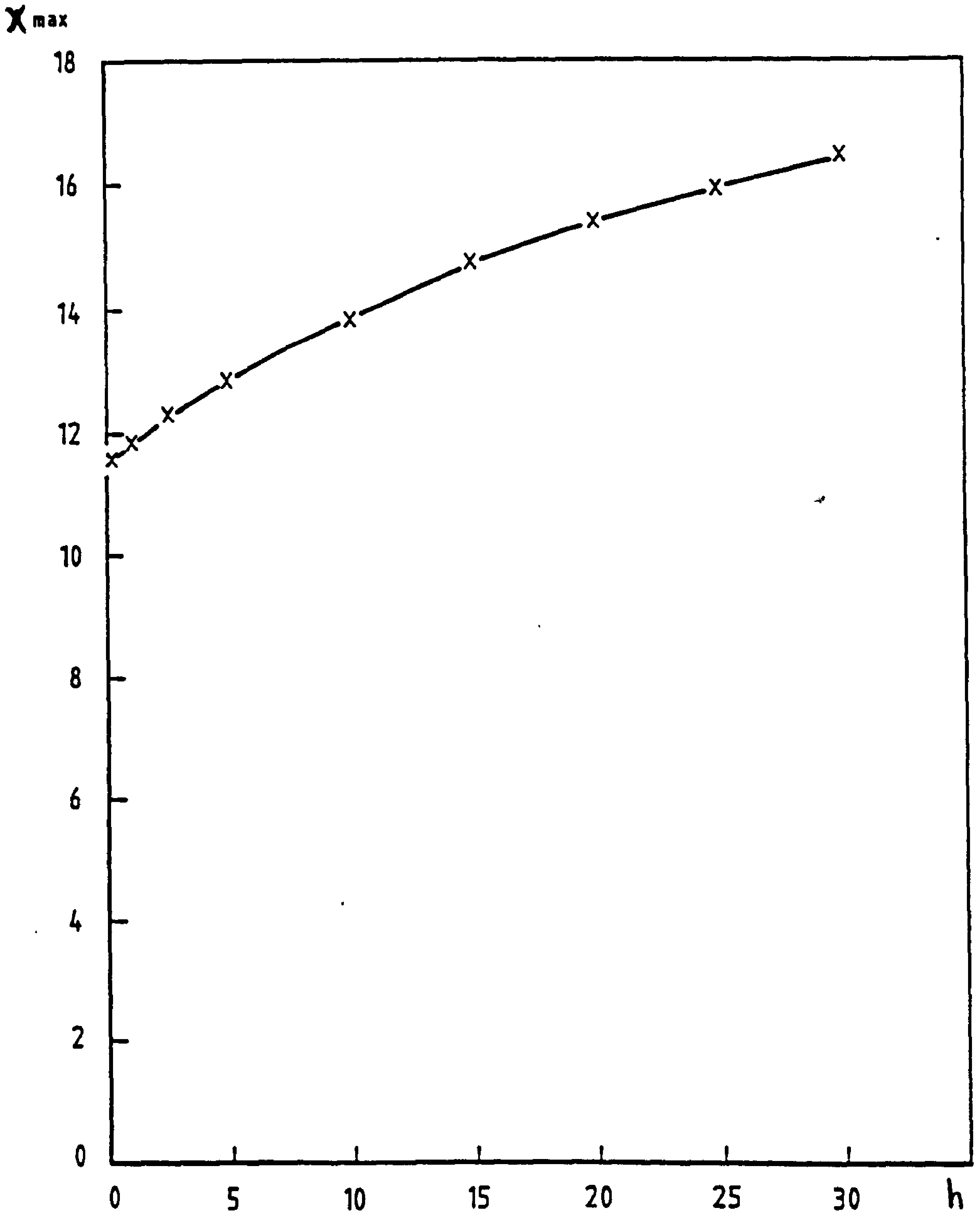

Figure 43. Graph to show half width of signal with varying notch depth for scan height=20, notch width=1 (Arbitrary units).

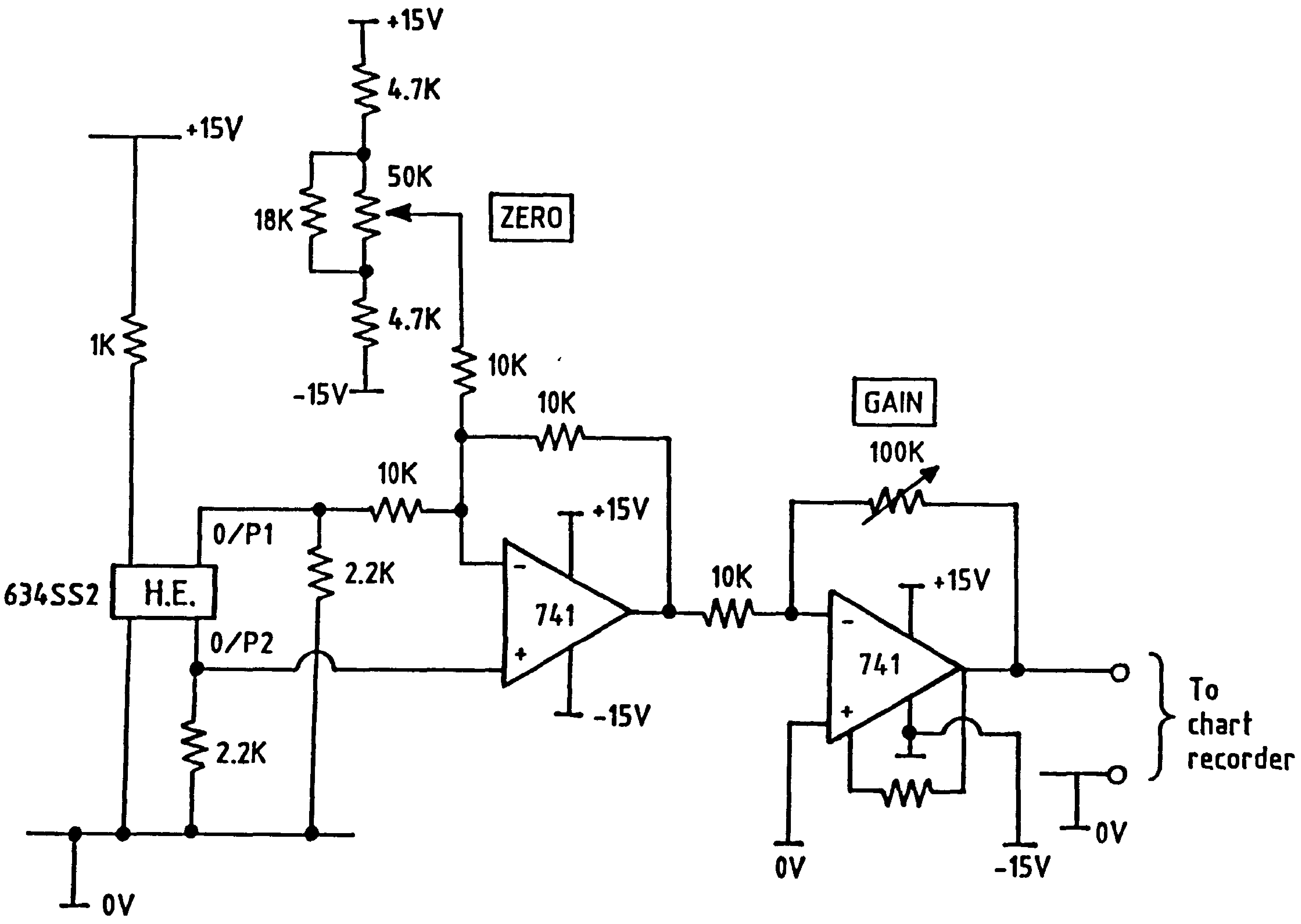

FIGURE 44. 634SS2 PROBE AMPLIFIER.

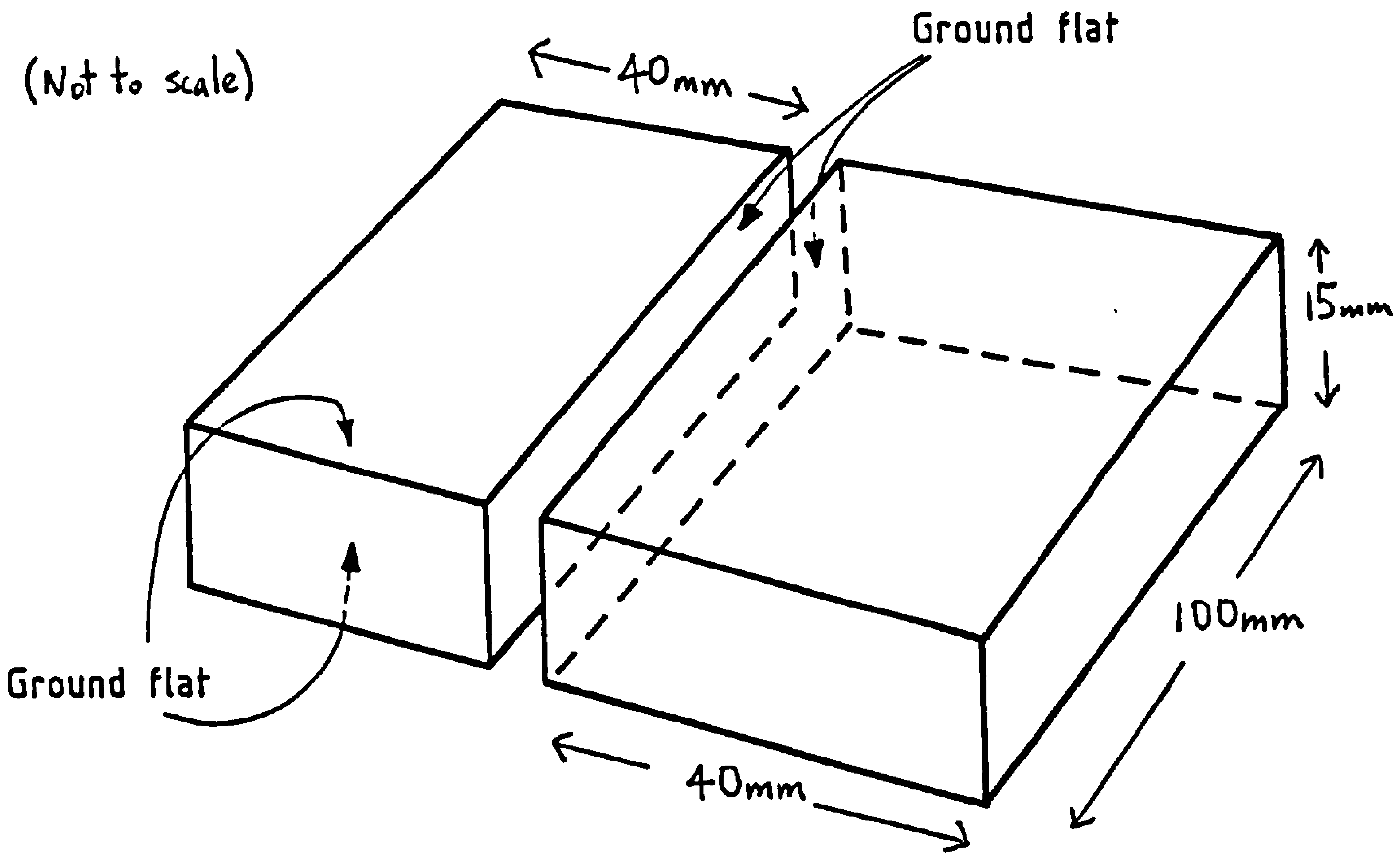

Figure 45. THE STEEL BLOCKS USED.

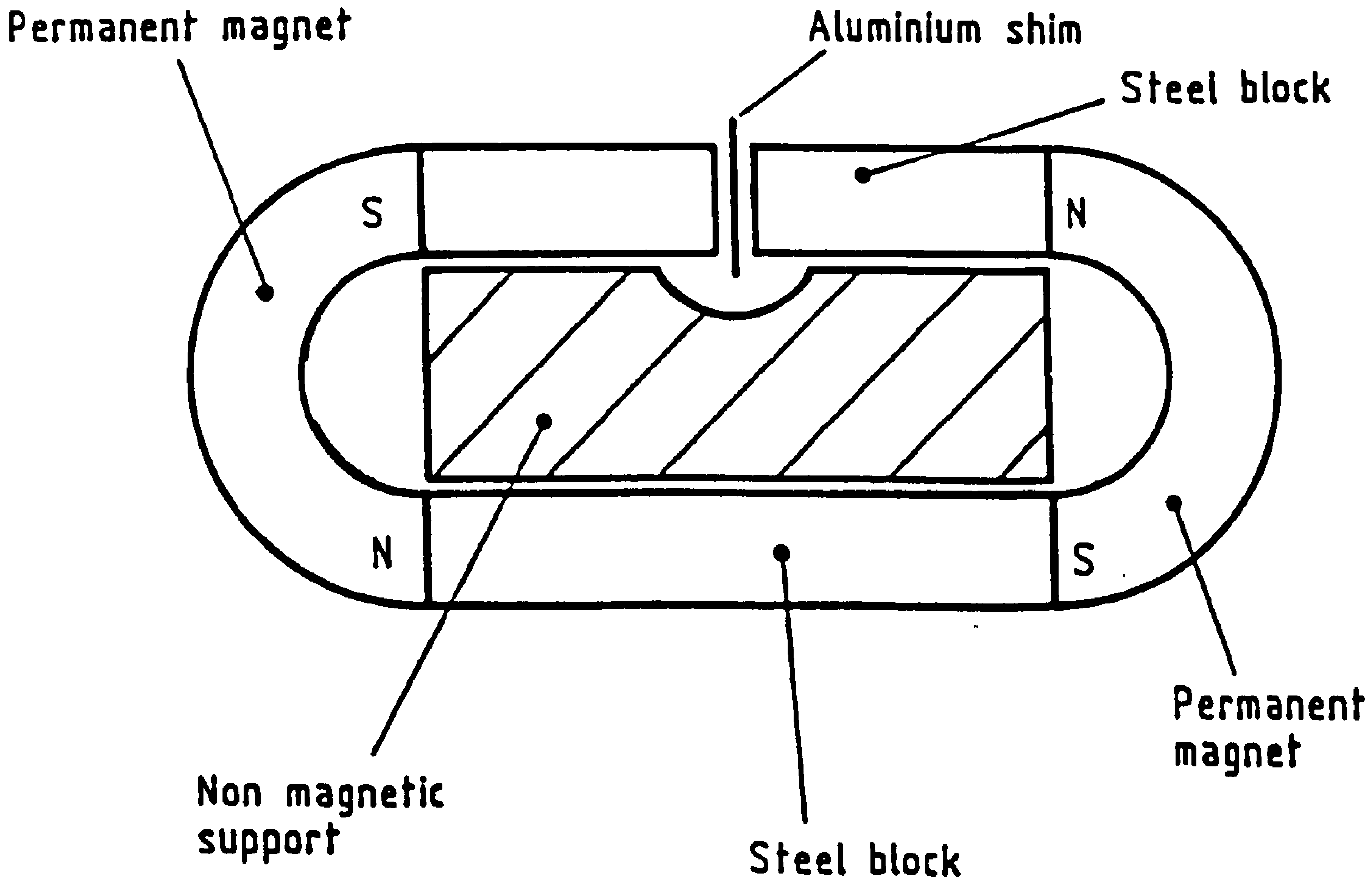

Figure 46. The magnetic circuit used in the experiments.

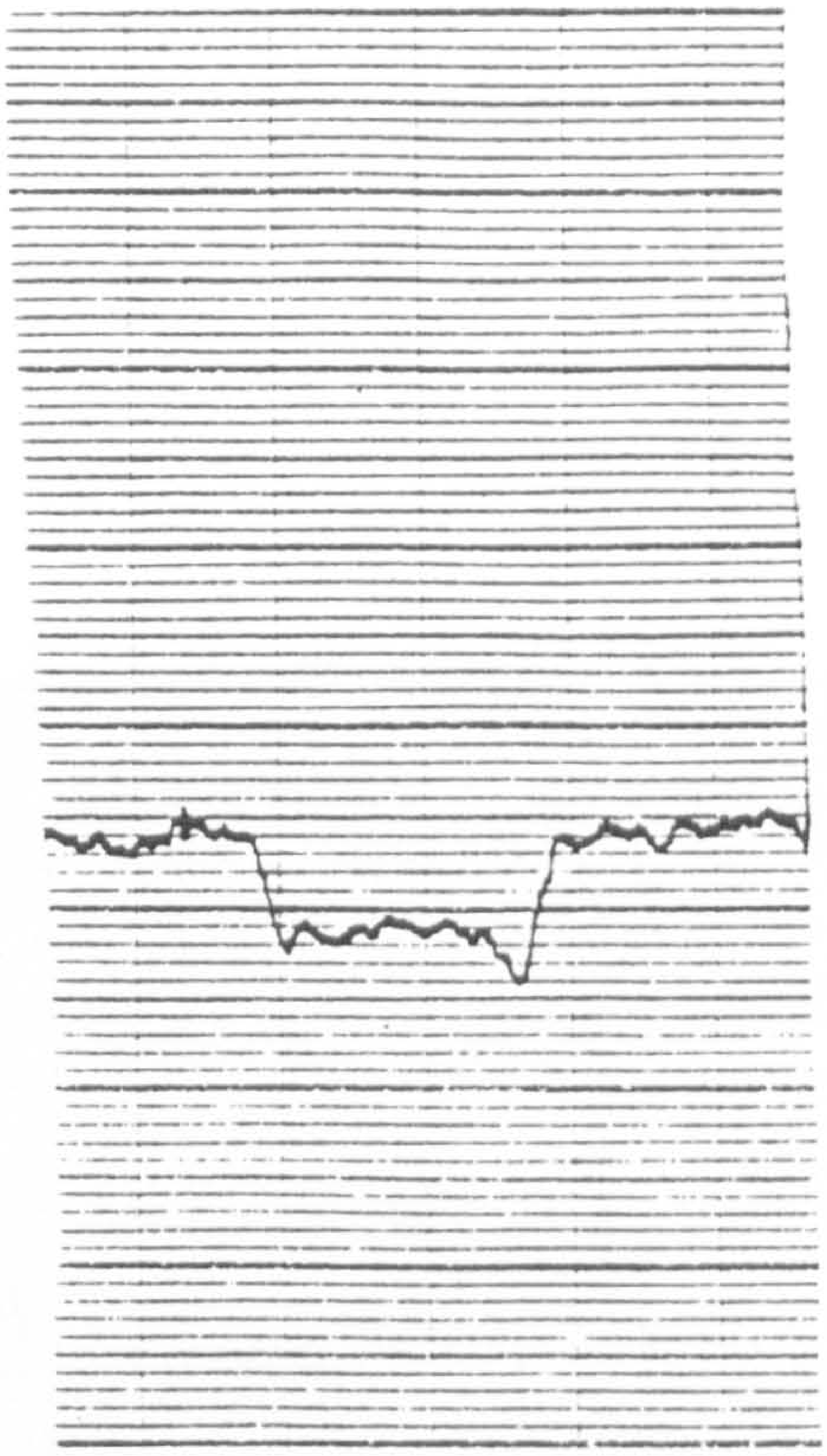

50mV f.s.d.

Figure 47. The earth's magnetic field with ±180° rotation of the probe (2 × 0.18 gauss).

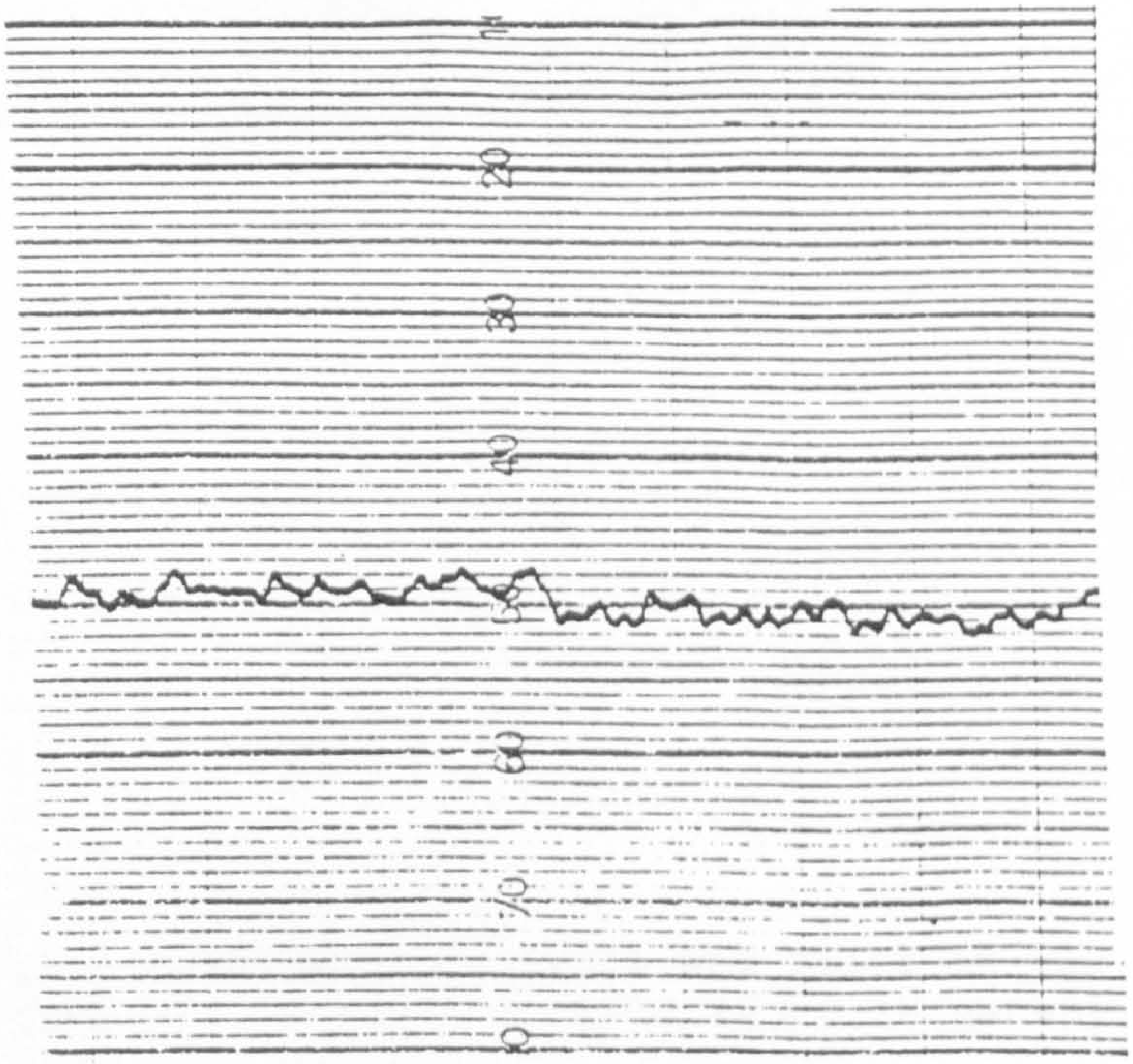

50mV f.s.d.

Figure 48. Noise from the 634SS2 probe.

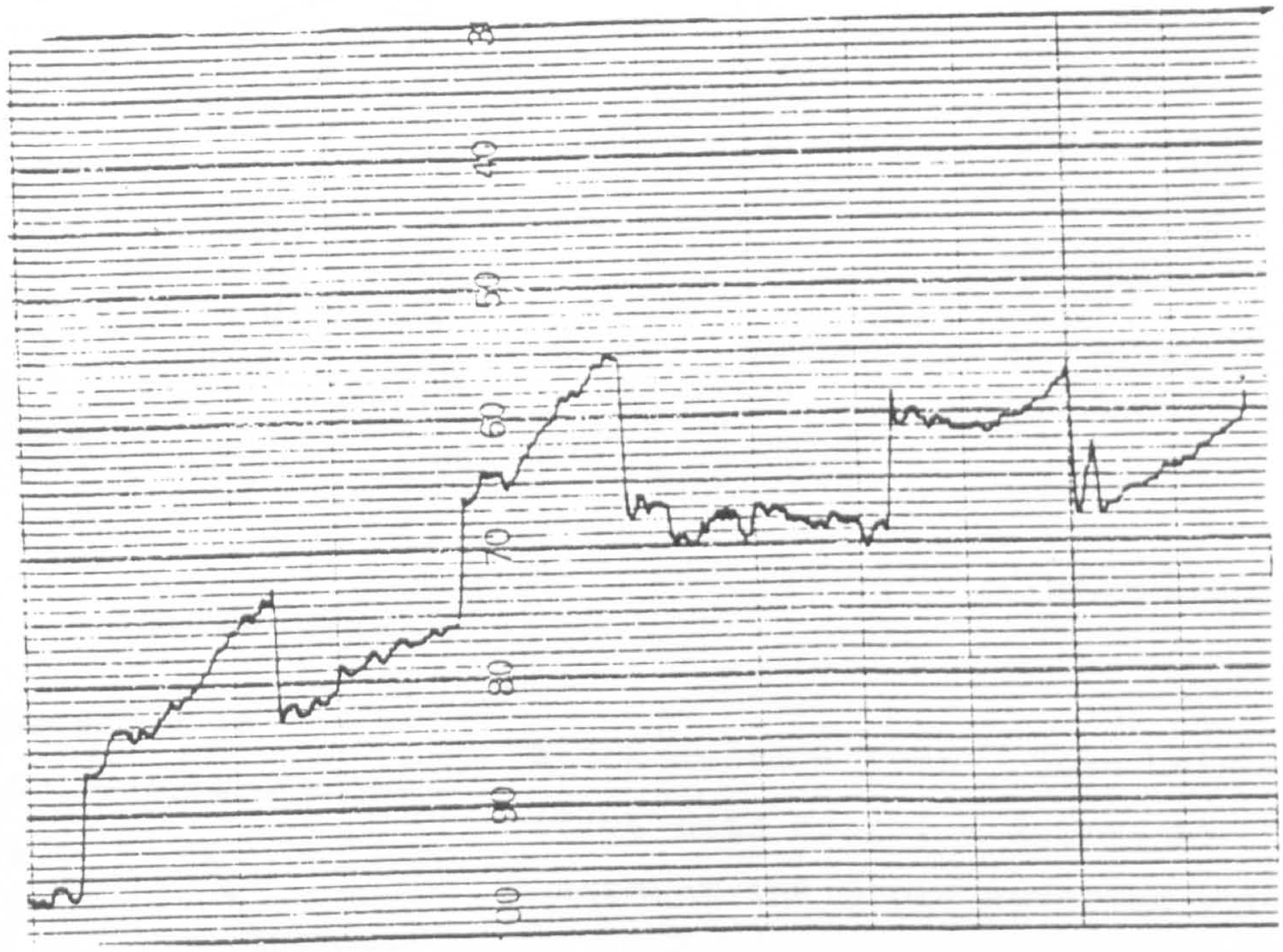

Figure 49. The effect of temperature drift and noise in the measurement of the earth's field (2 × 0.18 gauss).

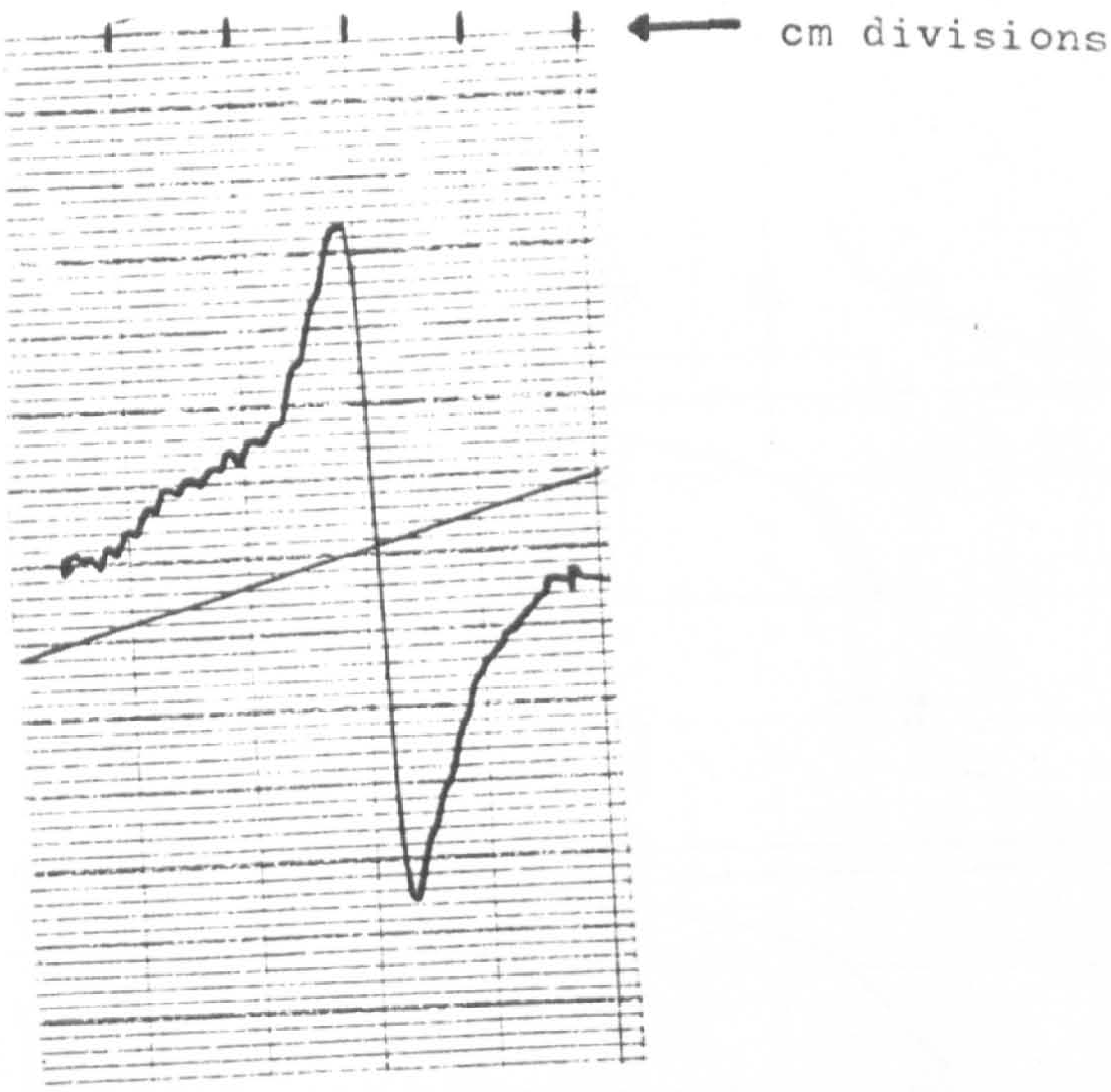

Width=100µm

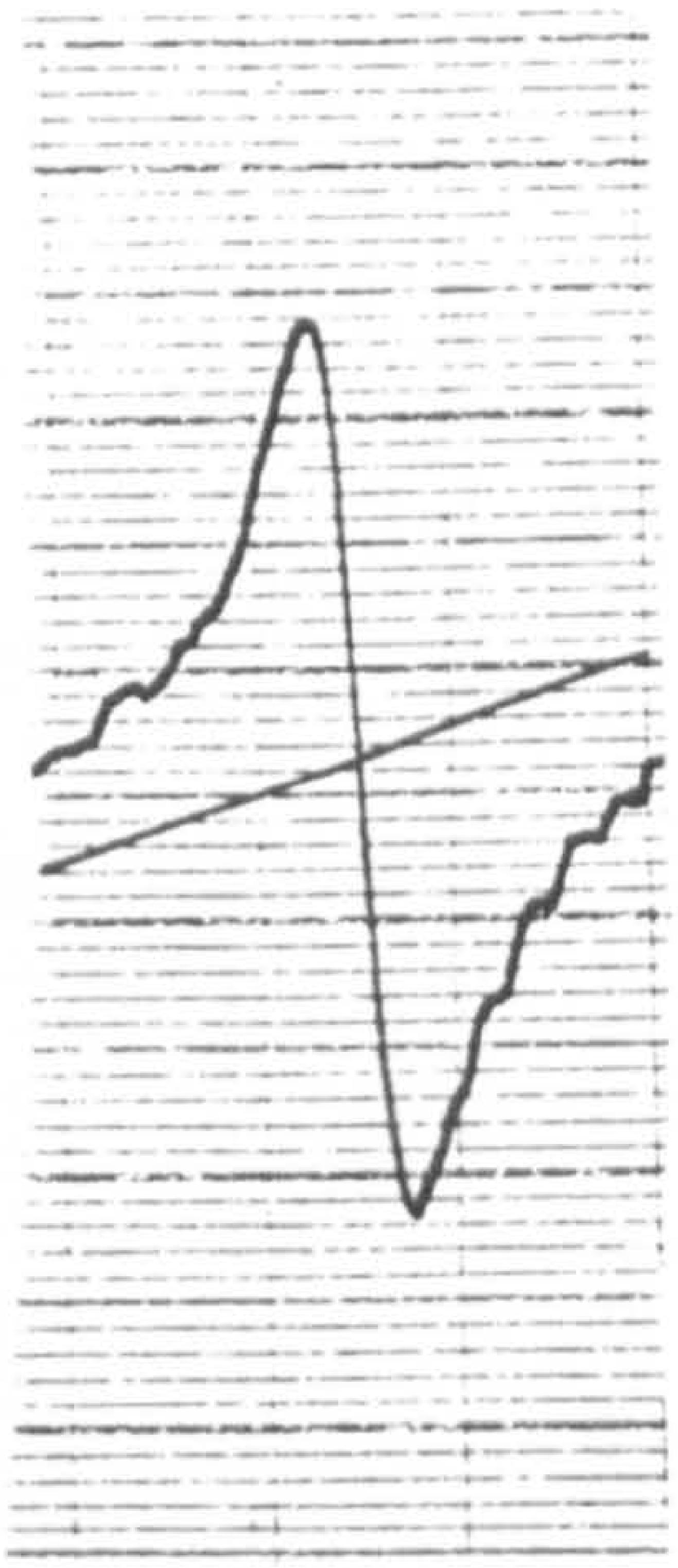

Width=75µm

Notch depth = 15mm. Scan height = 1.5mm. (True scan height = 2.5mm, taking into account the probe covering thickness).

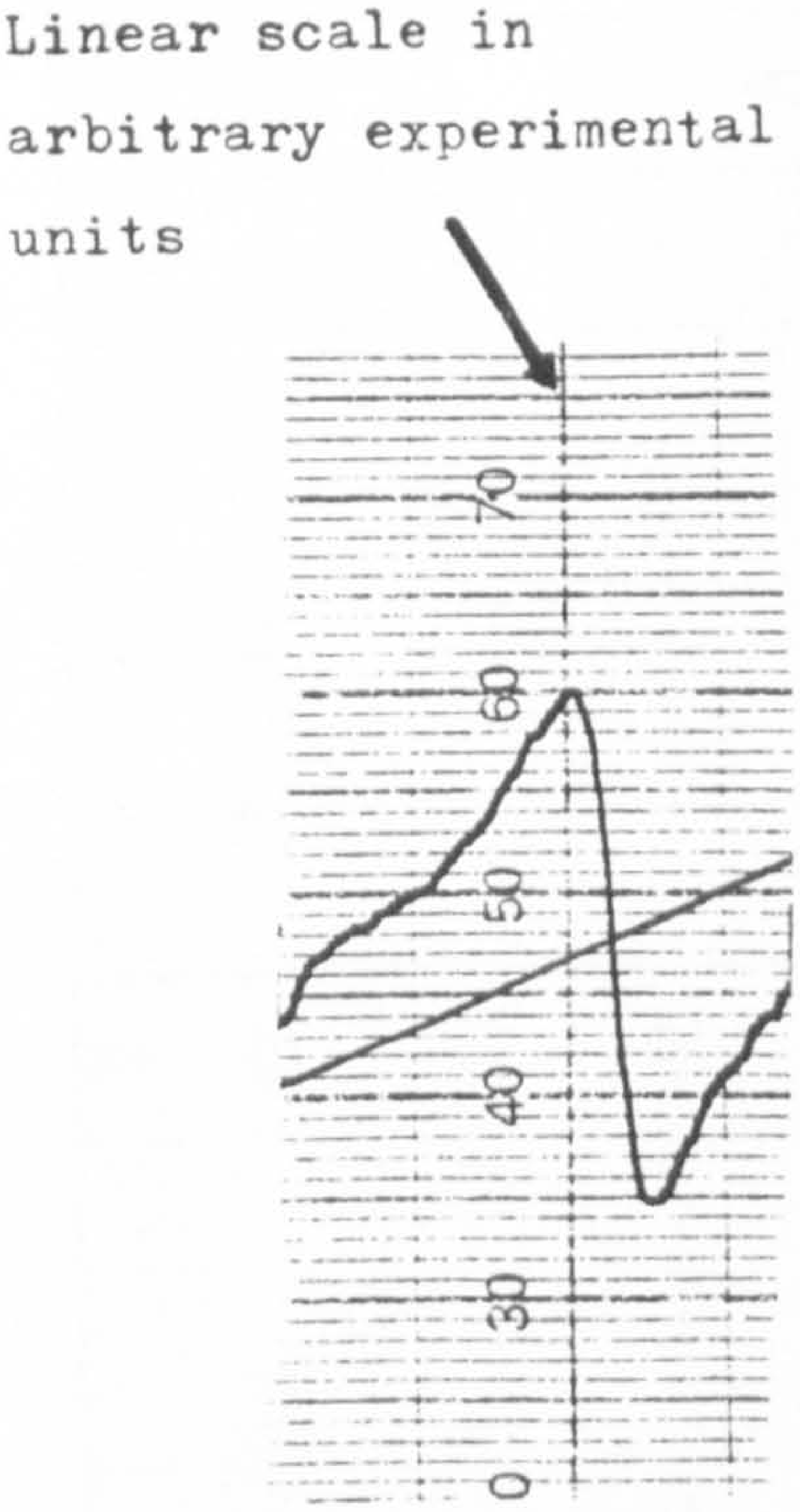

Width=50µm

Width=25µm

Figure 50. Some actual signals produced from notches.

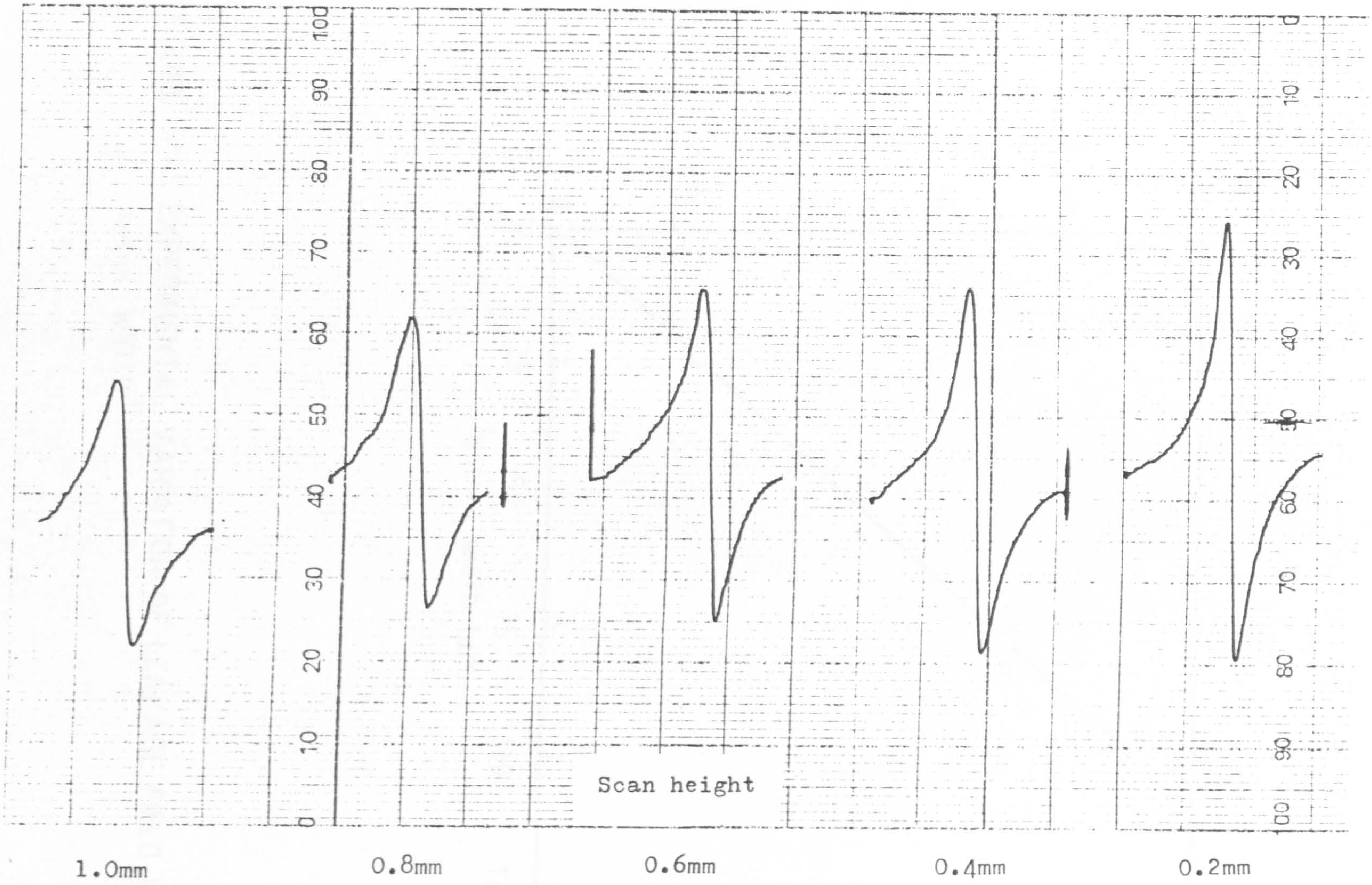

Figure 51. Variation of notch signature with scan height.

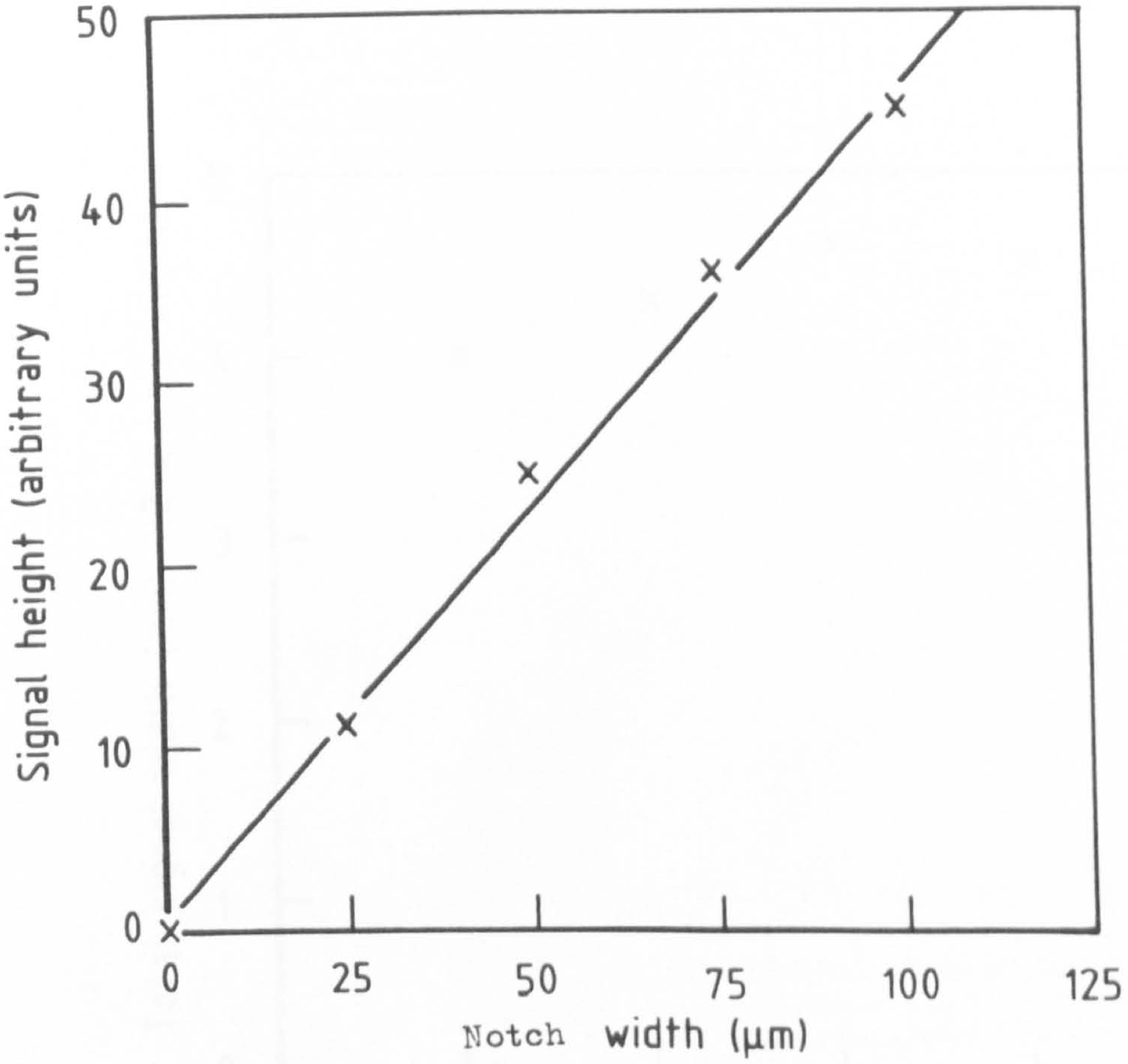

FIGURE 52. EXPERIMENTAL VARIATION OF LEAKAGE FIELD WITH notch WIDTH.

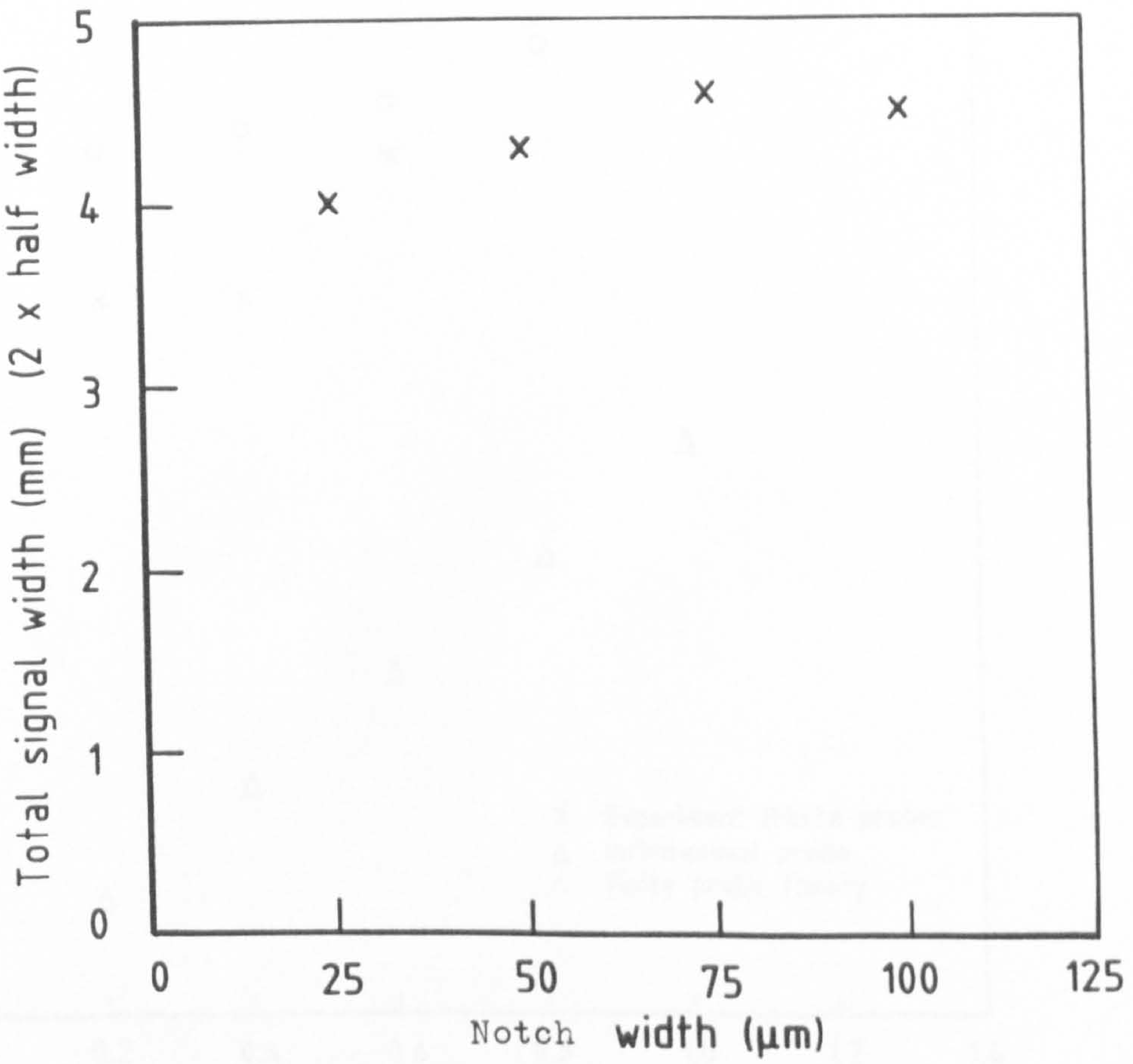

FIGURE 53. EXPERIMENTAL VARIATION IN SIGNAL WIDTH WITH notch WIDTH.

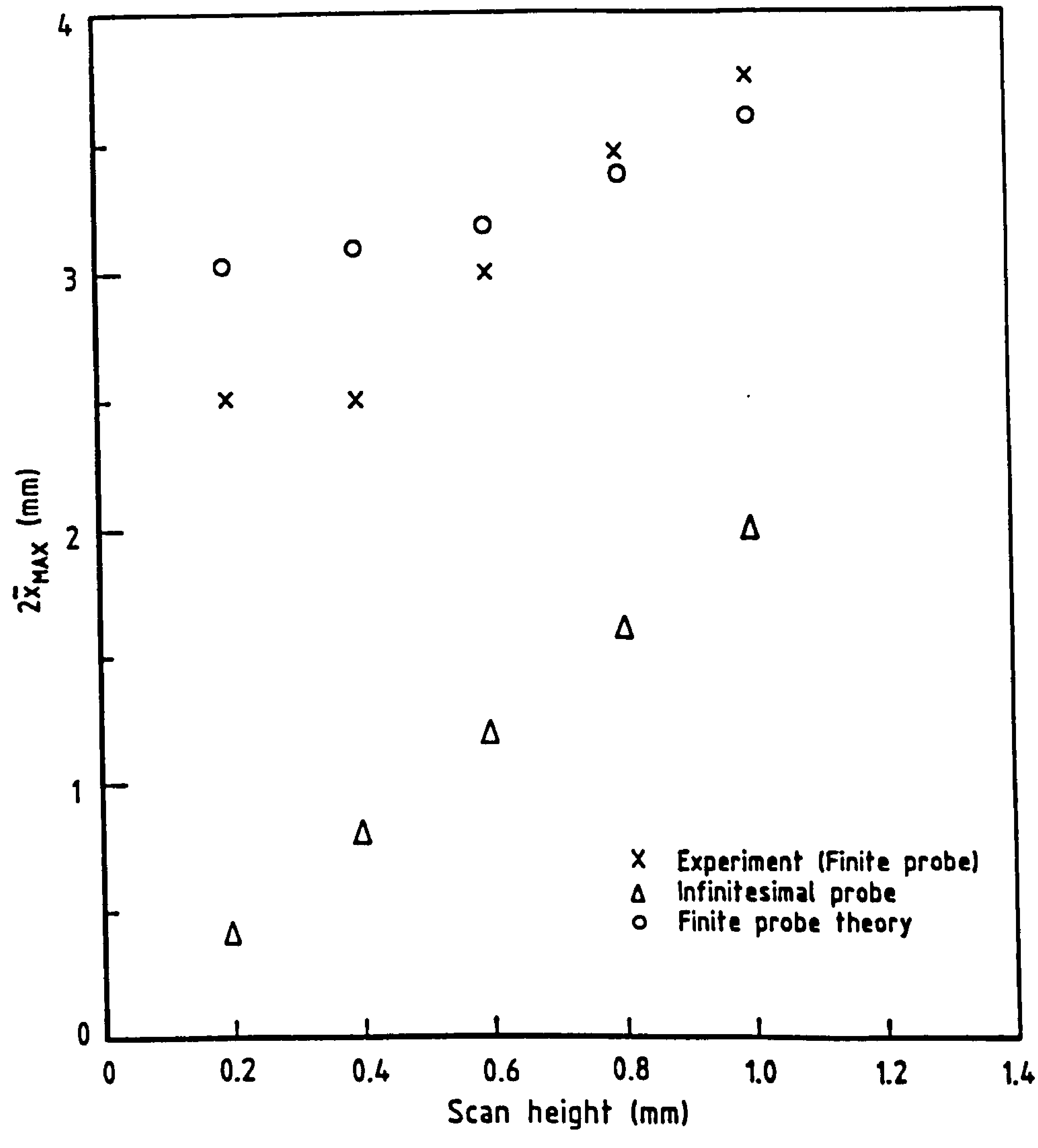

FIGURE 54. THEORETICAL AND EXPERIMENTAL VARIATION OF $\bar{x}_{MAX}$ WITH SCAN HEIGHT (Assuming width of probe 2K = 3mm)

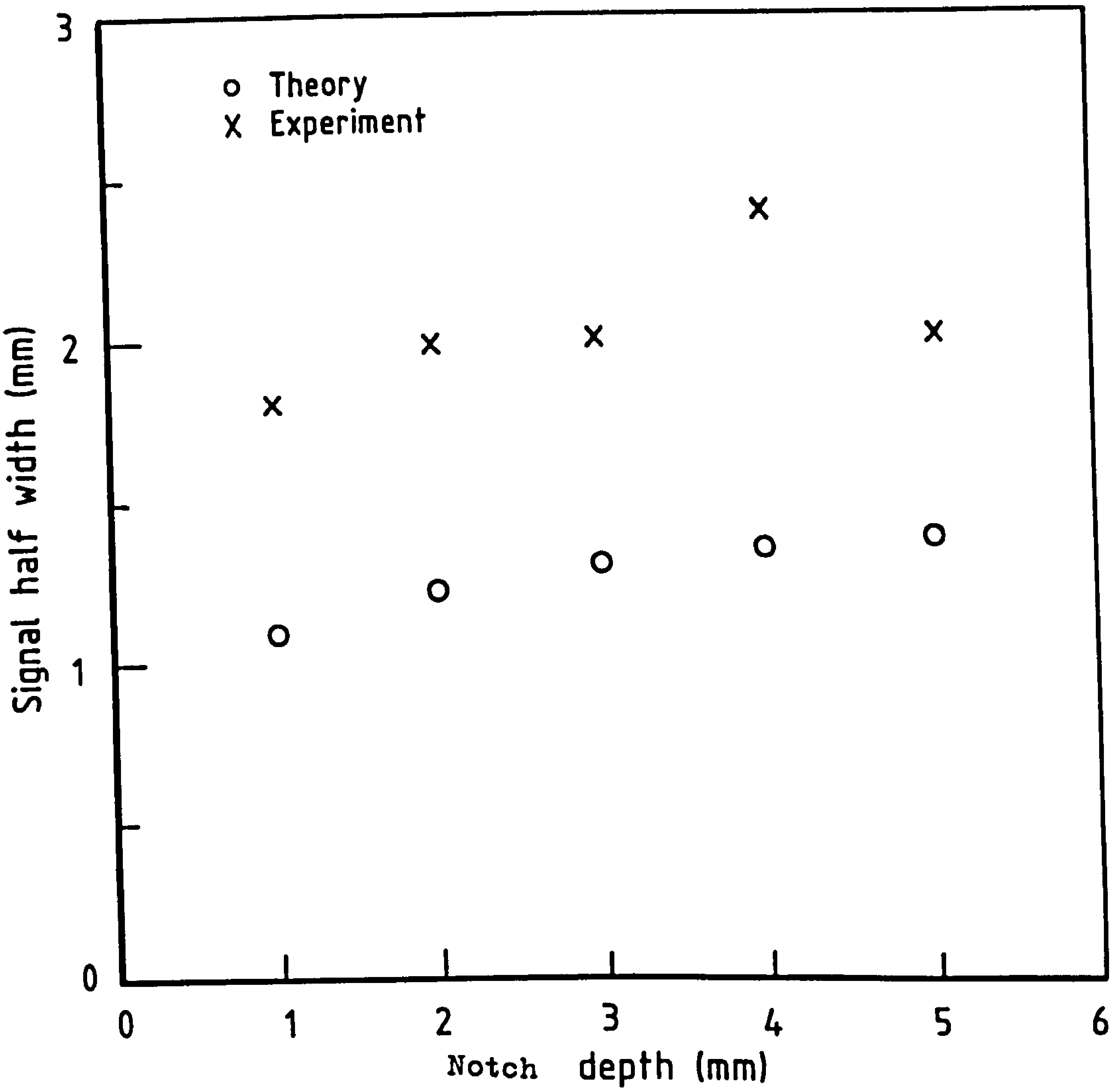

FIGURE 55. EXPERIMENTAL AND THEORETICAL VARIATION OF SIGNAL WIDTH WITH notch DEPTH. INFINITESIMAL PROBE THEORY IS USED.

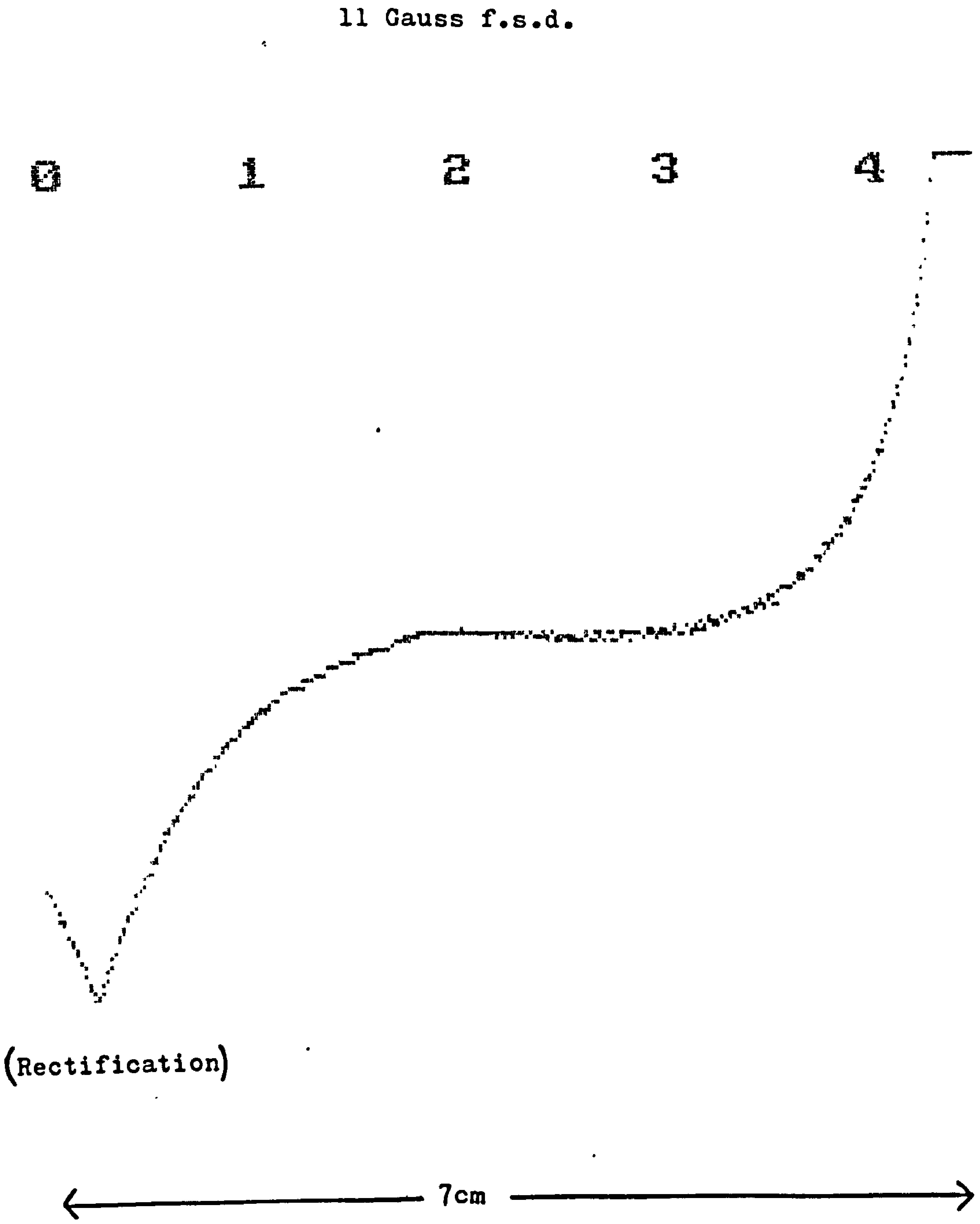

Figure 56. The background signal.

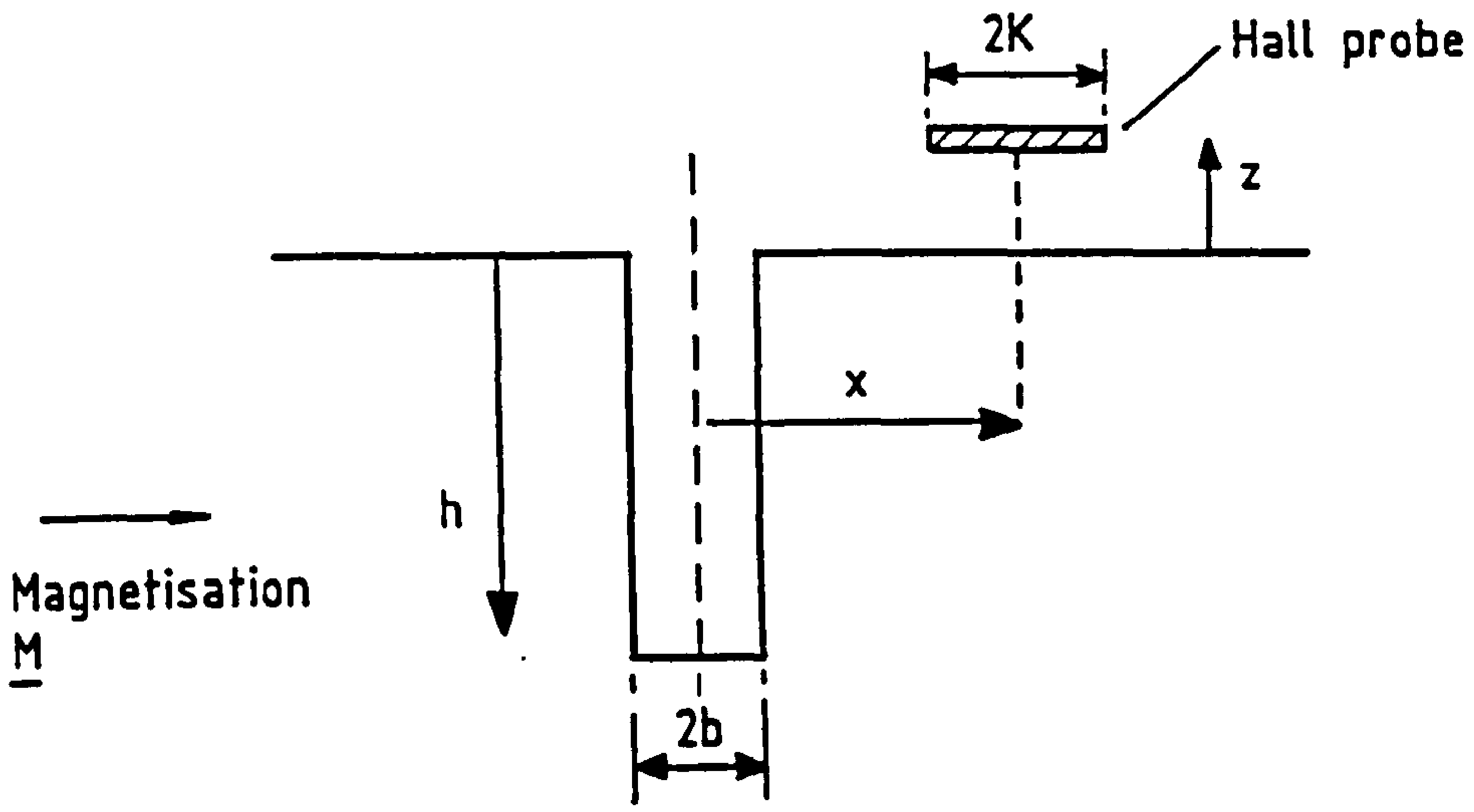

FIGURE 57. THE SUMMING EFFECT OF THE FINITE PROBE.

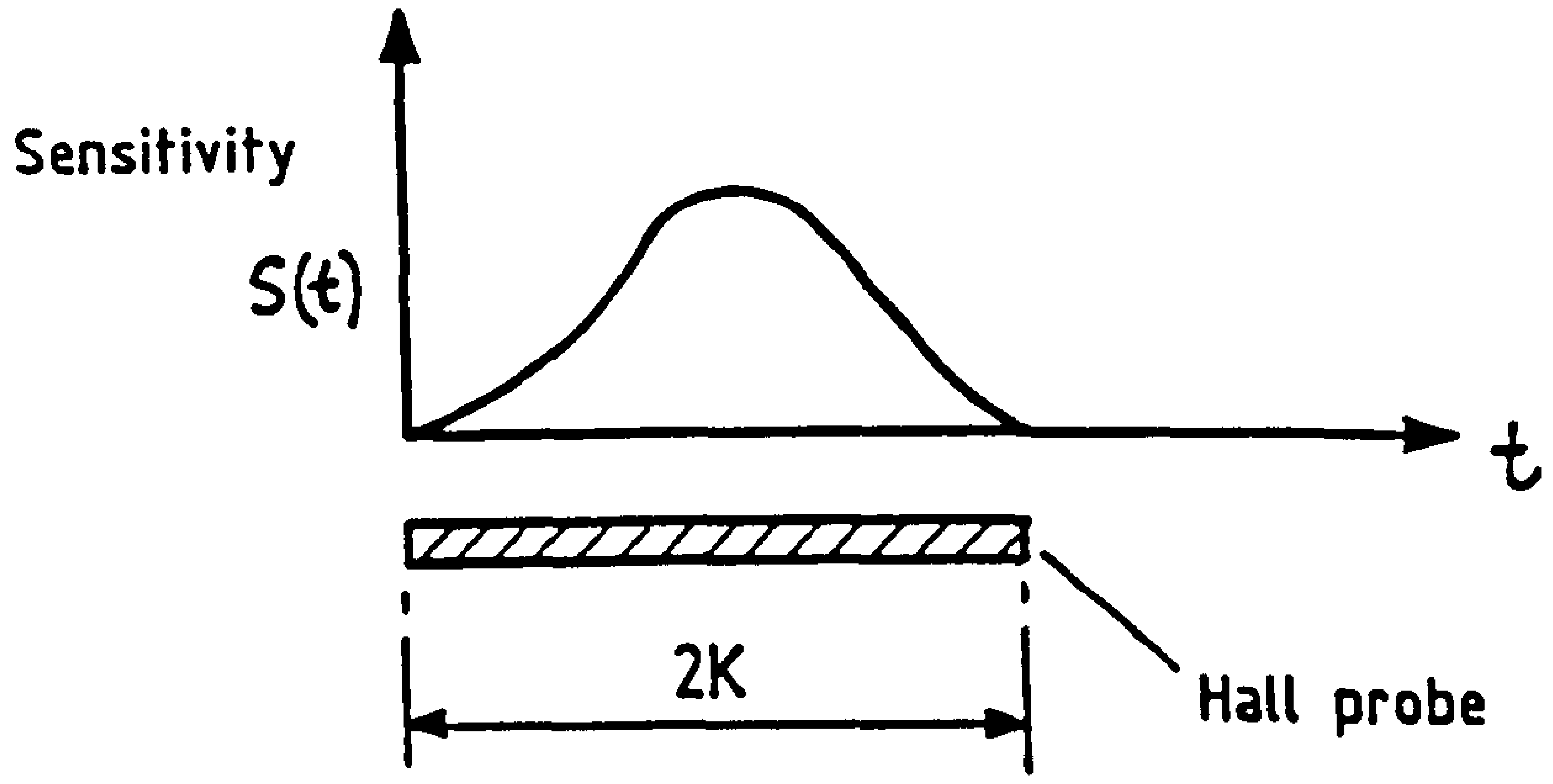

FIGURE 58. A POSSIBLE VARIATION IN SENSITIVITY OVER THE PROBE.

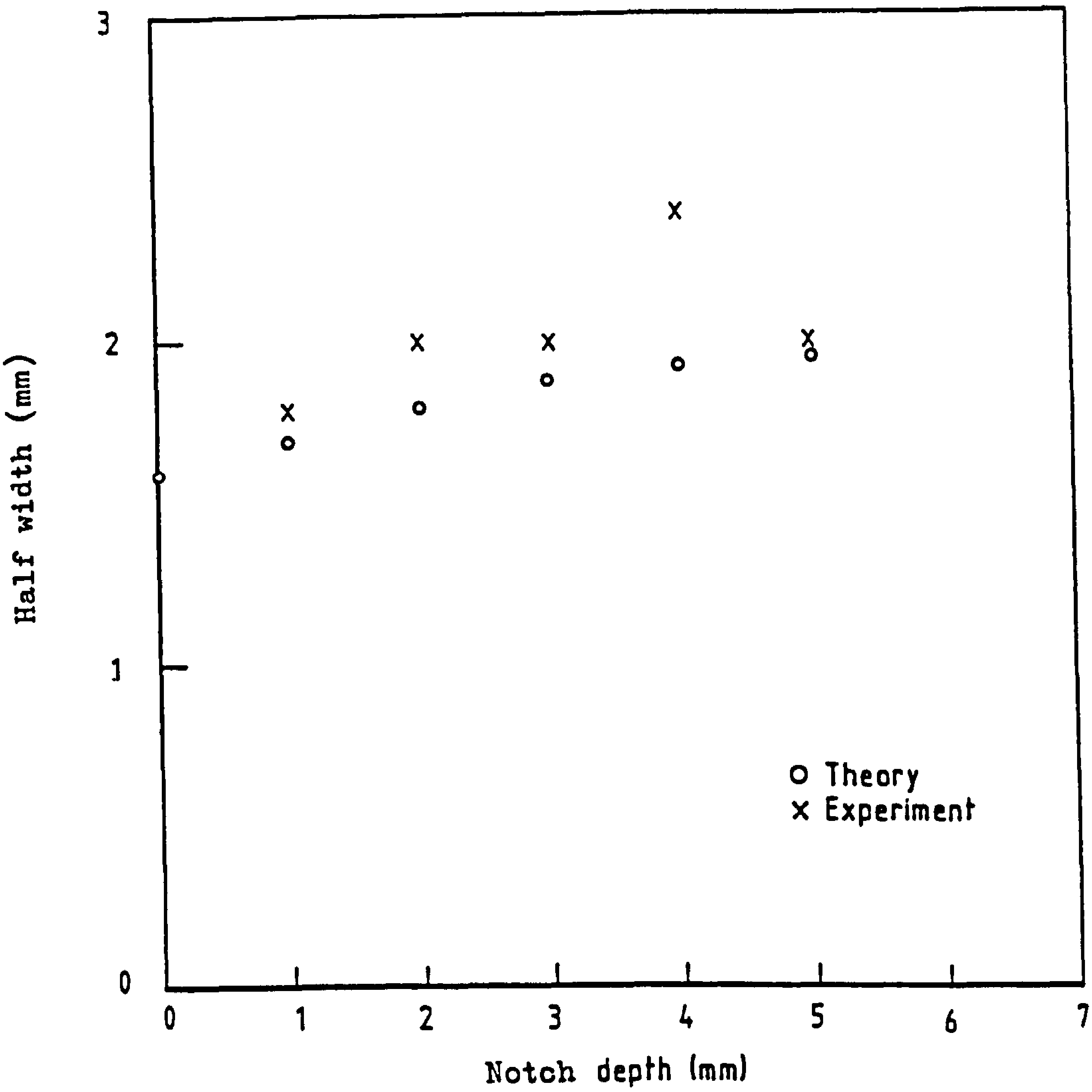

Figure 59. Theoretical and experimental variation of signal half width with notch depth.

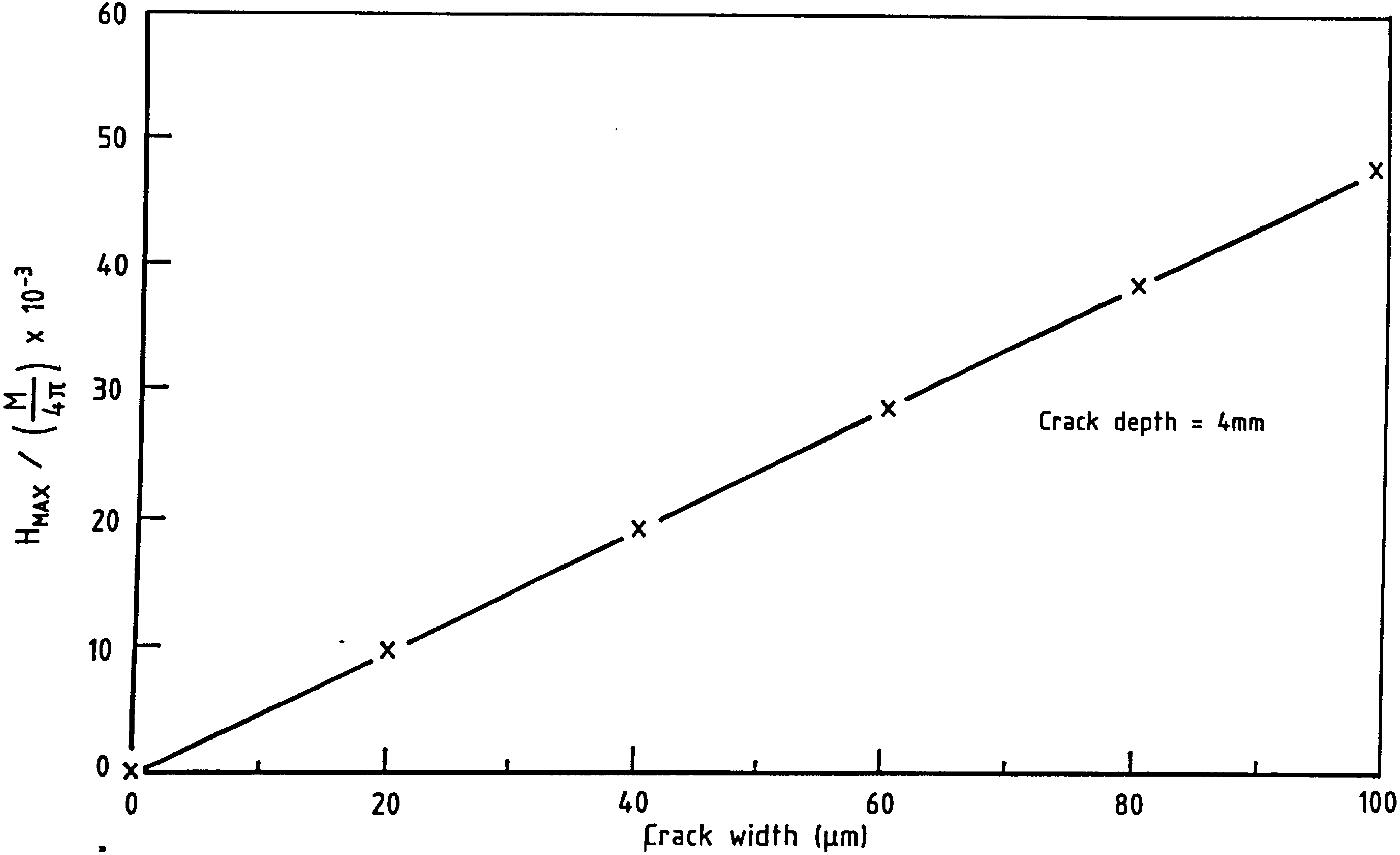

FIGURE 60. VARIATION OF SIGNAL AMPLITUDE WITH CRACK WIDTH USING FINITE PROBE THEORY.

'Crack' here refers to an equivalent artificial notch.

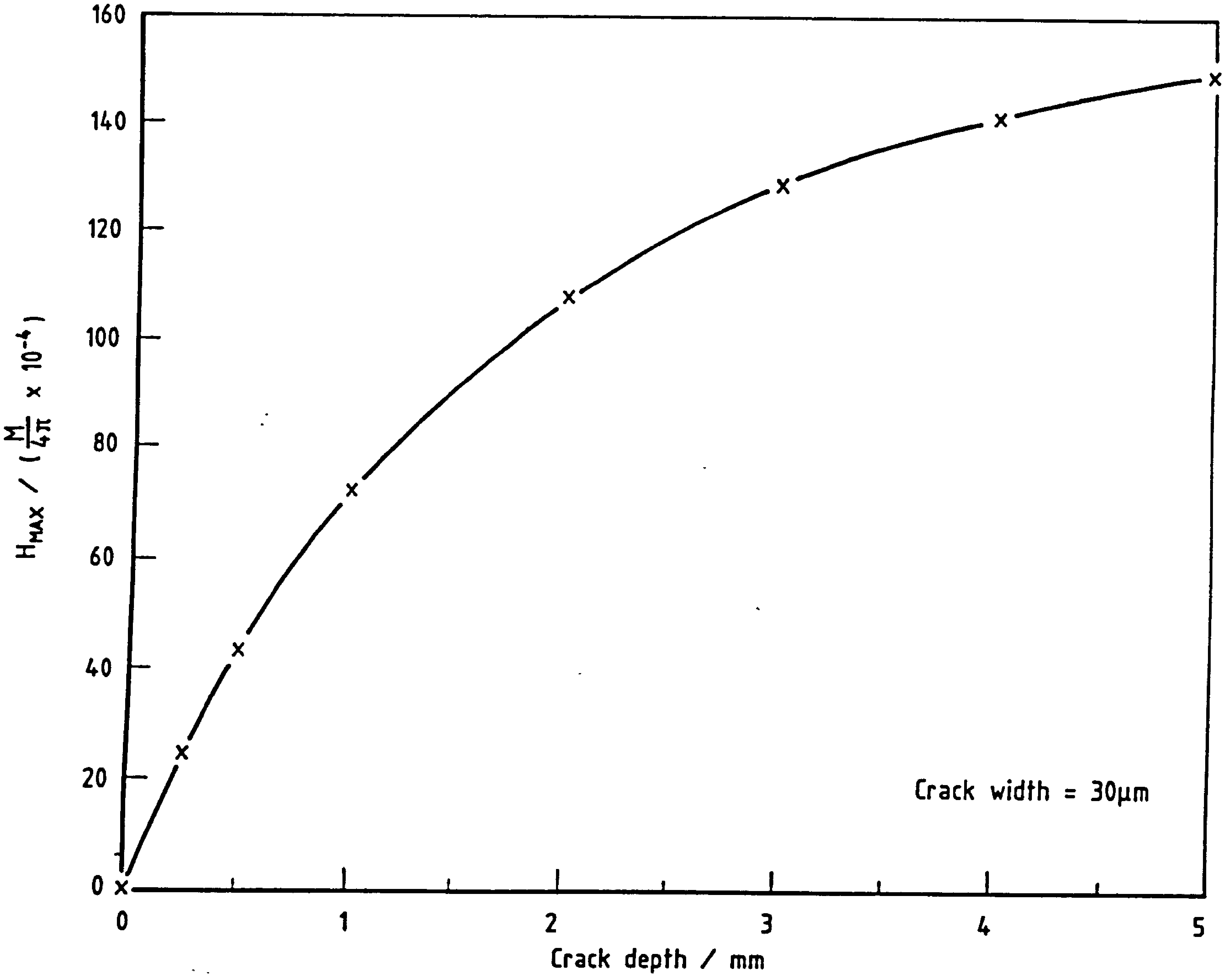

FIGURE 61. VARIATION OF SIGNAL AMPLITUDE WITH CRACK DEPTH USING FINITE PROBE THEORY.

'Crack' refers to an equivalent notch.

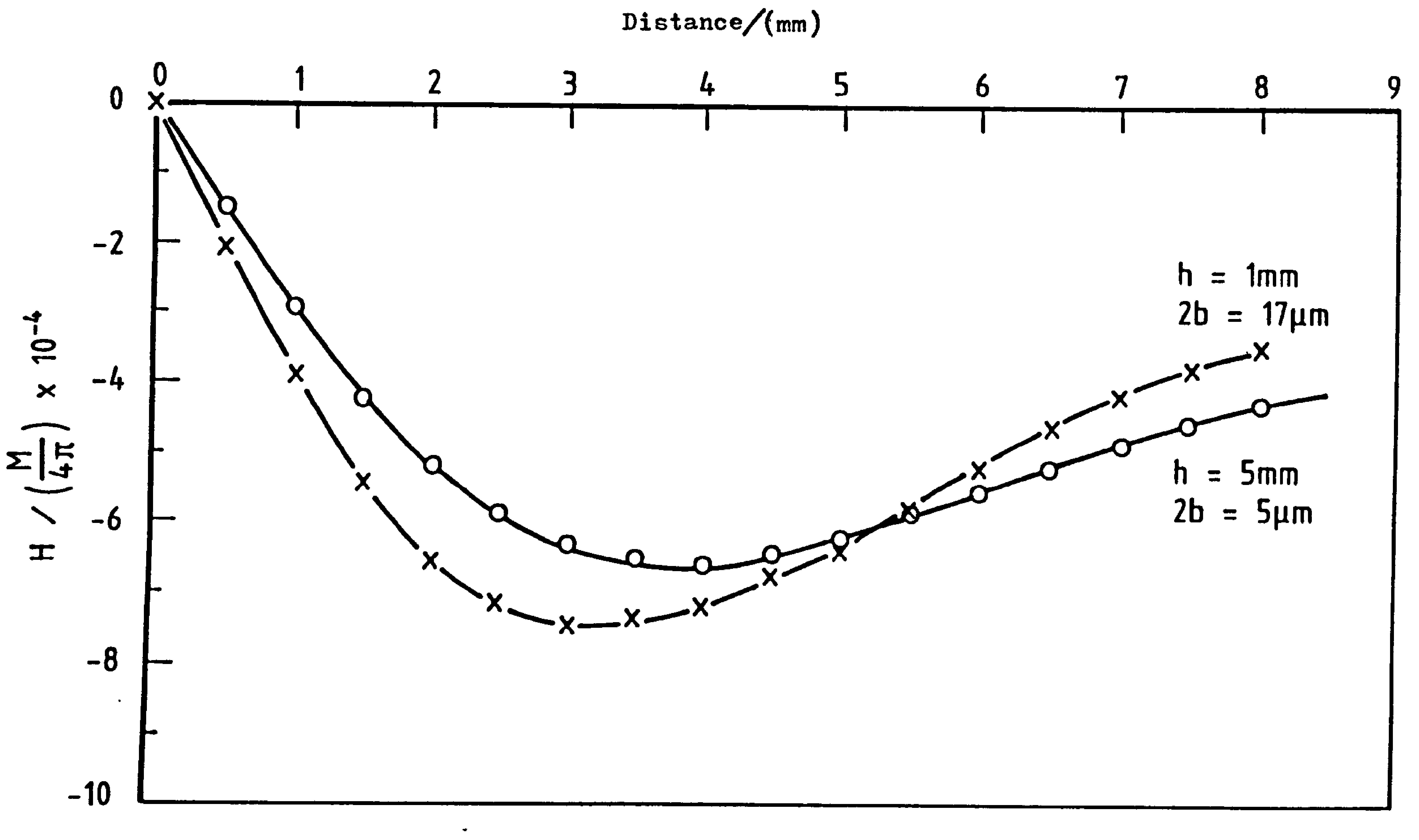

FIGURE 62. GRAPH SHOWING SIMILARITY OF SIGNALS FROM DIFFERENT CRACKS AT A SCAN HEIGHT OF 5mm.
'Crack' refers to an equivalent notch.

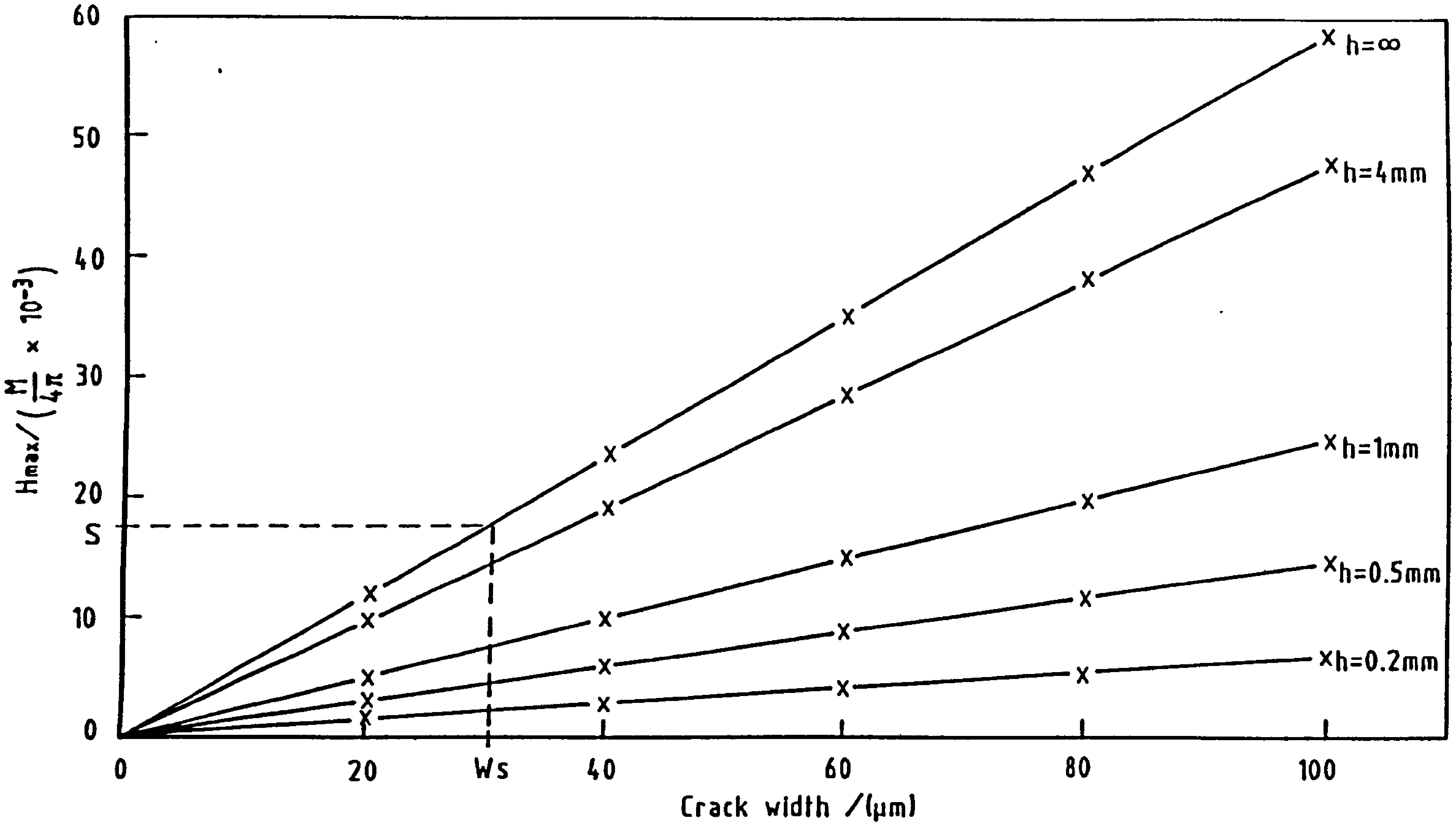

Figure 63. GRAPH TO SHOW PEAK SIGNAL AS A FUNCTION OF CRACK WIDTH AND DEPTH h.

'Crack' refers to an equivalent notch.

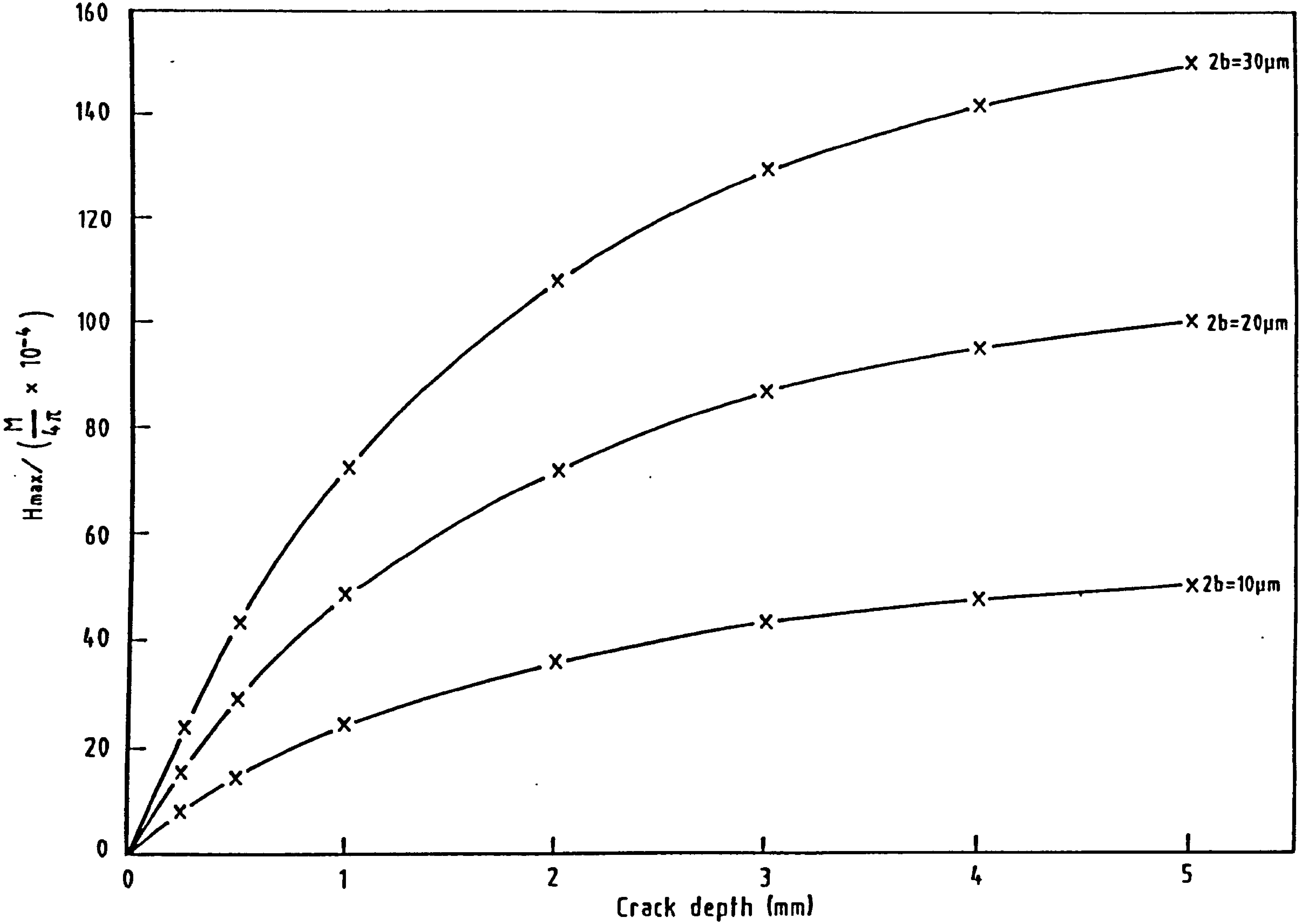

Figure 64. ALTERNATIVE DISPLAY OF H_{max} AS A FUNCTION OF CRACK DEPTH AND HEIGHT.

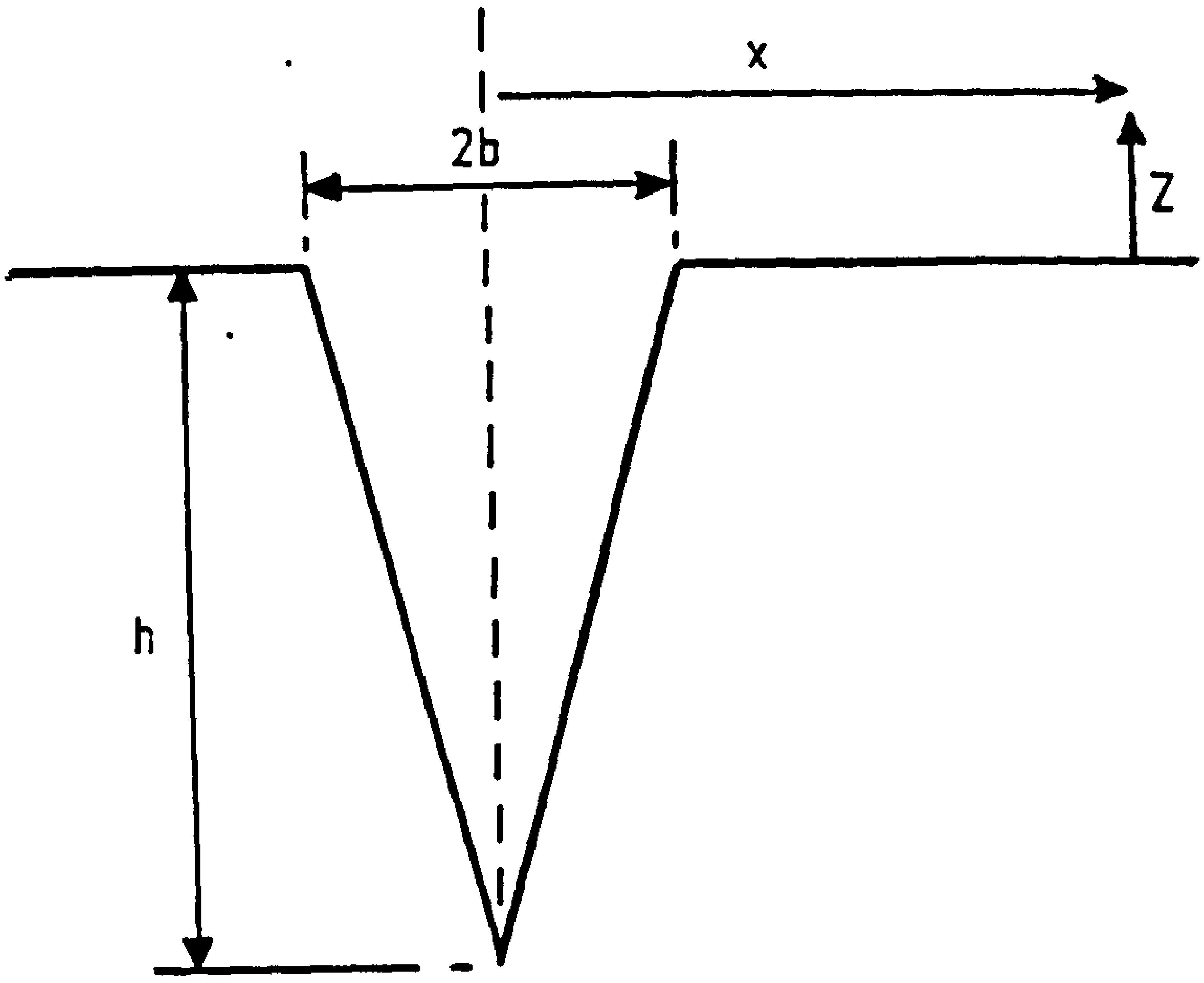

Figure 65. A tapered crack.

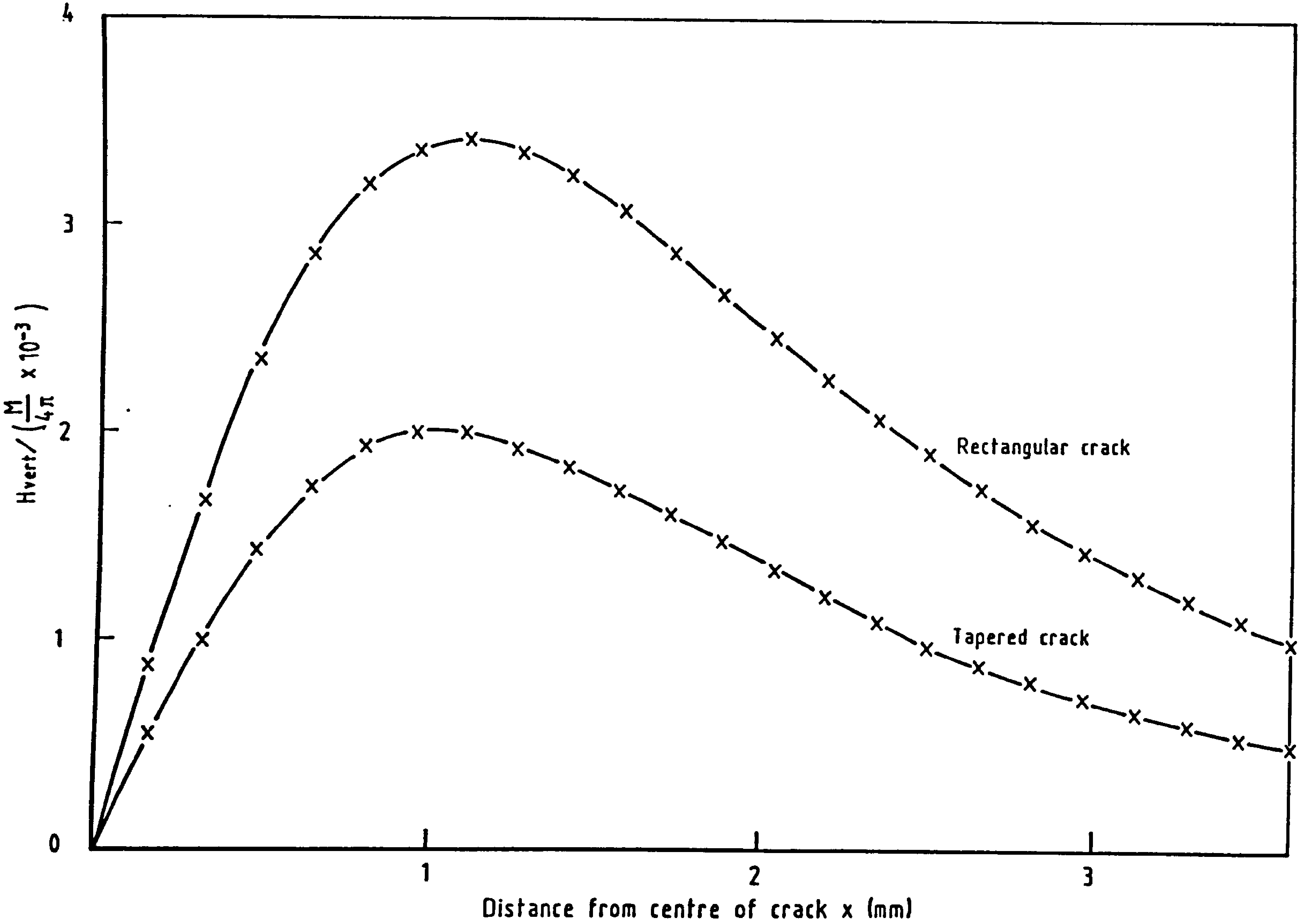

Figure 66. GRAPH TO SHOW THE EFFECT OF A TAPERED CRACK ON THE OBSERVED SIGNAL.

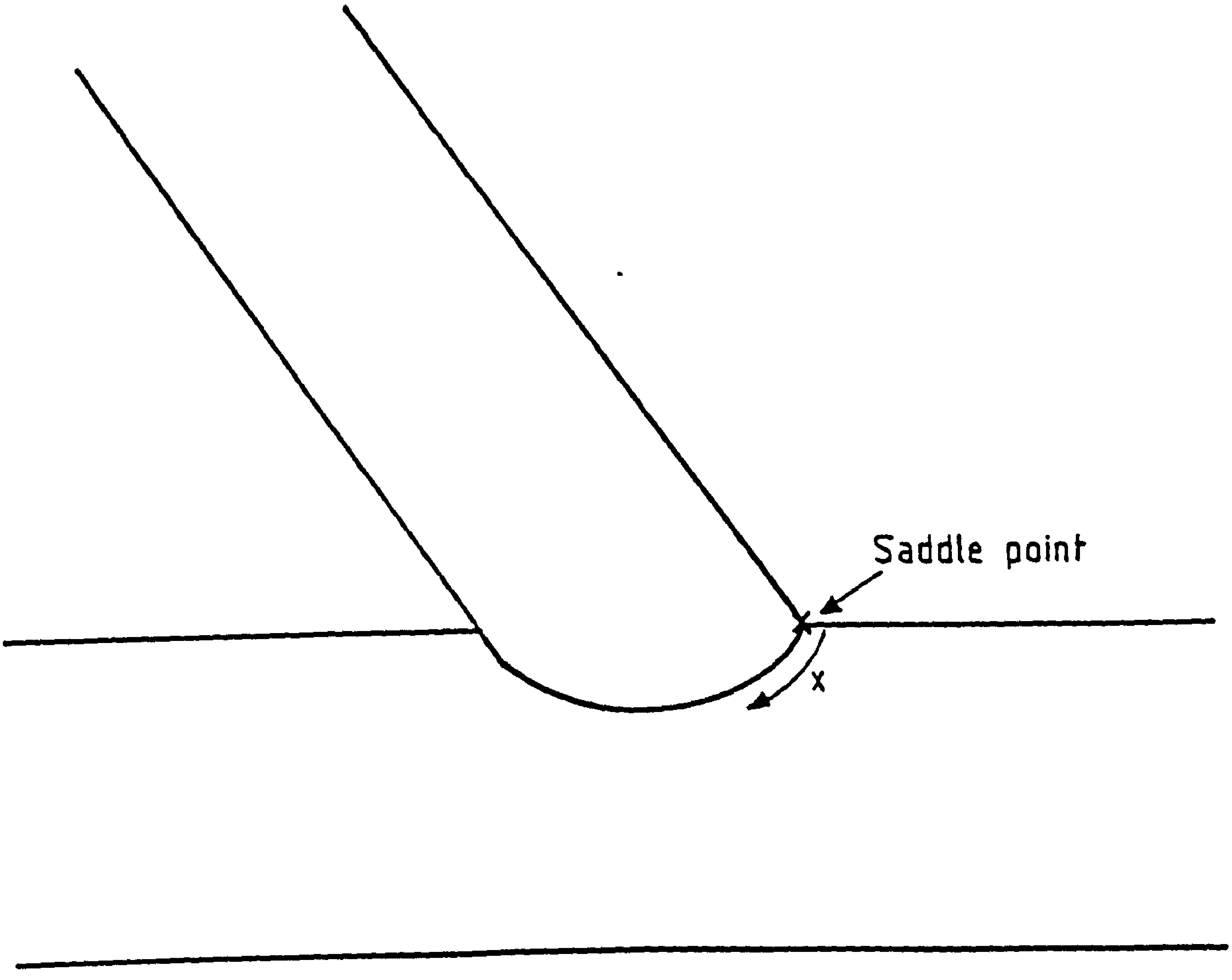

Figure 67. A cracked Y-joint.

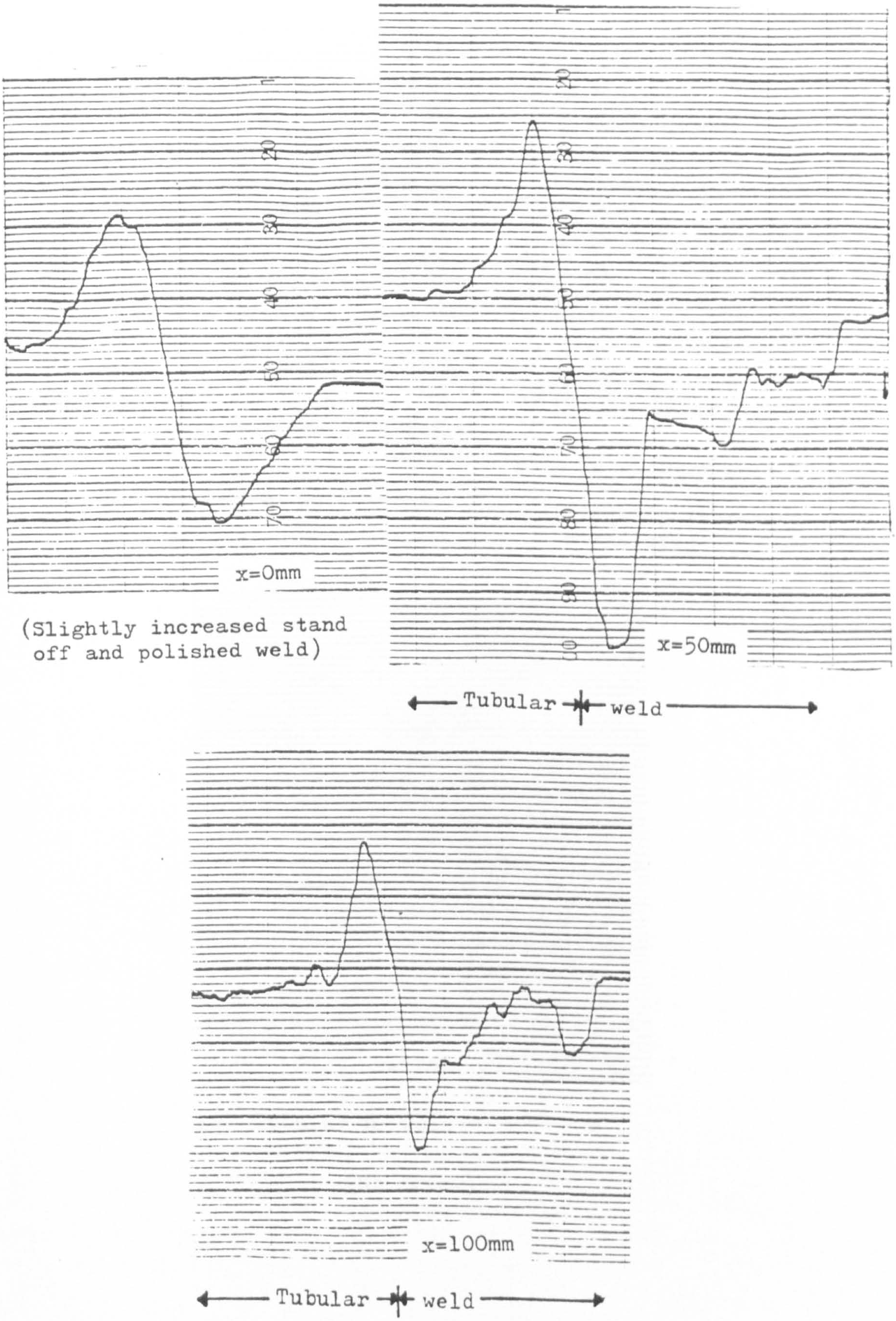

(Slightly increased stand off and polished weld)

Figure 68. Crack signatures produced from Y-joint.

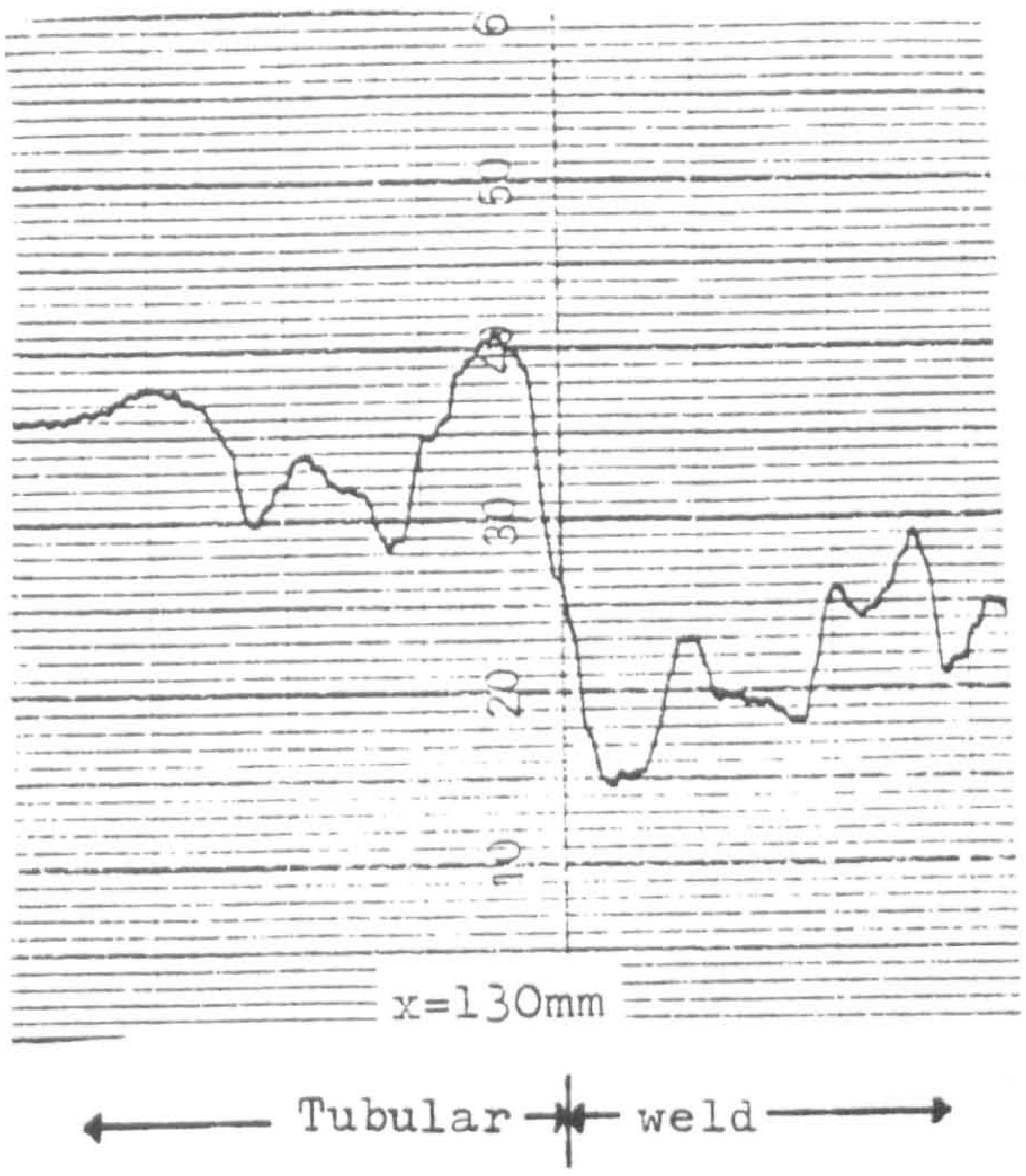

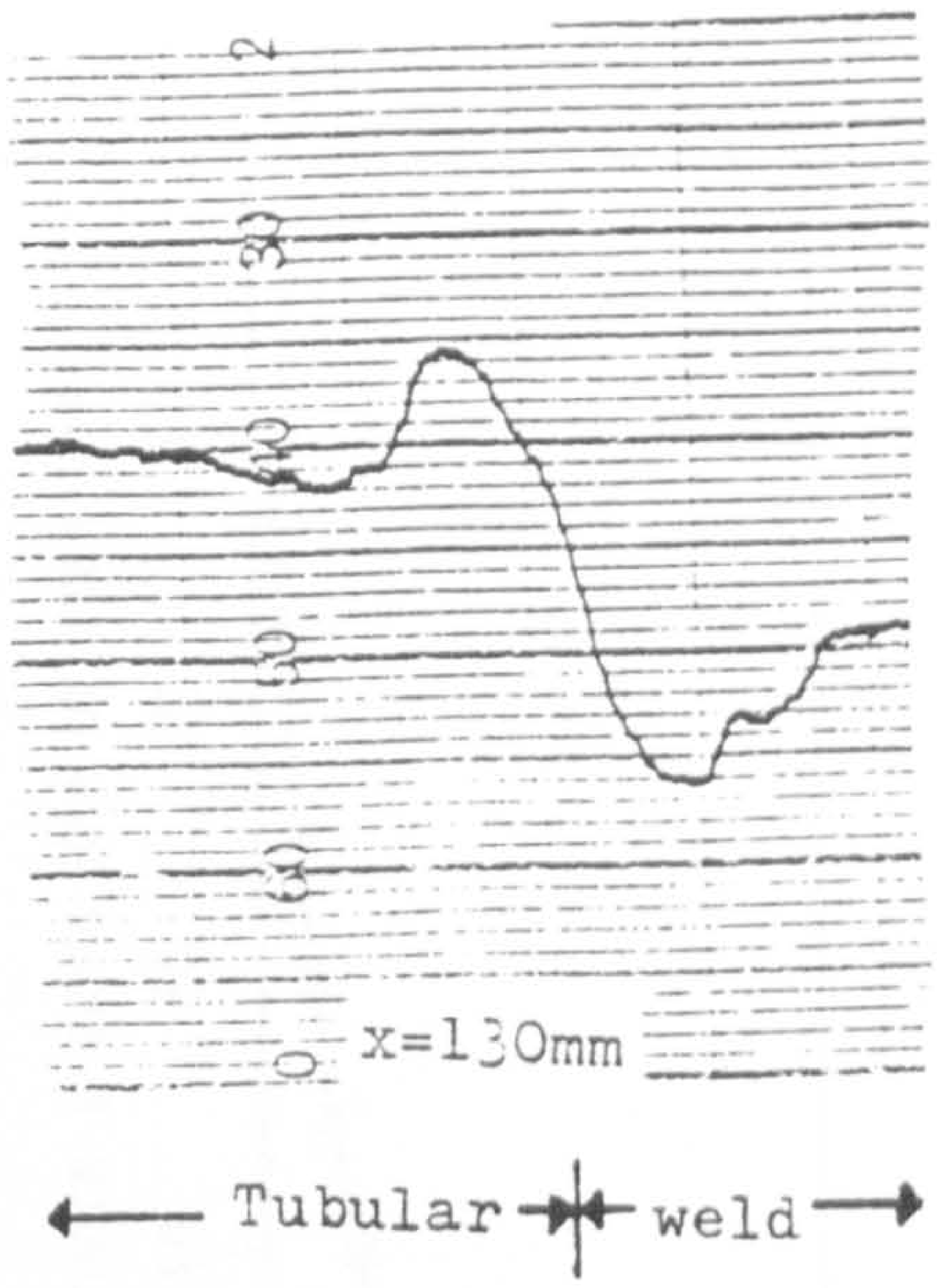

(Slightly increased stand off)

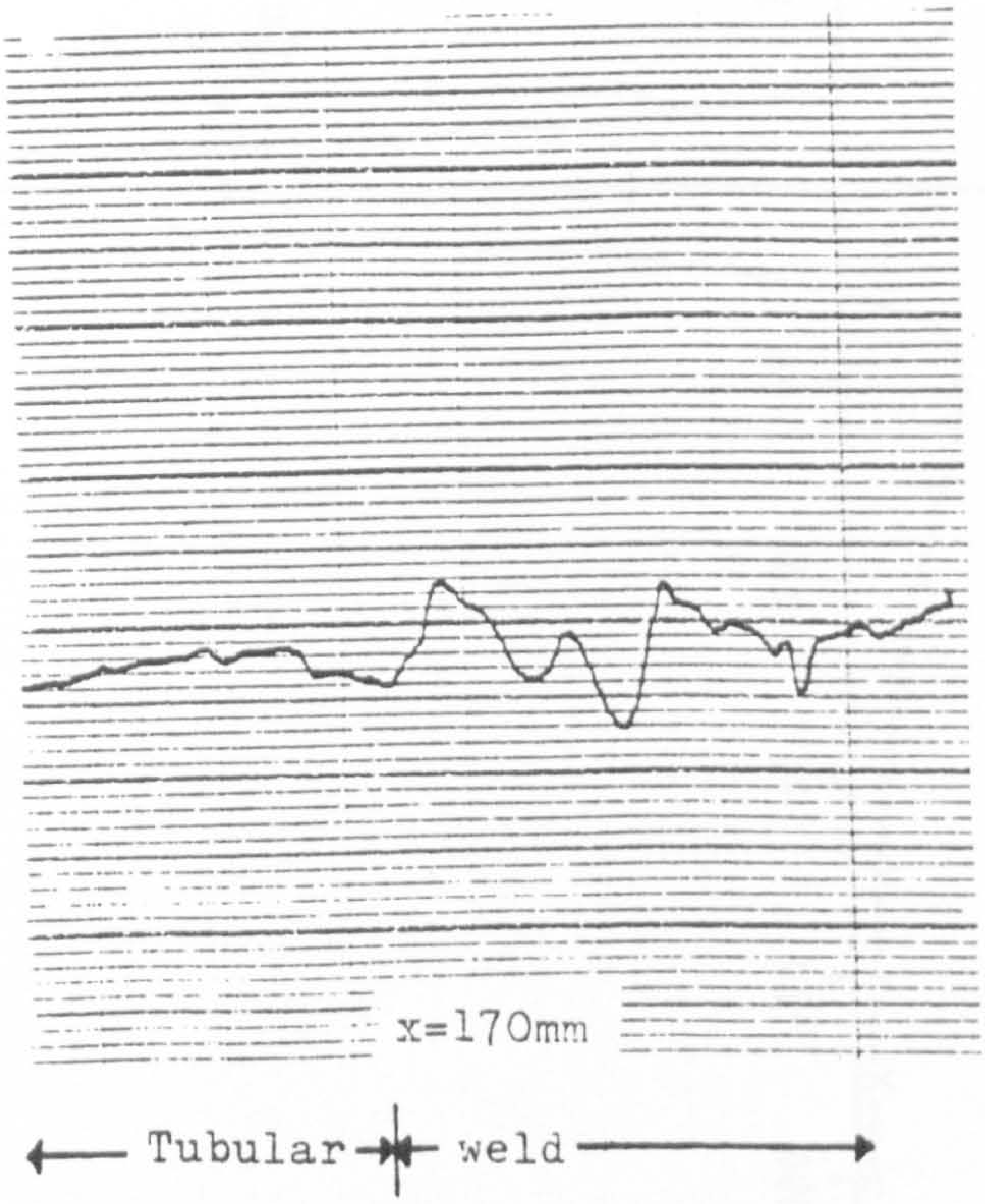

(No crack)

Figure 69. More crack signatures produced from Y-joint.

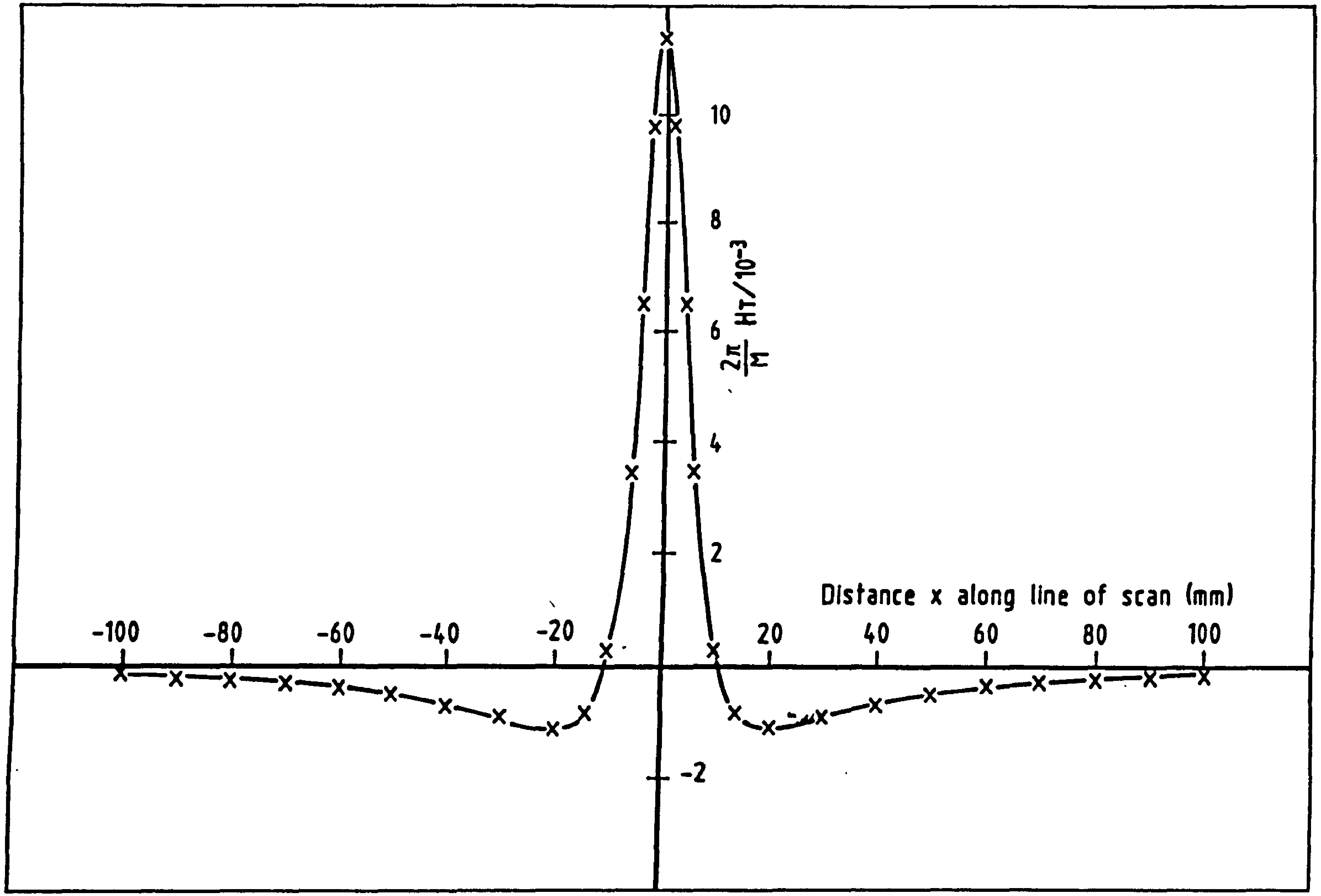

FIGURE 70. THEORETICAL TRANSVERSE MAGNETIC SIGNAL FOR 2b=0.1mm, h=13mm AND z=6mm

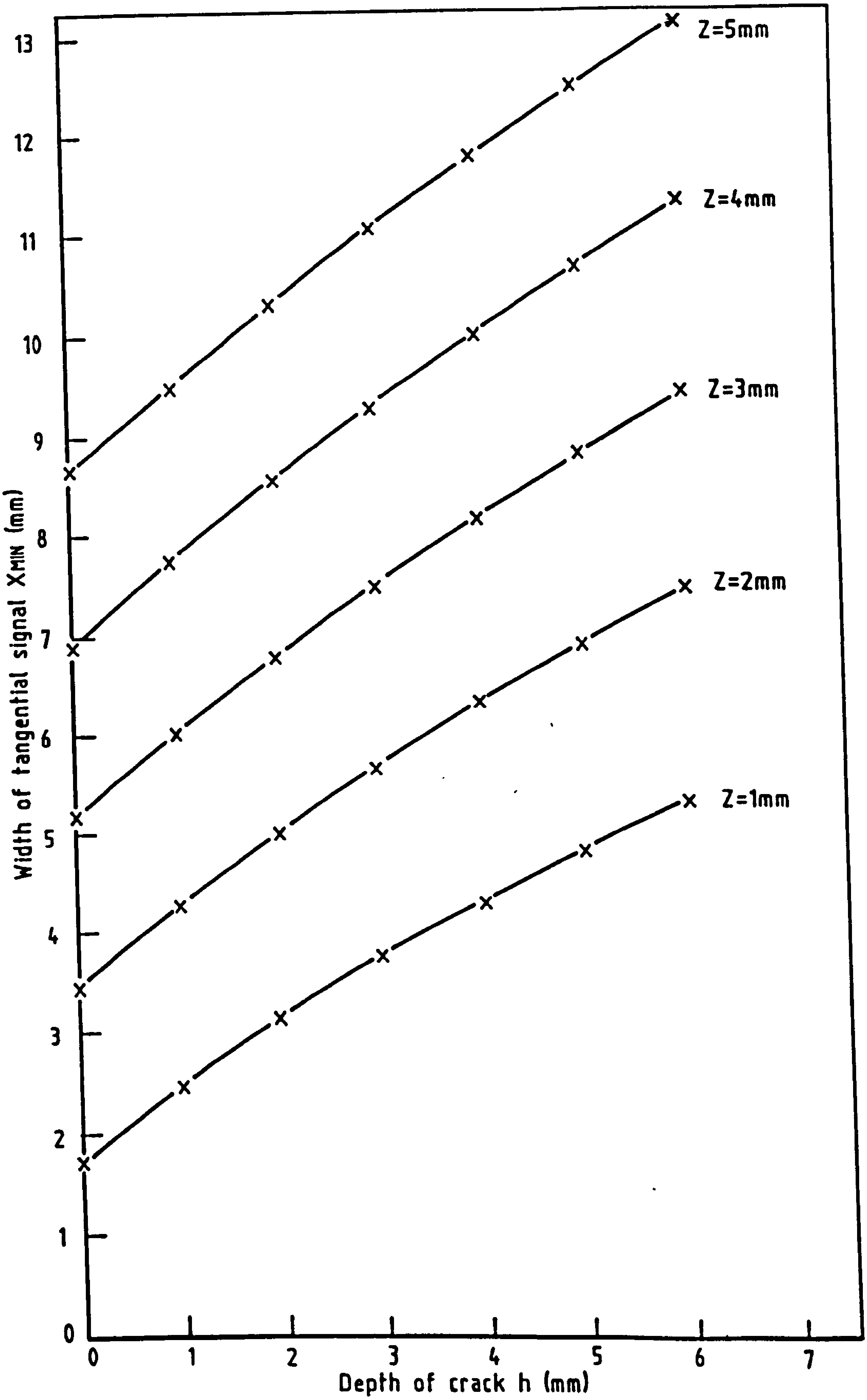

FIGURE 71. THEORETICAL SIGNAL WIDTH VARIATION WITH CRACK DEPTH h AND SCAN HEIGHT Z

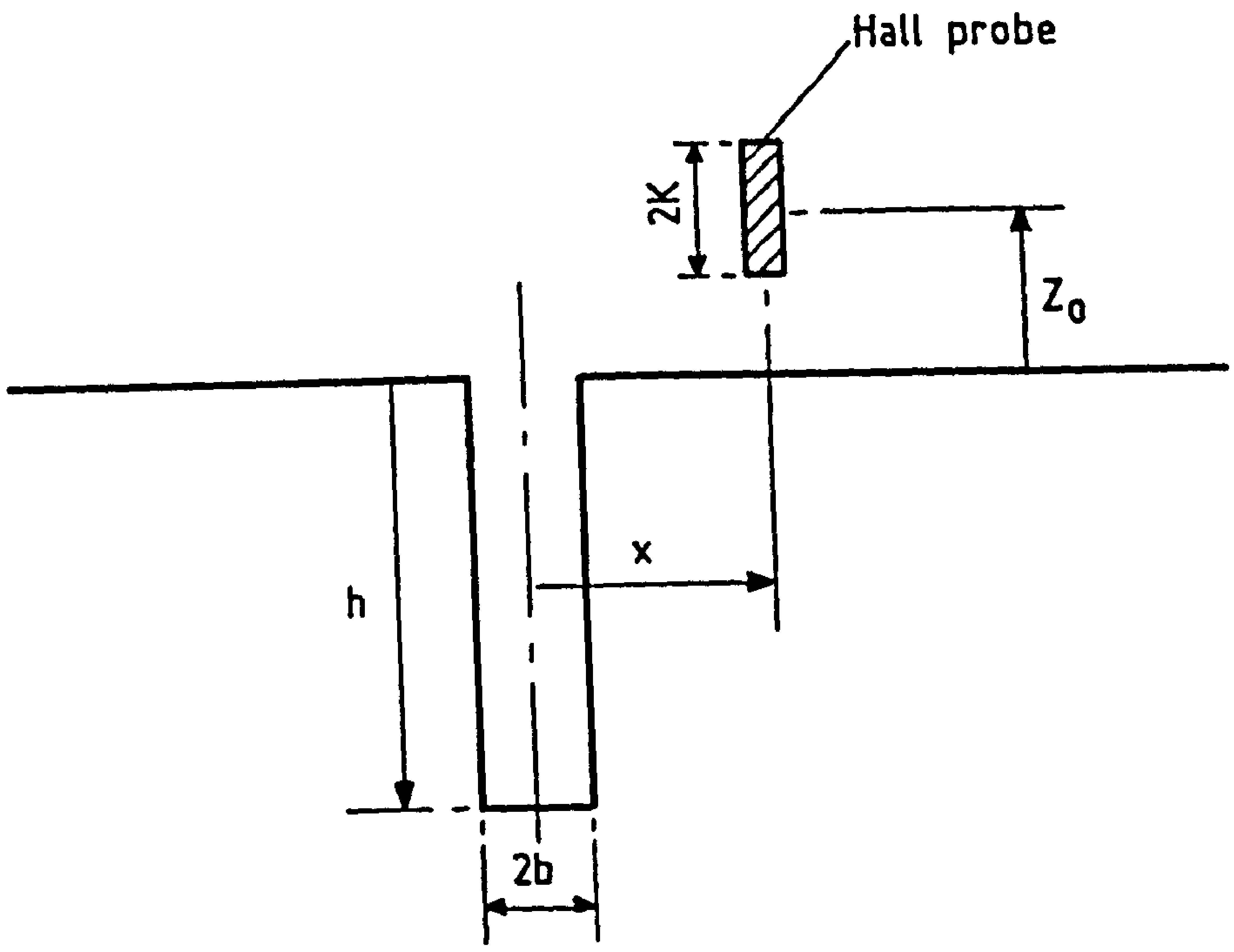

Figure 72. The application of a finite probe to the measurement of the tangential signal.

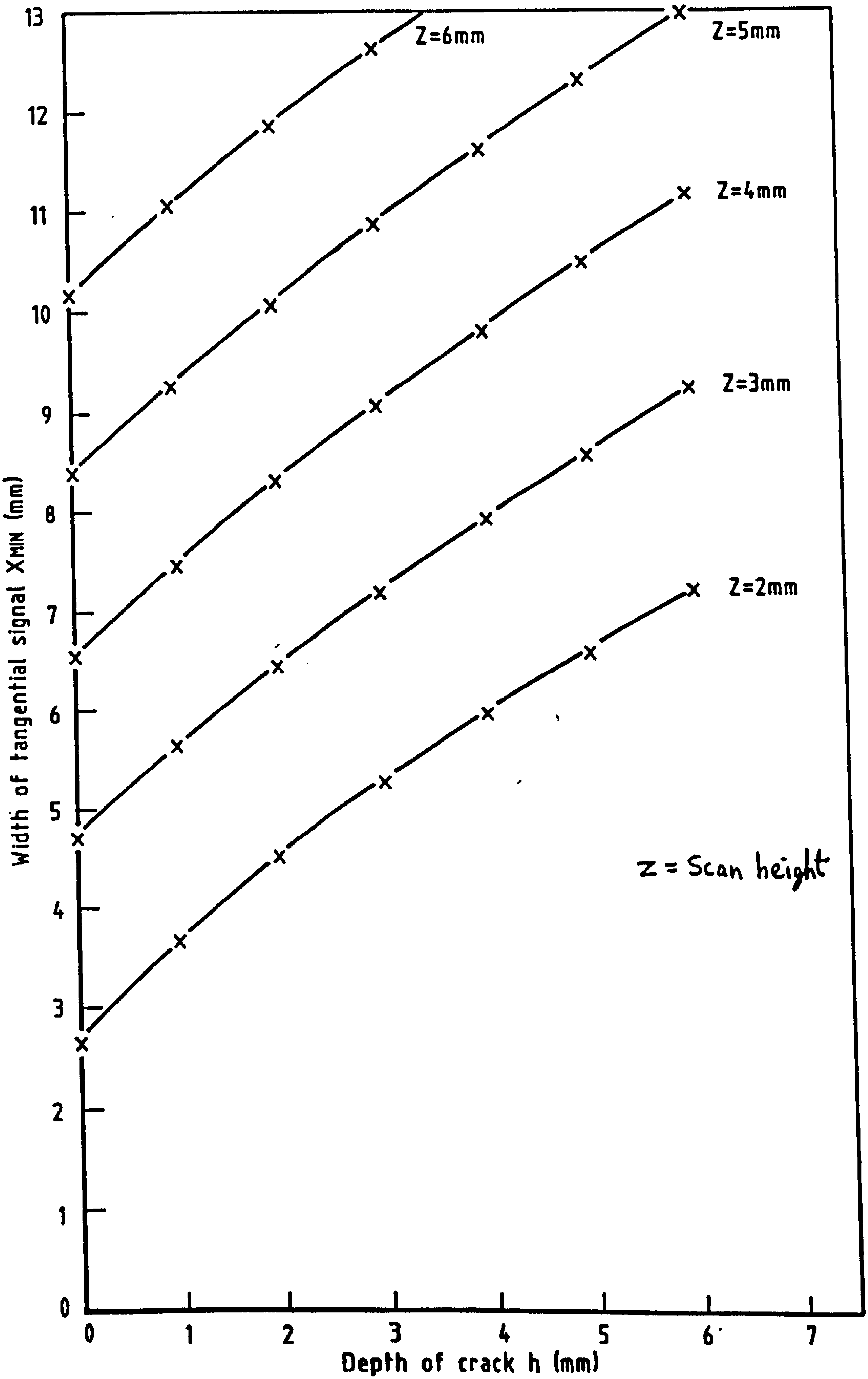

FIGURE 73. THEORETICAL VARIATION OF SIGNAL WIDTH FOR THE CASE OF A FINITE PROBE OF SIZE 2K=3mm

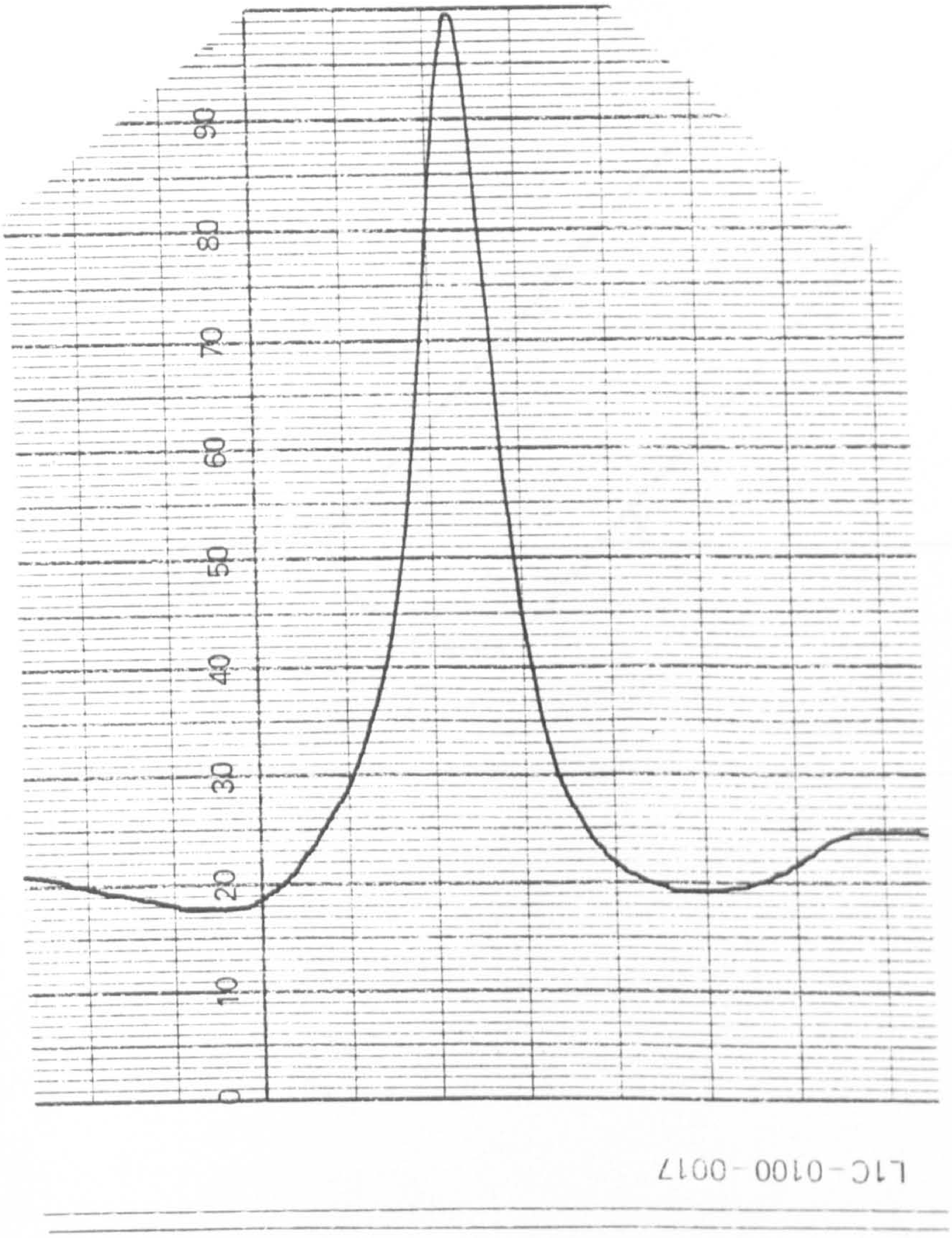

Figure 74. Tangential signal from a 13mm deep notch.

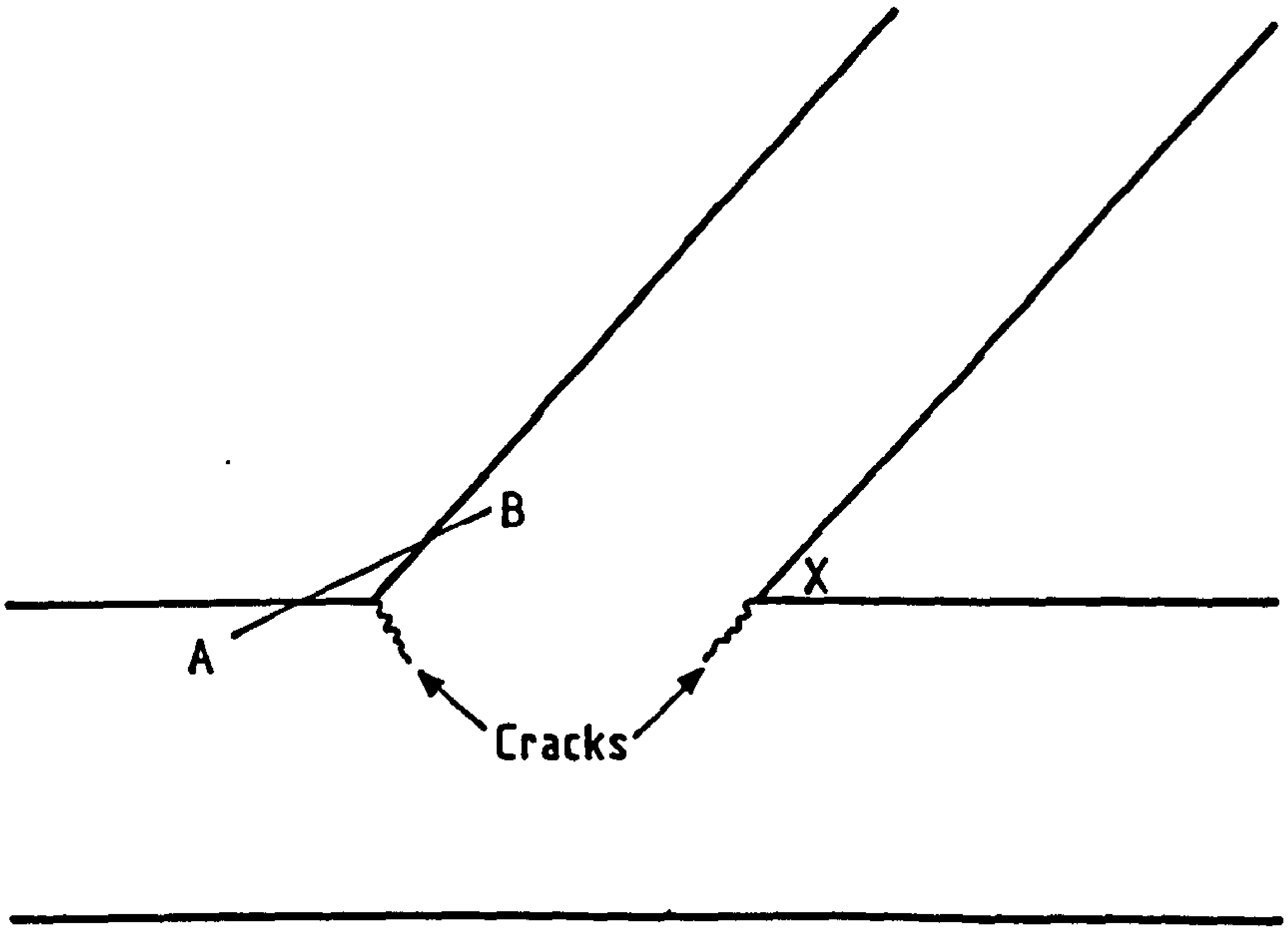

FIGURE 75. CONSIDERATION OF THE APPLICATION OF THE TANGENTIAL COMPONENT TO Y-JOINT.

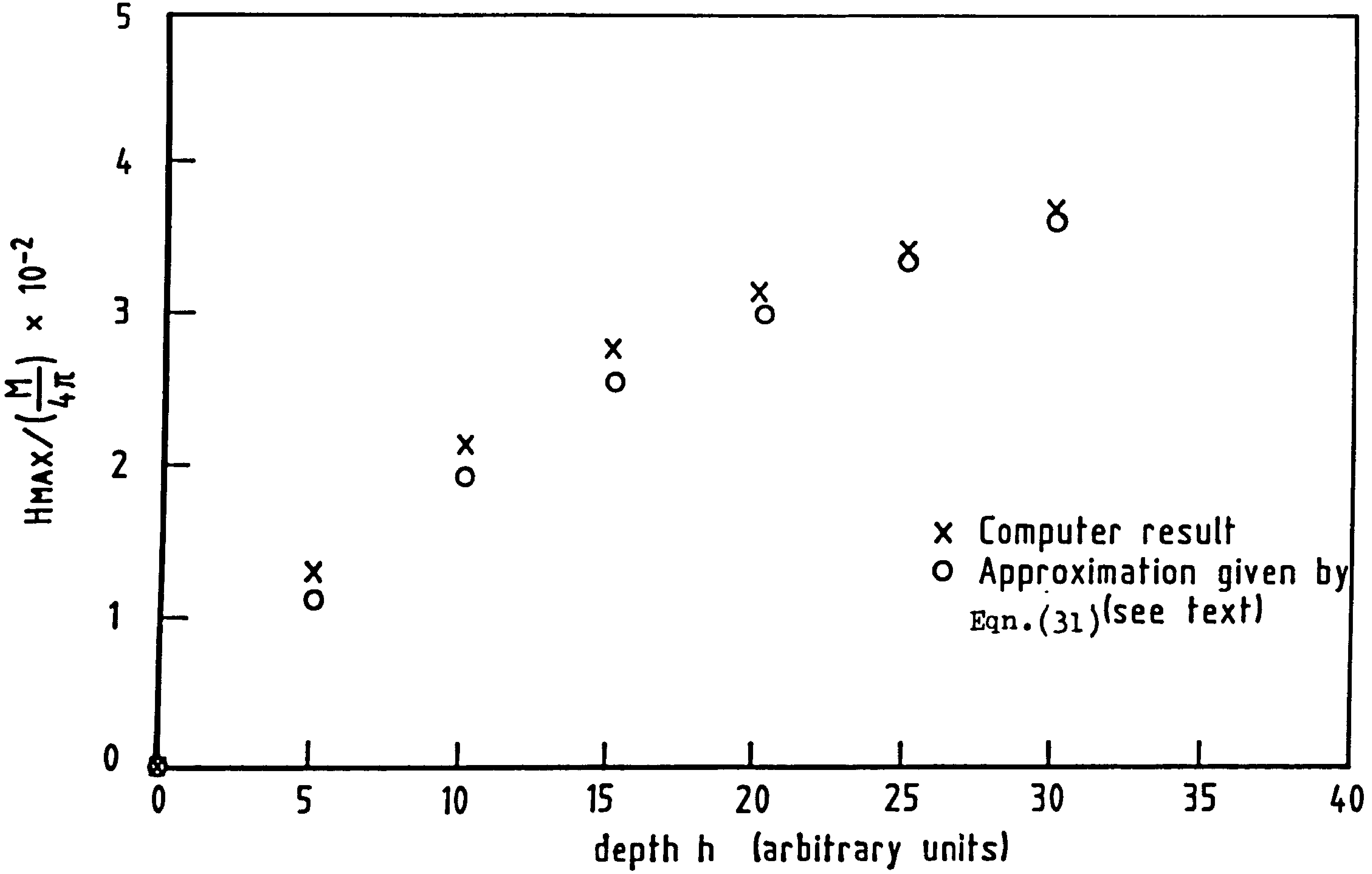

FIGURE 76. DEPENDENCE OF H_{MAX} ON h FOR b=0.5 AS PLOTTED BY COMPUTER AND USING EQU.(31).

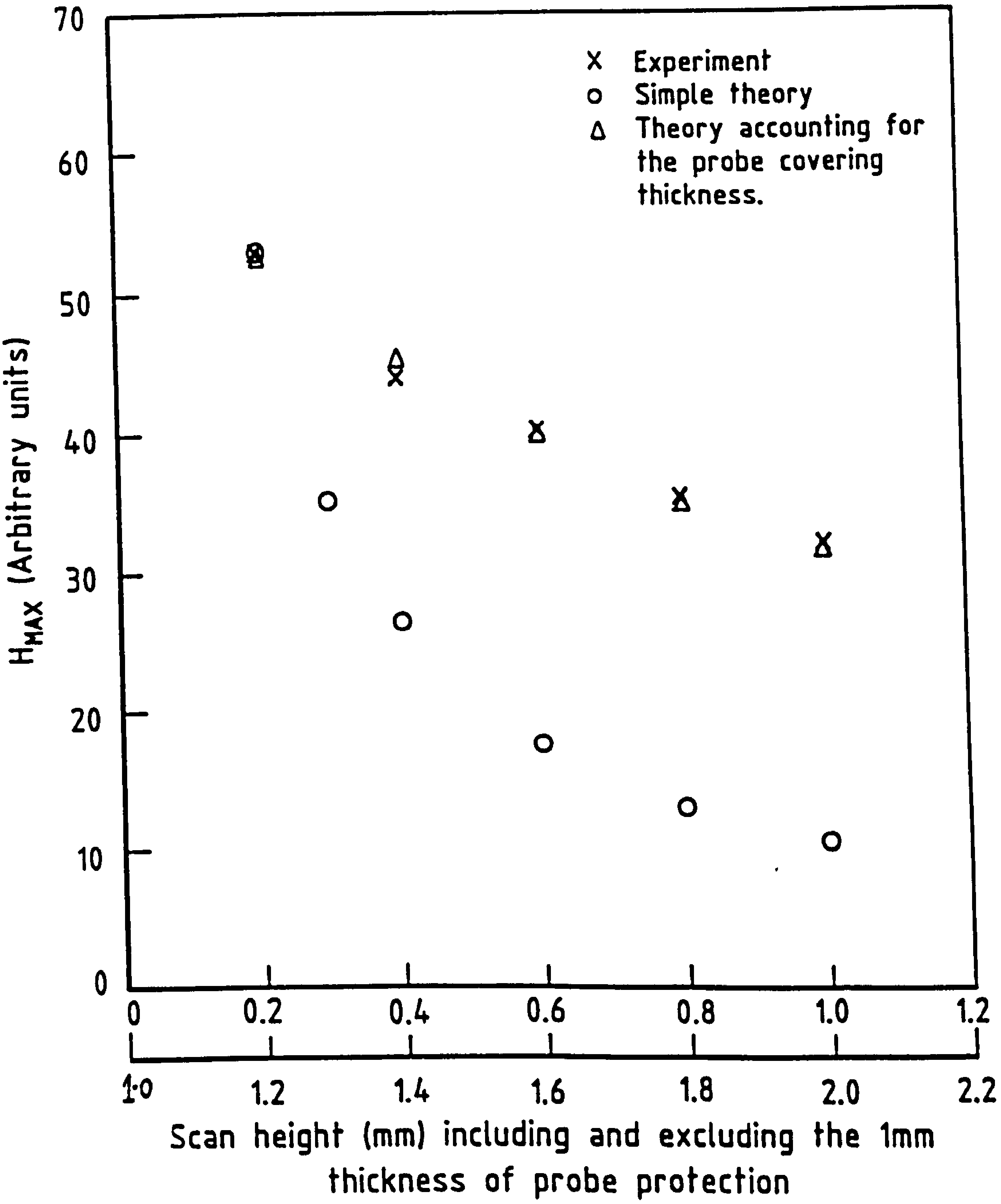

FIGURE 77. THEORETICAL AND EXPERIMENTAL VARIATION OF H_{MAX} WITH SCAN HEIGHT.

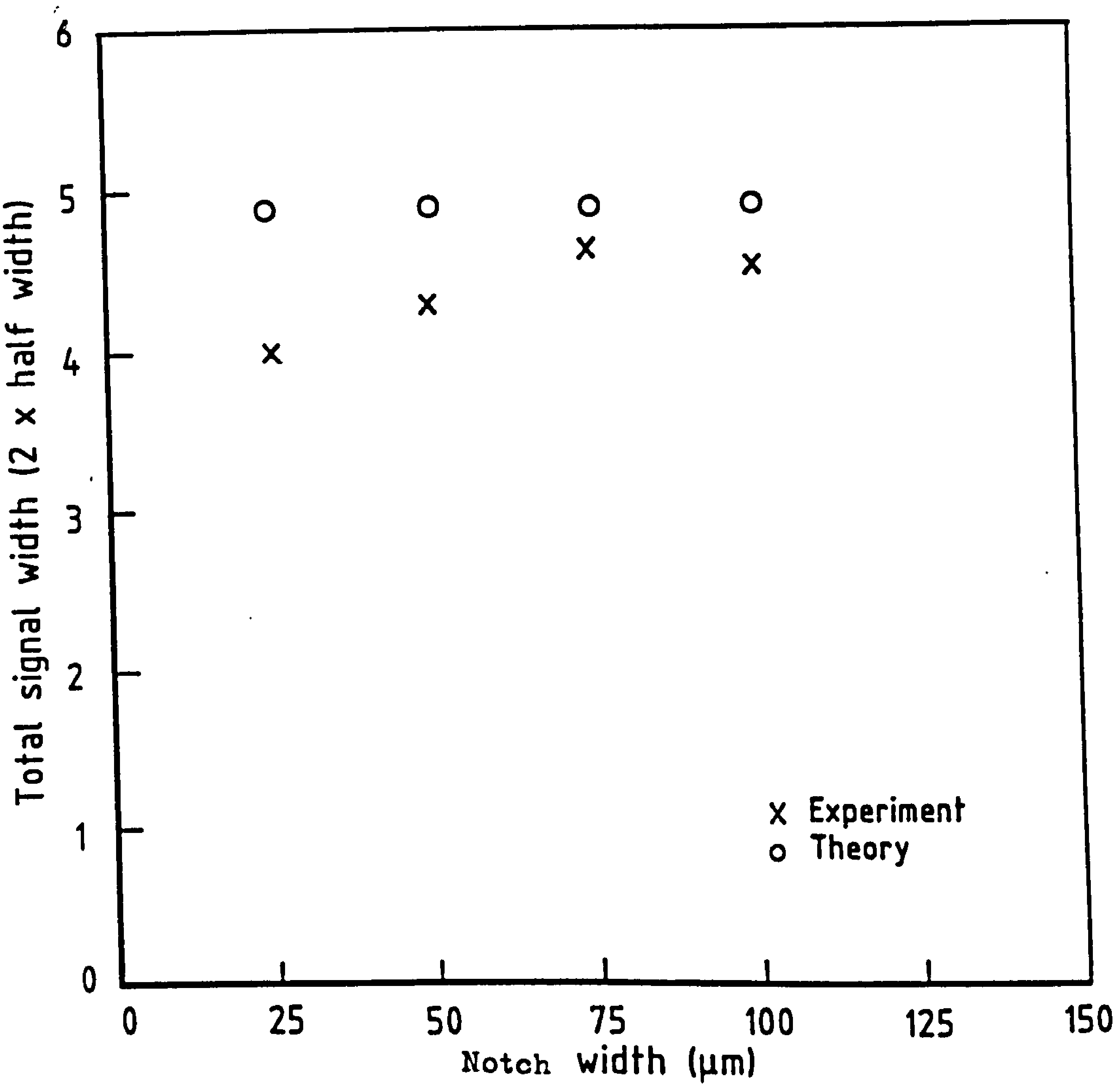

FIGURE 78. THEORETICAL AND EXPERIMENTAL VARIATION OF SIGNAL WIDTH WITH notch WIDTH FOR WIDTH OF PROBE 2K = 1mm AND SCAN HEIGHT Z = 2.5mm.

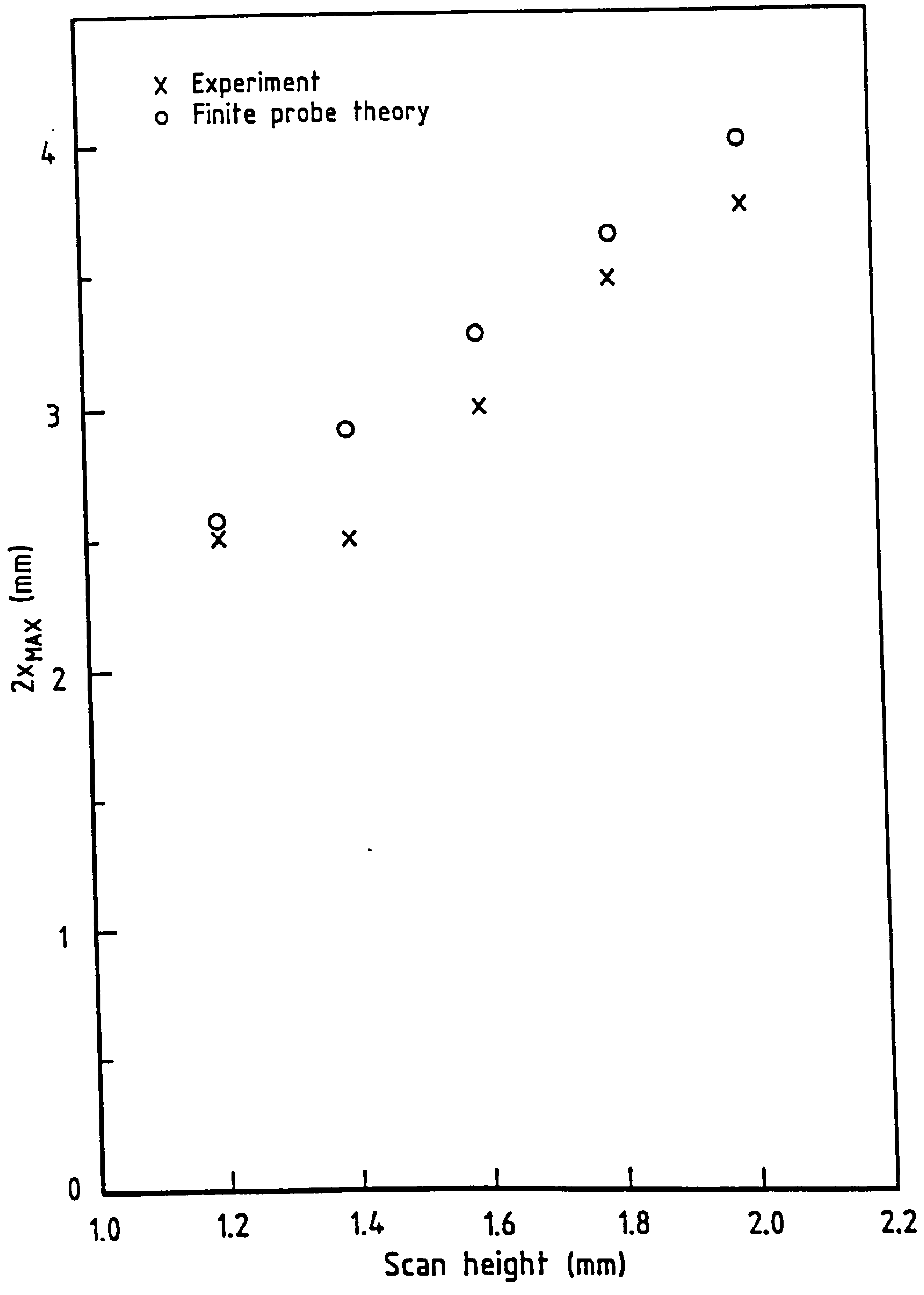

FIGURE 79. THEORETICAL AND EXPERIMENTAL VARIATION OF x_{MAX} WITH SCAN HEIGHT (Assuming width of probe 2K = 1mm)

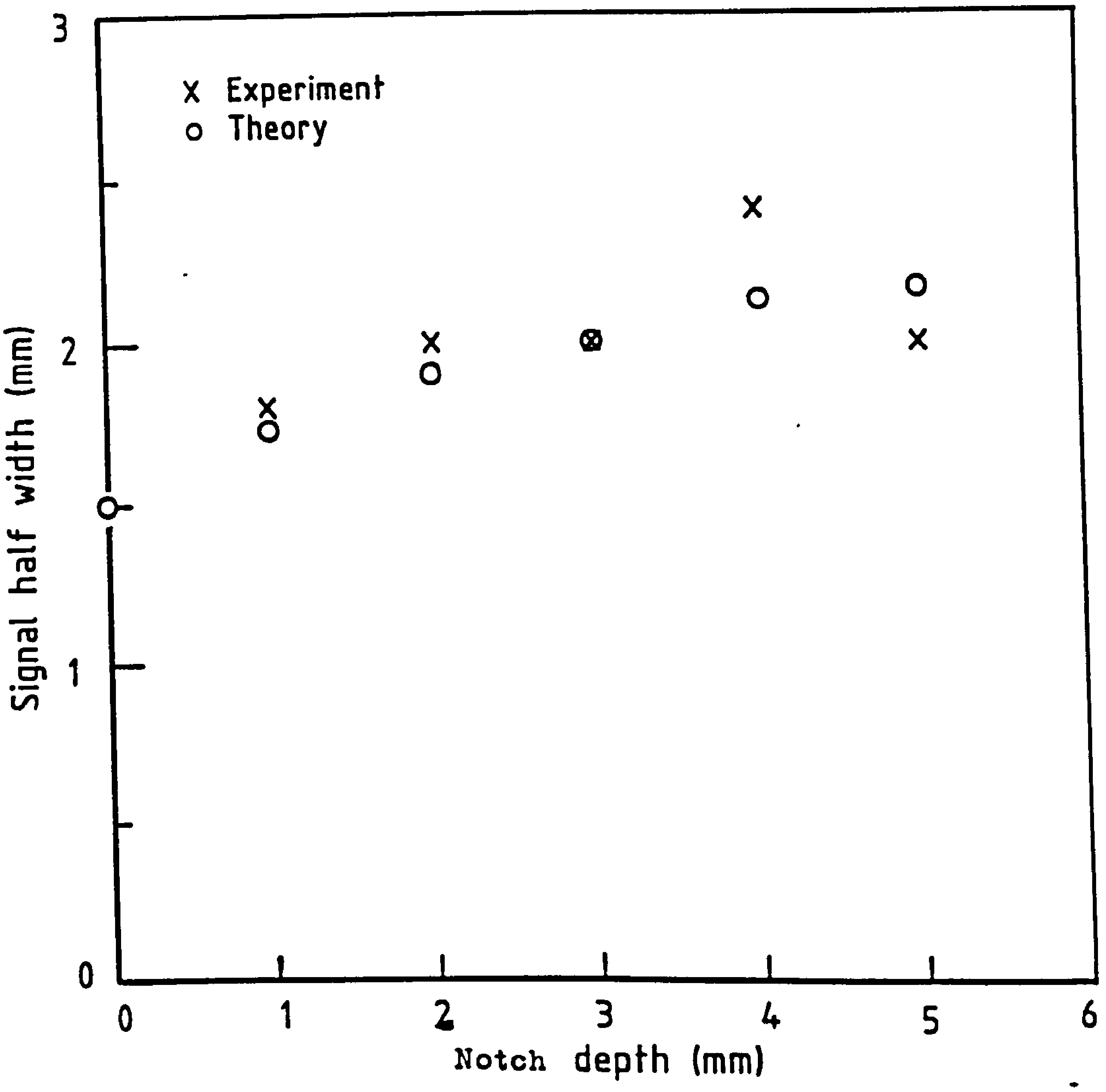

FIGURE 80. THEORETICAL AND EXPERIMENTAL VARIATION OF SIGNAL WIDTH WITH notch DEPTH. A PROBE WIDTH OF 2K = 1mm IS ASSUMED.

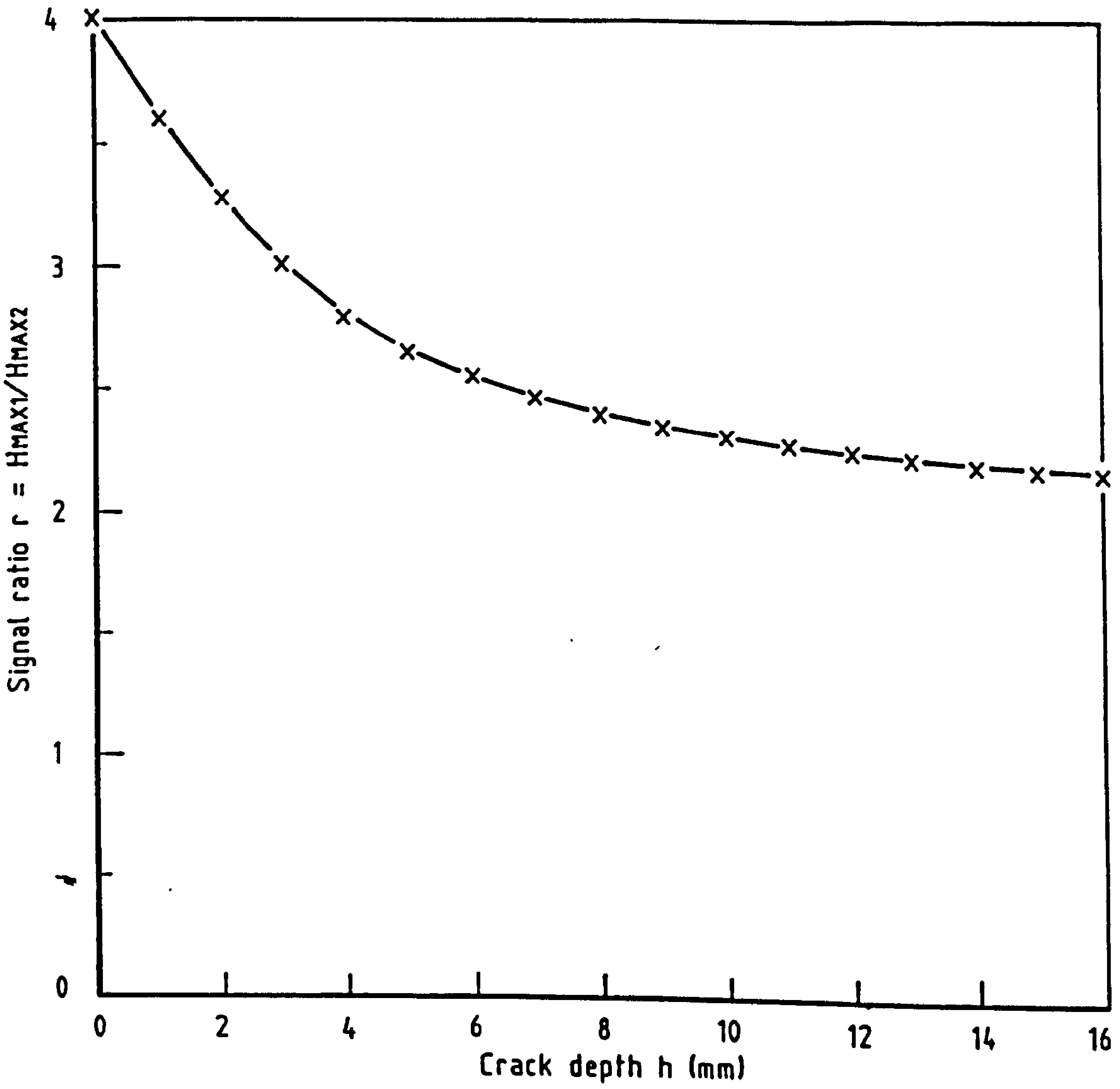

FIGURE 81. VARIATION IN r WITH h FOR Z_1=2.5mm, Z_2=5mm. Z_1 and Z_2 ARE THE PROBE SCAN HEIGHTS.

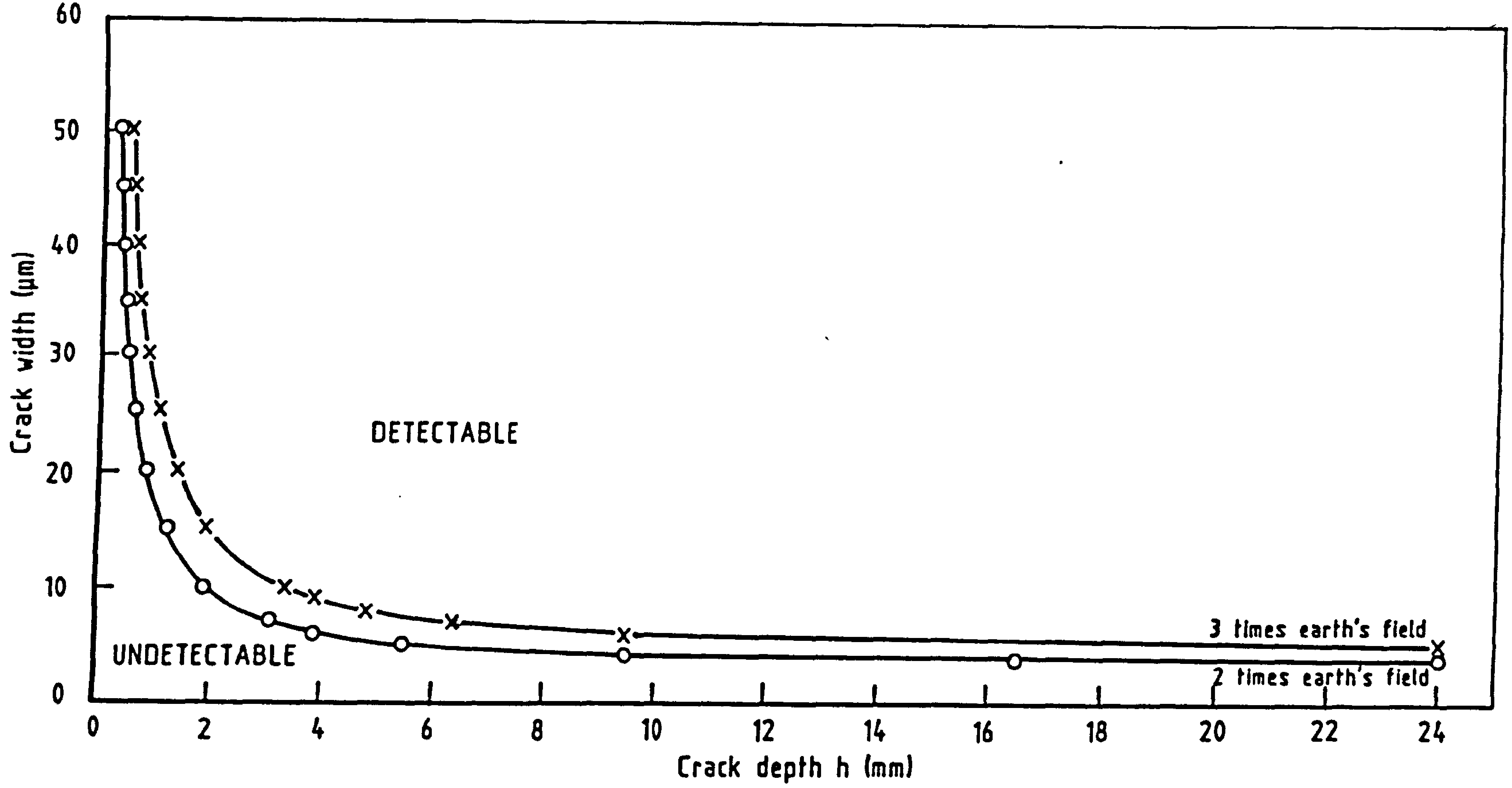

FIGURE 82. GRAPH SHOWING VALUES OF DEPTH AND WIDTHS OF CRACK WHICH ARE DETECTABLE UNDER CONDITIONS OF 5mm STAND OFF AND 0.72 TESLA MAGNETISATION.

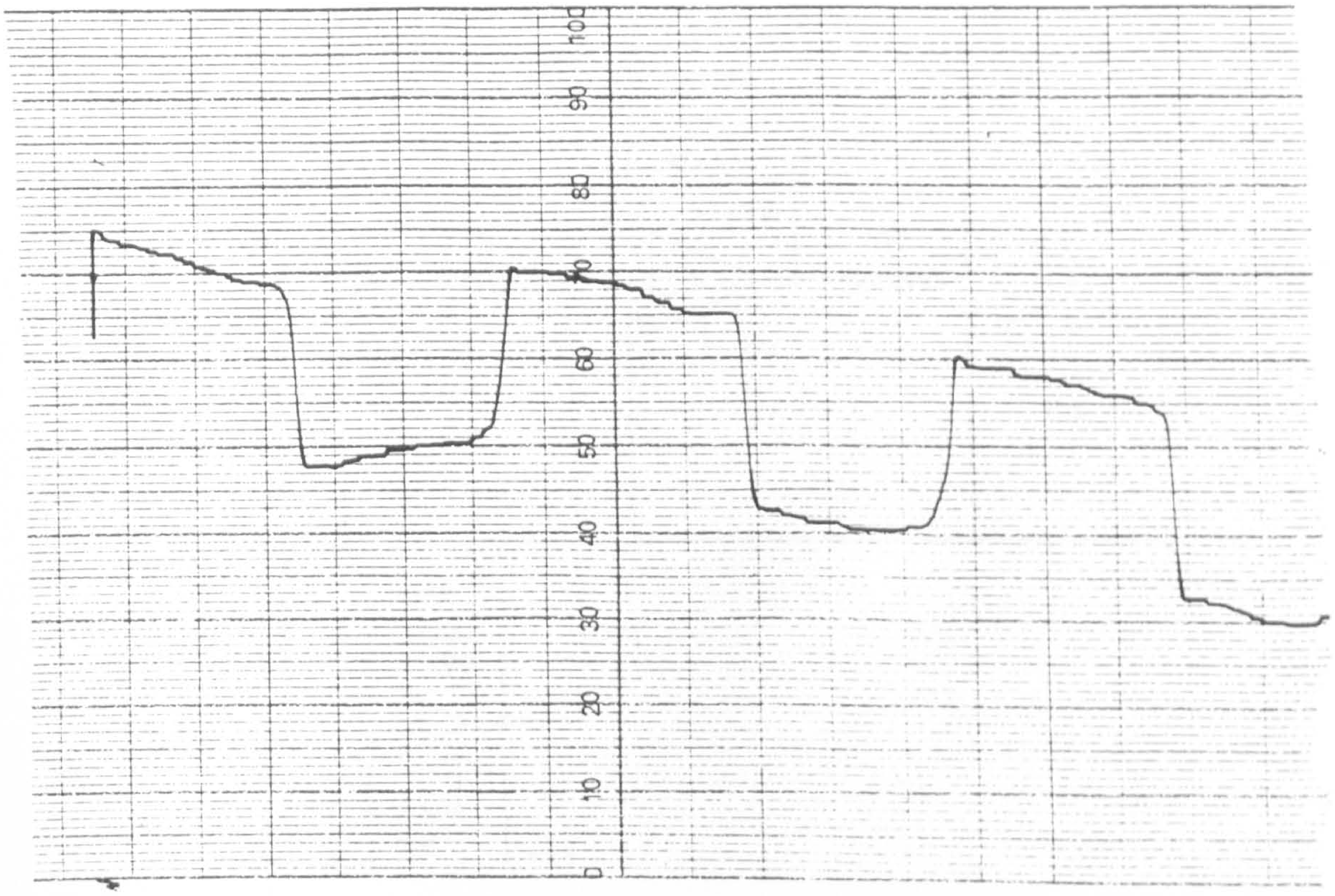

Figure 83. Detection of the earth's field (2 x 0.18 gauss) showing thermal drift.

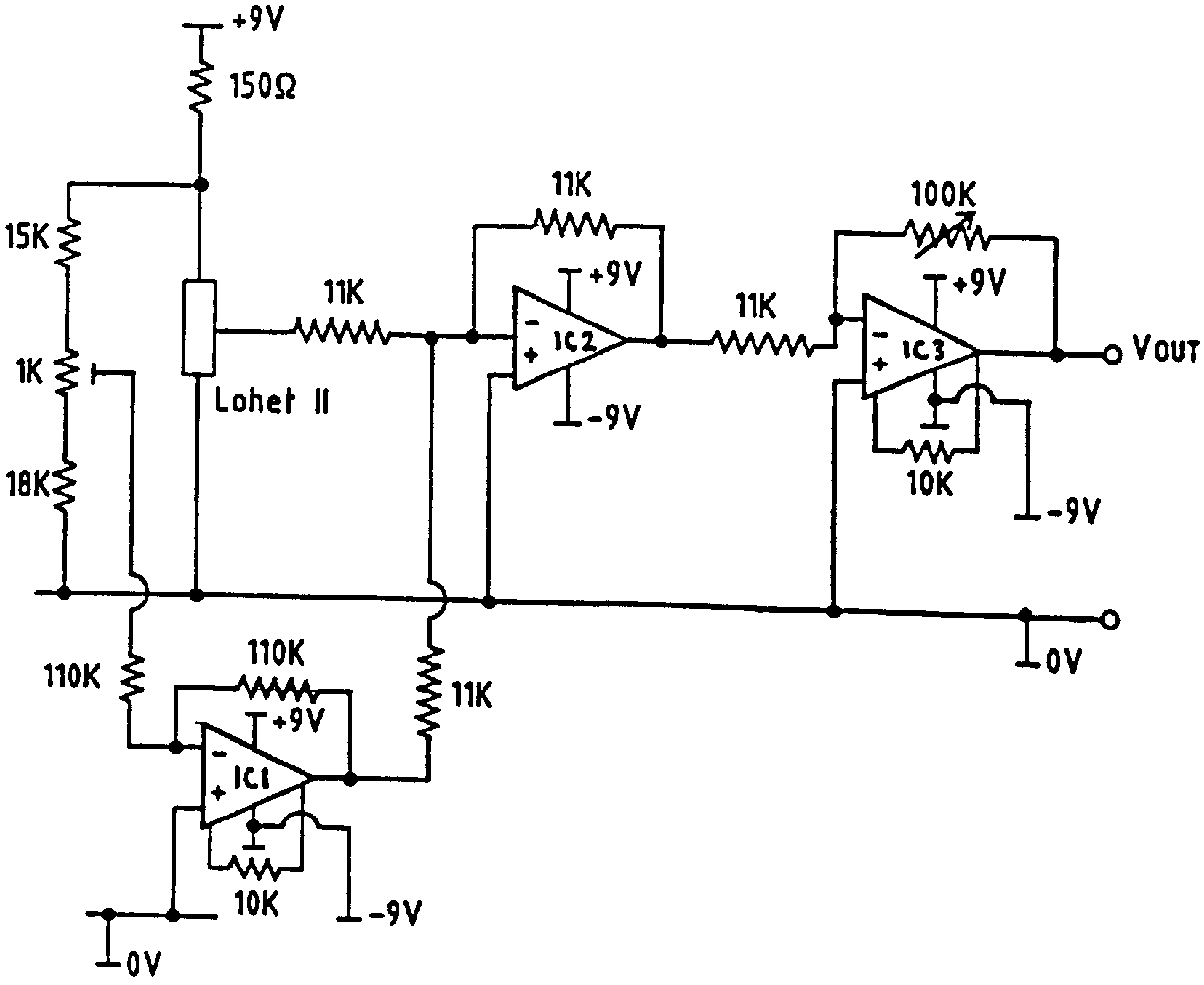

FIGURE 84. PROBE AMPLIFIER CIRCUIT.

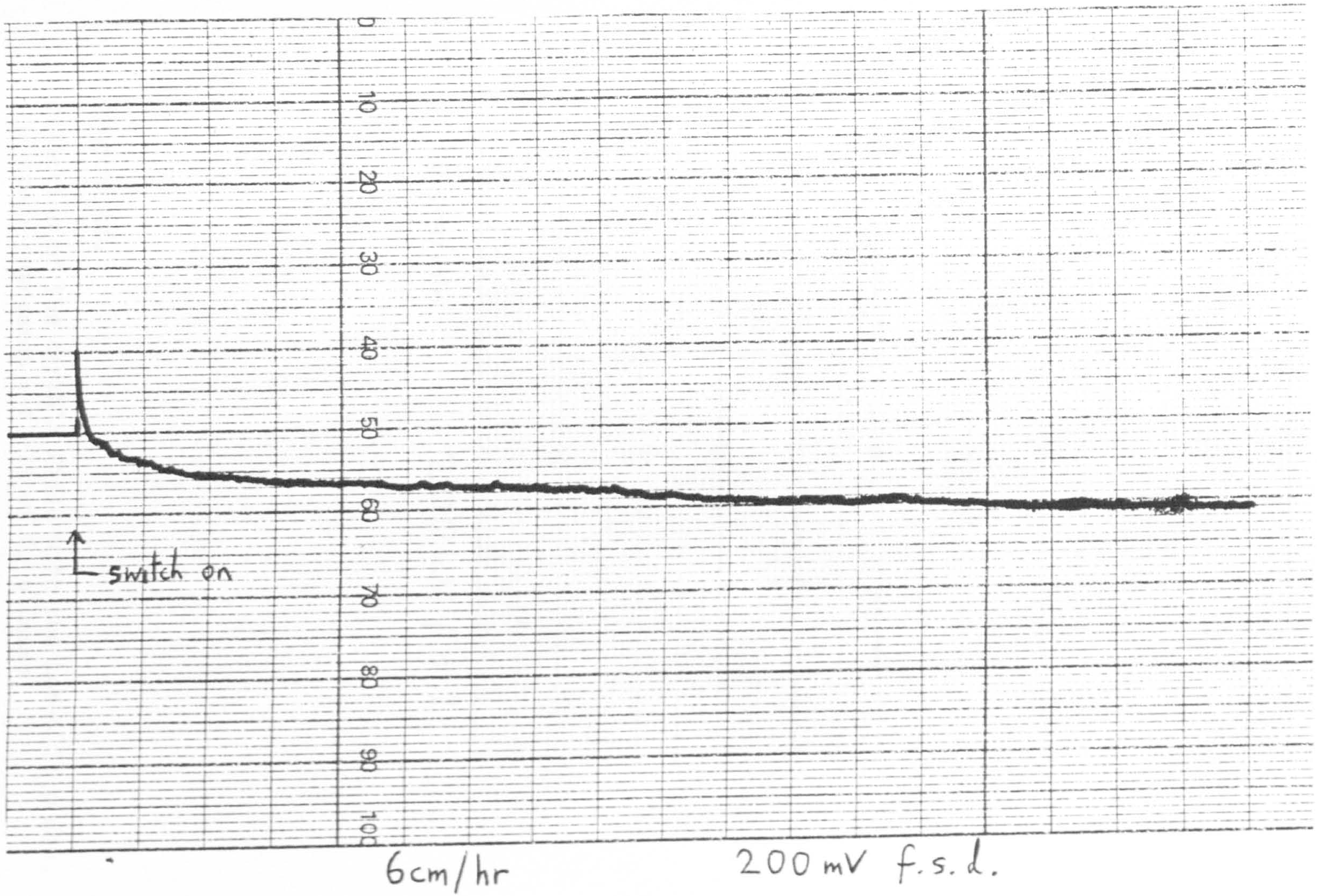

Figure 85. Zero drift obtained with circuit of Figure 78.

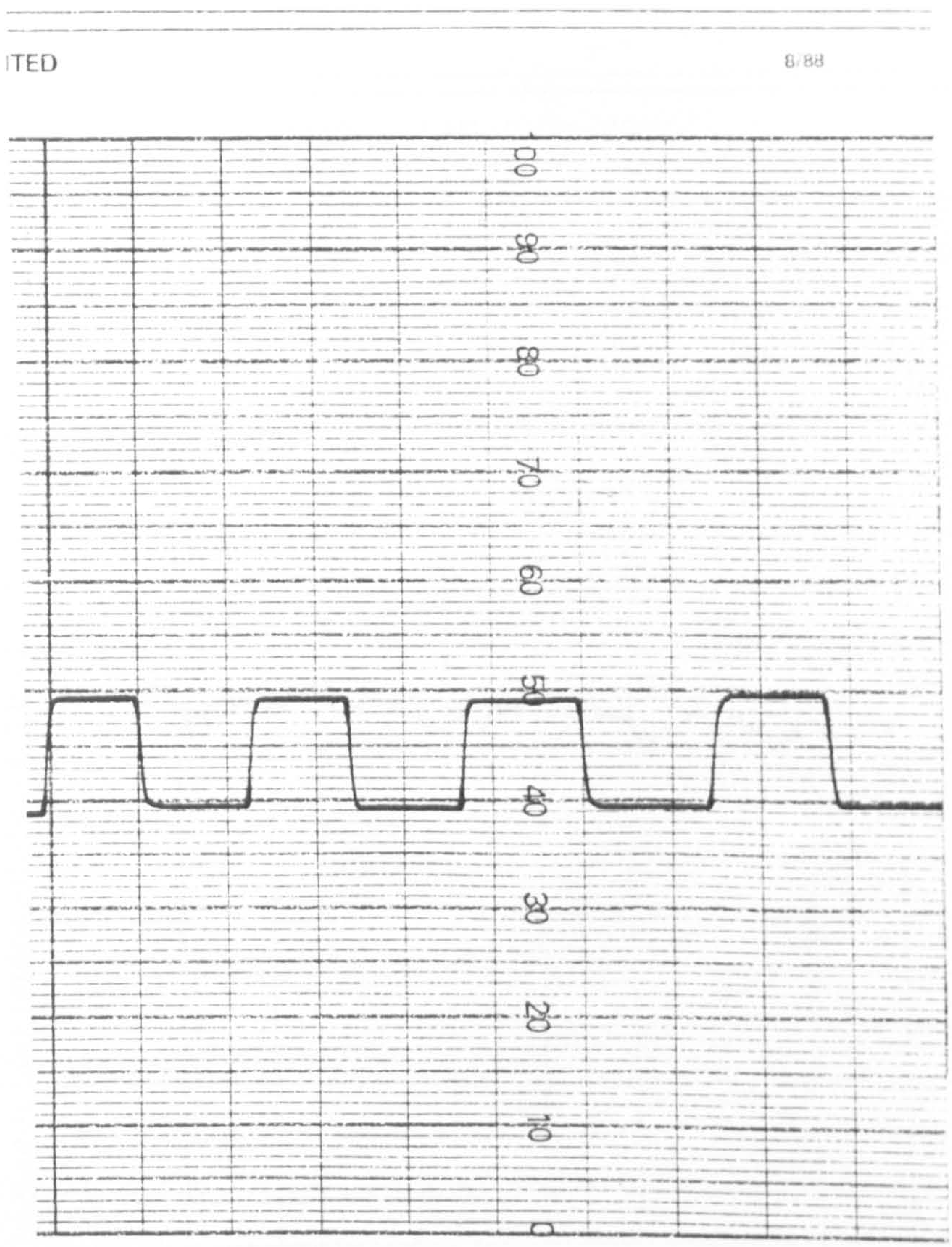

15 cm/min 200 mV f.s.d.

Figure 86.

Detection of the earth's field with the Lohet II probe. The steps represent a field of 0.36 Gauss

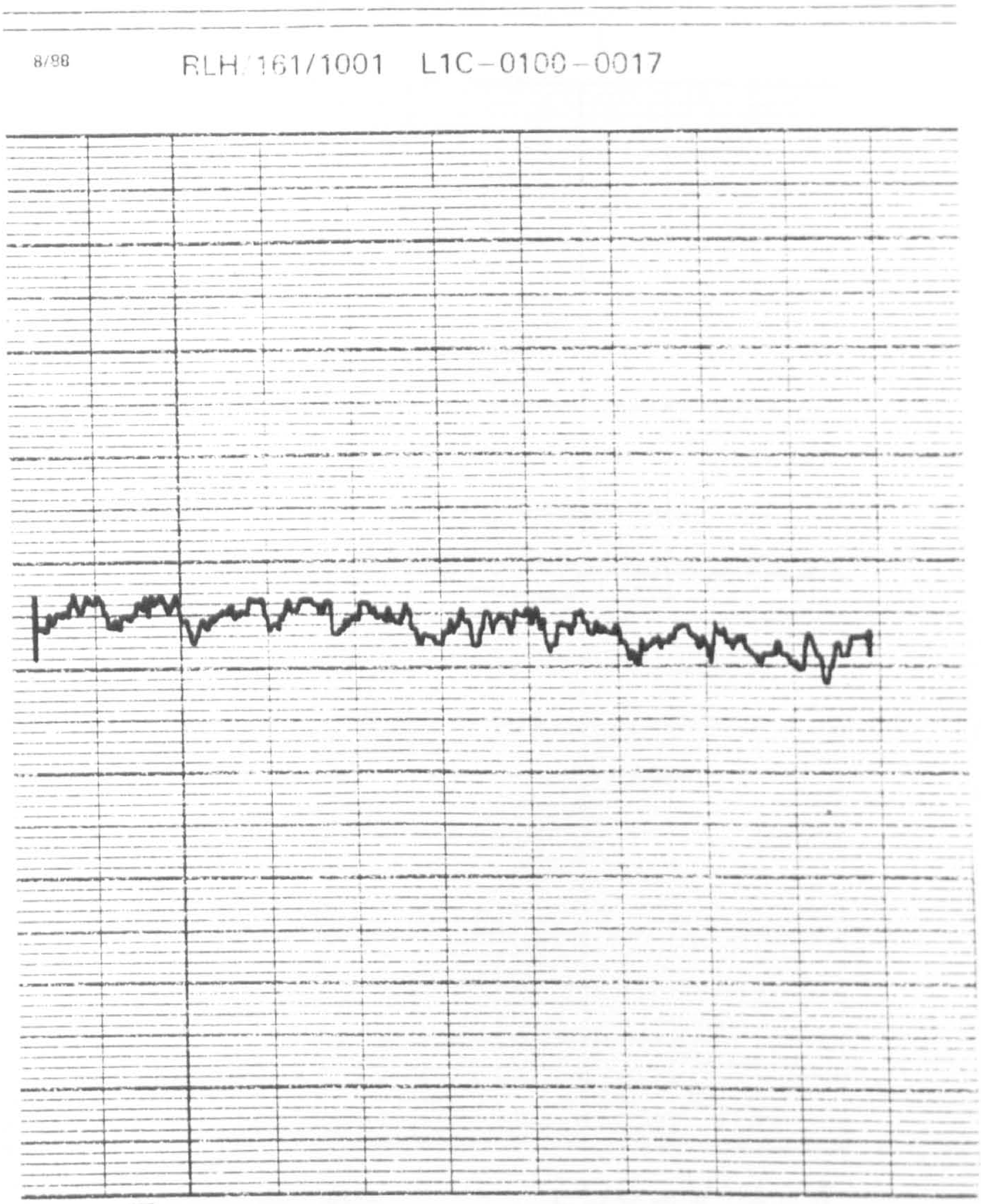

15 cm/min 20 mV f.s.d.

Figure 87.

Noise from the Lohet II probe at high amplification

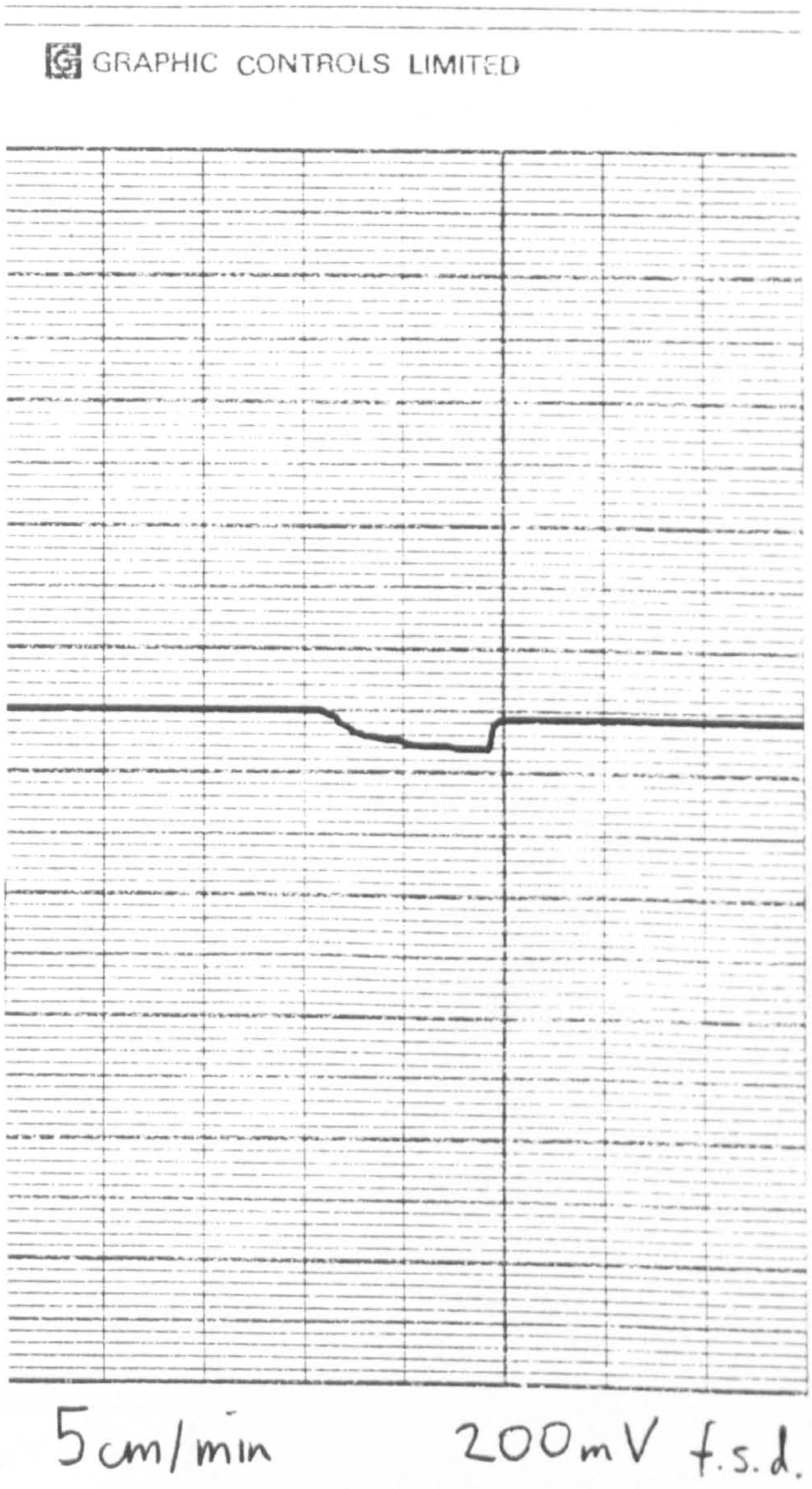

Figure 88.

Effect of heat on the Lohet II zero point

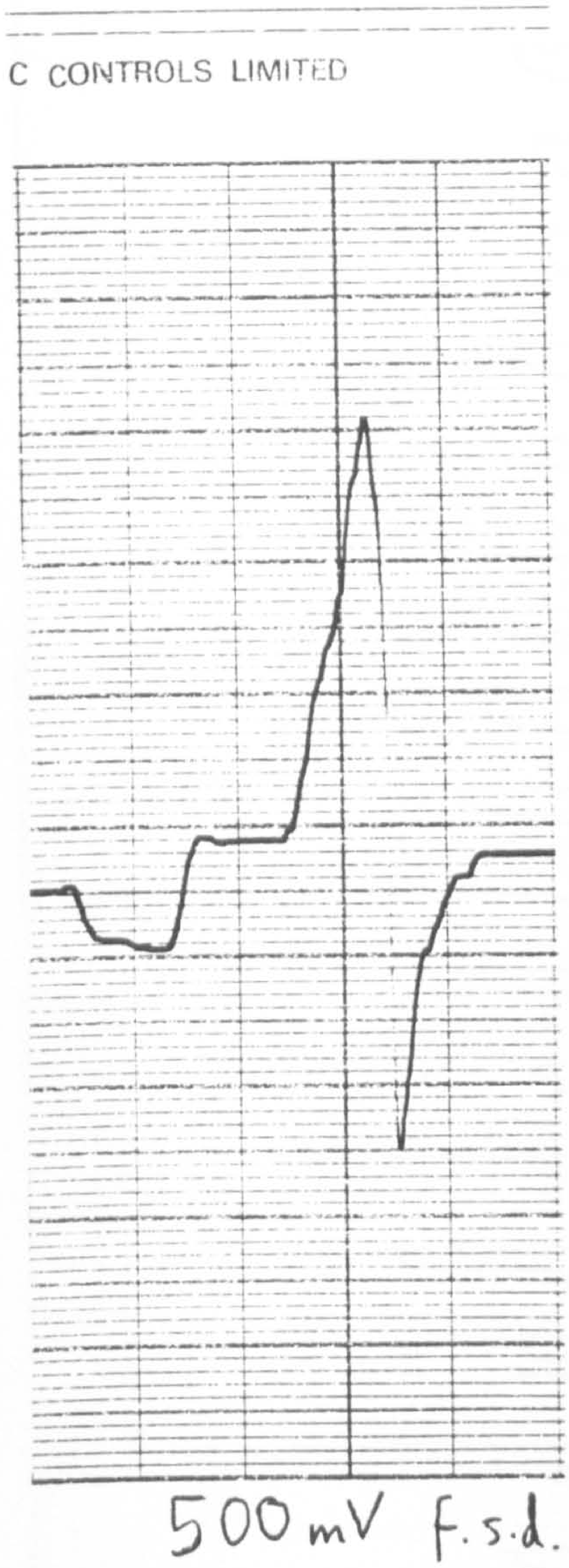

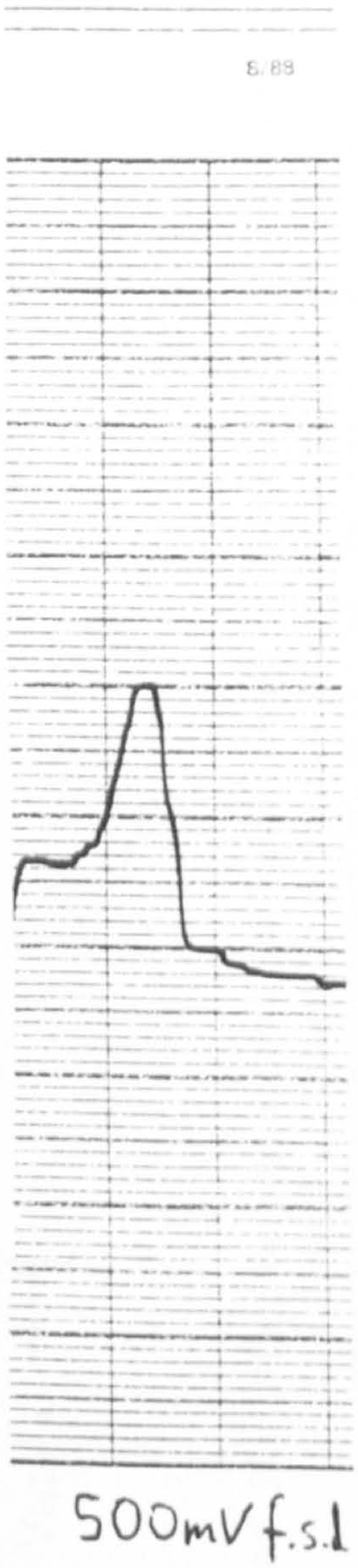

FIGURE 89.- Small stand off

FIGURE 90.- 5mm stand off

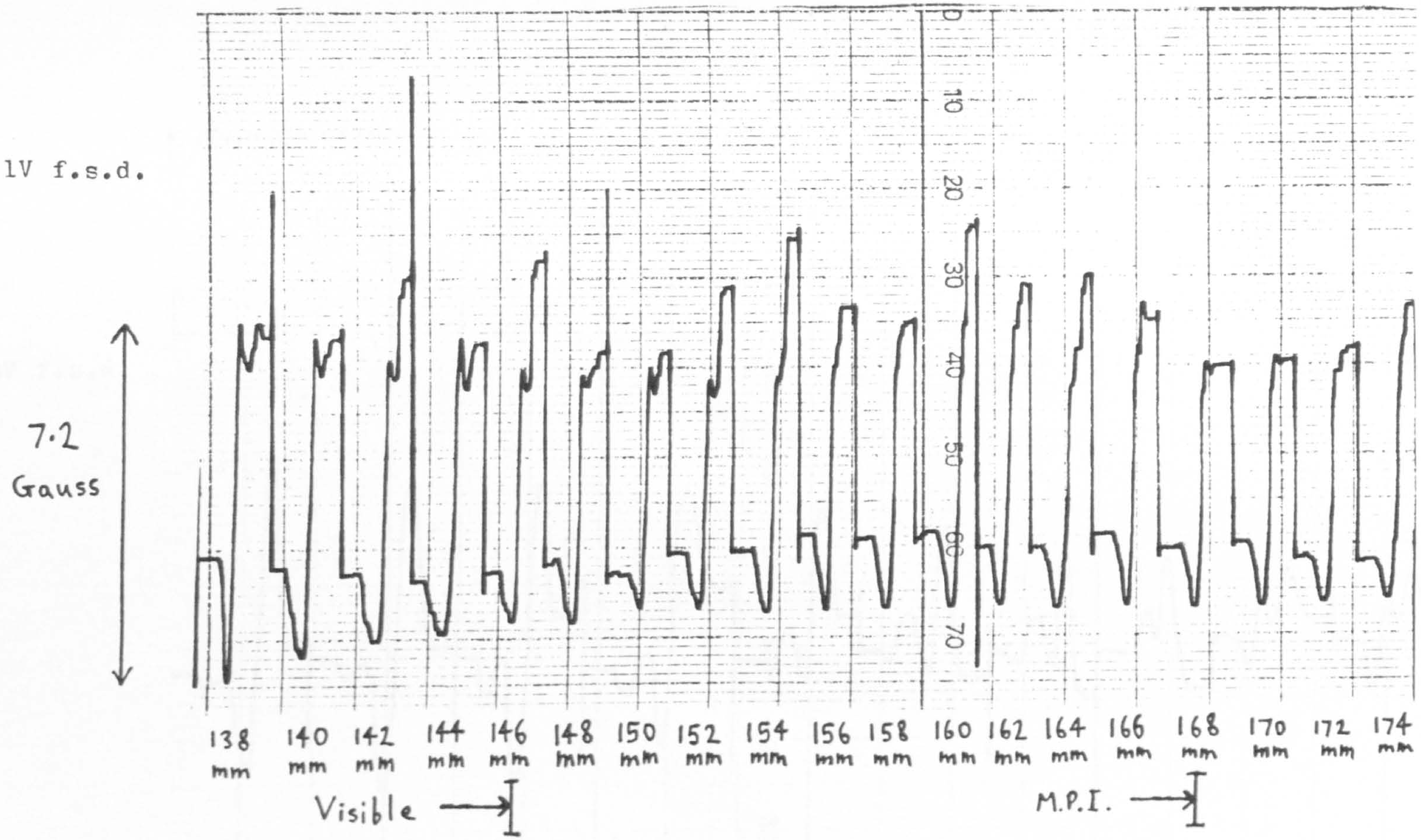

FIGURE 91. Signals taken from the weld crack at various positions along its length. Magnetic particle inspection under identical conditions of magnetisation gives an indication up to 168mm.

500mV f.s.d.

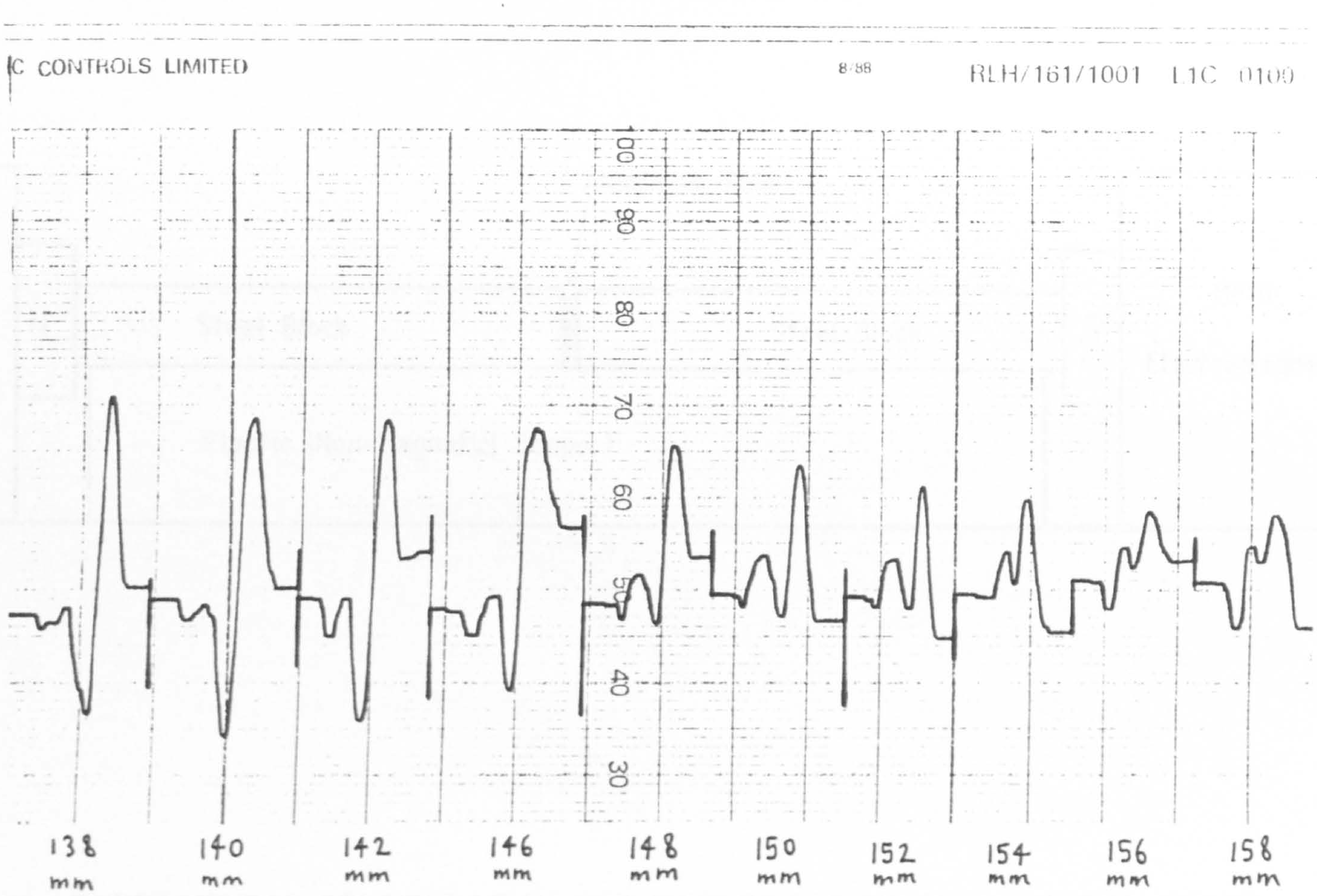

FIGURE 92. Signals taken from the weld crack at various positions along its length. The visible crack extends as far as 146mm.

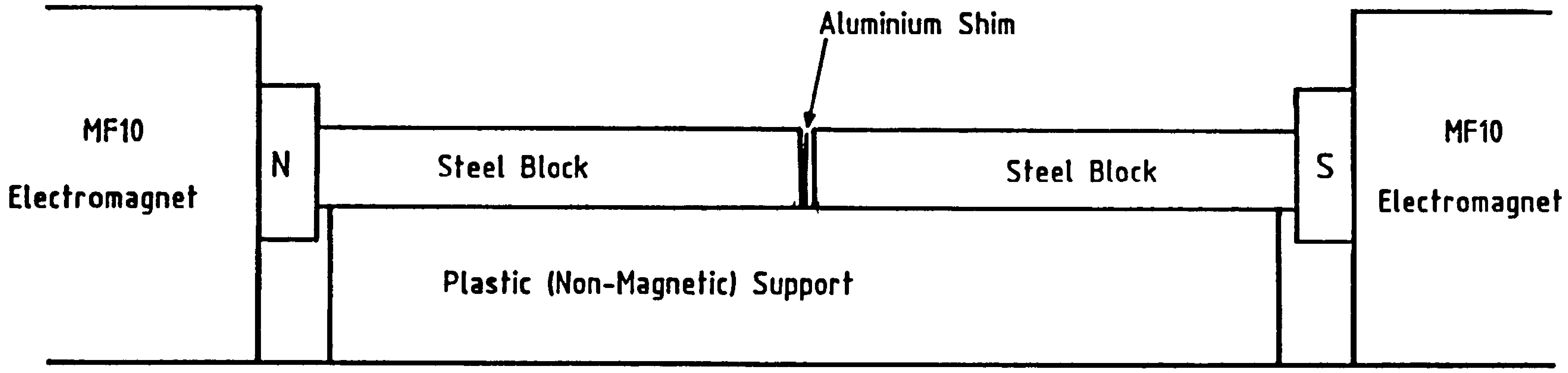

FIGURE 93. EXPERIMENTAL CONFIGURATION FOR MAGNETISATION OF ARTIFICIAL CRACK.

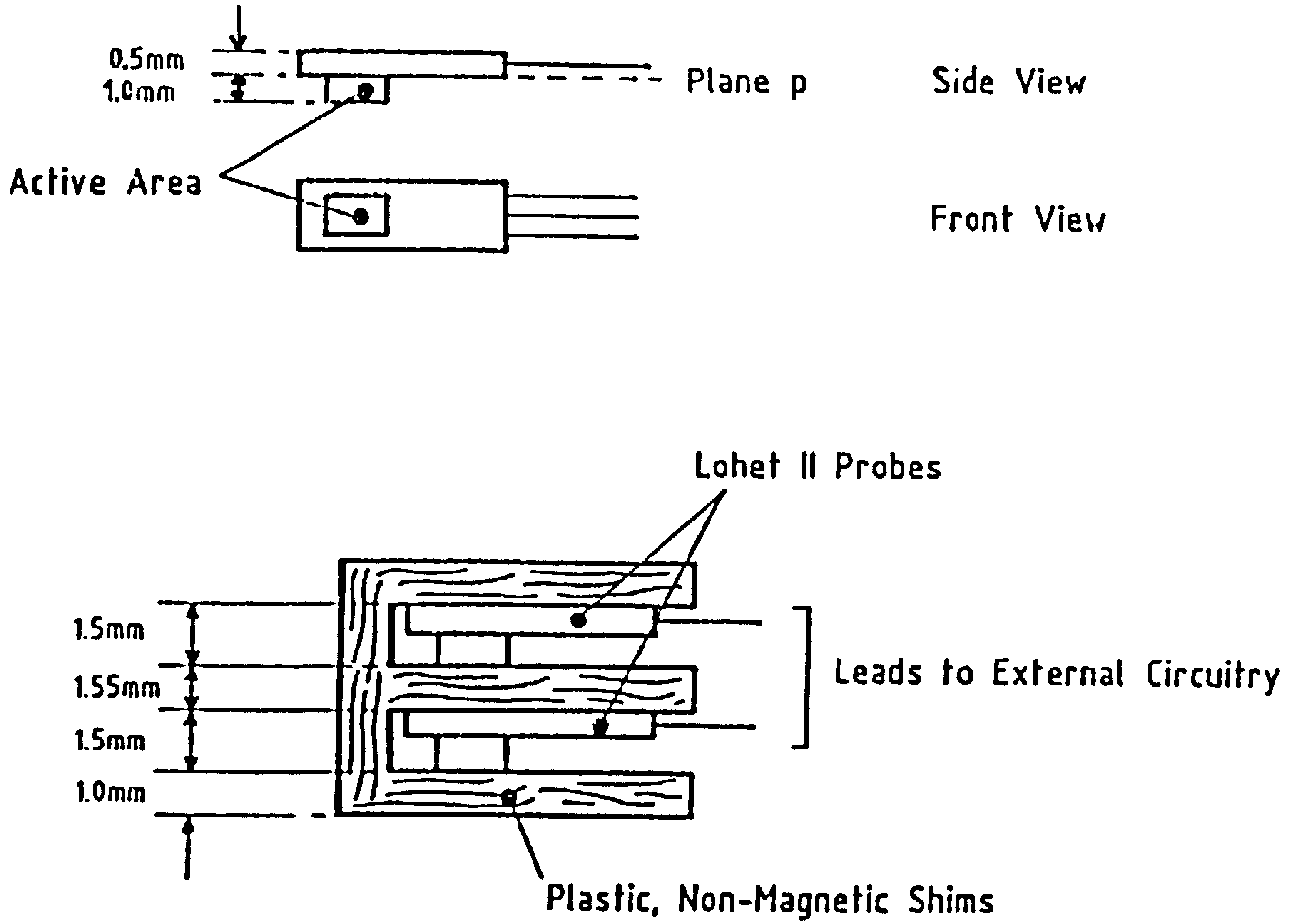

FIGURE 94. PHYSICAL ARRANGEMENT OF THE DOUBLE PROBE SYSTEM.

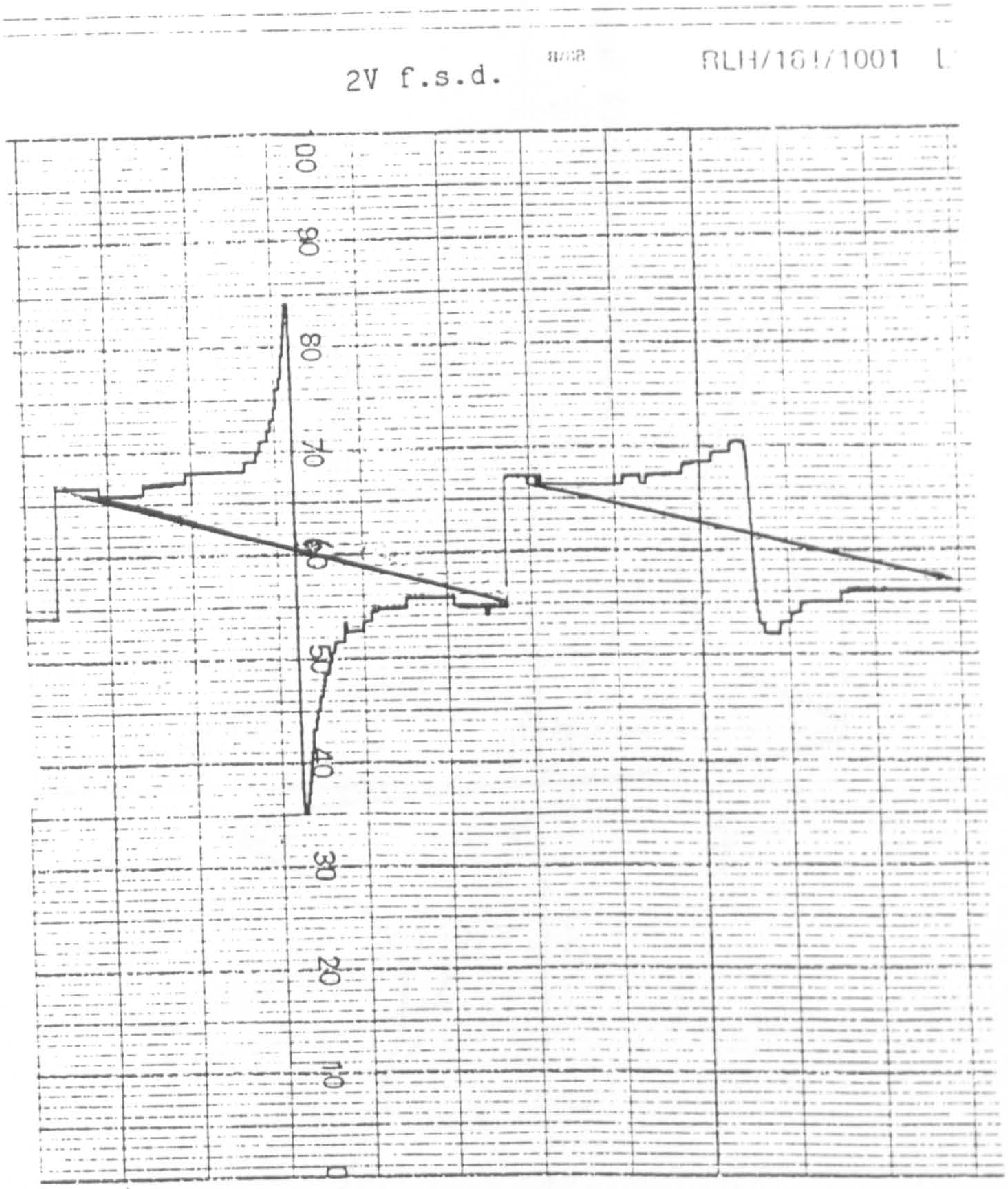

Near probe

Far probe

FIGURE 95. Signals recorded on the data logger at the near and far probes from the 10mm deep artificial crack, magnetised to the British Standard. 300mm long plates were used.

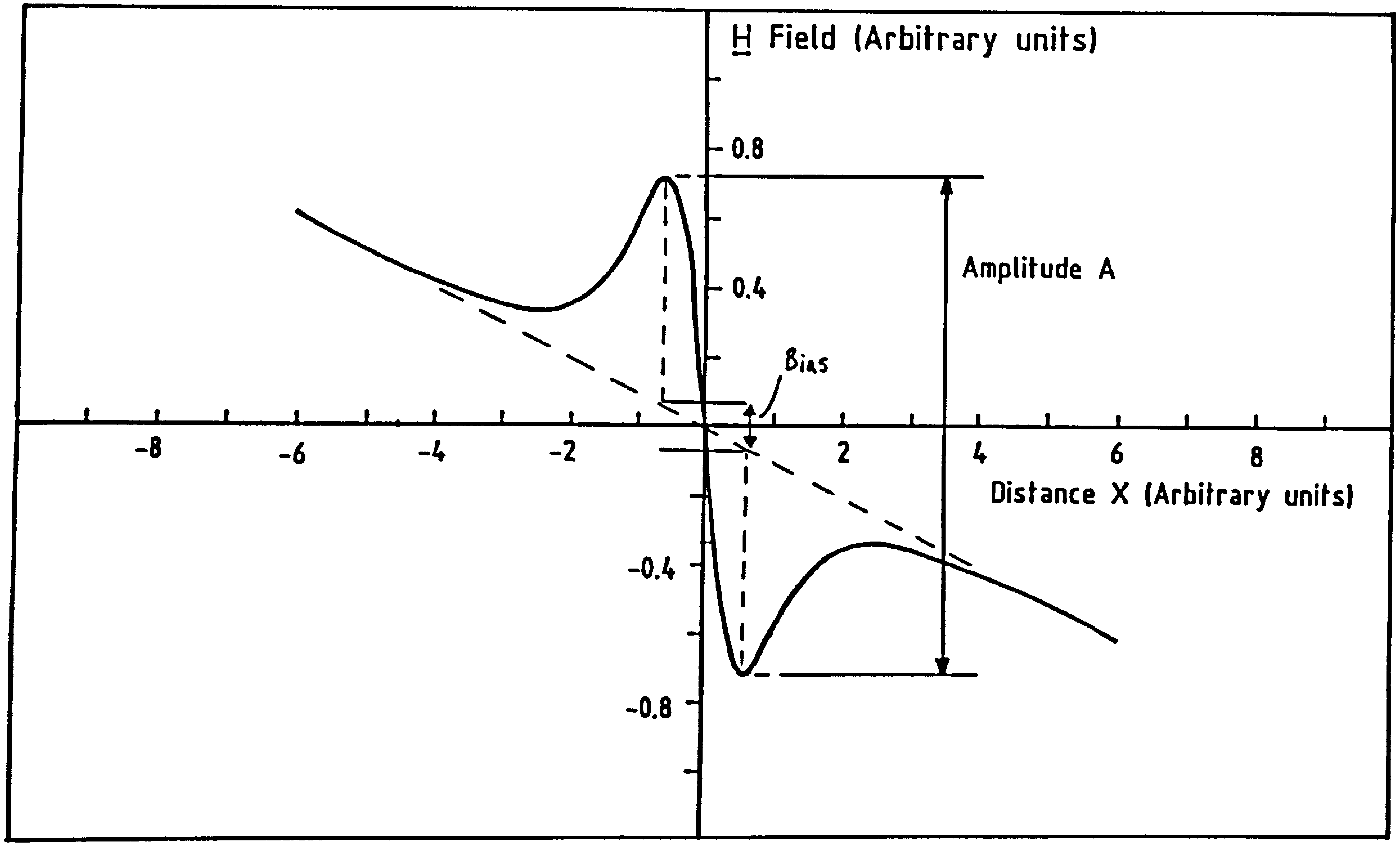

Figure 96. Plot of Eqn.(36) (See text) for z=1, D= -0.1, m=1, C=0 in arbitrary units.

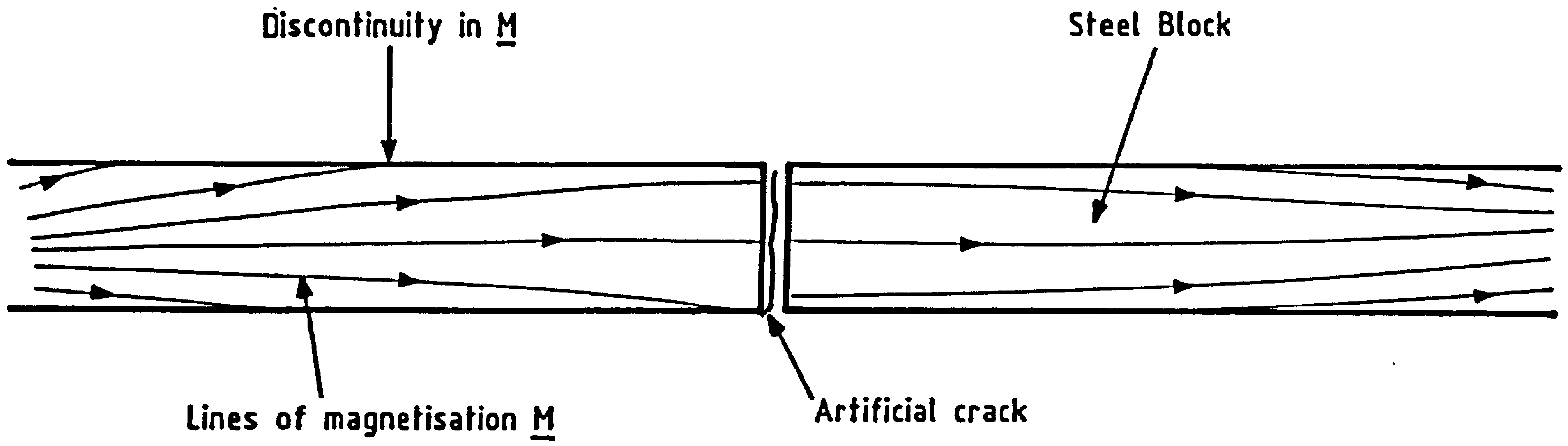

FIGURE 97. POSSIBLE ORIGIN OF BIAS FIELD IN FIG.95 SHOWING SOURCES OF $\underline{H}$ FIELD FROM DISCONTINUITIES IN $\underline{M}$ AT THE SURFACE DUE TO IMPERFECT PARALLEL ALIGNMENT. (Greatly exaggerated)

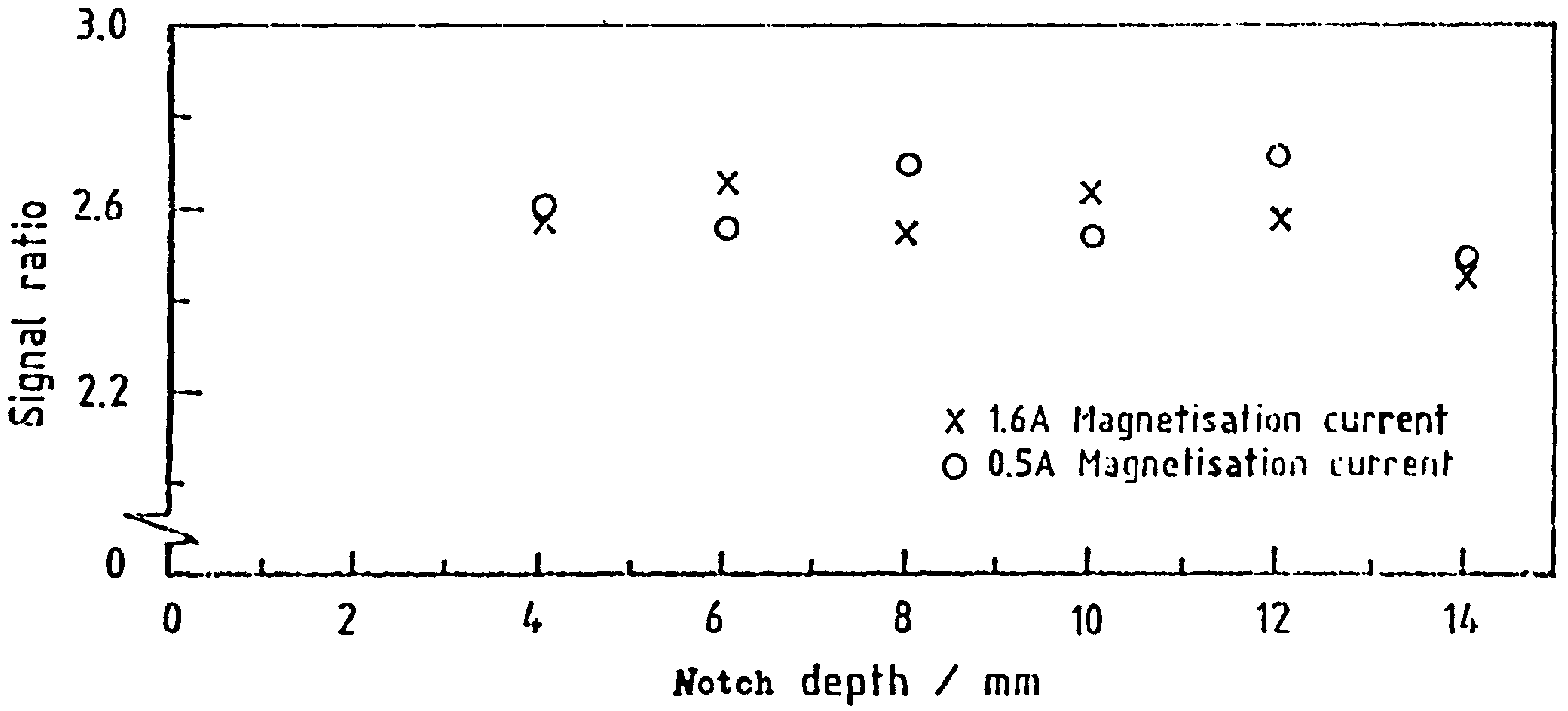

FIGURE 98. PLOT OF RATIO OF SIGNALS A (See Fig. 96) FROM NEAR AND FAR PROBES AGAINST DEPTH OF notch (notch width ≃ 40μm)

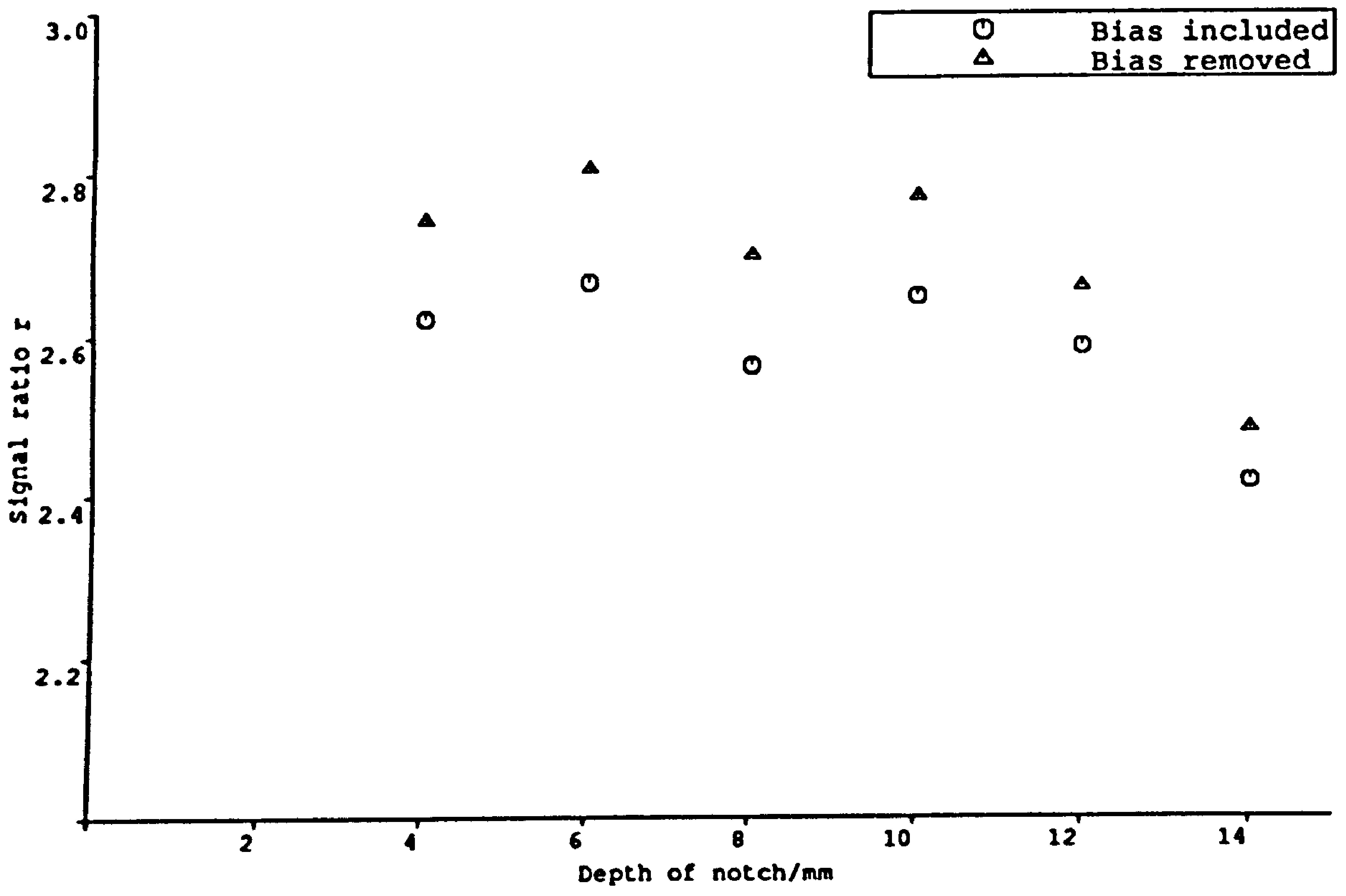

Figure 99. The effect of taking into account the reverse or negative bias on the signal ratio r.

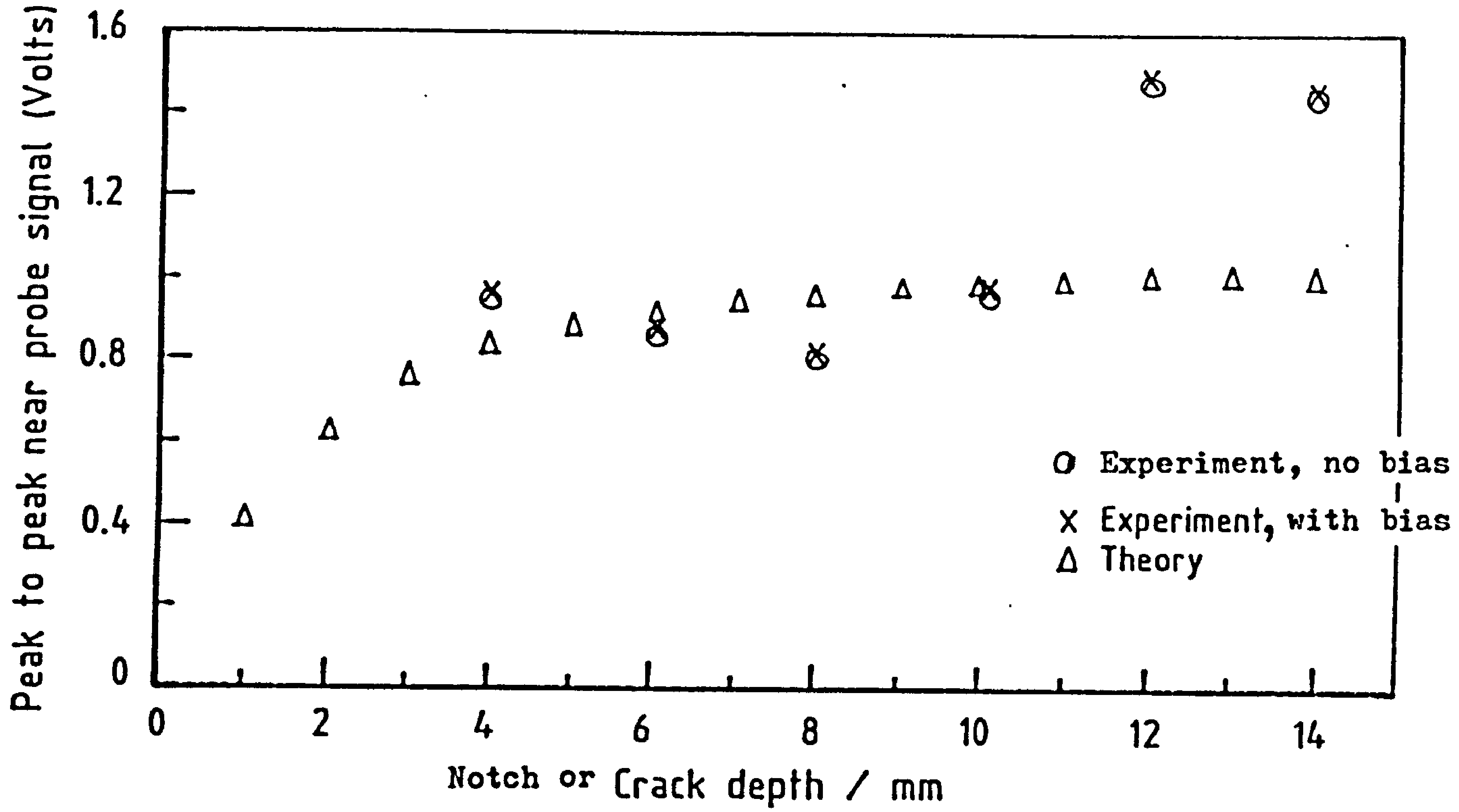

FIGURE 100. THEORETICAL AND EXPERIMENTAL NEAR PROBE / AMPLIFIER VOLTAGE SIGNALS. THEORY REFERS TO A CRACK WIDTH OF 40μm, AND SCAN HEIGHT OF 2mm. BRITISH STANDARD MAGNETISATION.

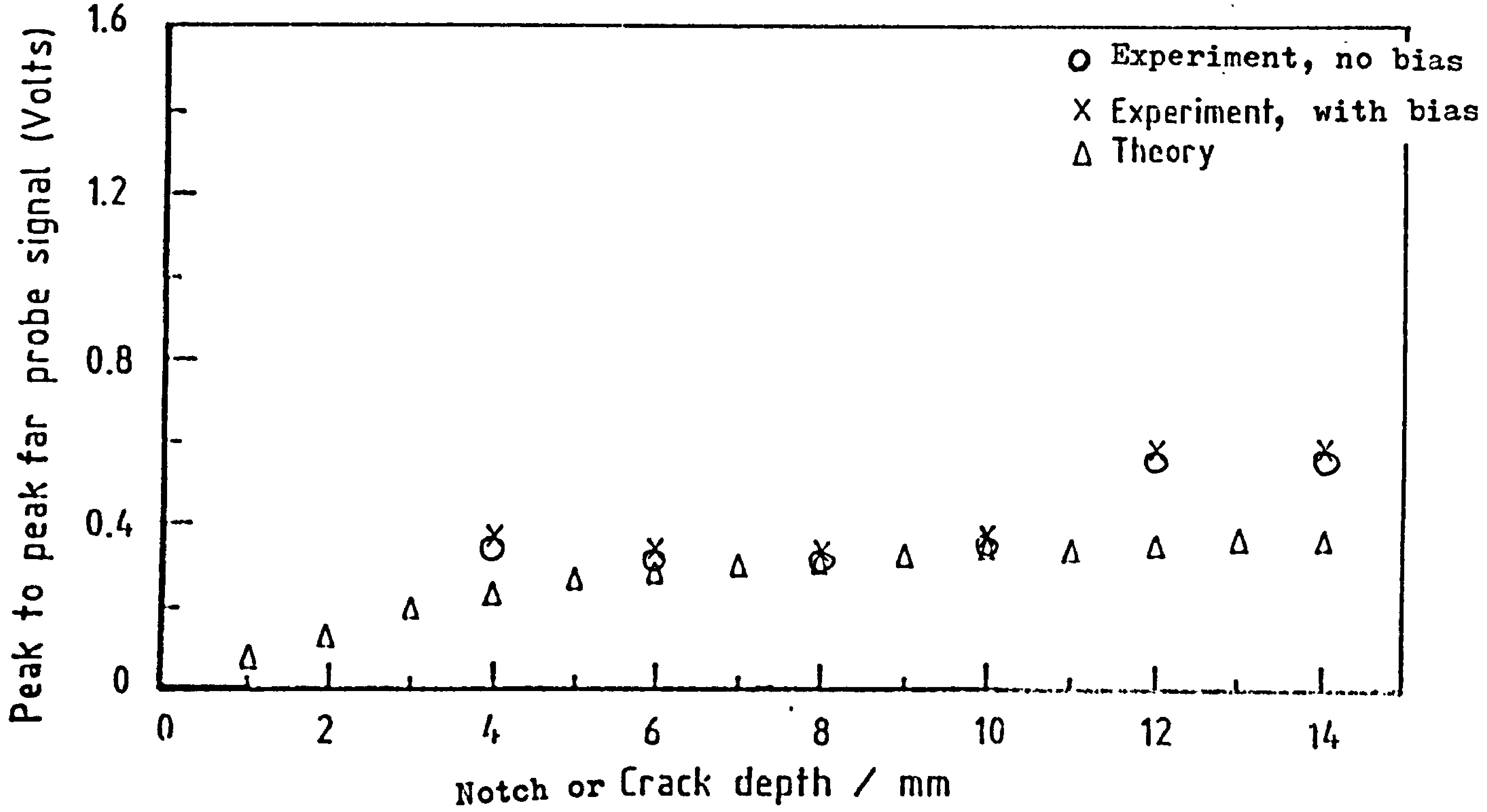

FIGURE 101. THEORETICAL AND EXPERIMENTAL FAR PROBE / AMPLIFIER VOLTAGE SIGNALS. THEORY REFERS TO A CRACK WIDTH OF 40μm, AND SCAN HEIGHT OF 5.05mm. BRITISH STANDARD MAGNETISATION.

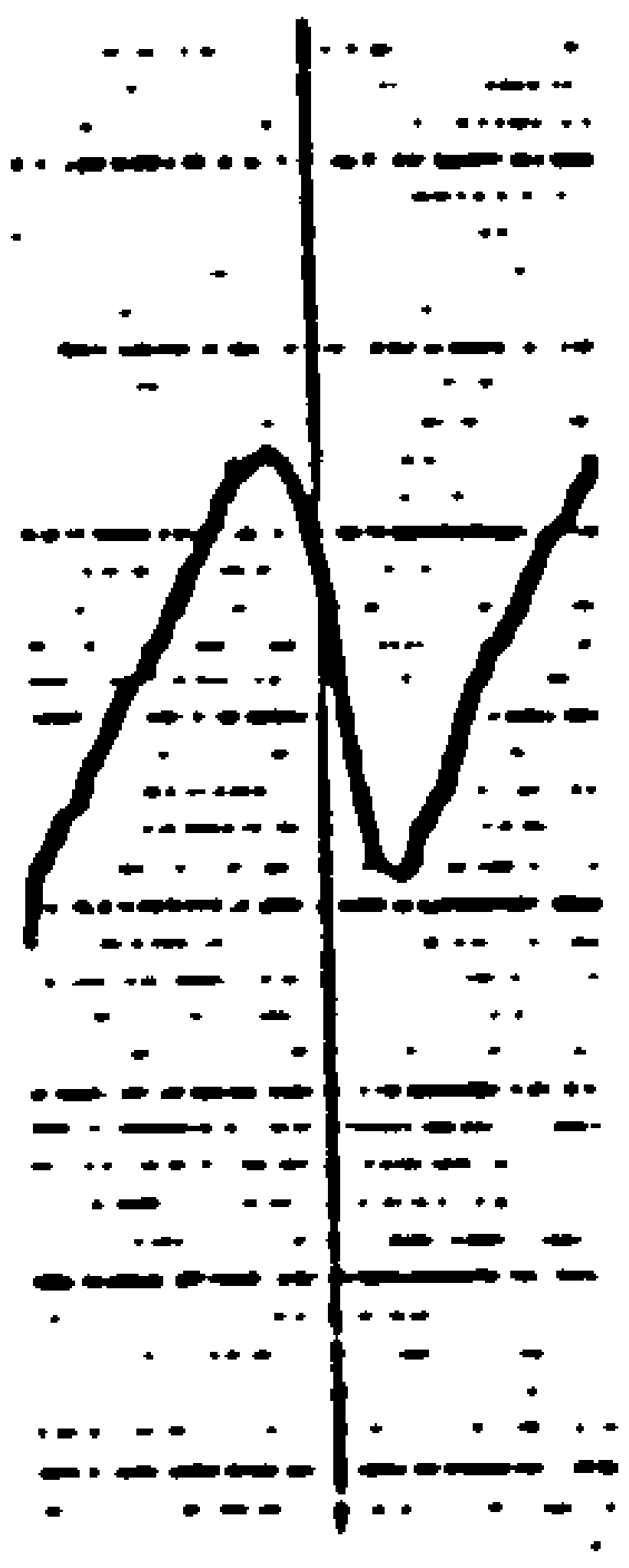

(above) FIGURE 102. Signal from 25μm notch.

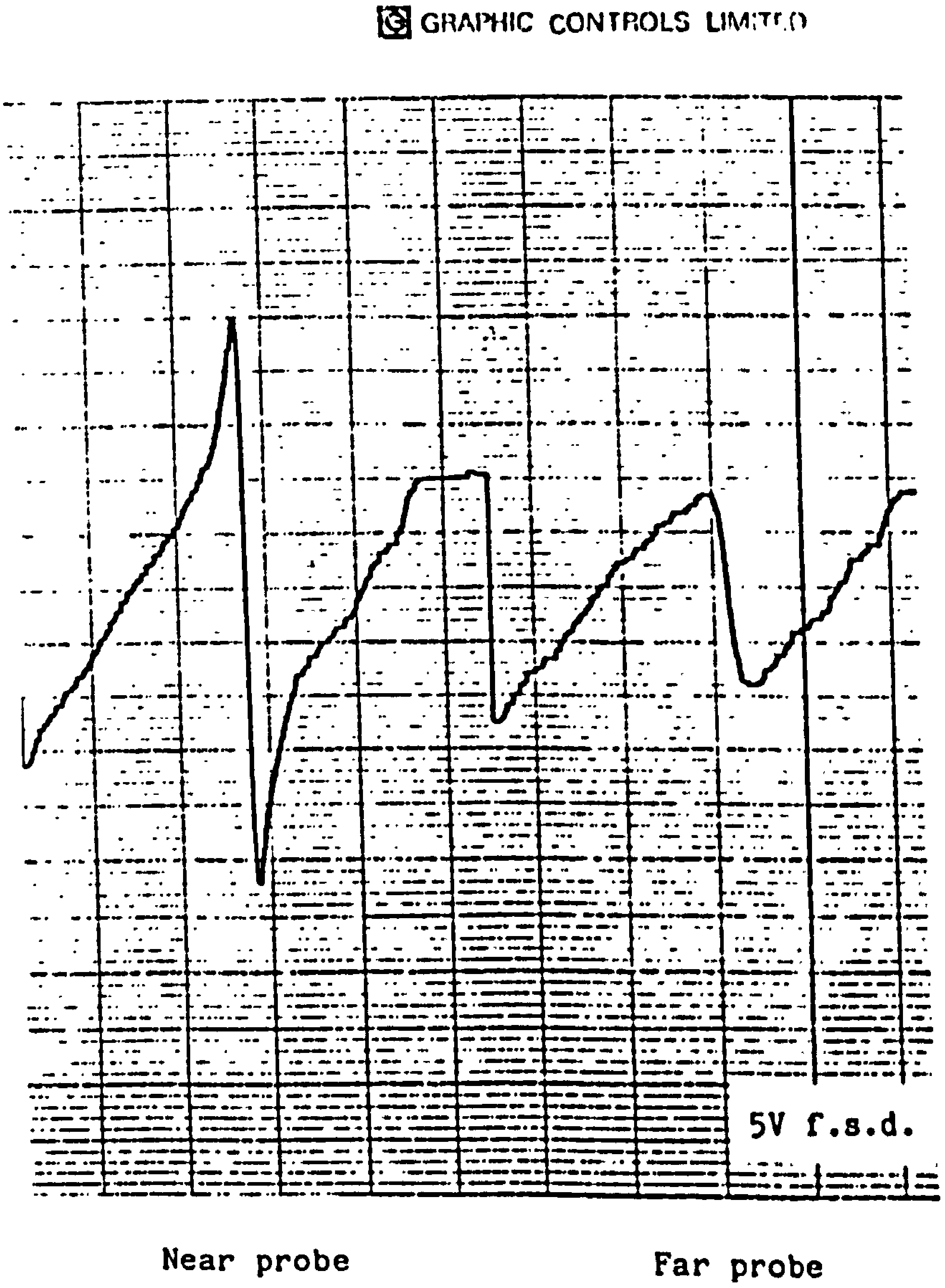

FIGURE 103. Typical signals from a short sample having an 8mm deep notch in it.

(above) FIGURE 102. Signal from 25μm notch.

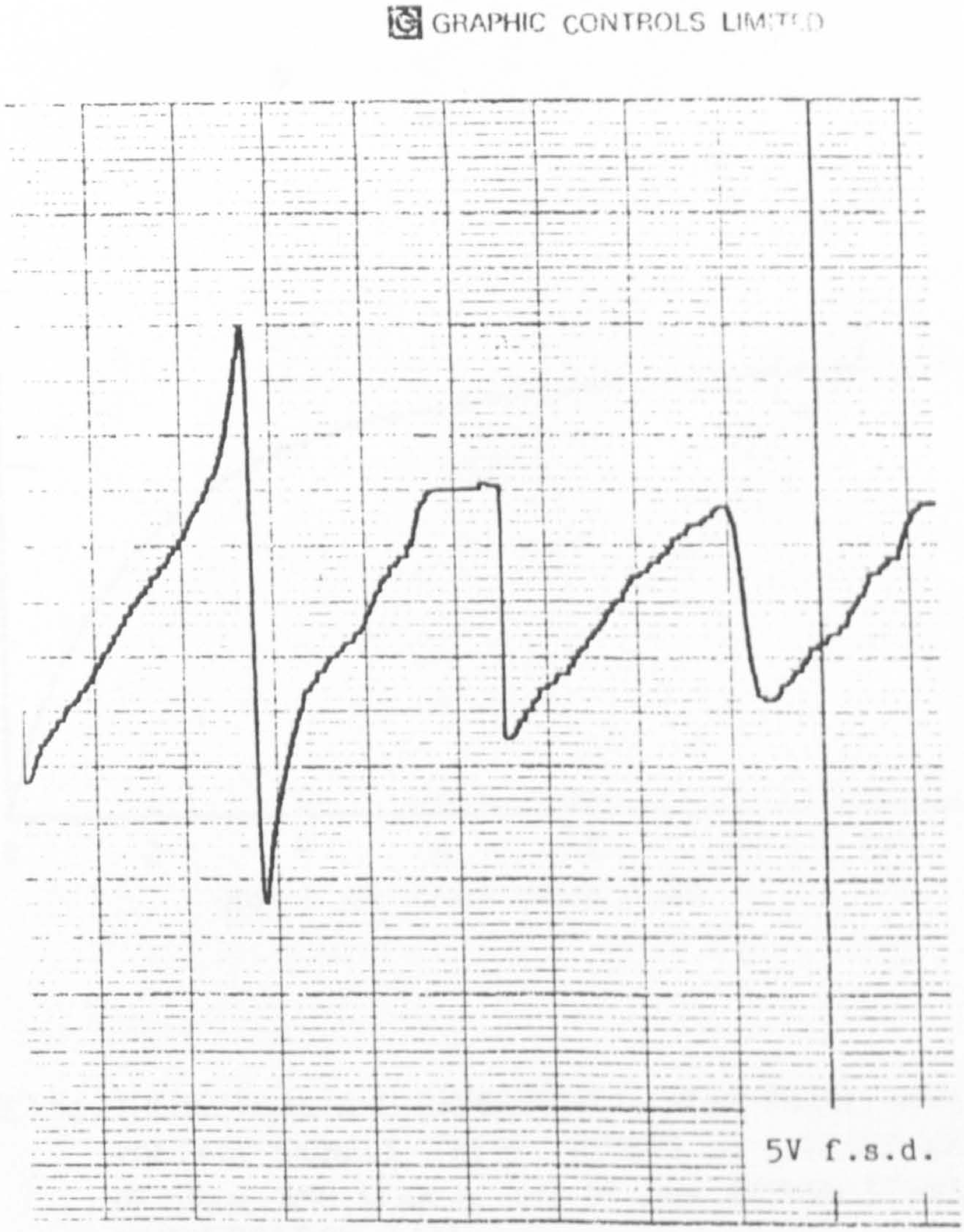

Near probe Far probe

FIGURE 103. Typical signals from a short sample having an 8mm deep notch in it.

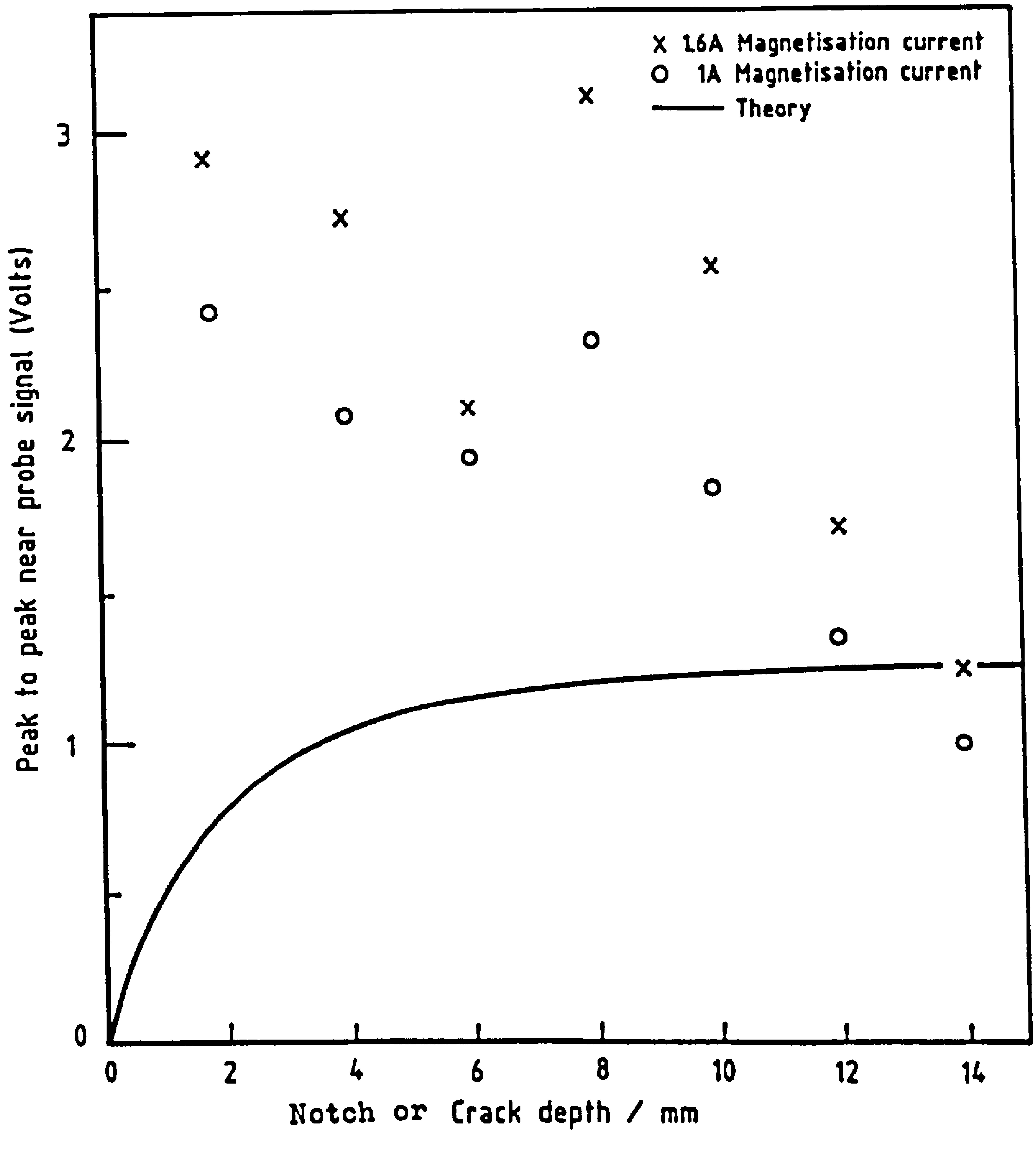

FIGURE 104. THEORETICAL AND EXPERIMENTAL NEAR PROBE/AMPLIFIER VOLTAGE SIGNALS. THEORY REFERS TO A CRACK WIDTH OF 50µm, AND SCAN HEIGHT OF 2mm; BRITISH STANDARD MAGNETISATION (1.6A)

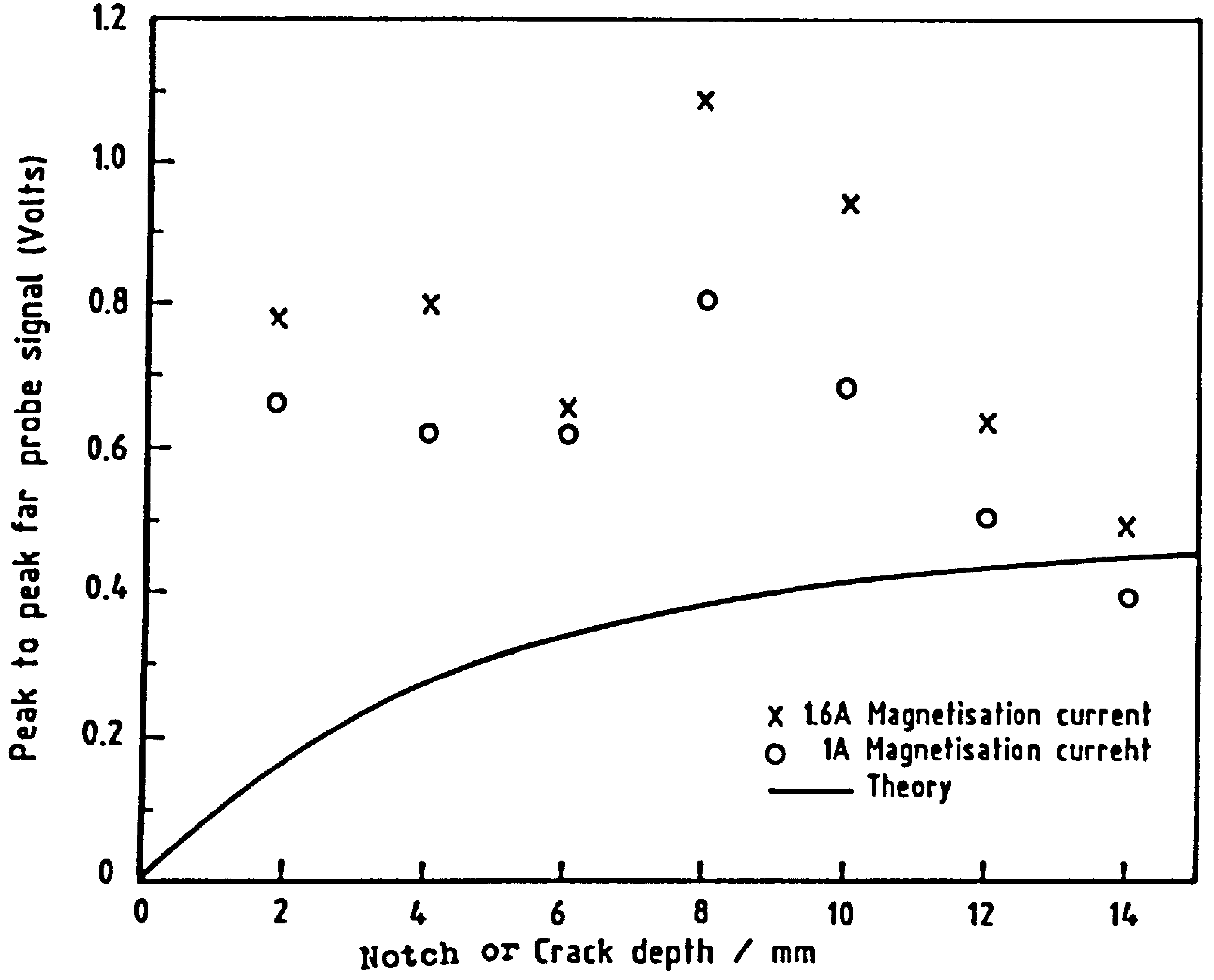

FIGURE 105. THEORETICAL AND EXPERIMENTAL FAR PROBE / AMPLIFIER VOLTAGE SIGNALS. THEORY REFERS TO A CRACK WIDTH OF 50μm, AND SCAN HEIGHT OF 5.05mm, BRITISH STANDARD MAGNETISATION (1.6A).

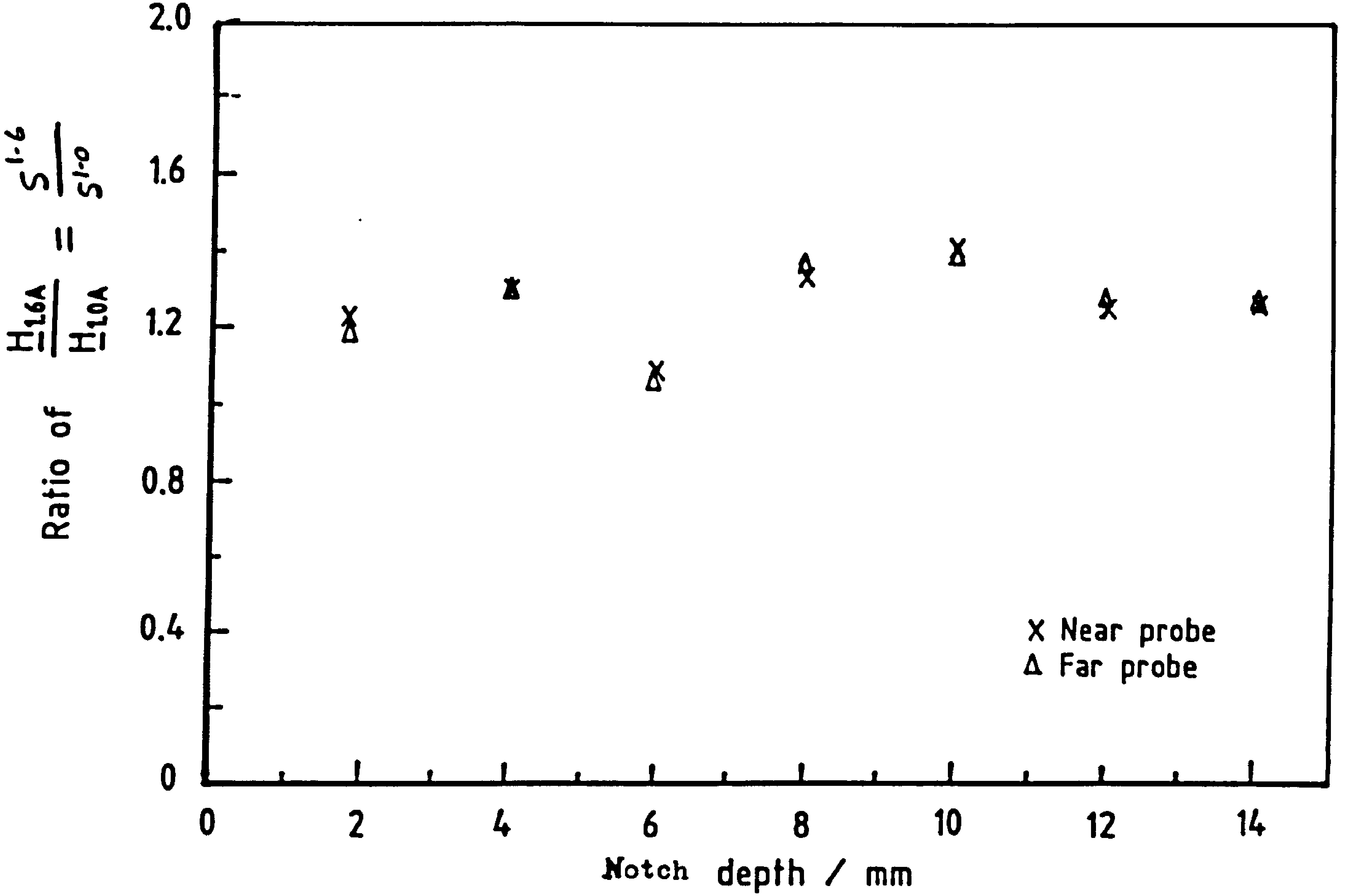

FIGURE 106. RATIO OF $S^{1.6} / S^{1.0}$ (See Eqn.38) FOR THE NEAR AND FAR PROBES, SHOWING THE CORRELATION.

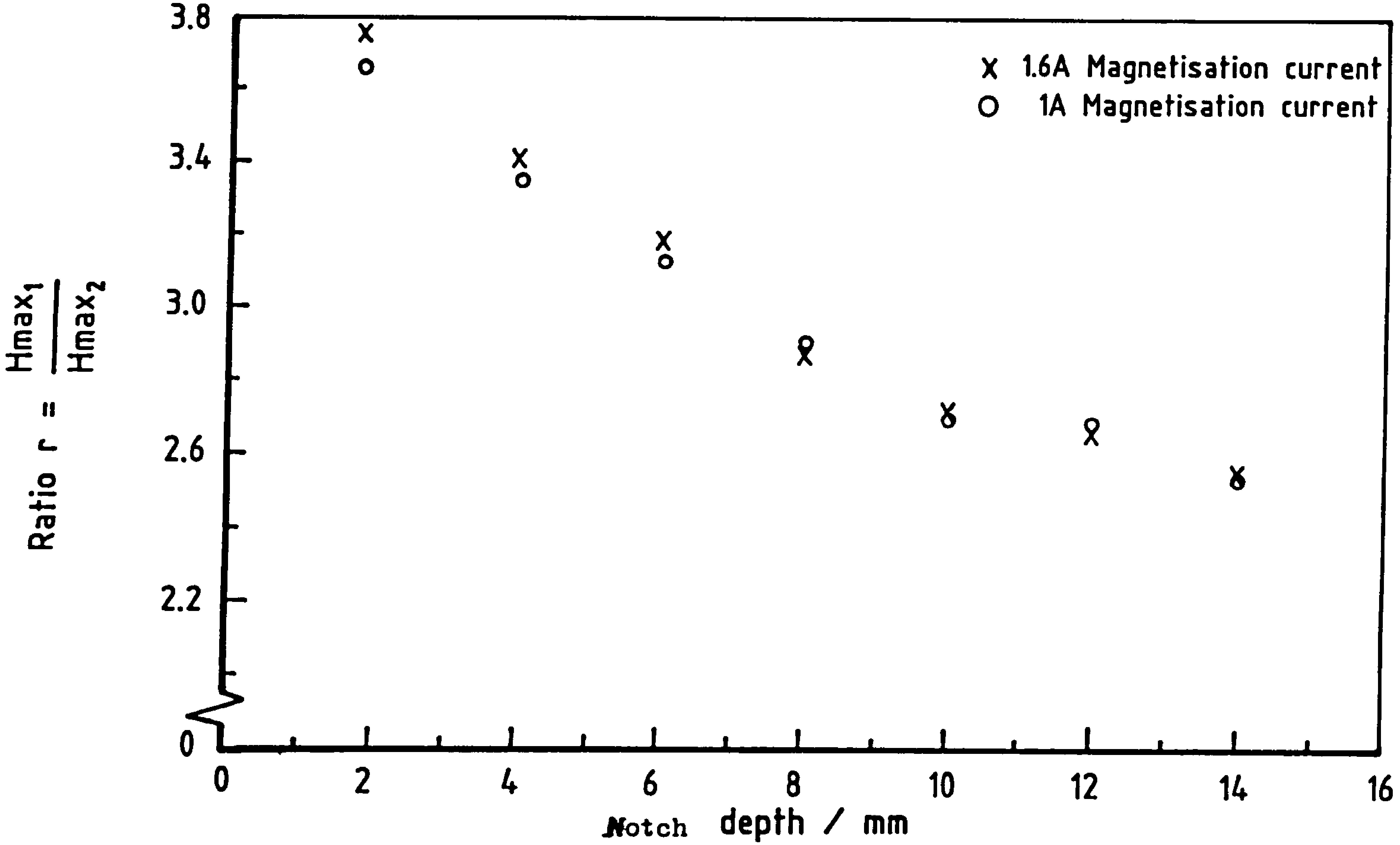

FIGURE 107. RATIO OF SIGNALS FROM THE NEAR AND FAR PROBES AS A FUNCTION OF notch DEPTH AT THE TWO MAGNETISATION LEVELS USED.

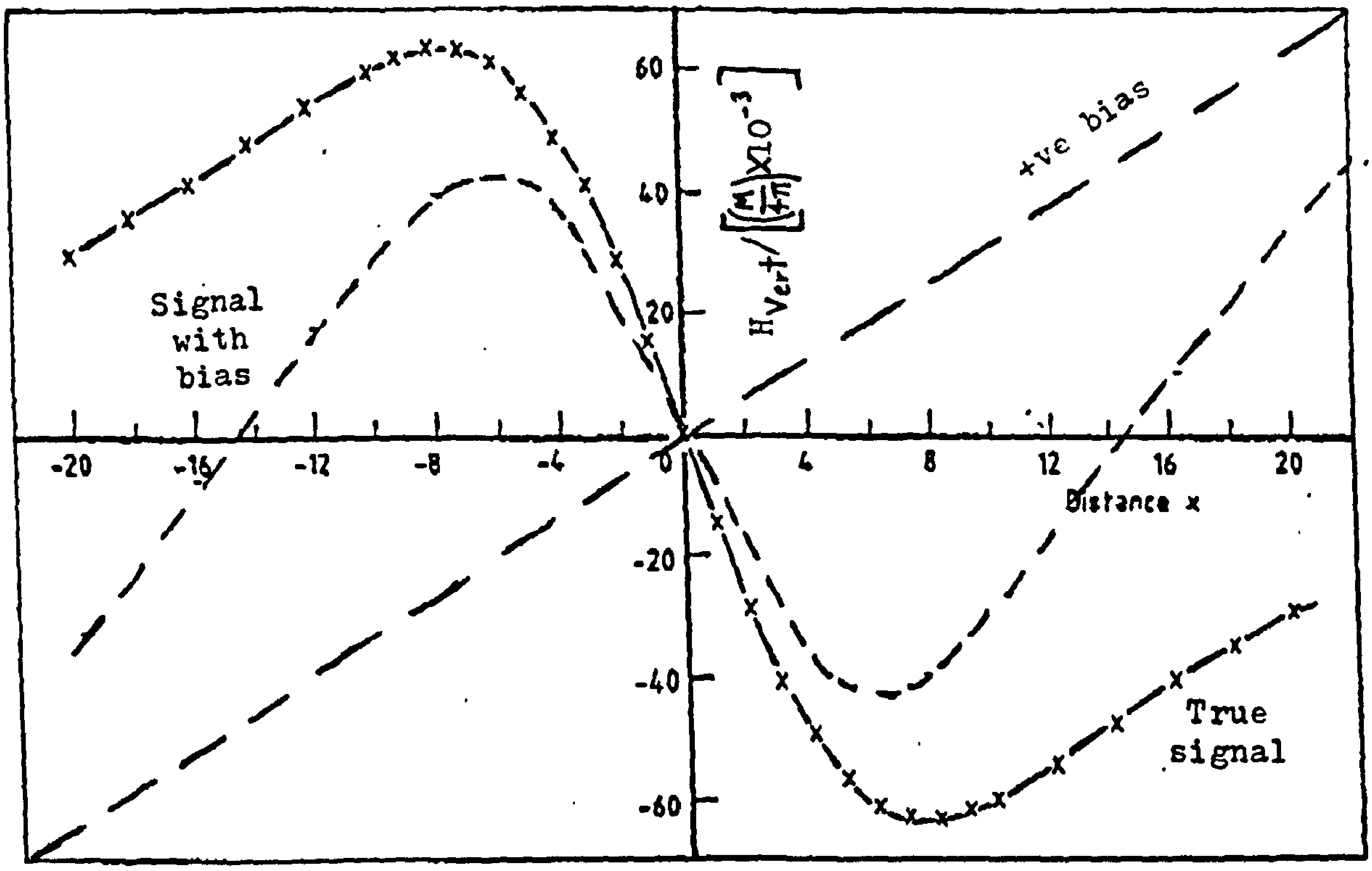

Figure 107(a). Theoretical vertical component of field over a crack for which 2b=1, h=10, z=10 (arbitrary units), showing the effect of a forward or positive bias.

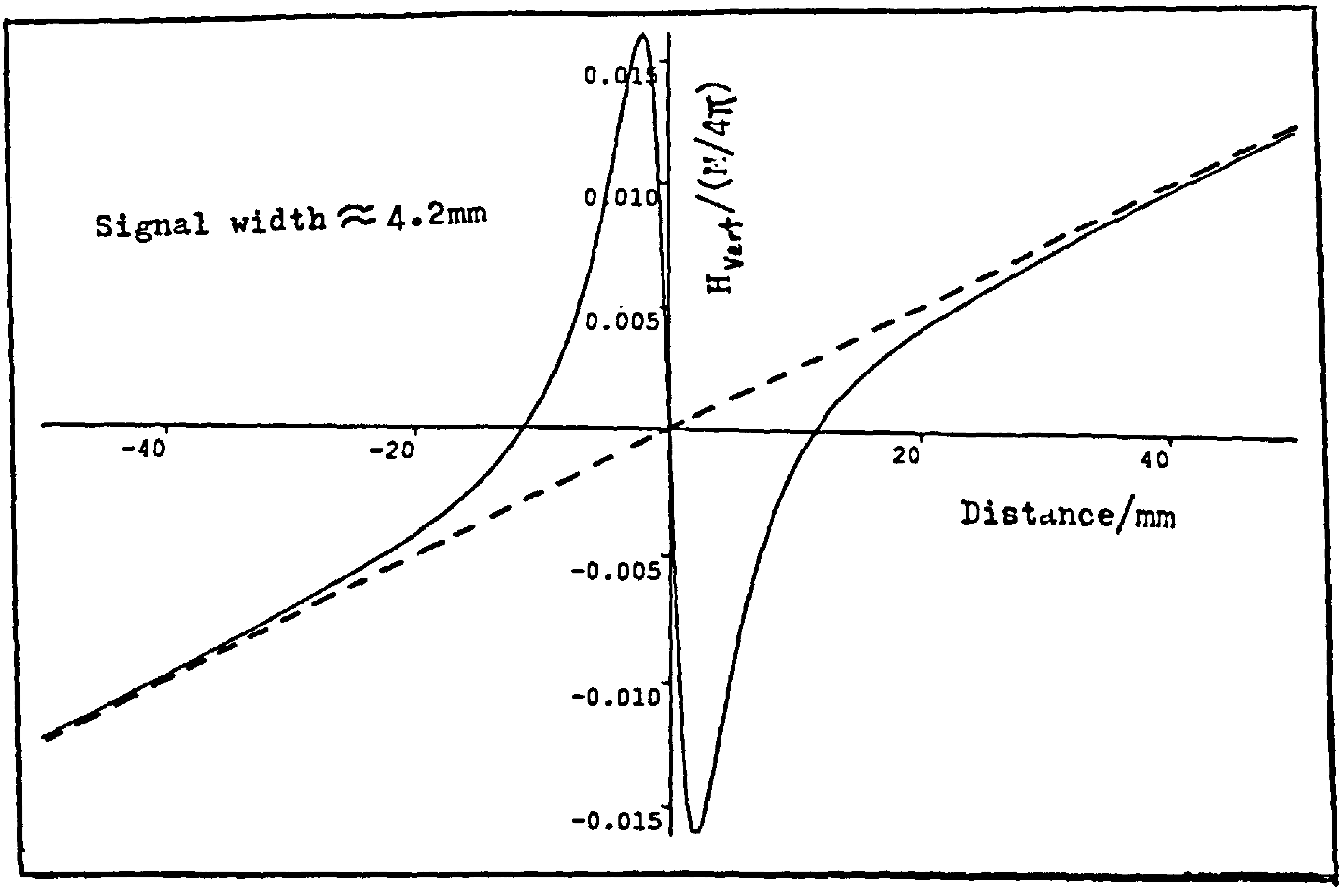

Figure 107(b). Theoretical vertical component of field over a crack for which 2b=0.04mm, h=8mm, z=2.2mm, showing the effect of a positive bias at a distance of 10 signal widths.

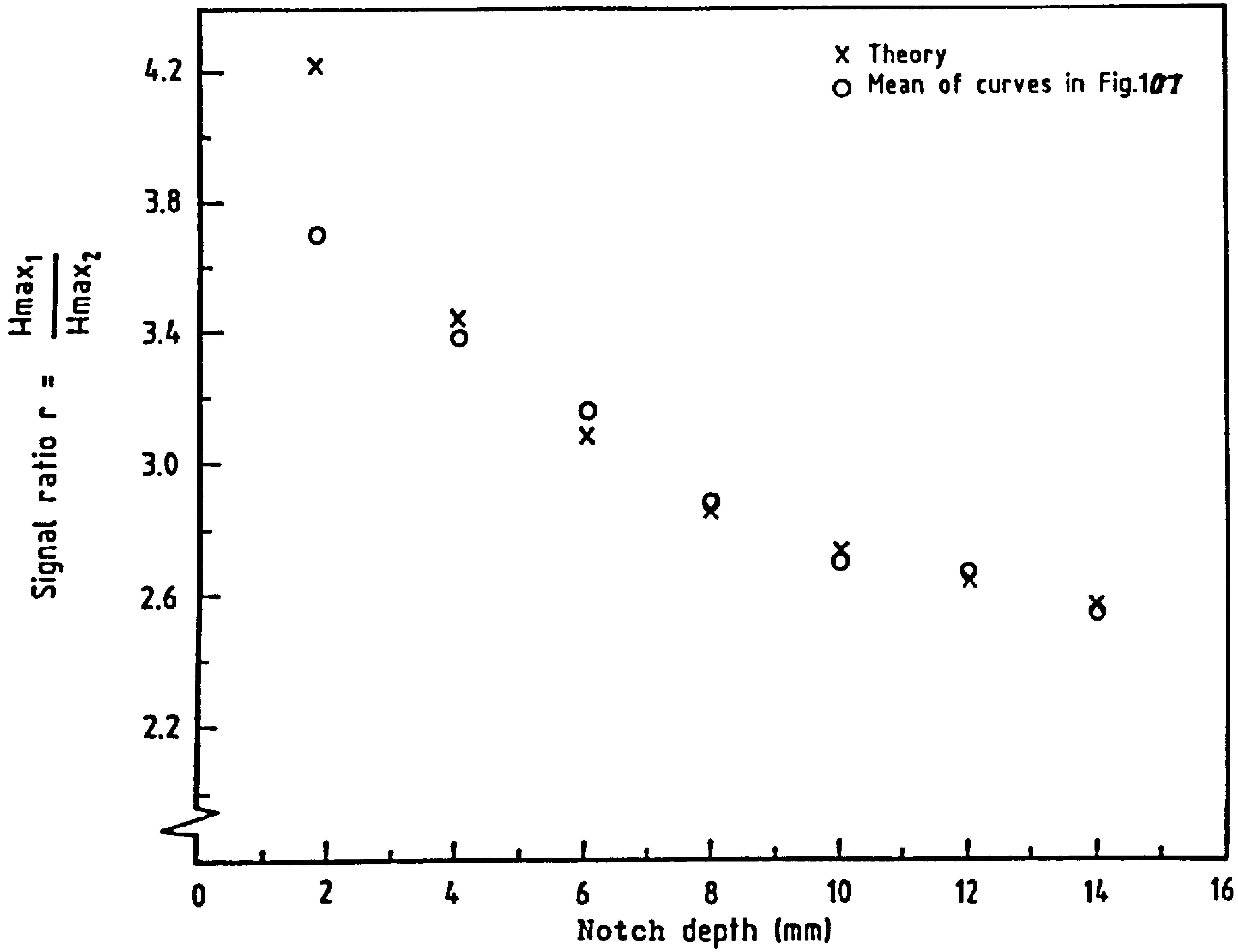

FIGURE 108. THEORETICAL AND EXPERIMENTAL VARIATION IN SIGNAL RATIO r AS A FUNCTION OF artificial crack DEPTH. THEORY REFERS TO SCAN HEIGHTS OF 2.2mm and 5.1mm, WITH EQUAL PROBE / AMPLIFIER SENSITIVITIES.

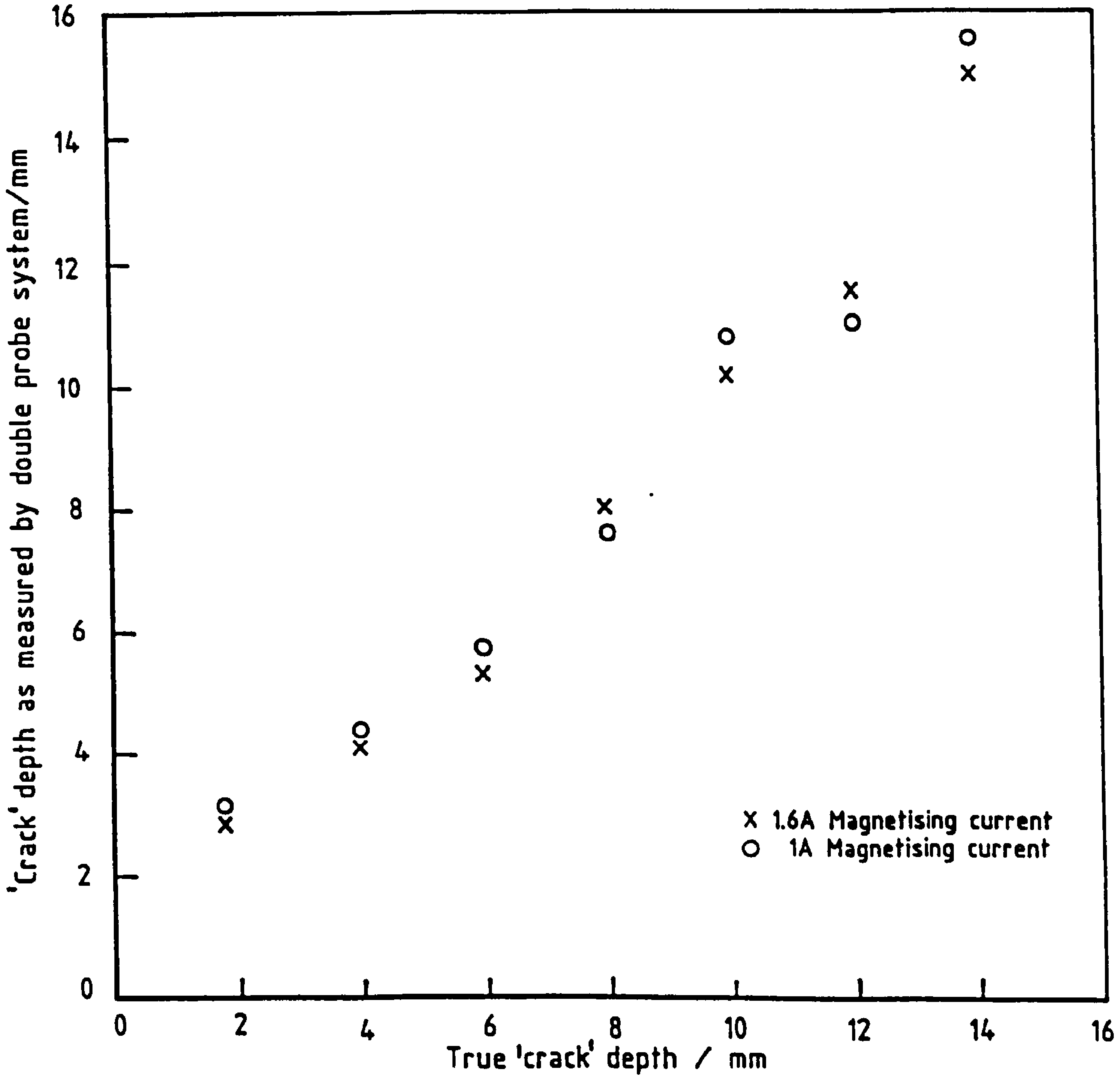

FIGURE 109. GRAPH TO SHOW HOW THE 'CRACK' DEPTH AS MEASURED BY THE DOUBLE PROBE SYSTEM COMPARES WITH THE ACTUAL 'CRACK' DEPTH, AT THE TWO MAGNETISATION LEVELS USED.

'Crack' refers to an artificial notch.

Magnetising current (Amps)	Extreme voltages (Volts)		Ratio of signals	Depth of specimen (mm)
	Near probe	Far probe		
1.6	-1.37 +1.56	-0.29 +0.49	3.756	1.8
1.0	-1.17 +1.25	-0.29 +0.37	3.667	
1.6	-1.38 +1.35	-0.41 +0.39	3.413	4.0
1.0	-1.09 +0.99	-0.31 +0.31	3.355	
1.6	-1.05 +1.05	-0.31 +0.35	3.182	6.0
1.0	-0.98 +0.96	-0.31 +0.31	3.129	
1.6	-1.50 +1.62	-0.49 +0.60	2.862	8.0
1.0	-1.11 +1.21	-0.35 +0.45	2.900	
1.6	-1.35 +1.21	-0.55 +0.39	2.723	10.0
1.0	-0.99 +0.84	-0.37 +0.31	2.691	
1.6	-0.92 +0.78	-0.37 +0.27	2.656	12.0
1.0	-0.74 +0.60	-0.29 +0.21	2.680	
1.6	-0.78 +0.47	-0.35 +0.14	2.551	14.0
1.0	-0.64 +0.35	-0.29 +0.10	2.538	

Figure 110. Results from the double probe system.

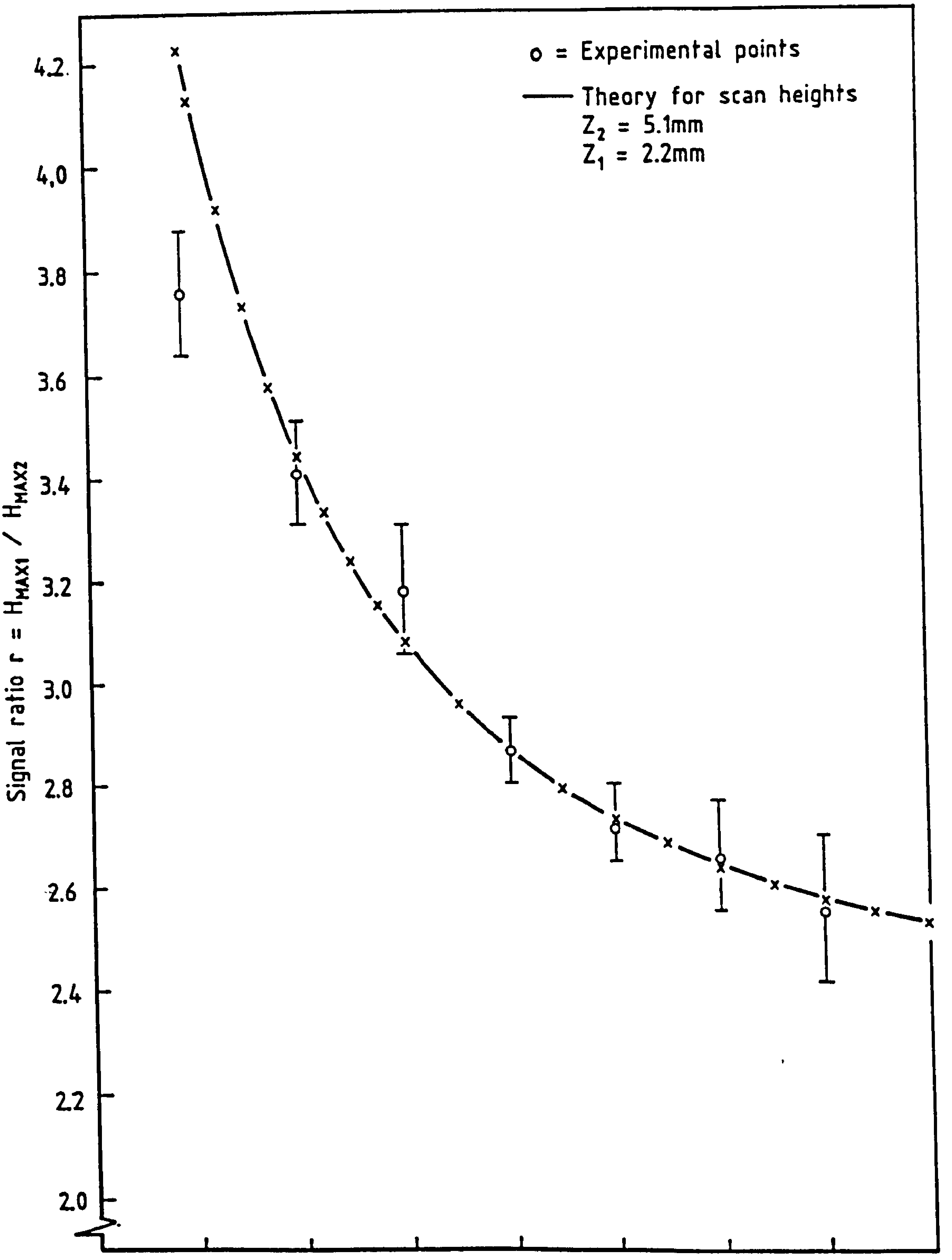

FIGURE 111. ERRORS INTRODUCED DUE TO LIMITED RESOLUTION IN MEASUREMENTS.

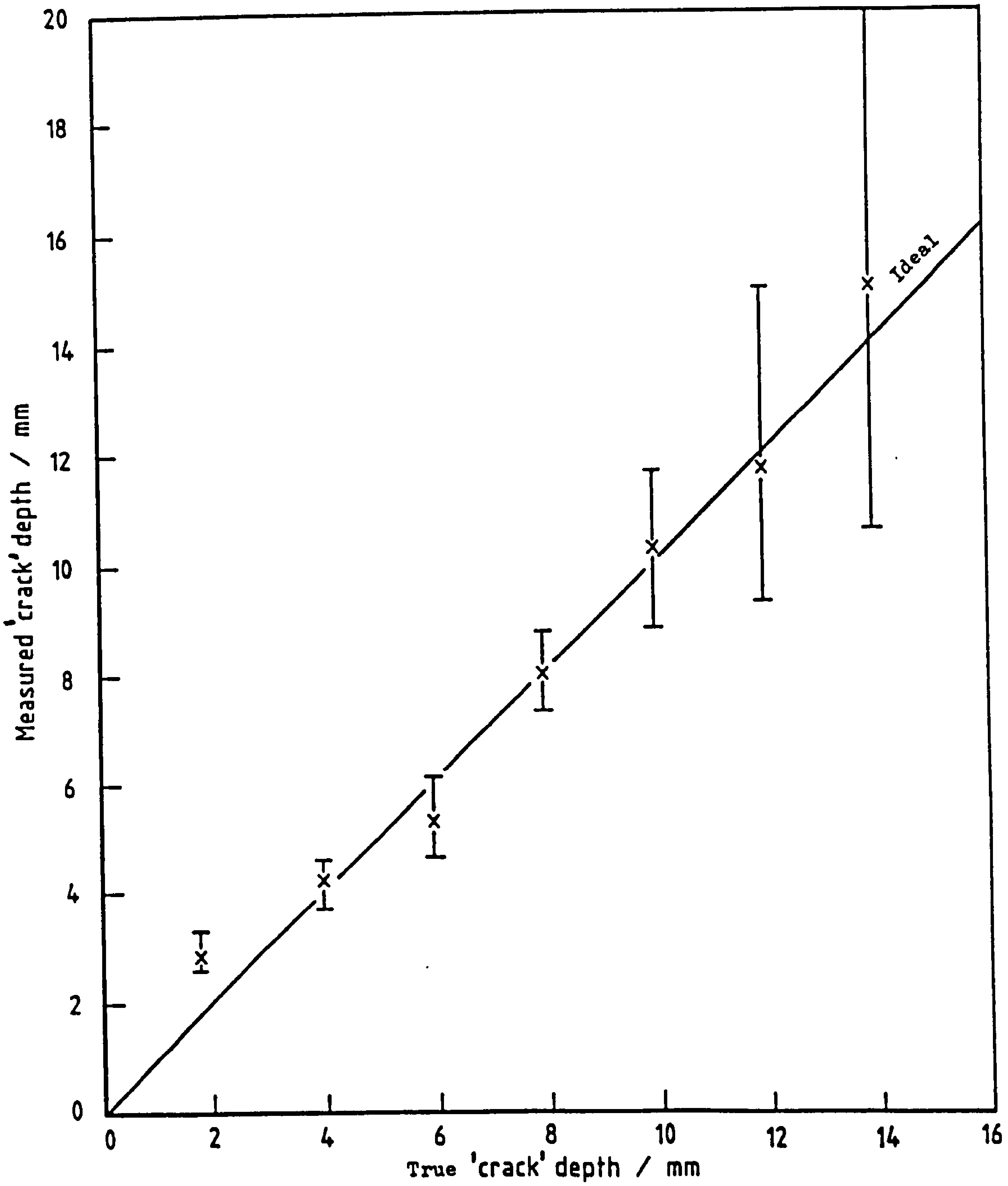

FIGURE112.PRACTICAL ERRORS IN MEASURED notch DEPTH DUE TO LIMITED RESOLUTION IN MEASUREMENTS.

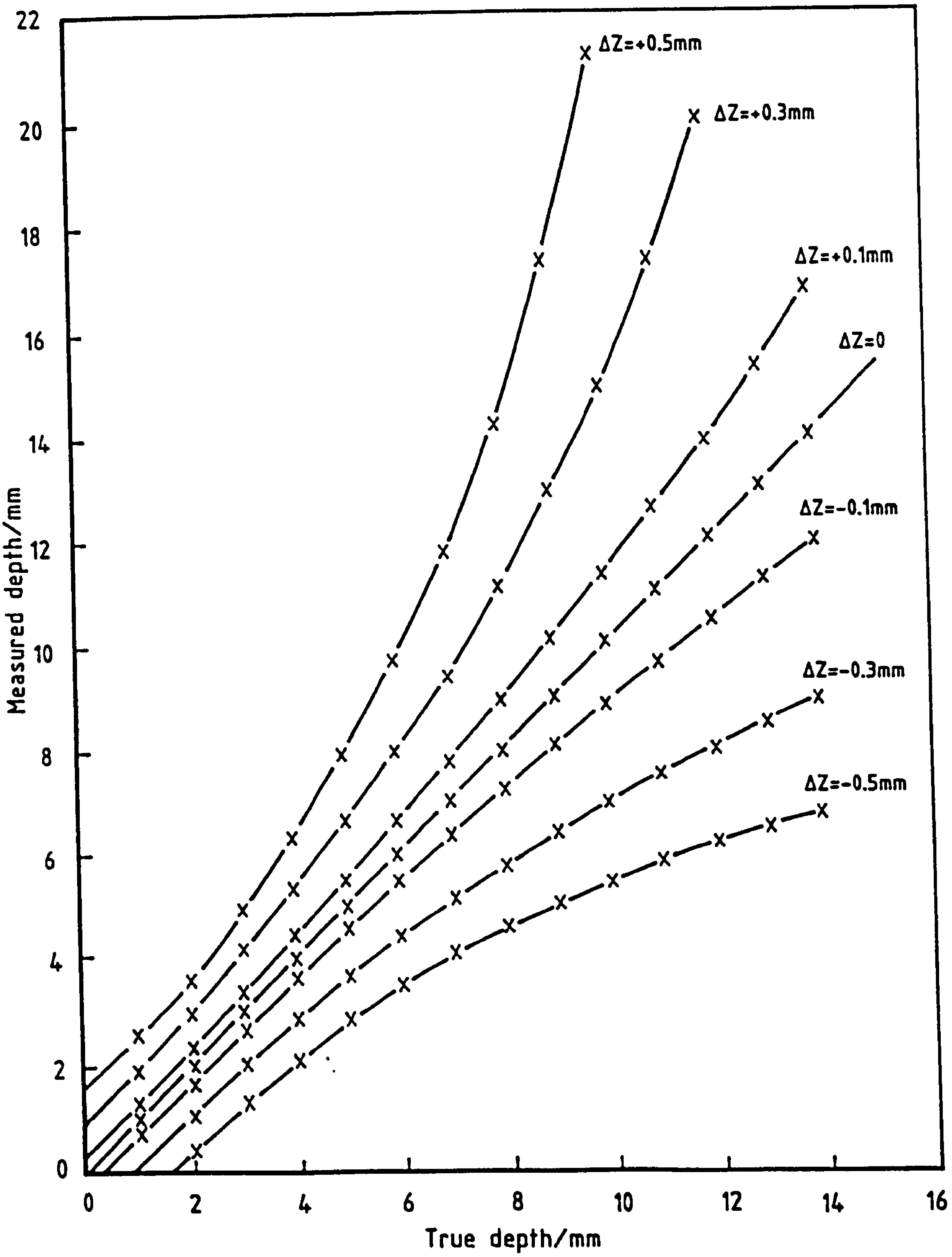

FIGURE 113. GRAPH TO SHOW HOW A COMMON ERROR IN STAND OFF ΔZ AFFECTS THE MEASURED 'CRACK' DEPTH, FOR NOMINAL SCAN HEIGHTS OF 2.2mm and 5.1mm IN THE DOUBLE PROBE SYSTEM.

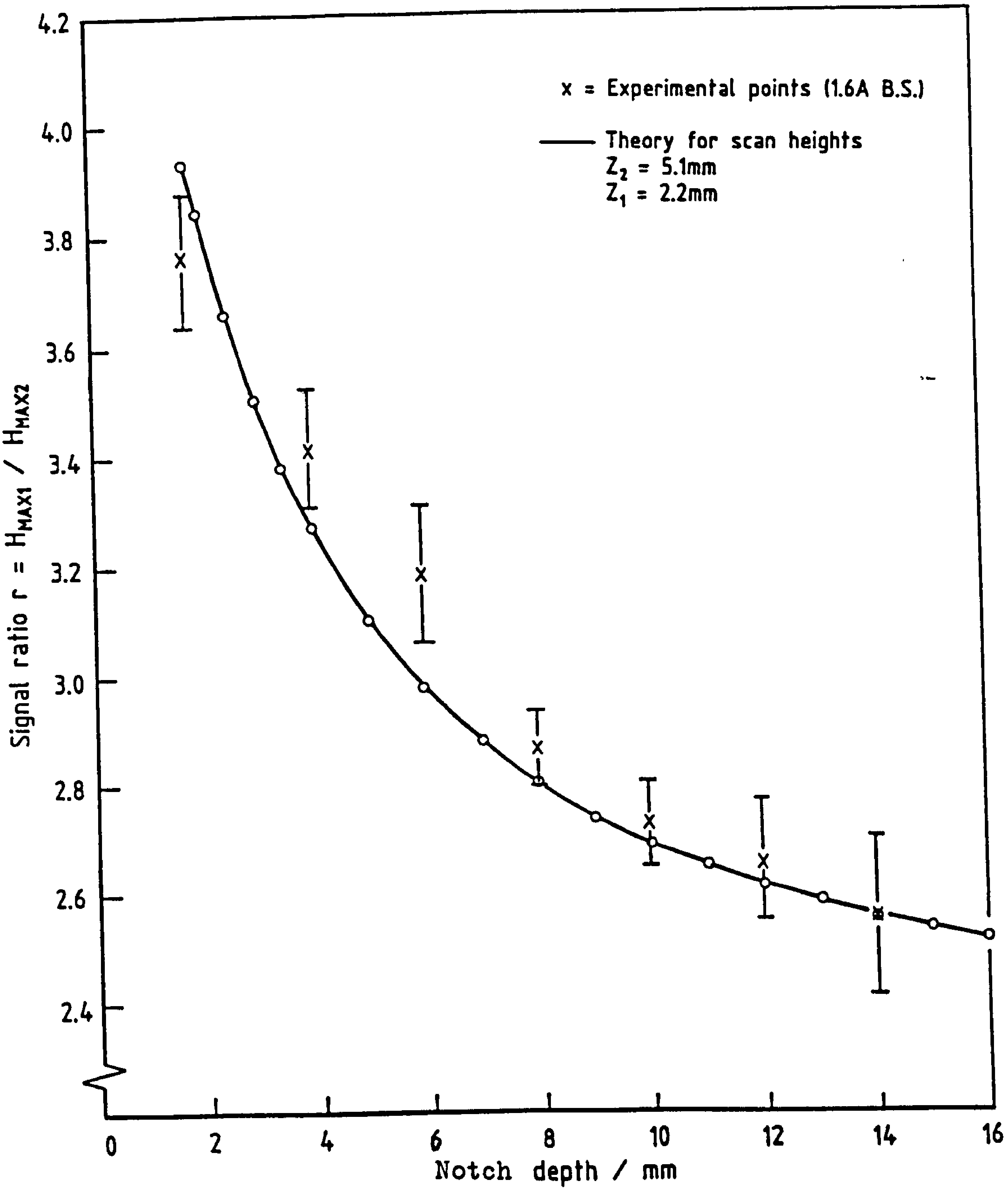

FIGURE 114. REFINED CALIBRATION CURVE WITH EXPERIMENTAL POINTS USING FINITE PROBE THEORY.

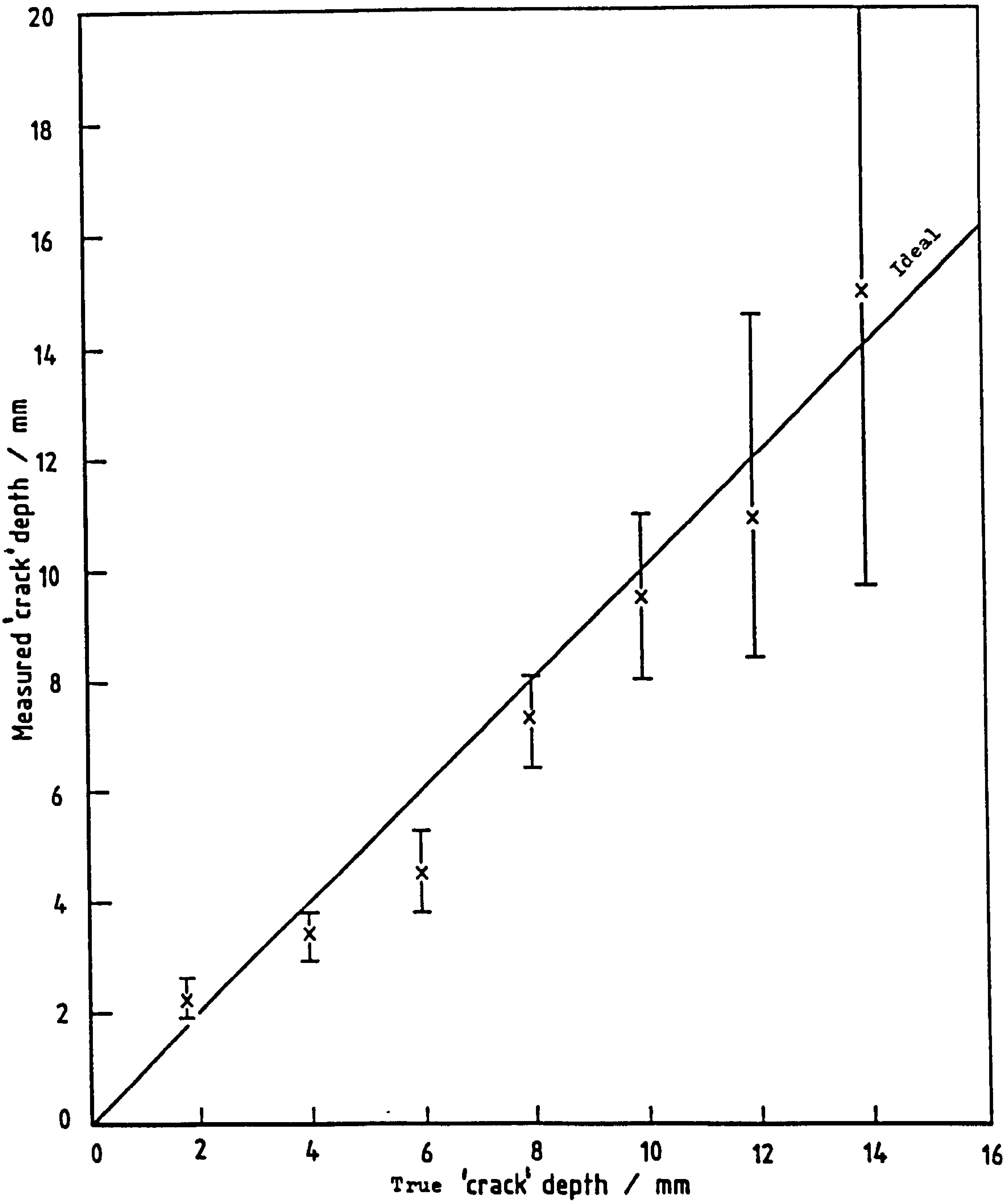

FIGURE 115. MEASURED VALUES OF notch DEPTH USING REFINED THEORY.

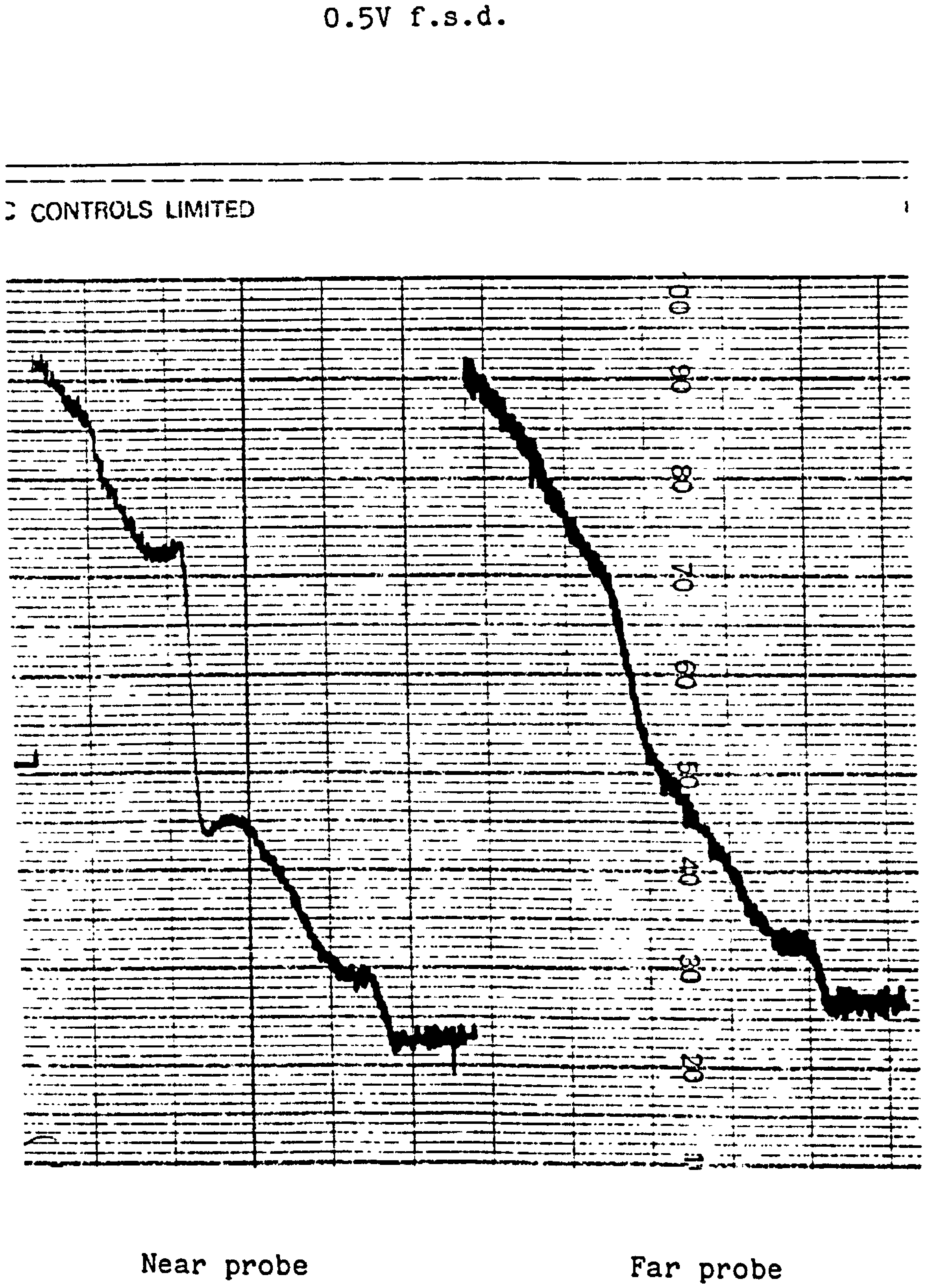

FIGURE 116. Signals produced by the double probe system from a genuine fatigue crack

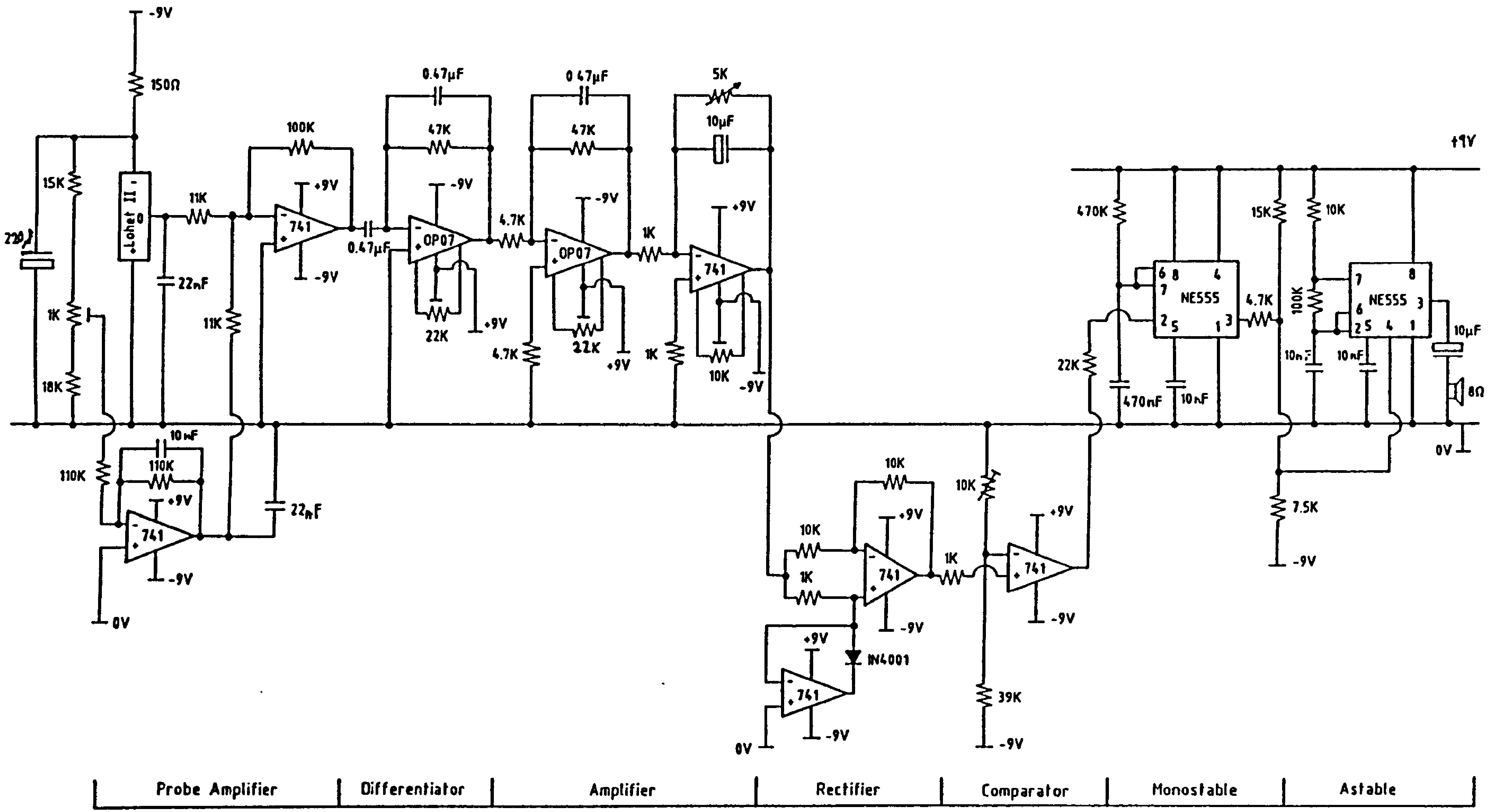

FIGURE 117. CRACK DETECTOR CIRCUIT.

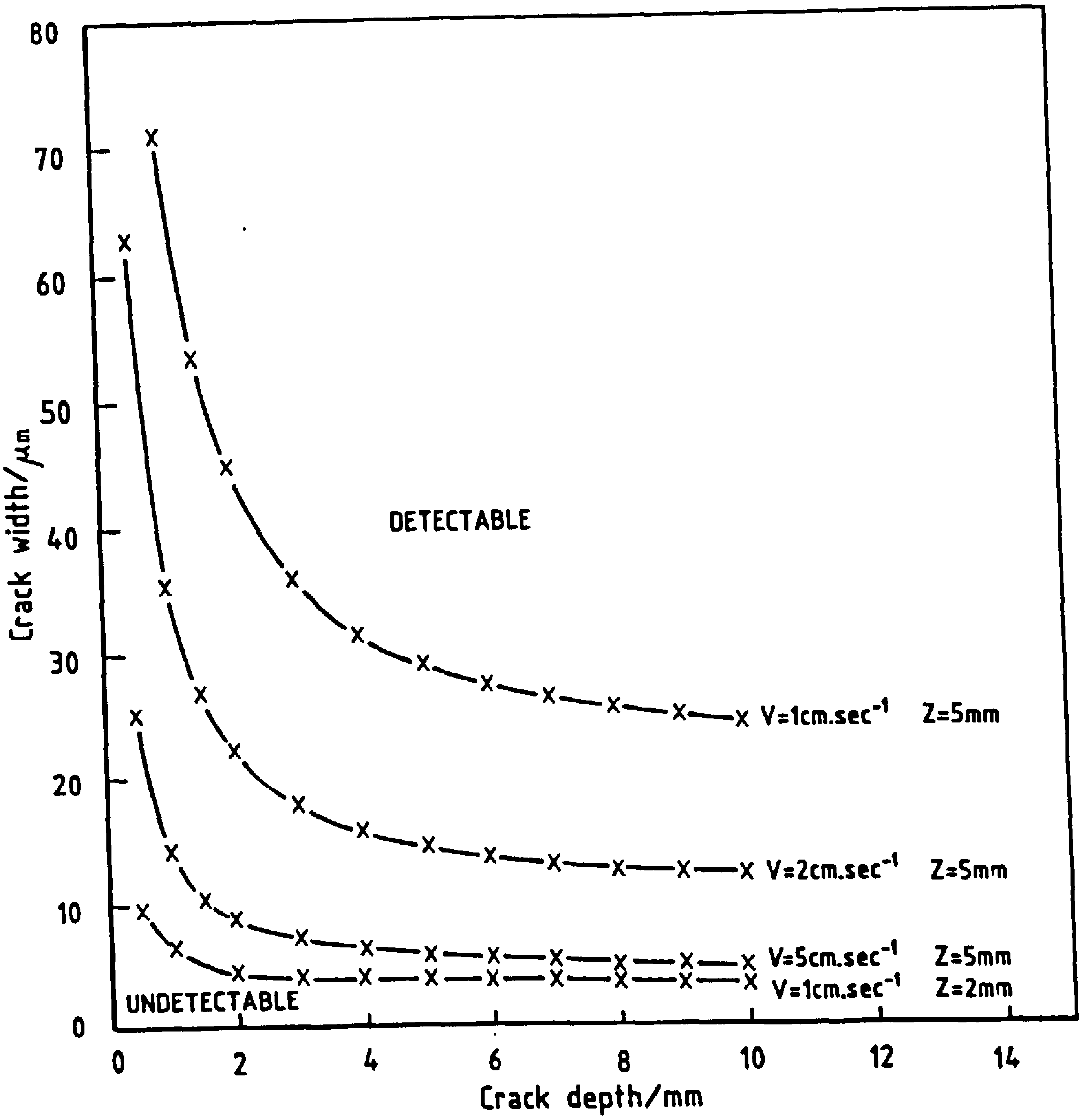

Figure 118. Graph to show limits of detection of differentiating probe for probe width 2K=0.178mm and varying probe speeds V and scan heights Z.

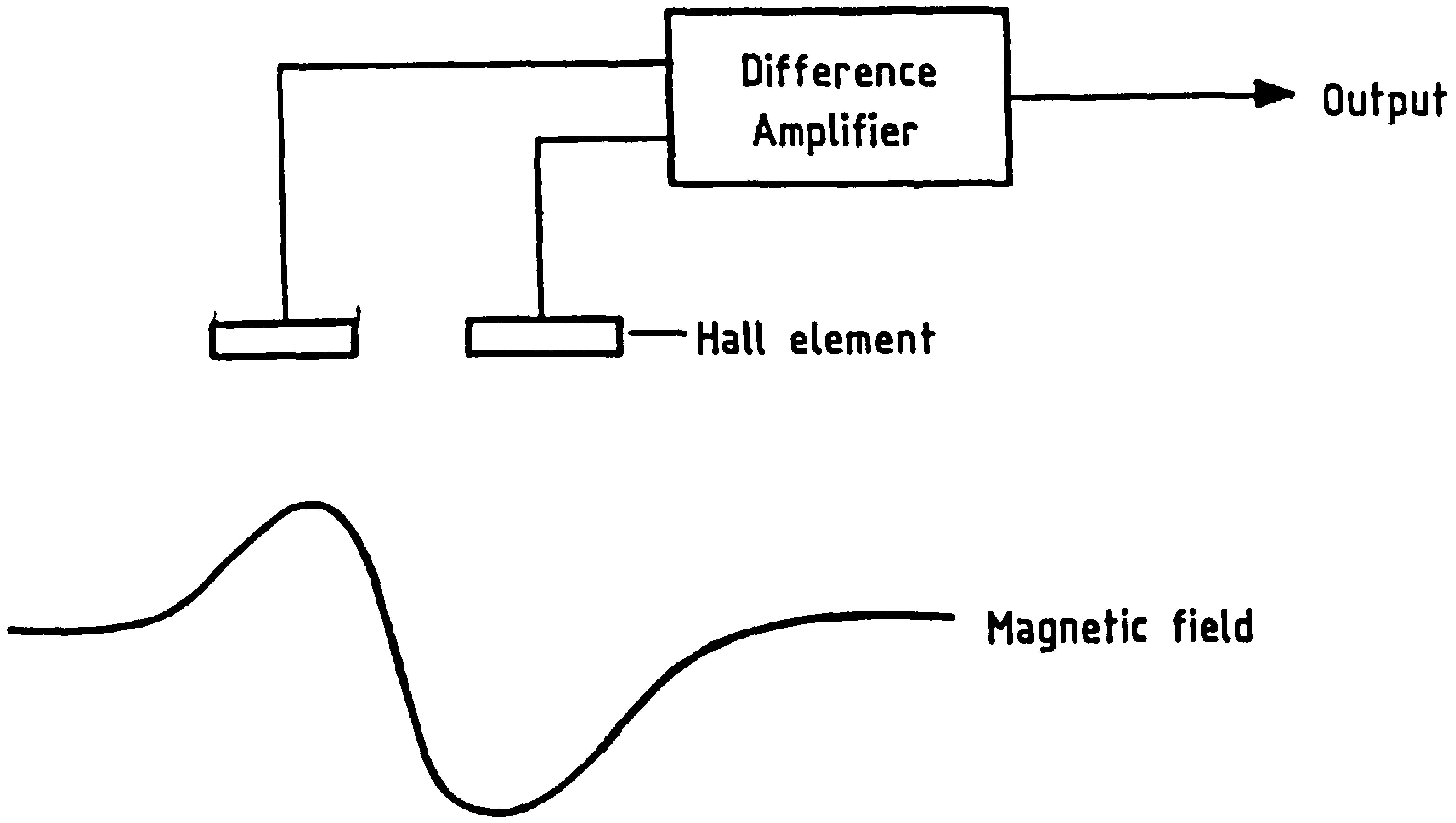

FIGURE 119. THE DIFFERENTIAL PROBE.

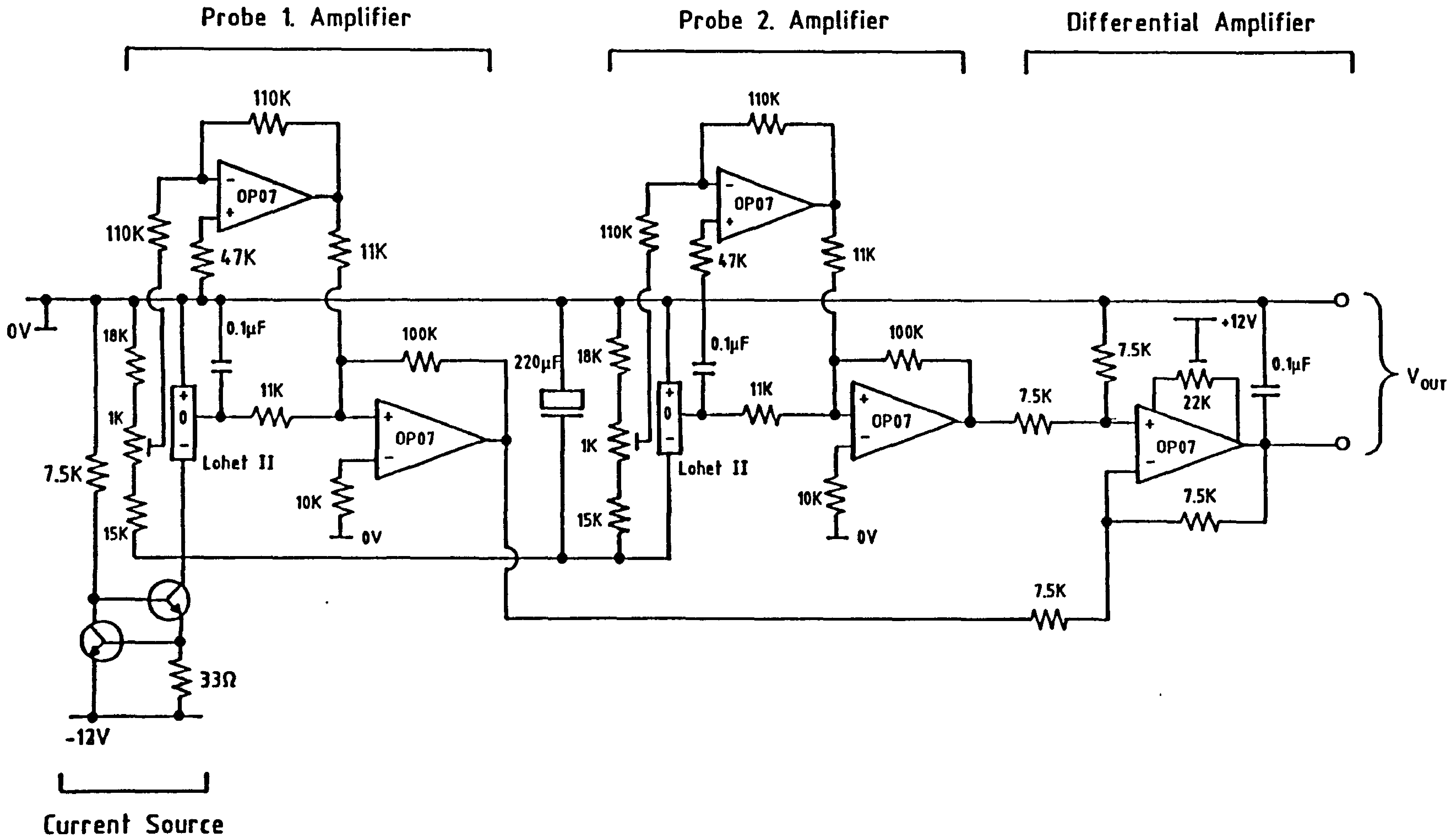

FIGURE 120. DIFFERENTIAL PROBE AMPLIFIER CIRCUIT.

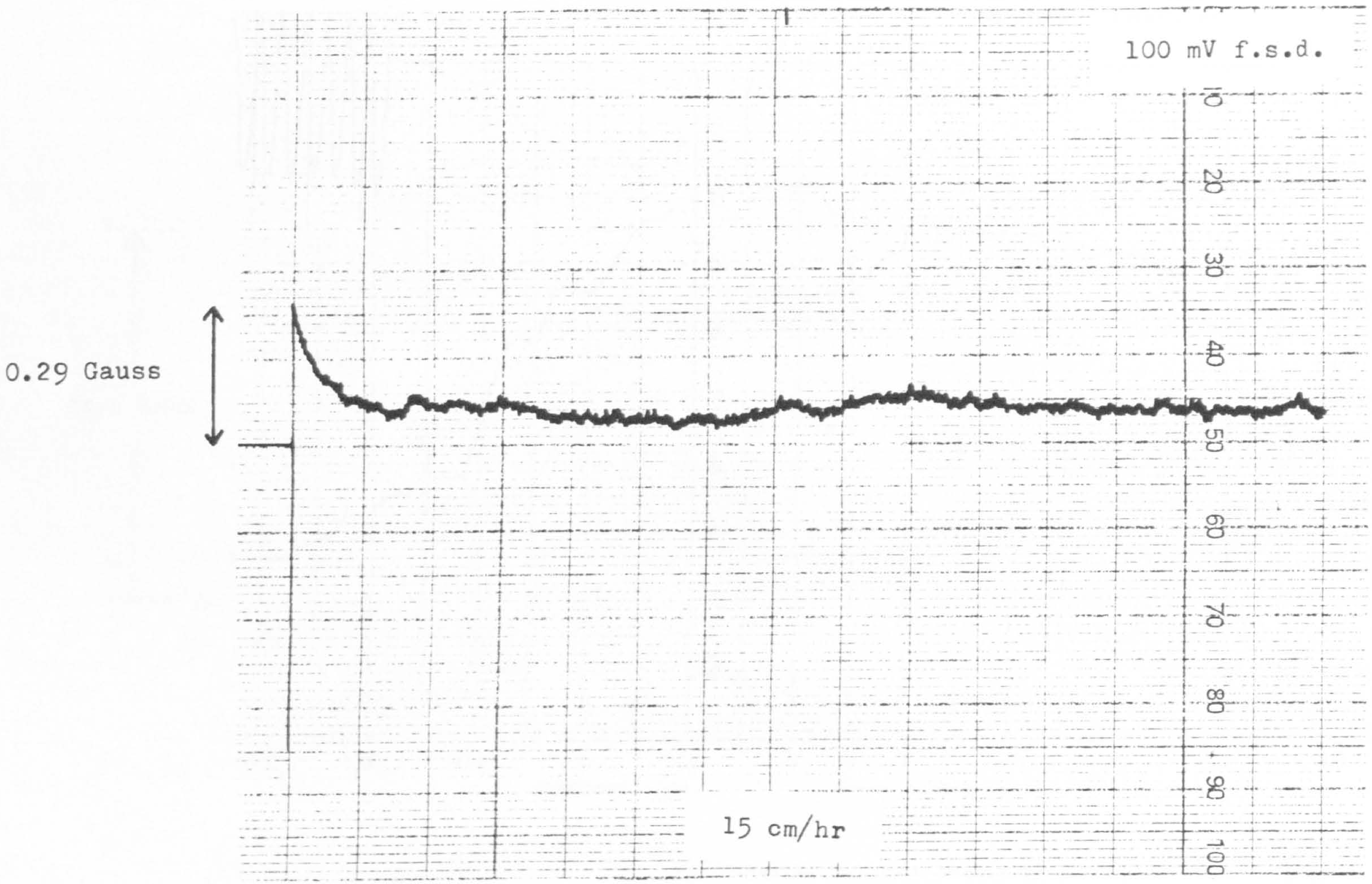

Figure 121. Differential probe zero drift.

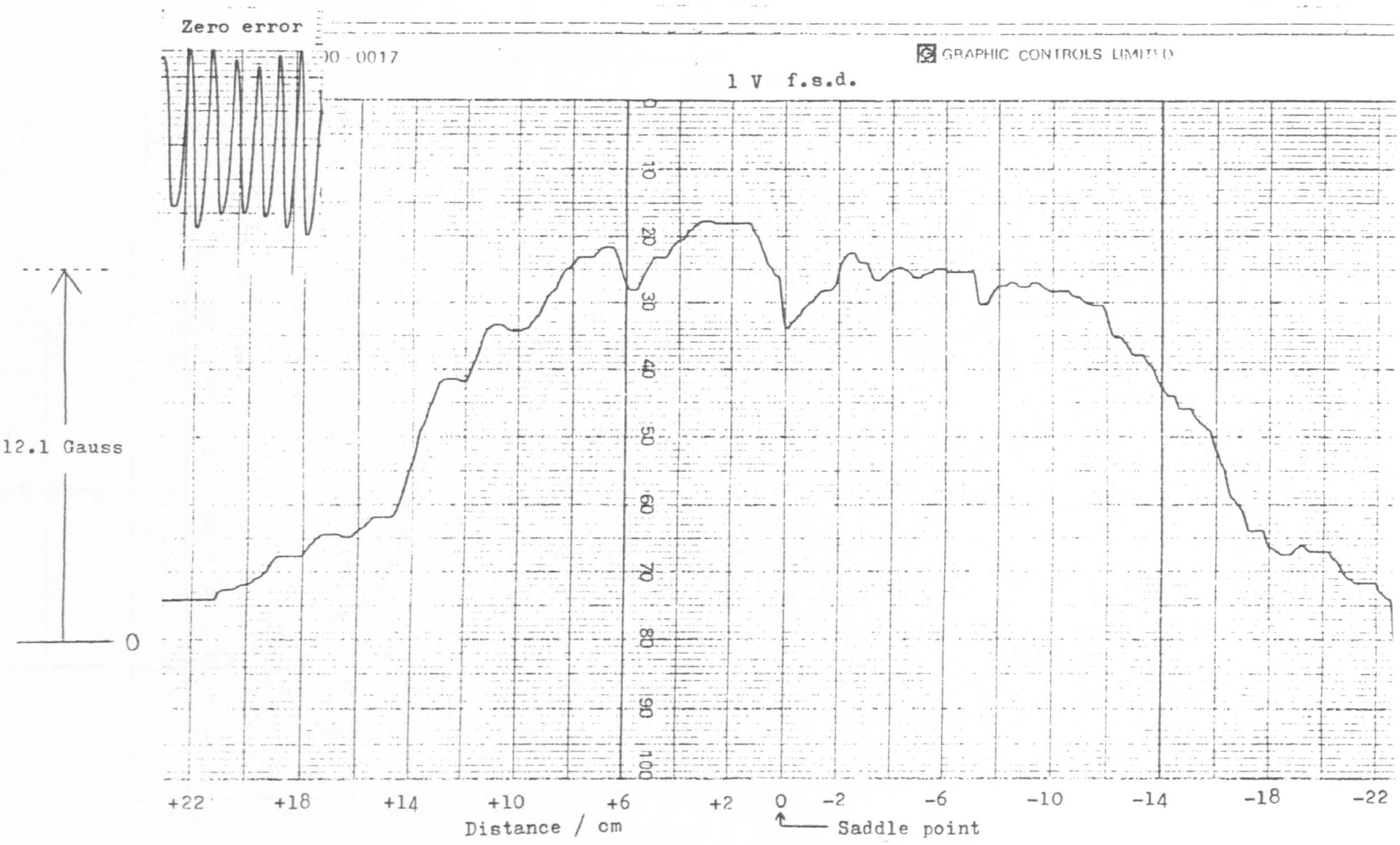

Differentiating probe D=30.9 cm
at 65 Gauss sec⁻¹ trigger level

FIGURE 122. Active Leakage Field - Forward direction.

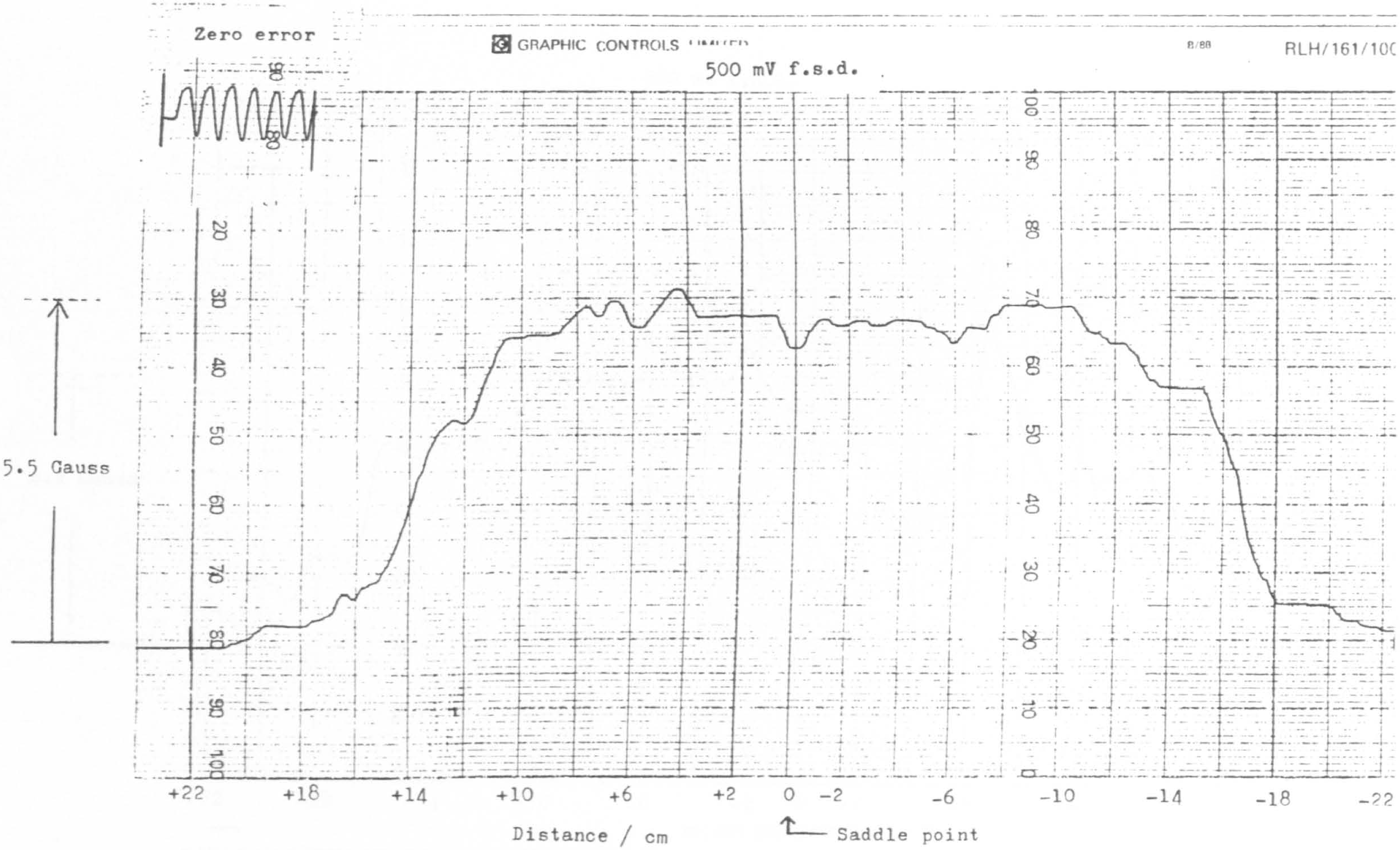

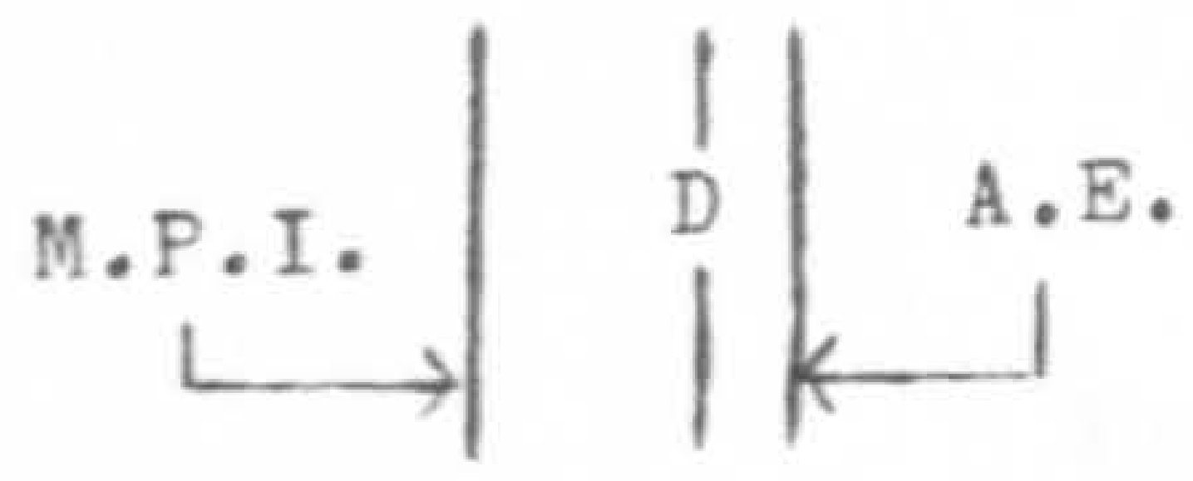

Acoustic Emissions = 29 cm

Differentiating Probe = 30.6 cm

M.P.I. = 34.2 cm (Full magnetisation)

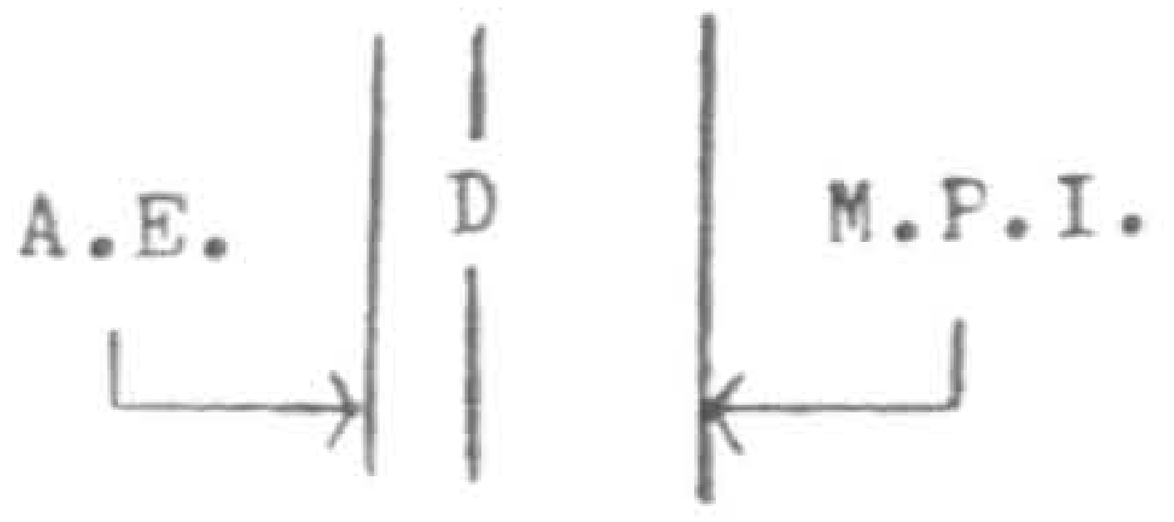

FIGURE 123. Residual Leakage Field.

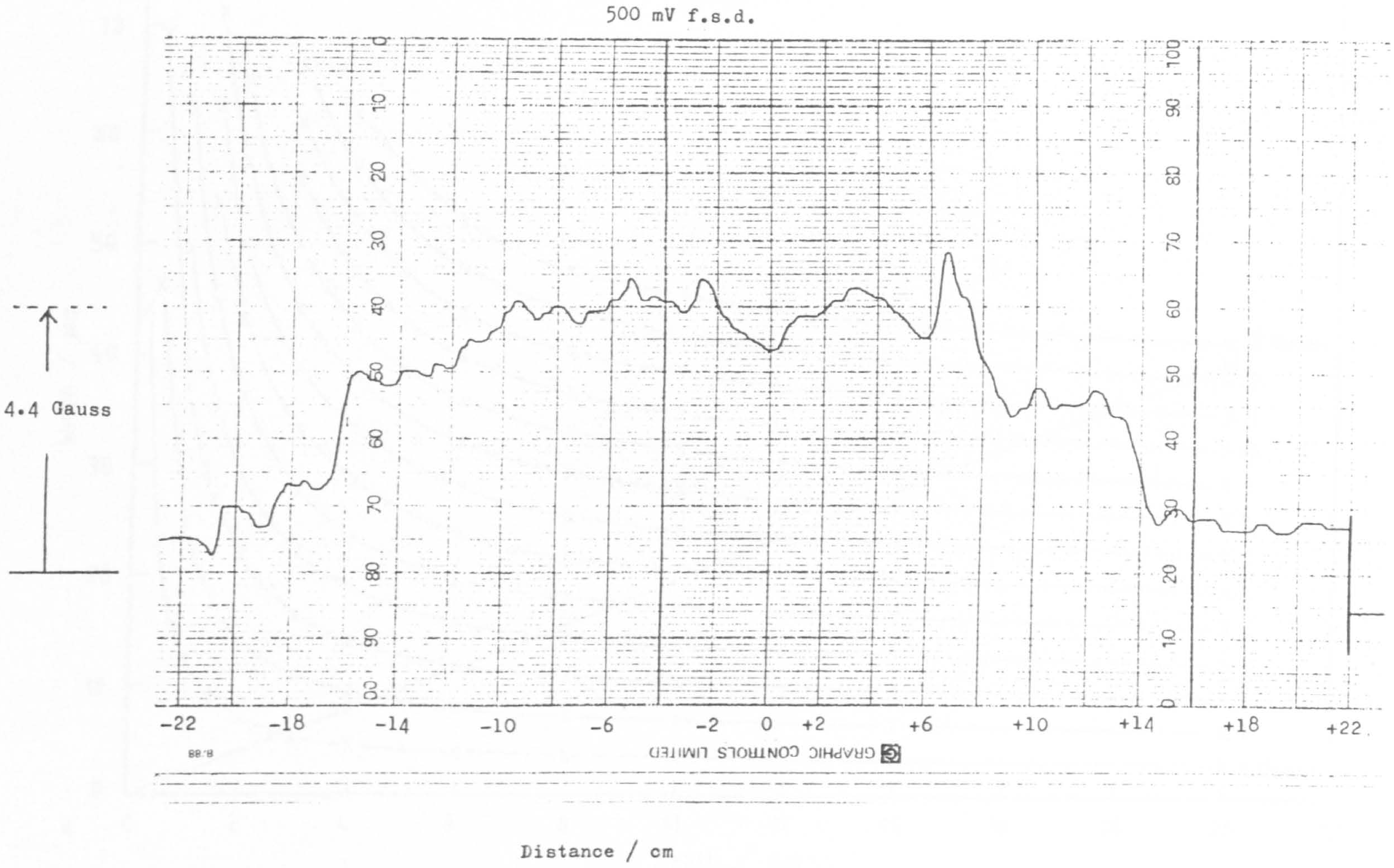

FIGURE 124. Active Leakage Field - Reverse direction.

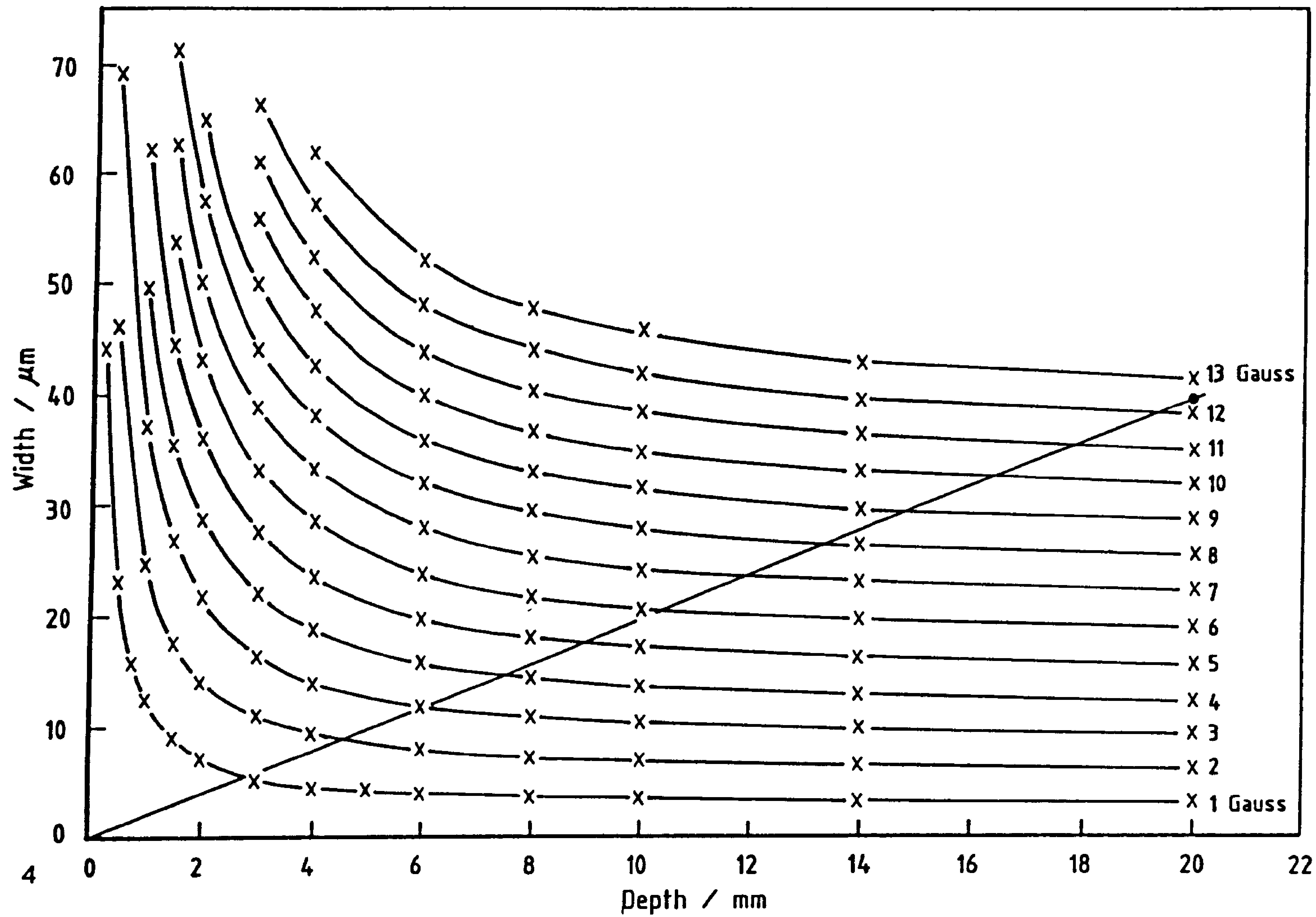

FIGURE 125. GRAPH TO ENABLE WIDTH AND DEPTH MEASUREMENT TO BE MADE ASSUMING A THROUGH CRACK (h = 20mm) AT THE HIGHEST LEAKAGE FIELD.

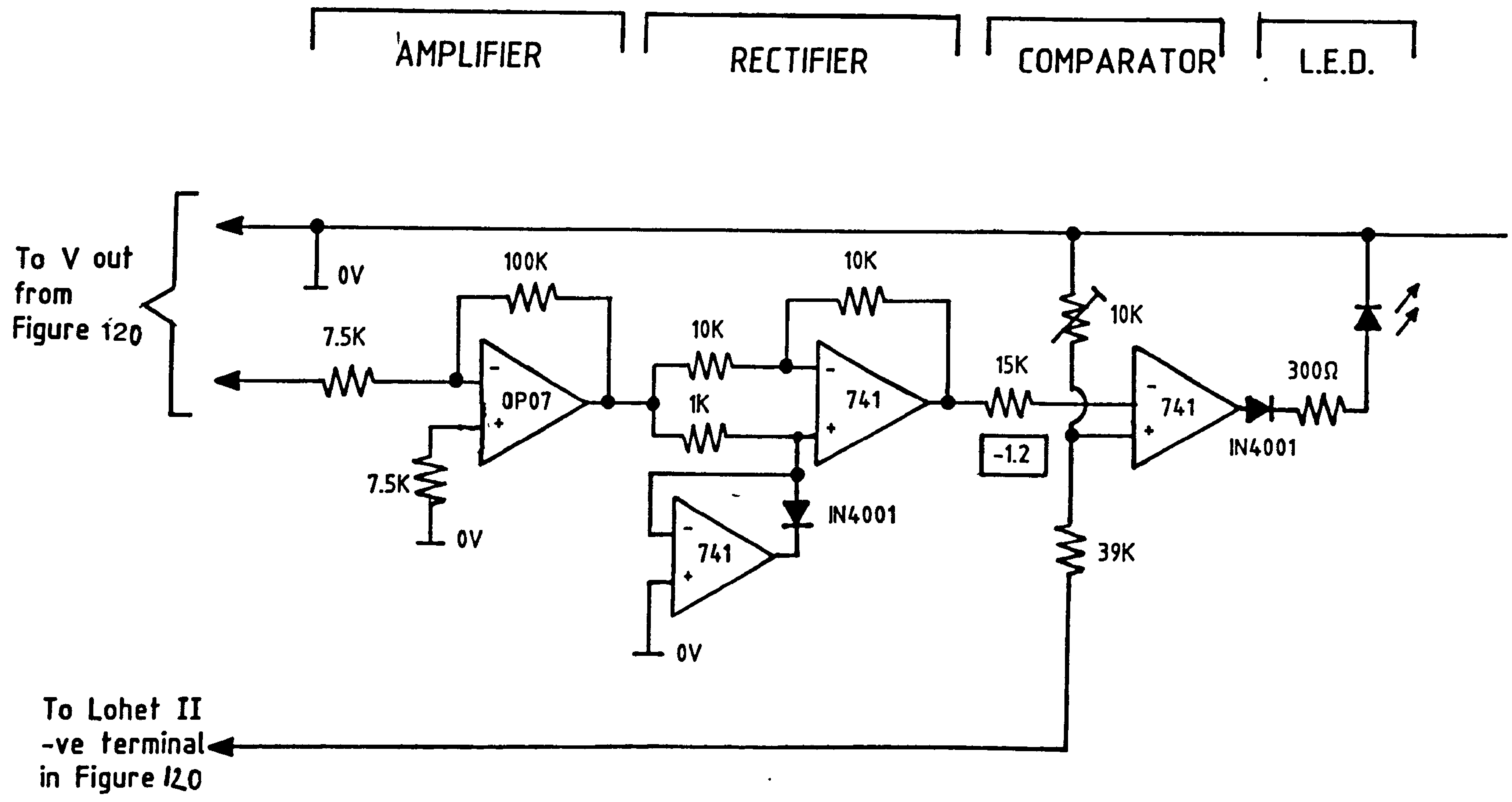

FIGURE 126. CIRCUIT TO TURN FIGURE 120 INTO A SIMPLE YES/NO CRACK DETECTOR.

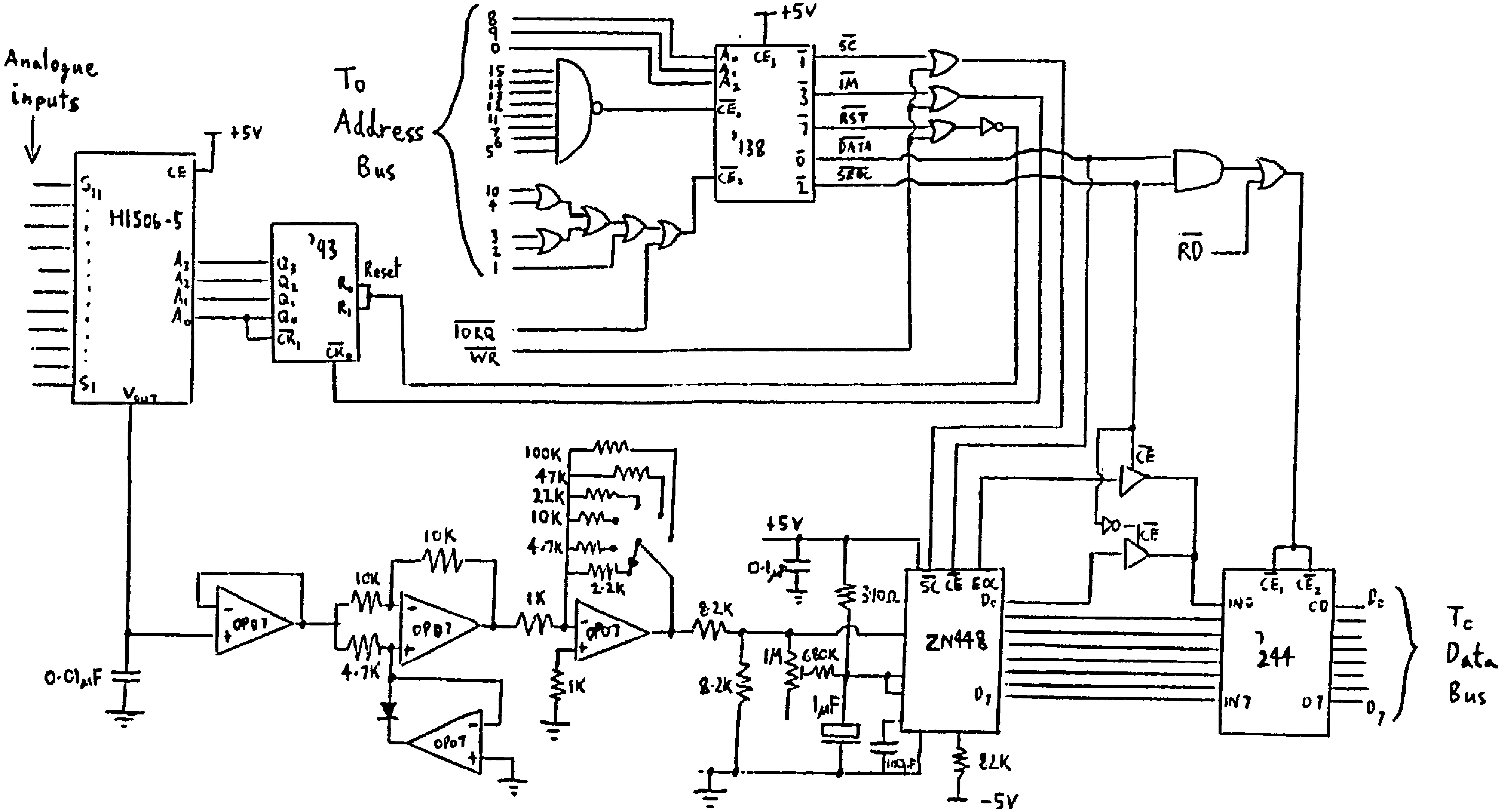

Address Decoding

A_{15}	A_{14}	A_{13}	A_{12}	/	A_{11}	A_{10}	A_9	A_8
1	1	1	1		1	0	X	X
A_7	A_6	A_5	A_4	/	A_3	A_2	A_1	A_0
1	1	1	0		0	0	0	X

A_0	A_9	A_8	
0	0	0	Data
0	0	1	Start Conversion (SC)
0	1	0	Search for end of conversion (SEOC)
0	1	1	Increment multiplexer (IM)
1	1	1	Reset multiplexer (RST)

Figure 127. Interface circuit for Amstrad CPC6128 computer.

11 Gauss f.s.d.

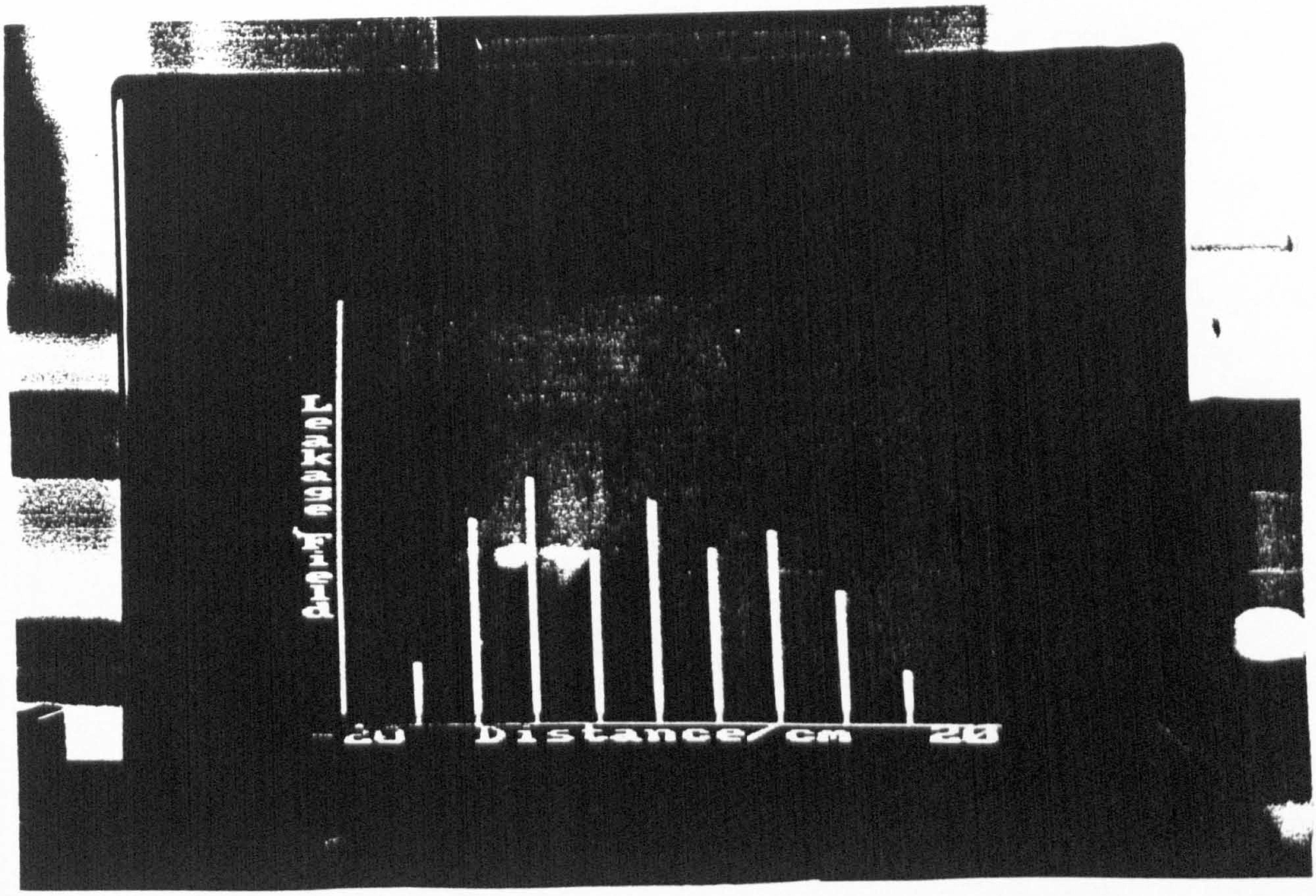

FIGURE 128. Multiple probe leakage field display